Geodynamic Modeling of Process Interactions at Continental Plate Boundaries

---

Esther Lina Heckenbach

Kumulative Dissertation
zur Erlangung des akademischen Grades
"doctor rerum naturalium"
(Dr. rer. nat.)
in der Wissenschaftsdisziplin Geophysik

eingereicht an der
Mathematisch-Naturwissenschaftlichen Fakultät
der Universität Potsdam
und
Sektion 2.5: Geodynamische Modellierung
des Helmholtz-Zentrum Potsdam Deutsches GeoForschungsZentrum GFZ

Ort und Datum der Disputation: Potsdam, den 3. Juli 2024

Betreuer
1. Dr. Sascha Brune, GFZ Potsdam, Universiät Potsdam
2. Dr. Matthias Rosenau, GFZ Potsdam

Gutachter
1. Dr. Sascha Brune, GFZ Potsdam, Universiät Potsdam
2. Dr. John Naliboff, New Mexico Institute of Mining and Technology
3. Dr. João Duarte, University of Lisbon

https://doi.org/10.25932/publishup-64750
https://nbn-resolving.org/urn:nbn:de:kobv:517-opus4-647500

Abstract

Plate tectonic boundaries constitute the suture zones between tectonic plates. They are shaped by a variety of distinct and interrelated processes and play a key role in geohazards and georesource formation. Many of these processes have been previously studied, while many others remain unaddressed or undiscovered. In this work, the geodynamic numerical modeling software ASPECT is applied to shed light on further process interactions at continental plate boundaries. In contrast to natural data, geodynamic modeling has the advantage that processes can be directly quantified and that all parameters can be analyzed over the entire evolution of a structure. Furthermore, processes and interactions can be singled out from complex settings because the modeler has full control over all of the parameters involved. To account for the simplifying character of models in general, I have chosen to study generic geological settings with a focus on the processes and interactions rather than precisely reconstructing a specific region of the Earth.

In Chapter 2, 2D models of continental rifts with different crustal thicknesses between 20 and 50 km and extension velocities in the range of 0.5–10 mm/yr are used to obtain a speed limit for the thermal steady-state assumption, commonly employed to address the temperature fields of continental rifts worldwide. Because the tectonic deformation from ongoing rifting outpaces heat conduction, the temperature field is not in equilibrium, but is characterized by a transient, tectonically-induced heat flow signal. As a result, I find that isotherm depths of the geodynamic evolution models are shallower than a temperature distribution in equilibrium would suggest. This is particularly important for deep isotherms and narrow rifts. In narrow rifts, the magnitude of the transient temperature signal limits a well-founded applicability of the thermal steady-state assumption to extension velocities of 0.5–2 mm/yr. Estimation of the crustal temperature field affects conclusions on all temperature-dependent processes ranging from mineral assemblages to the feasible exploitation of a geothermal reservoir.

In Chapter 3, I model the interactions of different rheologies with the kinematics of folding and faulting using the example of fault-propagation folds in the Andean fold-and-thrust belt. The evolution of the velocity fields from geodynamic models are compared with those from trishear models of the same structure. While the latter use only geometric and kinematic constraints of the main fault, the geodynamic models capture viscous, plastic, and elastic deformation in the entire model domain. I find that both models work equally well for early, and thus relatively simple stages of folding and faulting, while results differ for more complex situations where off-fault deformation and secondary faulting are present. As fault-propagation folds can play an important role in the formation of reservoirs, knowledge of fluid pathways, for example via fractures and faults, is crucial for their characterization.

Chapter 4 deals with a bending transform fault and the interconnections between tectonics and surface processes. In particular, the tectonic evolution of the Dead Sea Fault is addressed where a releasing bend forms the Dead Sea pull-apart basin, while a restraining bend further to the North resulted in the formation of the Lebanese mountains. I ran 3D coupled geodynamic and surface evolution models that included both types of bends in a single setup. I tested various randomized initial strain distributions, showing that basin asymmetry is a consequence of strain localization. Furthermore, by varying the surface process efficiency, I find that the deposition of sediment in the pull-apart basin not only controls basin depth, but also results in a crustal flow component that increases uplift at the restraining bend.

Finally, in Chapter 5, I present the computational basis for adding further complexity to plate boundary models in ASPECT with the implementation of earthquake-like behavior using the rate-and-state friction framework. Despite earthquakes happening on a relatively small time scale, there are many interactions between the seismic cycle and the long time spans of other geodynamic processes. Amongst others, the crustal state of stress as well as the presence of fluids or changes in temperature may alter the frictional behavior of a fault segment. My work provides the basis for a realistic setup of involved structures and processes, which is therefore important to obtain a meaningful estimate for earthquake hazards.

While these findings improve our understanding of continental plate boundaries, further development of geodynamic software may help to reveal even more processes and interactions in the future.

Zusammenfassung

Plattentektonische Grenzen bilden die Nahtstellen zwischen tektonischen Platten. Sie werden durch eine Vielzahl von unterschiedlichen und miteinander verknüpften Prozessen geformt und spielen eine Schlüsselrolle im Bereich der Georisiken und der Entstehung von Georessourcen. Viele dieser Prozesse sind bereits erforscht, während viele andere noch unbearbeitet oder unentdeckt sind. In dieser Arbeit wird die geodynamische numerische Modellierungssoftware ASPECT verwendet, um weitere Prozessinteraktionen an kontinentalen Plattengrenzen zu untersuchen. Im Gegensatz zu natürlichen Daten hat die geodynamische Modellierung den Vorteil, dass Prozesse direkt quantifiziert und alle Parameter über die gesamte Entwicklung einer Struktur analysiert werden können. Außerdem können Prozesse und Wechselwirkungen aus komplexen Zusammenhängen herausgefiltert werden, da der Modellierer volle Kontrolle über alle beteiligten Parameter hat. Um dem vereinfachenden Charakter von Modellen im Allgemeinen Rechnung zu tragen, habe ich mich für die Untersuchung allgemeiner geologischer Gegebenheiten entschieden, wobei der Schwerpunkt auf den Prozessen und Wechselwirkungen liegt, anstatt eine bestimmte Region der Erde genau zu rekonstruieren.

In Kapitel 2 werden 2D-Modelle von kontinentalen Rifts mit unterschiedlichen Krustendicken zwischen 20 und 50 km, sowie Extensionsgeschwindigkeiten im Bereich von 0,5–10 mm/Jahr verwendet, um eine Geschwindigkeitsgrenze für die Annahme eines thermischen Gleichgewichtszustandes zu erhalten, welcher üblicherweise verwendet wird, um die Temperaturfelder kontinentaler Rifts weltweit zu beschreiben. Da die Geschwindigkeit der tektonischen Deformation die der Wärmeleitung übersteigt, befindet sich das Temperaturfeld nicht im Gleichgewicht, sondern ist durch ein transientes, tektonisch induziertes Wärmestromsignal gekennzeichnet. Daraus ergibt sich, dass die Tiefen der Isothermen in den geodynamischen Entwicklungsmodellen flacher liegen, als es eine Temperaturverteilung im Gleichgewichtszustand vermuten ließe. Dies macht sich besondersbei tiefen Isothermen und *narrow Rifts* bemerkbar. In *narrow Rifts* begrenzt die Magnitude des transienten Temperatursignals eine fundierte Anwendbarkeit der thermischen Gleichgewichtsannahme auf Extensionsgeschwindigkeiten im Bereich von 0,5–2 mm/Jahr. Die Abschätzung des Temperaturfeldes der Erdkruste wirkt sich auf alle temperaturabhängigen Prozesse aus, von der Mineralzusammensetzung bis hin zur möglichen Nutzung eines geothermischen Reservoirs.

In Kapitel 3 modelliere ich die Wechselwirkungen verschiedener Rheologien mit der Kinematik von Auffaltungen und Verwerfungen am Beispiel von *fault-propagation folds* im andinen Falten- und Überschiebungsgürtel. Die Entwicklung der Geschwindigkeitsfelder aus geodynamischen Modellen wird mit denen aus *Trishear*-Modellen für dieselbe Struktur verglichen. Während letztere nur geometrische und kinematische Charakteristika der Hauptverwerfung verwenden, erfassen die geodynamischen Modelle sowohl viskose, wie auch plastische und elastische Verformung im gesamten Modellbereich. Meine Forschung zeigt, dass beide Modelle für frühe und damit vergleichbar einfache Phasen der Auffaltung und Verwerfung gleichermaßen gut anwendbar sind, während die Ergebnisse für komplexere Situationen, in denen Verformungen außerhalb der Hauptstörung sowie sekundäre Verwerfungen auftreten, auseinander gehen. Da *fault-propagation folds* eine wichtige Rolle bei der Bildung von Lagerstätten spielen können, ist Kenntnis zu Migrationswegen von Fluiden, zum Beispiel über Klüfte und Verwerfungen, für ihre Charakterisierung von entscheidender Bedeutung.

Kapitel 4 befasst sich mit Biegungen von Transformstörungen sowie den Zusammenhängen zwischen Tektonik und Oberflächenprozessen. Insbesondere wird die tektonische Entwicklung der Verwerfung am Toten Meer behandelt, wo eine von Extension geprägte Biegung der Verwerfung das *Pull-Apart*-Becken des Toten Meeres bildet, während eine weiter nördlich gelegene von Kompression geprägte Biegung zur Bildung eines Gebirgszuges im Libanon führte. Für dieses Kapitel habe ich gekoppelte 3D Modelle der Geodynamik und Oberflächenentwicklung genutzt sowie beide Arten von Biegungen in einem Modell erforscht. Das Testen von verschiedenen, zufälligen Initialspannungsverteilungen zeigte, dass die Asymmetrie des Beckens eine Folge der Spannungslokalisierung ist. Außerdem habe ich durch Variation der Oberflächenprozesseffizienz herausgearbeitet, dass die Sedimentierung im *Pull-Apart*-Becken nicht nur die Beckentiefe steuert, sondern auch zu einer Strömungskomponente von Erdkrustenmaterial führt, die die Ablift an der von Kompression geprägten Biegung der Transformstörung erhöht.

Anschließend stelle ich in Kapitel 5 die Implementierung von erdbebenähnlichem Verhalten unter Verwendung der *Rate-and-State* Gleichungen vor, welche die Grundlage für die Erweiterung der Komplexität von Plattengrenzenmodellen in ASPECT bildet. Obwohl Erdbeben auf einer relativ kurzen Zeitskala

stattfinden, gibt es viele Wechselwirkungen zwischen dem seismischen Zyklus und den langen Zeitspannen anderer geodynamischer Prozesse. Unter anderem können der Spannungszustand der Kruste sowie das Vorhandensein von Fluiden oder Änderungen der Temperatur das Reibungsverhalten eines Störungssegmentes verändern. Meine Arbeit liefert die Grundlage für einen realistischen Aufbau der beteiligten Strukturen und Prozesse, der wichtig ist, um eine aussagekräftige Abschätzung der Erdbebengefährdung zu erhalten.

Während diese Ergebnisse unser Verständnis der kontinentalen Plattengrenzen verbessern, kann die Weiterentwicklung geodynamischer Software dazu beitragen, in Zukunft weitere Prozesse und Wechselwirkungen aufzudecken.

Contents

Declaration of Author Contributions

Chapter 2 - published

Esther L. Heckenbach et al. (2021). "Is There a Speed Limit for the Thermal Steady-State Assumption in Continental Rifts?" en. In: *Geochemistry, Geophysics, Geosystems* 22.3, e2020GC009577

- Heckenbach: Main parts of modeling, writing - original draft, writing - review & editing, visualization
- Brune: model setup, modeling, writing - original draft, writing - review & editing, visualization
- Glerum: model setup, modeling, writing - original draft, writing - review & editing, visualization, software development
- Bott [Sippel]: writing - original draft, writing - review & editing

Chapter 3 - published

Berenice Plotek et al. (2022). "Kinematics of fault-propagation folding: Analysis of velocity fields in numerical modeling simulations". In: *Journal of Structural Geology* 162, p. 104703

- Plotek: Main parts of Methodology, Software, Validation, Formal analysis, Inves tigation, Data curation, Writing - original draft, Writing - review & editing.
- Heckenbach: Methodology, Software, Validation, Formal analysis, Investigation, Data curation, Writing - original draft, Writing - review & editing.
- Brune: Conceptualization, Methodology, Software, Validation, Formal analysis, Investigation, Data curation, Supervision, Project administration, Funding acquisition, Writing - original draft, Writing - review & editing.
- Cristallini: Conceptualization, Methodology, Software, Validation, Formal analysis, Investigation, Data curation, Supervision, Project administration, Writing - original draft, Writing - review & editing.
- Likerman: Formal analysis, Writing - review & editing.

Chapter 4 - minor revisions requested

Esther L. Heckenbach et al. (2024 subm.). "3D Interaction of Tectonics and Surface Processes explains Fault Network Evolution of the Dead Sea Fault". In: *Tektonika*

- Heckenbach: Main parts of model setup, modeling, writing - original draft, writing - review & editing, visualization, software development
- Brune: model setup, modeling, writing - original draft, writing - review & editing, visualization
- Glerum: model setup, modeling, writing - original draft, writing - review & editing, visualization
- Granot: writing & visualization: Regional geology of the Dead Sea Fault
- Hamiel: writing & visualization: Regional geology of the Dead Sea Fault
- Sobolev: guidance for modeling and concept
- Neuharth: software development, model setup

Chapter 5 - in preparation

Esther L. Heckenbach et al. (in prep.). "Implementing and benchmarking rate-and-state friction in ASPECT". in: *Preparation*

- Heckenbach: software development, model setup, writing
- Glerum: software development, review & guidance
- Brune: review & guidance
- Sobolev: guidance for model setup & software development

Chapter 5 - in preparation

Anne Glerum et al. (in prep.). "Particle-in-cell versus field methods in ASPECT". in: *Preparation*

- [...]
- Heckenbach: problem identification, small part of software development, preparation of one benchmark problem
- [...]

Glerum, Anne, Robert Myhill, John Naliboff, Dan Sandiford, Rene Gassöller, Juliane Dannberg, Elbridge Gerry Puckett, Mack Gregory, Cedric Thieulot, Esther Heckenbach, Maaike Weerdesteijn, Dylan Vasey, David Quiroga, Daniel Douglas, Derek Neuharth, Sascha Brune, and Fiona Clerc (in prep.). "Particle-in-cell versus field methods in ASPECT". In: *Preparation.*

Heckenbach, Esther L., Sascha Brune, Anne C. Glerum, and Judith Bott (2021). "Is There a Speed Limit for the Thermal Steady-State Assumption in Continental Rifts?" en. In: *Geochemistry, Geophysics, Geosystems* 22.3, e2020GC009577.

Heckenbach, Esther L., Sascha Brune, Anne C. Glerum, Roi Granot, Yariv Hamiel, Stephan V. Sobolev, and Derek Neuharth (2024 subm.). "3D Interaction of Tectonics and Surface Processes explains Fault Network Evolution of the Dead Sea Fault". In: *Tektonika.*

Heckenbach, Esther L., Anne C. Glerum, Sascha Brune, and Stephan V. Sobolev (in prep.). "Implementing and benchmarking rate-and-state friction in ASPECT". In: *Preparation.*

Plotek, Berenice, Esther Heckenbach, Sascha Brune, Ernesto Cristallini, and Jeremías Likerman (2022). "Kinematics of fault-propagation folding: Analysis of velocity fields in numerical modeling simulations". In: *Journal of Structural Geology* 162, p. 104703.

List of Figures

List of Tables

List of Abbreviations

CFL	Courant–Friedrichs–Lewy
DSB	Dead Sea Basin
DSF	Dead Sea Fault
FEM	finite element method
GPE	gravitational potential energy
PR	Pull Request
RSF	rate-and-state friction
VEP	visco-elast-plastic
VP	visco-plastic
VS	velocity strengthening
VW	velocity weakening

Introductory Explanations

Initially, the subject of this thesis was the modeling of great earthquakes on subduction zones including the implementation of a rate-and-state friction framework into the geodynamic modeling software ASPECT. However, this work could not be finished and published yet as my tests revealed a major miscommunication within the visco-elasto-plastic rheology of ASPECT for very short term scale processes. Fixing this flaw, though almost finished, took almost two and a half years as of today. To reflect the advances made and provide guidance for potential future users and developers, I include my work on this subject in Chapter 5 even though it did not produce publishable results yet. The revised visco-elastic-plastic rheology is soon going to be merged to ASPECT main as Pull Request (PR) #4370. A paper that includes detailed testing of the new functionalities is in preparation and will be submitted by Glerum et al. (in prep.) with the preliminary title *Particle-in-cell versus field methods in ASPECT*.

Glerum, Anne, Robert Myhill, John Naliboff, Dan Sandiford, Rene Gassöller, Juliane Dannberg, Elbridge Gerry Puckett, Mack Gregory, Cedric Thieulot, Esther Heckenbach, Maaike Weerdesteijn, Dylan Vasey, David Quiroga, Daniel Douglas, Derek Neuharth, Sascha Brune, and Fiona Clerc (in prep.). "Particle-in-cell versus field methods in ASPECT". In: *Preparation*.

1 General Introduction

Plate tectonics have been shaping our Earth for billions of years (e.g. Davies, 1992; Stern, 2007; Palin et al., 2021, and references therein). Plate boundaries are the sites of both major hazards (e.g. Isacks et al., 1968) and the accumulation of resources (e.g. Rona, 1983). Furthermore, they may reveal the constant movement within the Earth's interior to the naked eye e.g. when long built-up stresses are released during an earthquake or distinct topographical features like offset streams catch the eye (Wallace, 1968). But there are also many processes such as heat transport that are more hidden to the human observer since they evolve slowly and over long time scales or manifest deep within the Earth's crust. Nonetheless, it is some of these processes that are crucial for the formation of resources like hydrocarbons or geothermal heat.

Enhancing the understanding of plate boundary processes is a major challenge since observations of many variables are sparse, indirect or nonexistent and a multitude of interactions obscure the impact of single processes (e.g. Satake et al., 2007; McCaffrey, 2008). One key to approach this task is geodynamic modeling where processes can be singled out and their impact tested and quantified. State-of-the-art software can handle increasingly realistic models with many processes included. Furthermore, computation in 2D and 3D is possible on many temporal and spatial scales. Temporal scales may range from milliseconds when it comes to earthquakes, to millions of years e.g. when looking at mountain building. Similarly, spatial scales of millimeters to hundreds of kilometers may be relevant, depending on the research question (e.g. Zelst et al., 2021). Including the interactions of these multiple temporal and spatial scales is one of the goals of this thesis.

In this Chapter, I first present the three major plate boundary types before I give an overview about interactions at plate boundaries and the spatial and temporal scales present in the models of this thesis. I then introduce the geodynamic modeling software ASPECT (Kronbichler et al., 2012; Heister et al., 2017) and how it deals with the multitude of scales and interactions at plate boundaries.

1.1 Plate Boundary Types

There are three stress regimes that can be expected in the Earth's crust depending on the directions of the principal stresses (Fig. 1.1)(Zang et al., 2009, and references therein). This results in three types of plate boundaries:

- convergent boundaries characterized by thrust or reverse faulting with the maximum principal stress σ_1 being horizontal, orthogonal to the direction of faulting
- divergent boundaries characterized by normal faulting with σ_1 being vertical
- transform boundaries characterized by strike-slip faulting with σ_1 being horizontal, parallel to the direction of faulting

Examples of all three types of plate boundaries are being modeled in this thesis. Their occurrence is

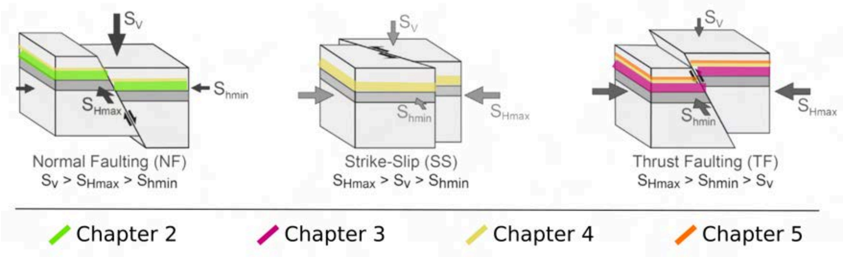

Figure 1.1: The three main stress regimes and resulting faults. The size of the arrows shows the relative magnitude of the stress directions. S_v vertical stress, S_{Hmax} maximum horizontal stress, S_{hmin} minimum horizontal stress. The colors show the main occurrences of these faulting regimes per Chapter of this thesis. Modified from Heidbach (2018)

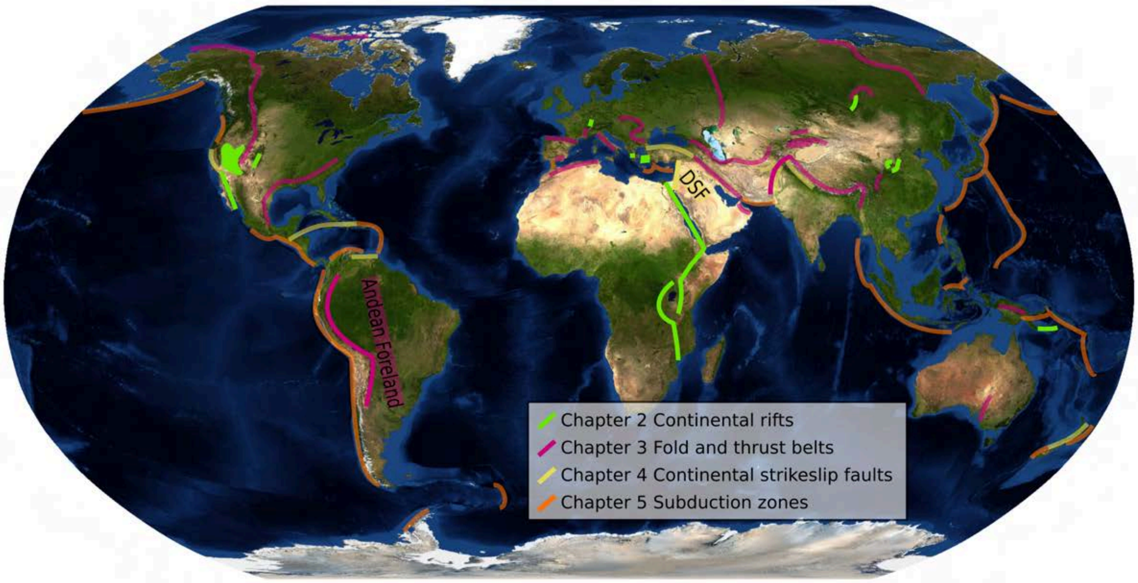

Figure 1.2: Main example areas for the plate boundaries types discussed in this thesis. Locations discussed in detail are opac while others are transparent. Green: Continental rifts in Chapter 2, locations from Heckenbach et al. (2021) and references therein. Red: Fold and thrust belts in Chapter 3, locations from Goffey et al. (2010). Yellow: Continental strike-slip faults in Chapter 4, locations from Mann (2007) and references therein. Orange: Subduction zones in Chapter 5, locations from Schellart et al. (2013).

visualized on the map in Figure 1.2. In the following, I will describe their characteristics in more detail by discussing main features during their formation, what kind of resources can be expected and what aspects are modeled in which chapters of this work.

(1) Convergent plate boundaries form where two tectonic plates move towards each other (Wortel et al., 1986; Catlos et al., 2023, and references therein). These zones are therefore characterized by high compressive stresses which results in crustal shortening by folding and faulting. Over long time scales of millions of years, this aggregates to large mountain ranges, while it may be expressed as a series of powerful earthquakes on shorter time scales of hundreds or thousands of years. The folding and faulting may furthermore form traps where fluids like hydrocarbons can accumulate. Additionally, erosional processes move material from high elevations to the foreland, which might again result in the accumulation of valuable resources (Cooper, 2007; Goffey et al., 2010; Hammerstein et al., 2020, and references therein). Convergent plate boundaries are the subject of Chapters 3 and 5 of this thesis. Chapter 3 is a published study on the comparison of geodynamic and kinematic models of potentially reservoir bearing folding and faulting with a focus on the Andean foreland. The modeled processes may further be applied to other fold-and-thrust belts such as in the forelands of the Alpine and the Pamir-Himalayan orogens. (Fig. 1.2, red). Chapter 5 is unpublished (see Introductory Explanations) and discusses great earthquakes and the seismic cycle at subduction zones. Furthermore, it describes the implementation of rate-and-state friction in the ASPECT code. Subduction zones with very powerful earthquakes are found all around the pacific plate such as in Chile, Alaska, Japan or New Zealand (Fig. 1.2, orange). At these places, an oceanic plate is being subducted beneath a continental, more buoyant plate (Stern, 2002, and references therein).

(2) At divergent plate boundaries, a tectonic plate splits in two parts which move into different directions (Brune et al., 2023, and references therein). On the Earth's continental surface this manifests as distinct valleys of several hundred to thousands of kilometer length. Ultimately, once break up has occured, these valleys may turn into a new ocean including an oceanic ridge where new crust forms. Divergent plate boundaries host less strong earthquakes than convergent plate boundaries. However, they play a major role for resources with many exploration sites for natural gas and oil that have been formed where crustal extension resulted in a graben topography trapping sediments. Furthermore, since the crust is thinning, high geothermal gradients can be found and exploited for geothermal energy in many of these places, e.g. in Iceland, and Kenia. Continental rifts (Fig. 1.2, green) are the focus of

Chapter 2. Here, I qualify and quantify the transient imprint of rifting on the geothermal heat flow for different rifting velocities.

(3) Transform tectonics are found where two plates slide past each other (Duarte, 2018, and references therein). A key feature of transform boundaries is the often relatively easily detectable fault trace at the surface which manifests as a linear feature in the topography with offset valleys, hills and other features to the sides. Transform plate boundaries may produce powerful earthquakes with several meters of offset as the recent Anatolian earthquake in February 2023 (Karabulut et al., 2023) has proven once more. Other segments of transform boundaries may be creeping without producing earthquakes as several fault segments of the San Andreas Fault in California (e.g. Steinbrugge et al., 1960; Schleicher et al., 2010). Furthermore, the bending of a strike-slip fault may alter crustal thickness (Mann, 2007, and references therein). Depending on the bending of the fault, compressional as well as tensional areas may be identified. Here, the processes listed above for divergent and convergent plate boundaries may take place, though at smaller scales. This includes the hosting of an increased amount of resources because of localised sediment accumulation or the formation of elevated topography. Bending transform plate boundaries are investigated in Chapter 4 where I model a restraining and a releasing bend using the coupling of ASPECT and FastScape to investigate the interactions between geodynamic and surface processes. Examplary sites for this setting are the Dead Sea Fault, the San Andreas Fault, and Jamaica (Fig. 1.2, yellow).

1.2 Process Interactions at Plate Boundaries

Plate boundaries are the sites of a multitude of processes that all potentially interact. Since most observational data only rarely spans the last century not to mention longer time scales, many interactions are obscured since the time of observation is very short when looking at processes that evolve over millions of years (e.g. Satake et al., 2007; McCaffrey, 2008). Furthermore, it can be difficult to distinguish between the different feedbacks. In the following, I will describe two examplary, prominent interaction chains at plate boundaries.

- The first example explores the interactions of the different processes altering mountain heights. On the one hand, surface uplift is driven by the compressive stresses resulting from plate tectonics. On the other hand, surface processes decrease maximum elevations through erosion. The eroded material is redeposited and in large parts moved out of the orogeny. This decreases vertical stresses, such that uplift due to the tectonic forcing of the horizontal compressive stresses becomes more efficient (Wolf et al., 2021; Wolf et al., 2022, and references therein). However, while faster uplift will increase mountain heights, increased mountain heights also increase erosional processes, e.g. through glaciers (e.g. Egholm et al., 2009) mostly covering high elevations or through more precipitation because higher orogens are a more efficient barrier for clouds (e.g. Willett, 1999; Whipple, 2009). At the same time, mountain heights are also controlled by isostasy (e.g. Gilchrist et al., 1994), where a thicker crust means more weight, such that the orogenic root will sink deeper into the mantle and vice versa. Feedbacks from isostatic adjustment do not act instantaneously and isostatic equilibrium postdates crustal thinning and thickening events because of the high viscosity of the mantle. This means that in the beginning of a fastly growing orogeny, mountain heights might first increase fast but will then be decreased first by erosion and then by isostatic adjustment. In an inactive orogeny, isostatic adjustment might, however, lead to further uplift by balancing ongoing erosion (e.g. Gołedowski et al., 2013). Additionally, uplift, erosion and isostatic adjustment also interact with the rheological behavior by altering crustal thickness: A thickening crust heats up internally such that ductile processes become more important (e.g. Goetze et al., 1979; Beaumont et al., 2006). This makes the compressive forces less efficient, since the crust is less stiff, and leads to a decrease in elevation through material flow to the sides. This in turn thins the crust and ultimately cools it until returning to a more brittle rheology. These changes in elevation again interact with erosion, stress field and isostatic adjustment induced deformation.
- Another prominent example is located at subduction dominated plate boundaries where an oceanic crust subducts below a thickening continental crust. This is the site where oceans and continents meet and the shore line as well as the growing mountain range further inland are subject to heavy erosion. The eroded sediment may be transported to the subduction channel where they alter the frictional properties of the fault zone and thereby influence the seismic behavior (e.g. Kurzawski et

al., 2018). At the same time, the interaction of coastal erosion and episodic uplift of the shore due to an earthquake may create a steplike landscape (e.g. Kelsey, 1990; Berryman, 1993). Furthermore, the earthquake may change the pore pressure and water supply of the region (e.g. Albano et al., 2017) as well as creating frictional heat that changes the temperature field (e.g. Dey et al., 2003).

While these are rather well-studied examples, there might be many more processes and interactions, still unknown or hidden behind more dominant interaction chains. However, to better understand the entire systems of the different plate boundaries, it is these processes and interactions that need to be disentangled and studied. With geodynamic modeling there is a tool to both analyze over geodynamic time scales and control the processes included. This thesis uses geodynamic modeling to look at interactions of

- the present-day heat flow field with transient temperature signals due to rifting-induced changes in crustal thickness and faulting in Chapter 2,
- the kinematics of folding and faulting in the light of different rheological rock properties in Chapter 3,
- neighboring restraining and releasing bends on major strike-slip faults including surface and geodynamic processes in Chapter 4,
- earthquakes and longer term geodynamic processes as a work in progress in Chapter 5.

1.3 Scales in Geodynamic Modeling

The many processes and interactions at plate boundaries act on a multitude of spatial and temporal scales with most of them being present in this work (Fig. 1.3). In the following, I match the scales involved in this work with the associated chapters.

1.3.1 Spatial Scales

< 1 m The smallest spatial scale of this work is on the order of µm and mm for slip localization processes in fault zones hosting earthquakes (e.g. Ben-Zion, 2008; Rice, 2017). Even though earthquake modeling is part of Chapter 5, no models have been run using a resolution this small. Instead, this scale is represented by the rate-and-state friction framework. Spatial scales of <1 m are furthermore relevant in Chapter 4, though again not as a model resolution, but in terms of rock properties for the sediment unit. Sediment transported by rivers has grain sizes that are in the order of mm to cm and it is the entirety of these grains that transmit effects of surface processes and link them to tectonics.

1 m – 10 km This is the scale of faulting and folding that are the focus of Chapter 3. However, faults and fault zones are primary features for all chapters. Furthermore, mesh size resolution also falls into this spatial scale with cell sizes ranging from 125 m to 4 km for the models in this work.

>10 km – 100 km This is the scale of regional tectonics which are present in all chapters of this work. It is especially relevant in the bending of the strike-slip fault in Chapter 4 and the associated crustal processes as well as in the rift models in Chapter 2.

>100 km This is the scale of plate boundaries. Chapters 2 and 4 explicitely use model domains of this size. Furthermore, Chapter 2 and 5 discuss 2D plate boundary models. These models represent plate boundaries that may have lengths of several thousand kilometers in the model perpendicular direction. Examples are the East African Rift System and the Andean subduction zone, respectively.

1.3.2 Temporal Scales

<1 hour This temporal scale of very short-lived events is discussed in Chapter 5 as one part of an earthquake cycle. Earthquakes nucleate within milliseconds and the rupture may last several minutes (Ben-Zion, 2008). This also manifests as time step lengths.

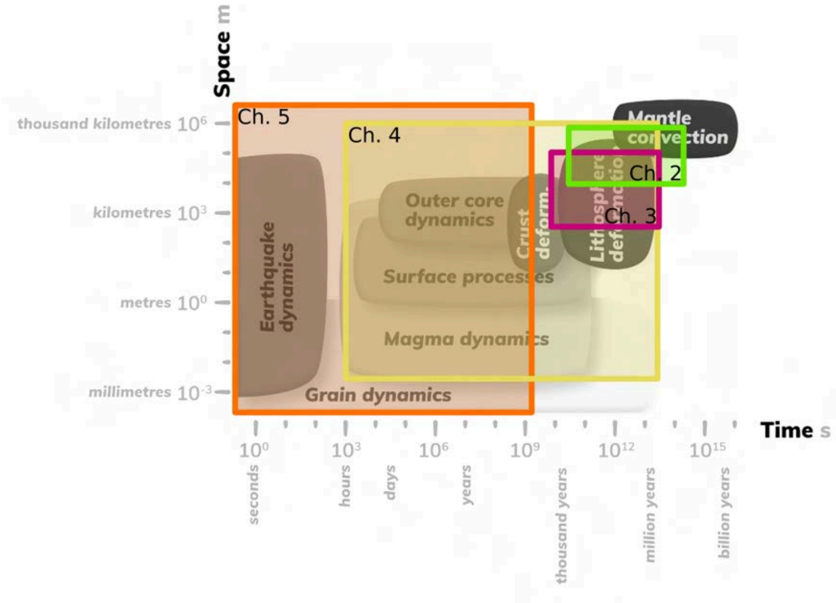

Figure 1.3: The spatial and temporal scales involved in this work. The colored boxes show their occurence per chapter. Green: Chapter 2, red: Chapter 3, yellow: Chapter 4, orange: Chapter 5. Adapted from Zelst et al. (2021).

1 hour – 1 000 years In Chapter 4, I am investigating the interactions of surface and geodynamic processes. Here, I use time steps of 1000 years for the surface processes modeling software FastScape. These represent the entirety of erosional and depositional processes that naturally occur on smaller temporal scales, e.g. hours of rain, climate variability over decades or centuries, etc.

1 000 – 1 million years This is the scale of local to regional deformation. The models in Chapter 3 deal with regional scale features of folding and faulting over a total time of 400 000 years computed with time step sizes of 20 000 years. As the sum of local and regional features accumulates in global tectonics, this time scale is furthermore present in terms of the size of the geodynamic time steps in the models of Chapters 2 and 4.

>1 million years This is the scale of long-term tectonic processes, of the uplift and subsidence of land, of rifting and mountain building, of plate boundaries and mantle convection. Here, several million or hundred million years may be relevant. Therefore, the models of Chapters 2 and 4 have a total simulation time of several tens of millions of years.

1.4 The Geodynamic Modeling Software ASPECT

I have used ASPECT, the Advanced Solver for Planetary Evolution, Convection, and Tectonics(Kronbichler et al., 2012; Heister et al., 2017; Glerum et al., 2018), for all models in this thesis and extended its functionality in the process. ASPECT is a state-of-the-art, open-source, community-built software using the finite element method (FEM). The governing equations concern the conservation of mass, momentum, and energy. Initially, ASPECT was designed to solve problems of mantle convection, but it has increasingly been used and extended for other problems including lithosphere dynamics and surface processes through the coupling with FastScape (Braun et al., 2013; Yuan et al., 2019). Key advantages of ASPECT are that it is easily extendable, modular, massively parallel, open-source, maintained by a lively community and that it uses adaptive mesh refinement. For the various models presented here, I have continuously been part of the development of ASPECT by reporting and fixing bugs as well as extending ASPECT for the means of my research (see Chapter 5.2.2 for examples). Some of the internal structure of ASPECT and parts of my additions are therefore a major part of Chapter 5.2. For the numerical model and governing equations of ASPECT, the reader is kindly refered to the supplements of Chapter 4 in appendix B.1.

In the following, I will present how ASPECT can be used to explore process interactions and how it deals with the different temporal and spatial scales.

1.4.1 Process Interactions in ASPECT

Because of ASPECT's modular structure, it is comparatively easy to add or remove single processes of an existing model with only a few additional arguments in the model's input file. Being able to turn processes on and off or make them more or less effective helps to quantify and qualify the impact of a parameter and of one process on another. Furthermore, ASPECT provides several options to extend and customize the code by writing a new module or postprocessor. These can be including directly to the installation or added as an additional library. This flexibility greatly enhances the modeling options and enables an advanced user to study a huge variety of process interactions throughout the Earth's surface, crust, and mantle.

For this thesis, the most important crustal processes I simulated with ASPECT are heat transport mainly by convection and conduction, mechanical deformation using a visco-plastic rheology, and the addition of surface processes in geodynamic models. These all interact with each other and many more parameters. Changes in temperature or strain rate may for example induce spatio-temporal variations in the location of the brittle-ductile transition. Subsequent changes in rheological behavior manifest in folding, faulting or creeping amongst others. These deformational processes result in alterations of crustal thickness which in turn leads to changes in surface elevations due to isostatic adjustment. Changes in surface elevations then interact with surface processes and so forth. In geodynamic modeling the integrated and coupled effects of these processes are computed within each advection time step, although coupled processes such as landscape evolution and chemical reactions may utilize a series of smaller time steps within a given geodynamic advection time step. Therefore, the time step length matters as it may have implications on the intensity of feedbacks between different processes. It must thus be tested with care and should not be too large which may, however, be in conflict with the use of computational hours.

1.4.2 Scales in ASPECT

As discussed in Chapter 1.3, there are many spatial and temporal scales that are relevant for plate boundary processes. ASPECT is known for its built-in adaptive mesh refinement, which facilitates the modeling of different spatial scales in a single model. At the same time, it helps decreasing the need for computational resources and time when a fine resolution is only needed for specific processes with a spatially limited impact.

ASPECT also provides adaptive time stepping based on a CFL (Courant–Friedrichs–Lewy) criterion. This is suitable for tectonic and geodynamic processes occuring on larger time scales, but is insufficient for the modeling of earthquakes. I therefore took part in the introduction of new time stepping routines in ASPECT (Chapters 5.2.2 and 5.2.4). These change the way to determine the needed time step length and also include the possibility of repeating a time step with a smaller length. This is crucial for the correct timing when modeling a rupturing fault as in Chapter 5.

1.5 Motivation and Outline of this Thesis

This work is a compilation of many different processes, scales and tectonic settings. Its ultimate goal is to bring all of them together in a single modeling framework and software to be able to study, single out and quantify all kinds of processes and interactions. This is possible because of all the advancements made in the field of geodynamic modeling in general and the many features already included in the geodynamic modeling software ASPECT together with its flexibility and extensibility. To reach this goal, a major part of this thesis has been software development to enable the joint computation of additional processes.

The thesis is composed of four main chapters. These include two published papers, one submitted study and an additional chapter. I will present them in the order of their publication date which simultaneously corresponds to an increase in model dimensions and complexity, since Chapters 2 and 3 include models in 2D, while Chapter 4 and 5 are about models in 3D.

Chapter 2 is a study about tectonic-induced transients in the heat flow of continental rifts in dependence of crustal thickness and extension velocity. It is published as (Heckenbach et al., 2021). In Chapter 3, I explore the applicability of the purely kinematic trishear model for fault-propagation folds in more realistic geodynamic models. This study is published as (Plotek et al., 2022). Chapter 4 includes transtensional and transpressional processes related to Chapters 2 and 3 within a strike-slip environment and explores their interactions. It is submitted as Heckenbach et al. (2024 subm.). Finally, Chapter 5 gives an overview about the current state of the unpublished rate-and-state friction implementation in ASPECT. Its ultimate goal would be to model great earthquakes at subduction zones or to restart models similar to those in Chapter 4 at smaller time scales with eathquake-like behavior enbaled.

After the four main Chapters, I will discuss their findings in the superordinated framework of interactions of processes at continental plate boundaries and draw overall conclusions. At the end, I include the supplements of the published and submitted papers as well as my references and acknowledgements in the appendix.

References

Albano, Matteo, Salvatore Barba, Giuseppe Solaro, Antonio Pepe, Christian Bignami, Marco Moro, Michele Saroli, and Salvatore Stramondo (2017). “Aftershocks, groundwater changes and postseismic ground displacements related to pore pressure gradients: Insights from the 2012 Emilia-Romagna earthquake”. In: *Journal of Geophysical Research: Solid Earth* 122.7, pp. 5622–5638.

Beaumont, Christopher, M. H. Nguyen, R.A. Jamieson, and S. Ellis (2006). “Crustal flow modes in large hot orogens”. In: *Channel Flow, Ductile Extrusion and Exhumation in Continental Collision Zones.* Geological Society of London.

Ben-Zion, Yehuda (2008). “Collective behavior of earthquakes and faults: Continuum-discrete transitions, progressive evolutionary changes, and different dynamic regimes”. In: *Reviews of Geophysics* 46.4.

Berryman, Kelvin (1993). “Age, height, and deformation of Holocene marine terraces at Mahia Peninsula, Hikurangi Subduction Margin, New Zealand”. In: *Tectonics* 12.6, pp. 1347–1364.

Braun, Jean and Sean D. Willett (2013). “A very efficient O(n), implicit and parallel method to solve the stream power equation governing fluvial incision and landscape evolution”. en. In: *Geomorphology* 180-181, pp. 170–179.

Brune, Sascha, Folarin Kolawole, Jean-Arthur Olive, D. Sarah Stamps, W. Roger Buck, Susanne J. H. Buiter, Tanya Furman, and Donna J. Shillington (Apr. 2023). “Geodynamics of continental rift initiation and evolution”. In: *Nature Reviews Earth & Environment* 4.4, pp. 235–253.

Catlos, Elizabeth J. and Ibrahim Cemen (May 4, 2023). *Compressional Tectonics: Plate Convergence to Mountain Building.* John Wiley & Sons. 357 pp.

Cooper, Mark (Jan. 1, 2007). “Structural style and hydrocarbon prospectivity in fold and thrust belts: a global review”. In: *Deformation of the Continental Crust: The Legacy of Mike Coward.* Ed. by A. C. Ries, R. W. H. Butler, and R. H. Graham. Vol. 272. Geological Society of London.

Davies, Geoffrey F (1992). “On the emergence of plate tectonics”. In.

Dey, S. and R. P. Singh (Dec. 31, 2003). “Surface latent heat flux as an earthquake precursor”. In: *Natural Hazards and Earth System Sciences* 3.6, pp. 749–755.

Duarte, Joao C. (Sept. 25, 2018). *Transform Plate Boundaries and Fracture Zones.* Elsevier. 480 pp.

Egholm, D. L., S. B. Nielsen, V. K. Pedersen, and J.-E. Lesemann (Aug. 2009). “Glacial effects limiting mountain height”. In: *Nature* 460.7257, pp. 884–887.

Gilchrist, A. R., M. A. Summerfield, and H. A. P. Cockburn (Nov. 1, 1994). “Landscape dissection, isostatic uplift, and the morphologic development of orogens”. In: *Geology* 22.11, pp. 963–966.

Glerum, Anne, Cedric Thieulot, Menno Fraters, Constantijn Blom, and Wim Spakman (2018). “Nonlinear viscoplasticity in ASPECT: benchmarking and applications to subduction”. English. In: *Solid Earth* 9.2, pp. 267–294.

Goetze, Christopher and Brian Evans (Dec. 1, 1979). “Stress and temperature in the bending lithosphere as constrained by experimental rock mechanics”. In: *Geophysical Journal International* 59.3, pp. 463–478.

Goffey, Graham P., Jonathan Craig, Tim Needham, and Robert Scott (Jan. 2010). “Fold–thrust belts: overlooked provinces or justifiably avoided?” In: *Geological Society, London, Special Publications* 348.1, pp. 1–6.

Gołedowski, Bartosz, David L. Egholm, Søren B. Nielsen, Ole R. Clausen, and Eoin D. McGregor (Oct. 1, 2013). “Cenozoic erosion and flexural isostasy of Scandinavia”. In: *Journal of Geodynamics* 70, pp. 49–57.

Hammerstein, James A., Raffaele Di Cuia, Michael A. Cottam, Gonzalo Zamora, and Robert W. H. Butler (2020). “Fold and thrust belts: structural style, evolution and exploration – an introduction”. In: *Geological Society, London, Special Publications* 490.1, pp. 1–8.

Heckenbach, Esther L., Sascha Brune, Anne C. Glerum, and Judith Bott (2021). “Is There a Speed Limit for the Thermal Steady-State Assumption in Continental Rifts?” en. In: *Geochemistry, Geophysics, Geosystems* 22.3, e2020GC009577.

Heckenbach, Esther L., Sascha Brune, Anne C. Glerum, Roi Granot, Yariv Hamiel, Stephan V. Sobolev, and Derek Neuharth (2024 subm.). “3D Interaction of Tectonics and Surface Processes explains Fault Network Evolution of the Dead Sea Fault”. In: *Tektonika.*

Heidbach, Oliver (2018). “The World Stress Map database release 2016_ Crustal stress pattern across scales”. en. In.

Heister, Timo, Juliane Dannberg, Rene Gassmöller, and Wolfgang Bangerth (2017). “High accuracy mantle convection simulation through modern numerical methods – II: realistic models and problems”. In: *Geophysical Journal International* 210.2, pp. 833–851.

Isacks, Bryan, Jack Oliver, and Lynn R. Sykes (1968). “Seismology and the new global tectonics”. In: *Journal of Geophysical Research (1896-1977)* 73.18, pp. 5855–5899.

Karabulut, Hayrullah, Sezim Ezgi Güvercin, James Hollingsworth, and Ali Özgün Konca (May 5, 2023). “Long silence on the East Anatolian Fault Zone (Southern Turkey) ends with devastating double earthquakes (6 February 2023) over a seismic gap: implications for the seismic potential in the Eastern Mediterranean region”. In: *Journal of the Geological Society* 180.3, jgs2023–021.

Kelsey, Harvey M. (1990). “Late Quaternary deformation of marine terraces on the Cascadia Subduction Zone near Cape Blanco, Oregon”. In: 9.5, pp. 983–1014.

Kronbichler, M., T. Heister, and W. Bangerth (2012). “High Accuracy Mantle Convection Simulation through Modern Numerical Methods”. In: *Geophysical Journal International* 191, pp. 12–29.

Kurzawski, Robert Marek, André Rik Niemeijer, Michael Stipp, Delphine Charpentier, Jan Hinrich Behrmann, and Christopher James Spiers (2018). “Frictional Properties of Subduction Input Sediments at an Erosive Convergent Continental Margin and Related Controls on Décollement Slip Modes: The Costa Rica Seismogenesis Project”. In: *Journal of Geophysical Research: Solid Earth* 123.10, pp. 8385–8408.

Mann, Paul (2007). “Global catalogue, classification and tectonic origins of restraining- and releasing bends on active and ancient strike-slip fault systems”. en. In: 290, pp. 13–142.

McCaffrey, Robert (Mar. 1, 2008). “Global frequency of magnitude 9 earthquakes”. In: *Geology* 36.3, pp. 263–266.

Palin, Richard M. and M. Santosh (Dec. 1, 2021). “Plate tectonics: What, where, why, and when?” In: *Gondwana Research.* SPECIAL ISSUE: GR-100 100, pp. 3–24.

Plotek, Berenice, Esther Heckenbach, Sascha Brune, Ernesto Cristallini, and Jeremías Likerman (2022). “Kinematics of fault-propagation folding: Analysis of velocity fields in numerical modeling simulations”. In: *Journal of Structural Geology* 162, p. 104703.

Rice, James R. (Aug. 21, 2017). “Heating, weakening and shear localization in earthquake rupture”. In: *Philosophical Transactions of the Royal Society A: Mathematical, Physical and Engineering Sciences* 375.2103, p. 20160015.

Rona, Peter A. (1983). “Potential Mineral and Energy Resources at Submerged Plate Boundaries”. In: *Natural Resources Forum* 7.4, pp. 329–338.

Satake, Kenji and Brian F. Atwater (2007). “Long-Term Perspectives on Giant Earthquakes and Tsunamis at Subduction Zones”. In: *Annual Review of Earth and Planetary Sciences* 35.1, pp. 349–374.

Schellart, W. P. and N. Rawlinson (2013). “Global correlations between maximum magnitudes of subduction zone interface thrust earthquakes and physical parameters of subduction zones”. In: *Physics of the Earth and Planetary Interiors* 225, pp. 41–67.

Schleicher, A.M., B.A. van der Pluijm, and L.N. Warr (July 1, 2010). “Nanocoatings of clay and creep of the San Andreas fault at Parkfield, California”. In: *Geology* 38.7, pp. 667–670.

Steinbrugge, Karl V., Edwin G. Zacher, Don Tocher, C. A. Whitten, and C. N. Claire (July 1, 1960). “Creep on the San Andreas fault”. In: *Bulletin of the Seismological Society of America* 50.3, pp. 389–415.

Stern, R. J. (Mar. 1, 2007). “When and how did plate tectonics begin? Theoretical and empirical considerations”. In: *Chinese Science Bulletin* 52.5, pp. 578–591.

Stern, Robert J. (2002). “Subduction Zones”. In: *Reviews of Geophysics* 40.4, pp. 3–38.

Wallace, Robert E. (1968). “Notes on stream channels offset by the San Andreas Fault, Southern Coast Ranges, California”. In.

Whipple, Kelin X. (Feb. 2009). “The influence of climate on the tectonic evolution of mountain belts”. In: *Nature Geoscience* 2.2, pp. 97–104.

Willett, Sean D. (1999). “Orogeny and orography: The effects of erosion on the structure of mountain belts”. In: *Journal of Geophysical Research: Solid Earth* 104 (B12), pp. 28957–28981.

Wolf, Sebastian G., Ritske S. Huismans, Jean Braun, and Xiaoping Yuan (June 2022). “Topography of mountain belts controlled by rheology and surface processes”. In: *Nature* 606.7914, pp. 516–521.

Wolf, Sebastian G., Ritske S. Huismans, Josep-Anton Muñoz, Magdalena Ellis Curry, and Peter van der Beek (2021). “Growth of Collisional Orogens From Small and Cold to Large and Hot—Inferences From Geodynamic Models”. In: *Journal of Geophysical Research: Solid Earth* 126.2, e2020JB021168.

Wortel, M. J. R. and S. A. P. L. Cloetingh (Jan. 1, 1986). “On The Dynamics of Convergent Plate Boundaries and Stress in the Lithosphere”. In: *Developments in Geotectonics*. Ed. by F. -C Wezel. Vol. 21. The Origin of Arcs. Elsevier, pp. 115–139.

Yuan, X. P., J. Braun, L. Guerit, B. Simon, B. Bovy, D. Rouby, C. Robin, and R. Jiao (2019). “Linking continental erosion to marine sediment transport and deposition: A new implicit and O(N) method for inverse analysis”. en. In: *Earth and Planetary Science Letters* 524, p. 115728.

Zang, Arno and Ove Stephansson (2009). *Stress Field of the Earth’s Crust*. en. Springer Science & Business Media.

Zelst, Iris van, Fabio Crameri, Adina E. Pusok, Anne C. Glerum, Juliane Dannberg, and Cedric Thieulot (2021). “101 Geodynamic modelling: How to design, carry out, and interpret numerical studies”. en. In.

2 Is there a Speed Limit for the Thermal Steady-State Assumption in Continental Rifts?

This study was published in:
Esther L. Heckenbach[1,2], Sascha Brune[1,2], Anne C. Glerum[1], Judith Bott [Sippel][1]
(2021): Is there a Speed Limit for the Thermal Steady-State Assumption in
Continental Rifts? *Geochemistry, Geophysics, Geosystems(G3)*, 22, 3,
e2020GC009577.
`https://doi.org/10.1029/2020GC009577`

[1] GFZ German Research Centre for Geosciences, 14473 Potsdam, Germany
[2] Institute of Geosciences, University of Potsdam, 14476 Potsdam-Golm, Germany

Additional material can be found at: `10.5281/zenodo.3778176`

Abstract

The lithosphere is often assumed to reside in a thermal steady-state when quantitatively describing the temperature distribution in continental interiors and sedimentary basins, but also at active plate boundaries. Here, we investigate the applicability limit of this assumption at slowly deforming continental rifts. To this aim, we assess the tectonic thermal imprint in numerical experiments that cover a range of realistic rift configurations. For each model scenario, the deviation from thermal equilibrium is evaluated. This is done by comparing the transient temperature field of every model to a corresponding steady-state model with identical structural configuration. We find that the validity of the thermal steady-state assumption strongly depends on rift type, divergence velocity, sample location and depth within the rift. Maximum differences between transient and steady-state models occur in narrow rifts, at the rift sides, and if the extension rate exceeds 0.5–2 mm/a. Wide rifts, however, reside close to thermal steady-state even for high extension velocities. The transient imprint of rifting appears to be overall negligible for shallow isotherms with a temperature less than 100°C. Contrarily, a steady-state treatment of deep crustal isotherms leads to underestimation of crustal temperatures, especially for narrow rift settings. Thus, not only relatively fast rifts like the Gulf of Corinth, Red Sea, and Main Ethiopian Rift, but even slow rifts like the Kenya Rift, Rhine Graben, and Rio Grande Rift must be expected to feature a pronounced transient component in the temperature field and to therefore violate the thermal steady-state assumption for deeper crustal isotherms.

Keypoints:

- We use numerical forward modeling to quantify the transient thermal imprint during continental extension.
- The validity of the thermal steady-state assumption in narrow rifts is limited to extension velocities less than 0.5-2 mm/a.
- Transient thermal effects are particularly significant for deep isotherms, narrow rifts, and beneath the rift shoulders.

Plain Language Summary

Temperature distribution is a key factor when studying Earth's interior. Here, we quantify the influence of rift velocity on temperature distribution with numerical simulations. As a continent begins to split, forming a rift, hot material beneath the rift center moves

upwards increasing the temperatures at shallow crustal depth. However, simple thermal models often assume an equilibrated, constant temperature field. To evaluate tectonically induced changes in temperatures, we compare lithosphere-scale dynamic models to models with the same material configuration but with a steady-state temperature distribution and no deformation. We find that the latter approach well represents locations outside the rift valley, and shallow crustal depths where comparably low temperatures prevail. Contrarily, at the sides of the rift valley, or for deeper-lying isotherms like 400°C, the assumption of an equilibrated thermal field leads to an underestimation of crustal temperatures. Furthermore, we show that temperatures in narrow rifts like the Kenya Rift and the Rhine Graben are more strongly modified by tectonic movements than temperatures in wide rifts, like the Basin and Range Province. Finally, we conclude that the assumption of constant temperatures is only valid for wide rifts and very slowly diverging narrow rifts with a speed limit of < 0.5–2 mm/a.

2.1 Introduction

The temperature distribution within the lithosphere exerts key control on major geological and geodynamic processes such as long-term tectonic deformation, seismicity and geochemical reactions. To better understand the localization of deformation, for instance, one may describe the thermo-mechanical state of the lithosphere (Afonso et al., 2004; Burov, 2011) in order to numerically simulate forward tectonic deformation (e.g. Buck, 1991; Huismans et al., 2005). Additional to these fundamental processes, shallow crustal temperatures hold strong implications for applied research on the formation of georesources. For example, the depth of the 60°C and the 120°C isotherms are important indicators for a region's geothermal potential in terms of heat production and electricity, respectively (e.g. Gudmundsson, 1988), while the depth of the oil window (80-100°C) (e.g. Tissot et al., 1987) controls the sites of hydrocarbon formation. The thermal evolution of tectonically active regions may be reconstructed using thermochronological techniques, which in turn require the present-day temperature distribution as a key constraint. Hence, quantifying the present-day thermal field of the sediments, crust and lithospheric mantle is of profound relevance for a variety of applied and fundamental research problems.

Deducing the temperature distribution within sedimentary basins is an immense challenge, because borehole-derived subsurface temperatures and surface heat flow measurements are notoriously sparse compared to the dimensions of sedimentary basins. Hence, for the gapless assessment of present-day thermal field variations in a region, the scientific community reverts to a variety of predictive models that range from purely mathematical approaches (interpolation algorithms ignoring geological structure; e.g., Agemar et al. (2014)) to heat transport simulations that take into account lithology controlled thermal property variations. The latter type of models typically considers how efficiently the rocks at depth conduct heat (since solid-state heat diffusion is the main heat transport process in the lithosphere; Scheck-Wenderoth et al. (2014)), how much heat is produced by radioactive decay, and how much heat is transferred across the external boundaries of the modeled system. Hence, the setup of such models involves an extensive analysis of observational data (e.g. wells, seismic profiles, gravity anomalies) to integrate the subsurface geological structure (rock types and related thermal properties) as well as proper boundary conditions. Thereby, the amount of heat entering the system from the mantle has to be defined at the lower boundary, which implies that the models are at least crustal or even lithospheric in scale (e.g. Bayer et al., 1997; Tesauro et al., 2009; Fullea et al., 2009; Fullea et al., 2012; Balling et al., 2013; Carballo et al., 2015; Freymark et al., 2017; Sippel et al., 2017; Maystrenko et al., 2018; Jiménez-Munt et al., 2019). In the frame of this study, we refer to these regional-scale heat transport simulations as data-integrative thermal models.

Even if this type of models may be reasonably accurate in terms of the subsurface configuration of rock properties, there is one crucial assumption they are based on, which may not be valid everywhere: heat is assumed to be transported within an instantaneously thermally equilibrated lithosphere. In other words, these models assume a thermal steady-state condition where temperature does not change through time. A thermal steady-state, however, is in contrast to many active tectonic settings where transient processes are well-known to play a role. This has been shown, for example, by the misfits of steady-state thermal models with respect to measured temperature data, which have been interpreted to result from transient thermal processes as the remnants of the thermal evolution within the study region (e.g. Fullea et al., 2012; Freymark et al., 2017; Meeßen, 2019). Indeed, the transient nature of lithospheric

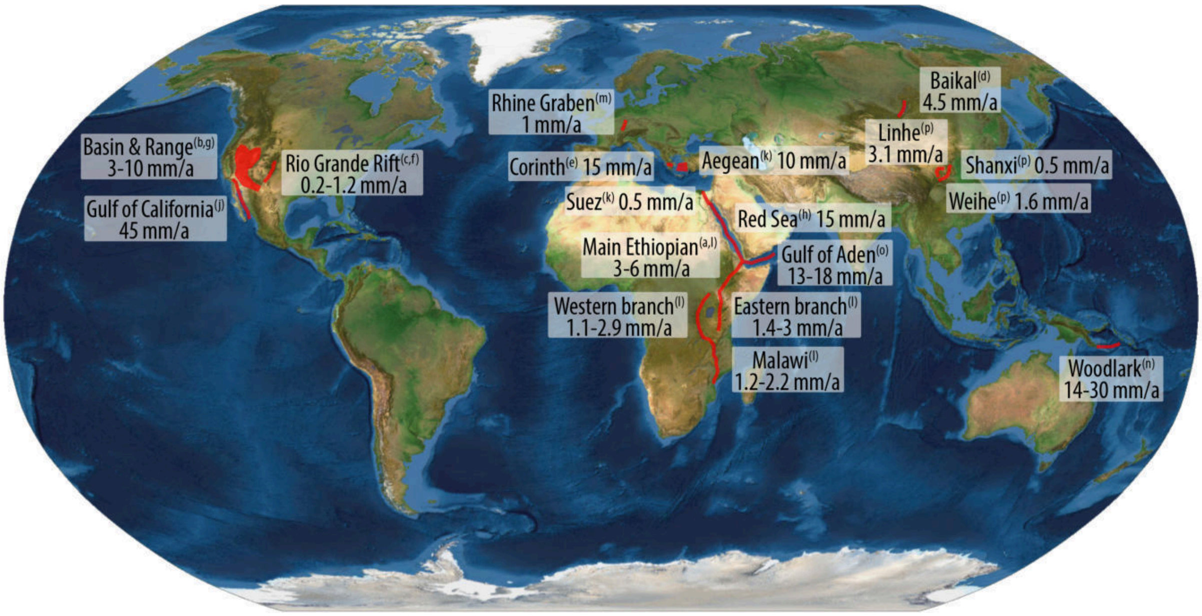

Figure 2.1: Locations of active continental rifts with their extension velocities. More information on the individual rifts is given in Table 2.1, including references (indicated here by superscripts).

temperature signals is a common problem (e.g. Tesauro et al., 2009; Artemieva, 2009; Balling et al., 2013) and can be expected in a variety of timescales affecting different depths of the lithosphere. This includes comparably shallow signals that arise from paleoclimate effects (e.g. Lane, 1923; Heckenbach et al., 2019) as well as lithospheric-scale perturbations related to the tectonic evolution (e.g. Peacock, 1996; Artemieva, 2009; Smye et al., 2019; Chenin et al., 2020). Transient perturbations of the thermal field should hence be mainly expected in active plate boundary settings where tectonic deformation, heat advection, and changing heat source distributions would generate time-dependent temperature fields (e.g. Ehlers et al., 2003; Davies et al., 2016; Hart et al., 2017).

In this study, we focus on currently active continental rifts as an example of actively deforming plate boundaries (see Figure 2.1 and Table 2.1). Continental rifts form where divergent lateral motions thin the lithosphere. This causes the lithosphere-asthenosphere boundary (LAB) to move upwards and hot material to be advected to shallower depths. Rifts can generally be categorized into narrow and wide rifts: Narrow rifts consist of a pronounced rift valley less than 100 km wide, such as large parts of the East African Rift System (Ebinger et al., 2012) or the Rhine graben (Brun et al., 1992), while wide rifts are characterized by several smaller horsts and grabens distributed over a larger area, as e.g., the Basin and Range Province or the Aegean (Hamilton, 1987; Rey et al., 2009; Brun et al., 2018). Numerical thermo-mechanical simulations show that narrow rifts form in strong crustal configurations, while deformation in wide rifts is less localized due to a weaker crustal rheology (Buck, 1991).

Here we perform a quantitative assessment of the systematic variations of tectonically induced thermal transients in narrow and wide rift settings. To this aim, we employ 2D thermo-mechanical forward models that account for visco-plastic deformation of the lithosphere, conductive and advective heat transport as well as heat generation due to radiogenic decay and shear heating. These models reproduce the time-dependent evolution of rift structures and the resulting thermal field on a lithospheric scale. The central approach of this study is to isolate the transient tectonic component of the temperature distribution from each model run. This is done by quantifying, for each time step, the temperature differences to the steady-state thermal field that would be associated with the structural configuration of this particular time step (Figure 2.2). Ultimately, this allows us to investigate the dependence of the transient temperature component on rift divergence velocity and to deduce general applicability limits for the thermal steady-state assumption in continental rifts.

With this paper we intend to provide: (1) a systematic overview of the sensitivity of thermal transients to extension rates and to the initial crustal configuration; and (2) a framework to assess, for any particular rift of known extension velocity and crustal geometry, the meaningfulness of a steady-state thermal modeling approach that neglects tectonically-induced transient signals.

Rift Name	$v_{extension}$ [mm/a]	Data Used to Constrain $v_{extension}$	Reference
Aegean	10	Geodesy	(k) Reilinger et al. (2010)
Baikal	4.5	Geodesy	(d) Calais et al. (1998) in [1]
Basin and Range – Walker Lane Fault Region	10	Geodesy	(b) Bennett et al. (1998) and Hammond et al. (2004) in [1]
Basin and Range – Wasatch Fault Zone	3	Geodesy	(g) Kreemer et al. (2010) in [1]
EARS – Eastern branch	1.4-3	Best fit model (GPS + Geology + EQ)	(l) Saria et al. (2014)
EARS – Western branch	1.1-2.9	Best fit model (GPS + Geology + EQ)	(l) Saria et al. (2014)
Gulf of Aden	13-18	Geodesy	(o) Vigny et al. (2006) and ArRajehi et al. (2010) in [1]
Gulf of California	44 (60-70° obliquity)	correlating Miocene volcanic strata	(j) Oskin et al. (2001) in McQuarrie et al. (2005), Brune (2014)
Gulf of Corinth	15	Geodesy	(e) Gawthorpe et al. (2018) and references therein
Linhe (Hetao graben)	3.1	geological reconstruction (2.4 Ma)	(p) Zhang et al. (1998)
Main Ethiopian Rift	3-6	Geodesy	(a) Bendick et al. (2006) and Kogan et al. (2012) in [1]
	5	Best fit model (GPS + Geology + EQ)	(l) Saria et al. (2014)
Malawi Rift	1.2-2.2	Best fit model (GPS + Geology + EQ)	(l) Saria et al. (2014)
Red Sea Rift	15	Geodesy	(h) McClusky et al. (2010) in [1]
Rhine Graben	1	Geodesy	(m) Tesauro et al. (2005)
Rio Grande Rift	1.2	Geodesy (4 years)	(c) Berglund et al. (2012) in [1]
	0.2	Geological reconstruction (26 Ma)	(f) Golombek et al. (1983) in [1]
Shanxi	0.5	geological reconstruction (2.4 Ma)	(p) Zhang et al. (1998)
Suez	0.5	Geodesy	(k) Reilinger et al. (2010)
Weihe	1.6	geological reconstruction (2.4 Ma)	(p) Zhang et al. (1998)
Woodlark	14-30	Geodesy	(n) Tregoning et al. (1998)

Table 2.1: Active rifts of the world with their extension velocities and the type of data used to determine the velocities. Locations are shown in Figure 2.1. EARS: East African Rift System, $v_{extension}$: extension velocity, EQ: earthquake slip vector data, GPS: velocities measured using the Global Positioning System. [1] Tetreault et al. (2018)

2.2 Methods

The relation between the validity of the thermal steady-state assumption and the extension velocity of continental rifts is assessed by evaluating 44 2D box models. In this section, we first state the governing equations of our numerical software. We then describe the setup of the thermo-mechanical forward models that compute the evolution of the transient temperature field. Last, we introduce the static models where we solve for the steady-state temperature distribution for a given lithospheric configuration. The entire workflow is furthermore graphically summarized in Figure 2.2.

All numerical modeling is carried out using the finite element geodynamic code ASPECT (Kronbichler et al., 2012; Heister et al., 2017; Bangerth et al., 2018; Rose et al., 2017b). In this study, it solves the incompressible flow equations of momentum, mass and energy (assuming an infinite Prandtl number) for velocity $\mathbf{v}$, pressure P and temperature T, combined with advection equations for each Eulerian compositional field c_i:

$$-\nabla \cdot (2\eta\dot{\epsilon}) + \nabla P = \rho \mathbf{g} \tag{2.1}$$

$$\nabla \cdot \mathbf{v} = 0 \tag{2.2}$$

$$\begin{aligned}
\bar{\rho} c_P \left(\frac{\partial T}{\partial t} + \mathbf{v} \cdot \nabla T \right) - \nabla \cdot k \nabla T &= \bar{\rho} H && \text{radioactive heating} \quad (2.3)\\
&+ (2\eta\dot{\epsilon}) : \dot{\epsilon} && \text{shear heating}\\
&+ \alpha T (\mathbf{v} \cdot \nabla P) && \text{adiabatic heating}
\end{aligned}$$

$$\frac{\partial c_i}{\partial t} + \mathbf{v} \cdot \nabla c_i = 0, \tag{2.4}$$

where η is the effective viscosity (see Eq. 2.5-2.8), $\dot{\epsilon}$ is the deviator of the strain rate tensor $\frac{1}{2}(\nabla \mathbf{v} + (\nabla \mathbf{v})^T)$, density $\rho = \rho_0(1-\alpha(T-T_0))$ with T_0 the reference temperature, and $\mathbf{g}$ gravity. $\bar{\rho}$ is the adiabatic reference density, c_P the specific isobaric heat capacity, k the thermal conductivity, and α the thermal expansivity, as given in Table 2.2. ASPECT is based on state-of-the-art numerical methods (Arndt et al., 2017), and we make use of the wide range of functionalities including non-linear rheologies, free surface, adaptive timestepping, mesh refinement and high performance iterative solvers (Kronbichler et al., 2012; Heister et al., 2017; Bangerth et al., 2018; Rose et al., 2017b).

The initial model domain of the dynamic models is 500 km wide and 125 km deep. Three steps of initial mesh refinement in the central rectangular areas shown in Figure 2.3 result in an effective resolution of 250 m in the rift area and a resolution of 2 km in the asthenosphere. The model includes four material layers (upper crust, lower crust, lithospheric mantle, and asthenosphere) with different compositions (Figure 2.3, Table 2.2). Except for the lithosphere-asthenosphere boundary (LAB), where a small perturbation is included in the model center, the layers are initially horizontal. We vary total crustal thickness, but for simplicity the upper crust is always chosen twice as thick as the lower crust. A thermal LAB is implemented at 120 km depth for all models (Figure 2.3), corresponding to a lithosphere thickness representative of typical intraplate environments (Artemieva, 2006). Initial temperature profiles are calculated with the boundary conditions of 0°C at the surface and 1300°C at the LAB assuming conductive heat transport and radioactive heating within an instantaneously equilibrated lithosphere (Eq. 2.10) and adiabatic conditions within the asthenosphere (Turcotte et al., 2014). The adiabatic surface temperature is set to 1284°C.

We employ a visco-plastic rheology (Glerum et al., 2018) with dislocation and diffusion creep rheologies as well as the Drucker-Prager yield criterion. In 2D, these are incorporated within ASPECT through the following equations:

$$\eta_{eff}^{comp} = \left(\frac{1}{\eta^{df}} + \frac{1}{\eta^{ds}} \right)^{-1} \qquad \text{composite viscosity} \tag{2.5}$$

$$\text{with} \quad \eta_{ds|df} = \frac{1}{2} A^{-\frac{1}{n_{ds|df}}} d \frac{m_{ds|df}}{n_{ds|df}} \dot{\epsilon}_{ii} \frac{1 - n_{ds|df}}{n_{ds|df}} exp\left(\frac{E_{ds|df} + PV_{ds|df}}{n_{ds|df} RT} \right) \qquad \text{ds—df creep} \tag{2.6}$$

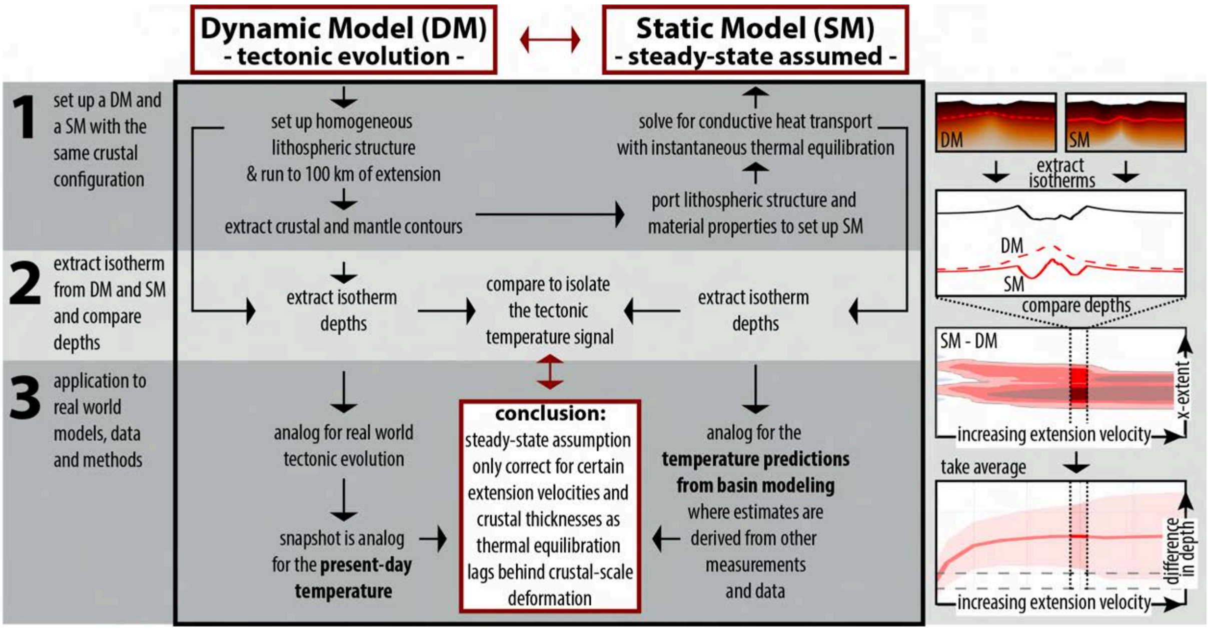

Figure 2.2: Graphical summary of the workflow used to assess the meaningfulness of a steady-state thermal modeling approach by comparing time-dependent dynamic (DM) and static models that assume a steady-state temperature distribution (SM).

When $2\eta_{eff}^{comp}\dot{\epsilon} > \sigma_y$, the plastic effective viscosity (Eq. 2.7) is used instead of the composite effective viscosity (Eq. 2.5):

$$\eta_{eff}^{pl} = \frac{\sigma_y}{2\dot{\epsilon}_{ii}} \qquad \text{plastic effective viscosity} \tag{2.7}$$

$$\text{with} \qquad \sigma_y = P \cdot sin(\phi) + C \cdot cos(\phi) \qquad \text{Drucker-Prager plasticity} \tag{2.8}$$

where η_{eff} is the effective viscosity, $ds|df$ corresponds to dislocation or diffusion creep, d is grain size, R is the gas constant, $A_{ds|df}$ are prefactors, $n_{ds|df}$ and $m_{ds|df}$ are stress and grain size exponents. For diffusion creep, $n_{df} = 1$, while for dislocation creep, $m_{ds} = 0$. $E_{ds|df}$ are the activation energies, $V_{ds|df}$ are the activation volumes, σ_y is the yield stress, ϕ is the internal angle of friction and C is cohesion. $\dot{\epsilon}_{ii}$ is defined as the square root of the second invariant of the deviatoric strain rate tensor. The final effective viscosity (Eq. 2.5 or Eq. 2.7) is capped by a user-defined minimum and maximum viscosity η_{min} and η_{max}. The parameters used are listed in Table 2.2.

Rift localization is facilitated by a thermal and compositional perturbation in the center of the model where the LAB is elevated maximally by 5 km using a Gaussian distribution with a half-width of 10 km (Brune et al., 2014). Furthermore, the initial strain field is constructed using random noise with a Gaussian distribution around the domain center of which the standard deviation is 200 km and the maximum amplitude is 0.2. The initial strain is smoothed out at 50 km depth. This results in a random distribution in terms of lateral heterogeneity of modeled friction angles through linear strain weakening on the plastic strain interval [0–0.5], reflecting the non-homogeneity of natural rocks and facilitating the localization of deformation (Jammes et al., 2016; Naliboff et al., 2017; Duclaux et al., 2018).

The top boundary is a free surface (Rose et al., 2017a) allowing for topography to evolve throughout the extension process, while material velocities are prescribed for all other boundaries with the bottom inflow matching the outflow through the sides (Fig. 2.3). Prescribing divergent velocities at model boundaries represents a wide range of driving forces of rifting, such as (1) plate divergence that is driven by large-scale mantle drag beneath the involved plates (Ulvrova et al., 2019), (2) back-arc extension due to slab-dynamics induced trench retreat (Sdrolias et al., 2006), and (3) rifting that is caused by plume-related gravitational potential energy gradients on a wavelength of thousands of kilometers (Stamps et al., 2010; Kendall et al., 2016). Each of these processes affects the ≈100 km wide plate boundary primarily through divergent plate motion, which we approximate by prescribing velocities at the model

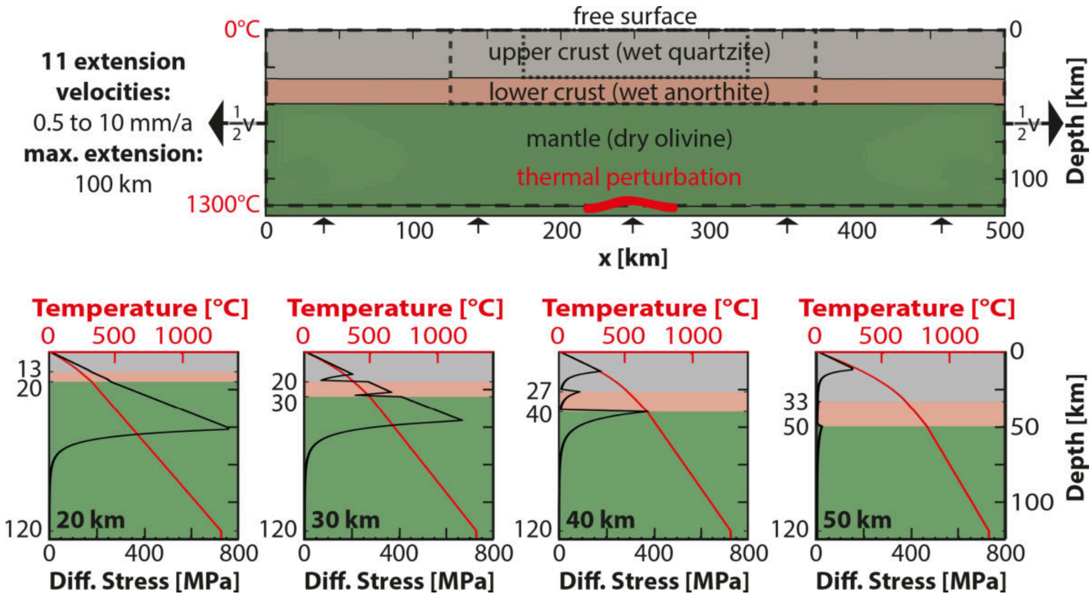

Figure 2.3: Top: Composition and initial geometry of the lithosphere with four horizontal layers and a thermal and compositional perturbation of the LAB. For the initial temperature field, we prescribe adiabatic conditions in the asthenosphere and a conductive temperature profile in the lithosphere (Eq. 2.10) that is bounded by 0°C at the surface and 1300°C at the bottom of the lithosphere. The boundary conditions for the governing equations are a fixed composition at the bottom boundary, and a fixed temperature at the top and bottom boundary. Furthermore, the top boundary is a free surface, while the sides and bottom boundary have prescribed velocities. The mesh-refined areas are framed with dashed lines with decreasing dash size indicating smaller element sizes of up to 250 m of resolution at the central surface compared to 2 km in the asthenosphere. **Bottom:** Initial temperature and yield strength profiles for the four crustal thicknesses modeled.

boundaries. Model properties like temperature, pressure, stress and strain fields are output every 2 km of applied extension. Models are stopped when 100 km of accumulated total extension is reached. The dynamic model suite includes eleven rift velocities (0.5,1,2,...,10 mm/a) and four crustal thicknesses (20, 30, 40, 50 km). We therewith cover the majority of modern rifts worldwide (Figure 2.1 and Table 2.1).

Further understanding of the dominant modeled processes is gained by calculating the Péclet number (Pe) for each model setup, which describes the ratio of conductive to advective heat transport. A small Péclet number ($Pe < 1$) indicates a predominantly conductive setting, while a large Péclet number ($Pe > 1$) designates dominantly advective heat transport (Sandiford, 2002). We calculate a Péclet number for each rift setting with:

$$Pe = \frac{L \cdot v}{\kappa} \tag{2.9}$$

according to Guillou-Frottier et al. (1995), where L is the initial thickness of the lithosphere [km], v is the prescribed vertical inflow velocity [mm a^{-1}] and κ is the thermal diffusivity [m^2 a^{-1}].

Contrary to the dynamic models that capture the entire rift evolution, our models assuming thermal steady-state only represent snapshots in time and hence do not include the tectonically inherited transient temperature field, nor any additional thermal perturbations. To ensure applicability of the results, the construction of these models is done in correspondence to the approach of data-integrative thermostructural models. These data-integrative models first generate a structural model of the area based on topography, gravity, seismic, and borehole data, which then serves as the framework for the modeling of the thermal field (Balling et al., 2013; Sippel et al., 2017; Jiménez-Munt et al., 2019). Analogous to this approach, we first extract the structural setting that is specific for a given time step of extension from the dynamic models, i.e. the material contours and model surface at the time when 50 km of extension has accumulated. We then use these structural interfaces to initialize a new set of models without deformation, where the thermal field is composed of 1D vertical profiles that are calculated by solving the 1D steady-state heat equation (Chapman, 1986; Turcotte et al., 2014)

$$0 = \kappa \frac{\partial^2 T}{\partial z^2} + \frac{H}{c_p} \tag{2.10}$$

	Upper crust (wet quartzite)	Lower crust (wet anorthite)	Lithospheric mantle and asthenosphere (dry olivine)	Unit
Thermal properties				
thermal diffusivity κ	0.772	0.731	0.838	$mm^2\ s^{-1}$
heat capacitiy c_p	1200	1200	1200	$J\ kg^{-1}\ K^{-1}$
density ρ	2700	2850	3280	$kg\ m^{-3}$
thermal expansivity α	2.70	2.70	3.00	$10^{-5}\ K^{-1}$
radioactive heating H	1.5	0.2	0	$\mu W\ m^{-3}$
Dislocation creep	$^{(a)}$	$^{(b)}$	$^{(c)}$	
prefactor A_{ds}	$8.57{\cdot}10^{-28}$	$7.13{\cdot}10^{-18}$	$6.54{\cdot}10^{-16}$	$Pa^{-n}\ s^{-1}$
stress exponent n_{ds}	4	3	3.5	-
activation energy E_{ds}	223	345	530	$kJ\ mol^{-1}$
activation volume V_{ds}	0	$3.80{\cdot}10^{-5}$	$1.80{\cdot}10^{-5}$	$cm^3\ mol^{-1}$
Diffusion creep	$^{(a)}$	$^{(b)}$	$^{(c)}$	
prefactor A_{df}	$5.97{\cdot}10^{-19}$	$2.99{\cdot}10^{-25}$	$2.25{\cdot}10^{-9}$	$Pa^{-1}\ s^{-1}$
grain size exponent m_{df}	2	3	0	-
activation energy E_{df}	223	159	375	$kJ\ mol^{-1}$
activation volume V_{df}	0	$3.80{\cdot}10^{-5}$	$6.00{\cdot}10^{-6}$	$cm^3\ mol^{-1}$
Drucker-Prager plasticity				
friction angle ϕ	26.56	26.56	26.56	°
cohesion C	20	20	20	MPa

Table 2.2: Material properties used in the numerical forward and steady-state models. Reference temperature $T_0 = 293K$, grain size $d = 1e-3$, the user-defined minimum and maximum viscosities are $\eta_{min} = 1e17$ and $\eta_{max} = 1e24$. $^{(a)}$ Rutter et al. (2004), $^{(b)}$ Rybacki et al. (2006), $^{(c)}$ Hirth et al. (2004).

where κ is the bulk thermal diffusivity [$m^2\ s^{-1}$], T is the temperature [K], H is the radiogenic heat production [$W\ m^{-3}$] and c_p is the heat capacity [$J\ K^{-1}$]. The steady-state temperature field hence entirely depends on the material properties κ, H and c_P of the three compositional layers (Table 2.2) and the assumption of conductive heat flow that leads to an instantaneous equilibration of the thermal field between the boundary conditions of 1300°C at the LAB and 0°C at the surface.

2.3 Results

In this section, we first present the outcome of the evolution of the dynamic models, which provide the structural setup for the steady-state models. We describe the general rift evolution patterns of the dynamic models, before we focus on the temperature distribution and compare it to the thermal fields of the steady-state models. Finally, we introduce a threshold value to quickly assess the validity of thermal steady-state models in the light of extension velocity.

Our dynamic models reproduce first-order rift characteristics, such as lithospheric thinning accommodated by crustal faulting and ductile shear zone formation at depth. They show foot wall uplift and hanging wall subsidence with pronounced basin formation for narrow rift scenarios. Highest topography contrasts emerge in models with the thinnest crust, as expected from classical studies (Braun et al., 1989; Buck, 1991). The development of dominant border faults and the migration of fault activity towards the center of the rift matches geologic observations, e.g. from the East African Rift System (Ebinger et al., 2012; Corti et al., 2018). The formation of major shear zones in the lower crust and upper mantle is supported by a range of published rift models (Huismans et al., 2003; Pourhiet et al., 2004; Duretz et al., 2016).

In agreement with further previous numerical studies, we find that crustal thickness and therefore crustal strength are the key parameters affecting whether narrow or wide rifts are formed (Tetreault et al., 2018; Brune et al., 2017; Armitage et al., 2018): Models with 20–30 km thick crust generate

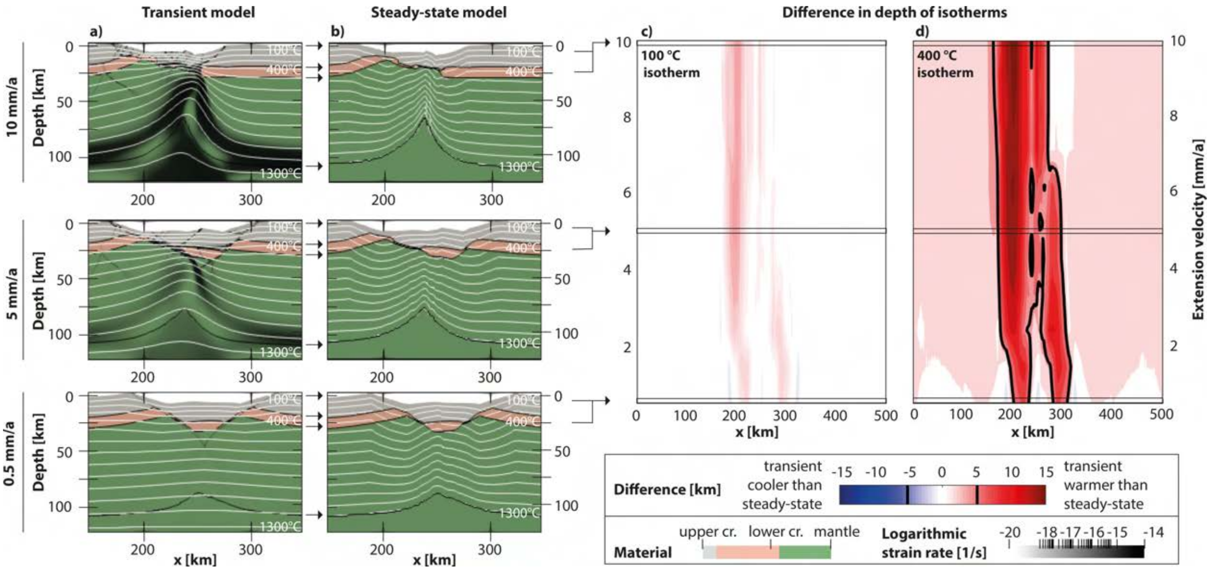

Figure 2.4: Left: Profiles of three exemplary **narrow rift models** with an initial crustal thickness of 30 km and different extension velocities (of 0.5, 5 and 10 mm/a, respectively). **(a)** The thermal, compositional, and deformation structure of the transient model at 50 km of total extension and **(b)** the corresponding steady-state model. Colors indicate the different materials used in the model as given in Figure 2.3 and Table 2.2. The strain rate is superposed in a transparent grey scale. White lines mark the depths of isotherms with a spacing of 100°C. Black arrows between (a) and (b) point at the material contours that are extracted from the transient models to define the material structure of the steady-state models. **Right:** Influence of the extension velocity on the difference between transient and steady-state models. Differences between transient and steady-state models are color-coded in terms of the respective $\Delta d_{\text{isotherm}}$ of **(c)** the 100°C isotherm and **(d)** the 400°C isotherm. Red colors indicate a warmer crust in the transient model with the isotherms being shallower compared to the steady-state model. The black contour marks a 5 km difference in depth.

distinct, ≈70 km wide half grabens within a few million years that develop into asymmetric narrow rifts (Figure 2.3). Over the modeled period, the rift valley reaches a width of about 180 km and the crust is thinned to only a few kilometers within the central parts of the rift. In models with thicker crust (40–50 km), however, deformation takes more time to localize and a wide rift evolves with strain and topography being distributed over the entire model domain. The material layers of the model are thinned more homogeneously over the width of the model due to the formation of several, roughly equally-spaced rift faults.

Based on this consistent structural evolution, we evaluate the temperature distribution in the crust. The temperature field of the dynamic models is affected by conduction and advection of heat, as well as its generation due to radiogenic, adiabatic, and shear heating. The interplay of these processes generates a thermal field of a complex transient nature (Figures 2.4a and 2.5a). Contrarily, in the steady-state models, the temperature field is only affected by heat conduction and radiogenic heating. This results in relatively evenly spaced isotherms for each 1D profile along the modeled sections (Figures 2.4b and 2.5b). It also leads to a strong influence of the surface topography on the geometry of shallow isotherms like the 100°C, while the deeper isotherms mimic the shape of the LAB. A strong impact of the LAB shape can be observed even for intermediate temperatures like the 400°C isotherm. Resulting amplitudes in the topography of the isotherms are distinctly larger in narrow rift models with 20–30 km of initial crustal thickness than in wide rift settings with 40–50 km of initial crustal thickness (Figures 2.4a,b and 2.5a,b). In Supplementary Figure A.S6 we show that the strong influence of the surface topography and the LAB on the shape of the isotherms can be avoided by using a 2D thermal steady-state approach (see supplement for methodology). The results for the exemplary 2D steady-state model demonstrate that the small scale variability of the depth difference is smoothed out for models employing a 2D thermal steady-state compared to those using 1D thermal steady-state computations. However, the magnitude and spatial distribution remains comparable for both approaches.

The comparison between transient and steady-state model temperatures shows that shallow, crustal isotherms predicted by steady-state models are generally deeper than those from the corresponding transient models (compare Figures 2.4b and 2.5b to Figures 2.4a and 2.5a). To a small degree, this effect

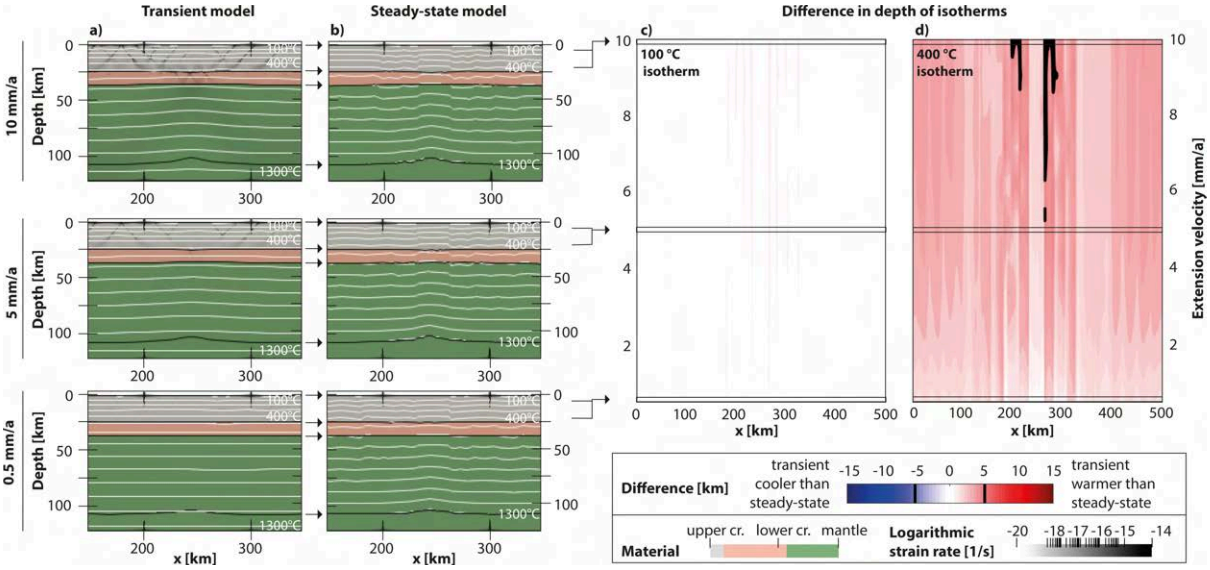

Figure 2.5: Left: Profiles of three exemplary **wide rift models** with an initial crustal thickness of 40 km and different extension velocities (of 0.5, 5 and 10 mm/a, respectively). **(a)** The thermal, compositional, and deformation structure of the transient model at 50 km of total extension and **(b)** the corresponding steady-state model. Colors indicate the different materials used in the model as given in Figure 2.3 and Table 2.2. The strain rate is superposed in a transparent grey scale. White lines mark the depths of isotherms with a spacing of 100°C. Black arrows between (a) and (b) point at the material contours that are extracted from the transient models to define the material structure of the steady-state models. **Right:** Influence of the extension velocity on the difference between transient and steady-state models. Differences between transient and steady-state models are color-coded in terms of the respective $\Delta d_{\text{isotherm}}$ of **(c)** the 100°C isotherm and **(d)** the 400°C isotherm. Red colors indicate a warmer crust in the transient model with the isotherms being shallower compared to the steady-state model. The black contour marks a 5 km difference in depth.

is caused by shear heating that releases heat in areas of active faulting. However, the key control on this effect can be understood when considering that the dynamic models feature a pronounced vertical advection component that is not represented in the steady-state models. In order to further explore the impact of heat advection, we explicitly compare the depth of a shallow and a deep crustal isotherm (100°C and 400°C, respectively) between transient and corresponding steady-state models (Figures 2.4c,d and 2.5c,d - results for more isotherms up to 600°C are shown in the supplementary Figures A.S5a,b.). These two isotherms provide a characteristic representation of the temperature spectrum relevant for georesources and geochronological applications. For example, the closure temperature for fission tracks in apatite is ≈100°C and ≈300°C in zircon (Braun et al., 2006). Isotherm depths are extracted from both the transient and the steady-state models over the entire width of the model domain and are then compared by subtracting one depth from the other at each coordinate as:

$$\Delta d_{\text{isotherm}} = d_{\text{steady-state}} - d_{\text{transient}} \tag{2.11}$$

with $\Delta d_{\text{isotherm}}$ being the difference in depth of the isotherm. This results in positive values when the transient isotherm is shallower than the steady-state isotherm (Figures 2.4c,d and 2.5c,d).

The resulting profiles of $\Delta d_{\text{isotherm}}$ for the different extension velocities in narrow and wide rift settings are shown in Figures 2.4c,d and 2.5c,d, respectively. For narrow rift settings, the evolving low topographical elevations determine the width of the overall positive values of $\Delta d_{\text{isotherm}}$ across the rift valley (Figure 2.4c,d). The 1D steady-state heat equation (Eq. 2.10) generates a relatively regular isotherm spacing between surface and LAB, which leads to deeper crustal steady-state isotherms below low topographical elevations. In the rift center the topographical effect is counteracted by the elevated LAB, which moves the steady-state isotherms upwards making them more similar to the shallowly advected transient isotherms and hence reduces values for $\Delta d_{\text{isotherm}}$. Contrarily, the maximum $\Delta d_{\text{isotherm}}$ is situated beneath the sides of the rift valley where the LAB is less elevated, but the topography low. Here, the transient isotherms still show an advection component while the relatively large distance between the surface and the LAB increases the spacing between steady-state isotherms, which moves them deeper into the crust. The calculated maximum $\Delta d_{\text{isotherm}}$ of the 100°C isotherm is

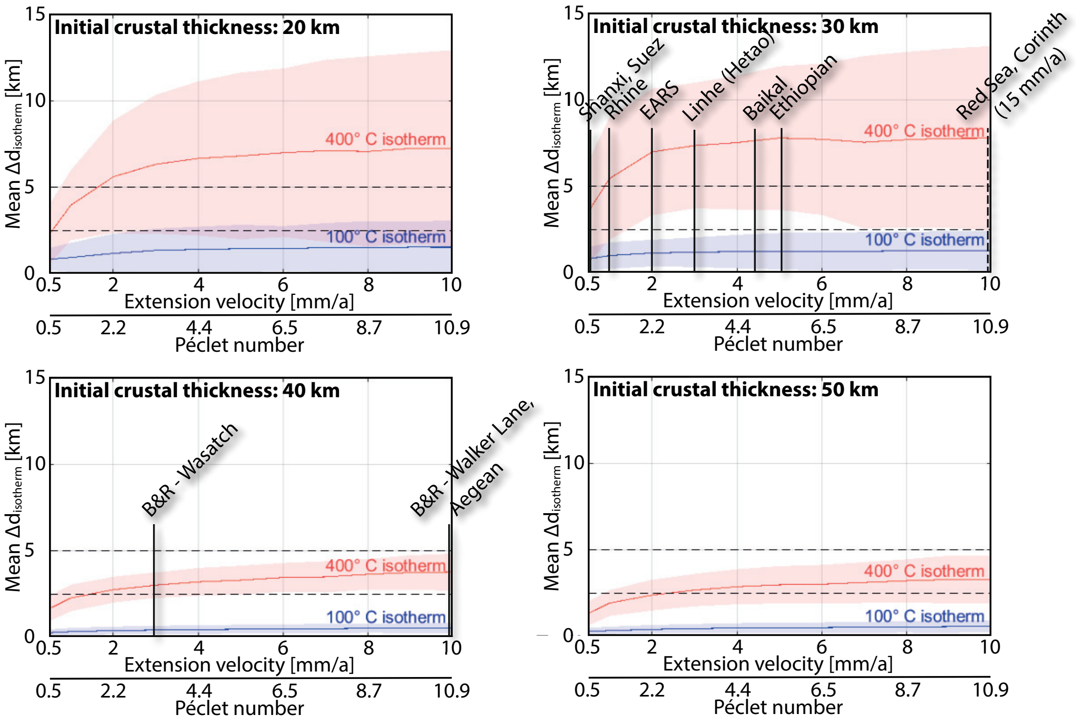

Figure 2.6: Mean differences of the isotherm depth after 50 km of extension as obtained from the central third of the model domain, which includes the entire rift region for all narrow rifts. Each image shows results for a different initial crustal thickness. The x-axis indicates both the extension velocity in mm/a and the corresponding Péclet number as calculated from the parameters at the start of each model (Eq. 2.9). Solid lines give the arithmetic mean of the deviation in the central third of the model. The one standard deviation interval is shown as a colored envelop. Examples of modern rifts are plotted for comparison, references for extension velocities are listed in Table 2.1 and locations are shown in Figure 2.1. The dashed lines represent the similarity thresholds $\epsilon = \pm\ 2.5$ and $\epsilon = \pm\ 5$ km. B&R: Basin and Range, EARS: East African Rift System.

less than 5 km, but exceeds 10–15 km for the 400°C isotherm for rifts faster than 1 mm/a. Wide rift settings, in contrast, lack a strong topographical relief and also the LAB is elevated only modestly across a wide region (Figure 2.5a,b). This results in a more homogeneous distribution of values for $\Delta d_{\mathrm{isotherm}}$ over the entire model width. The horst and graben topography nonetheless manifests as alternating values for $\Delta d_{\mathrm{isotherm}}$ along the x-axis, that, however, exceed 5 km only locally.

We employ standard statistics in order to quantify the first-order thermal transient effects for all configurations (Figure 2.6). To this aim, the arithmetic mean and standard deviation of the absolute differences in isotherm depth $\Delta d_{\mathrm{isotherm}}$ are calculated over all x-coordinates extracted from the central third of each model, which is where most surface deformation localizes for narrow rifts. The smaller the arithmetic mean and the standard deviation envelope, the more similar are the isotherm depths of a transient and corresponding steady-state model and thus the smaller is the transient signal. We therefore propose the concept of a similarity threshold ϵ. If the absolute difference in depth is smaller than ϵ, the analyzed set of models can be considered in thermal steady-state within the given assumptions of ϵ. We employ exemplary ϵ values of ± 2.5 and ± 5 km, which lie in the range of uncertainties of geophysical data interpretations at crustal depths. However, when evaluating LAB depths, these numbers could also be chosen significantly higher as the uncertainty of the thickness of the lithosphere may be $>$ 10–20 km depending on the database and LAB definition used (e.g. Eaton et al., 2009; Fischer et al., 2010). We therefore emphasize that the values for ϵ used here are exemplary and should be adjusted to the purpose of specific studies and data uncertainties. Depending on the resolution of the problem, ϵ can be applied both to the arithmetic mean along the entire profile (Figure 2.6) and to a single x-location (Figures 2.4c,d and 2.5c,d).

According to this workflow, we find that a steady-state modeling approach is not appropriate for: (1) The 100°C isotherm in a narrow rift setting for extension velocities $>$ 0.5 mm/a, as the maximum

$\Delta d_{\text{isotherm}}$ beneath the sides of the rift valley exceeds the similarity threshold $\epsilon = \pm 2.5$ km for 20–30 km of initial crustal thickness (Figure 2.4c). (2) The 400°C isotherm in a narrow rift setting regardless of the magnitude of the extension velocity and the initial crustal thickness, if $\epsilon = \pm 2.5$ km is used. For extension velocities > 1 mm/a and 20 km of initial crustal thickness as well as for > 0.5 mm/a and 30 km initial crustal thickness, the arithmetic mean $\Delta d_{\text{isotherm}}$ exceeds even $\epsilon = \pm 5$ km (Figure 2.6). The maximum $\Delta d_{\text{isotherm}}$ beneath the sides of the rift valley reaches values of 10–17 km (Figure 2.4d). (3) The 400°C isotherm in a wide rift setting where certain extension velocities occur: The arithmetic mean $\Delta d_{\text{isotherm}}$ exceeds $\epsilon = \pm 2.5$ km for extension velocities of > 1 mm/a and > 2 mm/a for initial crustal thicknesses of 40 km and 50 km, respectively (Figure 2.6). Beneath the sides of the rift valley, the maximum $\Delta d_{\text{isotherm}}$ exceeds $\epsilon = \pm 5$ km for extension velocities of > 5 mm/a (Figure 2.5d).

We furthermore consistently find that the mean $\Delta d_{\text{isotherm}}$ increases with extension velocity for all initial crustal thicknesses (Figure 2.6). The mean $\Delta d_{\text{isotherm}}$ first increases rapidly for extension velocities < 2 mm/a while the curve flattens, but continues to increase for extension velocities > 2 mm/a. For fast extending narrow rifts, the mean $\Delta d_{\text{isotherm}}$ reaches up to 1.5 km and 7.5 km for the 100°C and 400°C isotherm, respectively. For wide rifts the mean $\Delta d_{\text{isotherm}}$ reaches up to 0.5 km and 4 km for the 100°C and 400°C isotherm, respectively.

2.4 Discussion

In the following section, we first explore how present-day continental rifts compare to our generic findings. We then highlight implications and limitations of our models and explain the choice of the snapshot at 50 km of extension for thermal comparison. Finally, we discuss alternative ways to setup the steady-state models and to represent thermal steady-stateness.

In Figure 2.6, we assess the first-order thermal steady-stateness of natural rifts by mapping the associated divergence rate onto the diagram for the initial crustal thickness. Taking the Baikal Rift in the upper right panel as an example, it can be seen that the mean $\Delta d_{\text{isotherm}}$, the mean deviation of the steady-state from the transient models, for the modeled temperature of 400°C (red) exceeds both considered values of the similarity threshold ϵ (horizontal dashed lines). This means that according to the approach presented in this study, the Baikal Rift cannot be assumed in thermal steady-state for intermediate crustal temperatures. Contrarily, the mean $\Delta d_{\text{isotherm}}$ for 100°C (blue) is situated below both exemplary values for ϵ and can hence be considered suitable for a steady-state modeling approach (– to assess $\Delta d_{\text{isotherm}}$ at specific x-locations in a rift region, the reader is referred to Figures 2.4c,d and 2.5c,d).

Subsequently, Figure 2.6 shows that wide rifts, like the Basin and Range province and the Aegean, as well as slow narrow rifts, like the Shanxi and Suez rifts (0.5 mm/a), are better represented by a steady-state model than faster narrow rifts, like the African rifts or the Gulf of Corinth. However, even for an extension velocity of 0.5 mm/a, the maximum $\Delta d_{\text{isotherm}}$ for the shallow 100°C isotherm exceeds $\epsilon = \pm 2.5$ km locally, beneath the sides of the rift valley. The average $\Delta d_{\text{isotherm}}$ for 1 mm/a (e.g. Rhine graben) already exceeds $\epsilon = \pm 5$ km. The use of a thermal steady-state model for narrow rifts would thus introduce large uncertainties.

To further demonstrate the implications of these results, we consider a slow rift with an extension velocity of 1 mm/a and 30 km initial crustal thickness, which is similar to the Rhine graben. For this rift, the transient model predicts a temperature of around 450°C for a point at 20 km depth beneath the rift center. However, in the steady-state model, it is 20°C colder at that location. Beneath the sides of the rift valley, where the maximum $\Delta d_{\text{isotherm}}$ is located, a point at 20 km depth would be even 150°C colder in a steady-state model compared to a transient model. In terms of depth, maximum values of $\Delta d_{\text{isotherm}}$ reach 10–17 km for the 400°C isotherm, which is in the range of the actual 400°C isotherm depth in a typical continental setting: a temperature gradient of 25°C/km and 0°C at the surface implies a depth of 16 km for 400°C to occur. This means that in fast narrow rifts that feature a pronounced transient tectonic temperature component and therewith elevated temperature gradients, the introduced uncertainty might even be a multiple of the actual isotherm depth - a temperature gradient of 100°C/km and 0°C at the surface leads to a depth of 4 km for 400°C compared to maximum values of $\Delta d_{\text{isotherm}}$ of 10–17 km.

Errors introduced by neglecting transient thermal processes do not only affect models that directly assess the temperature distribution. They also impact other derived variables, as many physical and chemical processes as well as rock properties are temperature dependent. Ignoring the transients in the thermal field would for example change the estimated rheological behaviour by assuming a wider domain of brittle deformation inside the rift valley due to lower crustal temperatures. Whenever considering the thermal field to be in equilibrium, the presented analysis gives an estimate about the magnitude of uncertainty that is introduced into the model. In this study, we chose a continental rift setting, but large-scale transient thermal signals can also be expected in other tectonically active regions, e.g. around orogenic belts (Meeßen, 2019).

Our modeling approach focuses on first-order rift dynamics and accordingly includes several limitations. First of all, our models are two-dimensional. This is justified by the fact that rift segments are geometrically continuous in the rift-parallel direction, which is why major along-strike variations of the thermal field are not expected. For simplicity, we do not include second-order complexities such as magmatic activity, the influence of plumes, the thermal blanketing by a sedimentary cover or underground water circulation and mineral reactions (e.g Hacker et al., 2003; Bousquet et al., 2005; Scheck-Wenderoth et al., 2013; Scheck-Wenderoth et al., 2014; Koptev et al., 2018; Oliva et al., 2019). The models furthermore consist of four homogeneous layers (upper crust, lower crust, lithospheric mantle, asthenosphere) that do not account for potential spatial variability of thermal properties as these models are not designed to reflect a specific real-world example, but to generically investigate the process of isotherm advection during continental rifting. Fully aware of these simplifications, the so obtained dynamic models are taken as generalized analogues for a rift-typical tectonothermal history which is disregarded by steady-state approaches for thermal field modeling.

So far we presented the tectonothermal signal of all models after a fixed amount of 50 km of extension, even though we performed the analysis continuously until reaching 100 km of accumulated extension. When applying the workflow stepwise to other finite extension values and analyzing the variability of steady-stateness, we find the following general temporal development of mean $\Delta d_{\text{isotherm}}$ (Supplementary Figure A.S4): after a build-up phase, the general order of magnitude of the mean $\Delta d_{\text{isotherm}}$ first remains constant before decreasing slightly. This decrease corresponds to a closer approximation of the steady-state models to the transient ones. Considering an exemplary model with an initial crustal thickness of 30 km and an extension velocity of 3 mm/a, the decrease amounts to 2 km (Figure A.S4 upper left). Its onset varies according to extension velocity: for slowly and moderately extending rifts it occurs after 50 to 70 km of extension, while manifesting a few tens of kilometers of extension later for faster rifts. Tectonically, the decrease coincides with a change in border fault geometry, which has previously been described as the transition from stretching to thinning mode during rift evolution (Lavier et al., 2006; Chenin et al., 2018). Our modeling suite thus shows that steady-state thermal models become closer to their transient equivalents during the rift episode when the deformation style changes. In line with this finding, to obtain an estimate for a maximum error potentially introduced in steady-state models, we base the steady-state assessment on the evolutionary snapshots at 50 km of extension, where all models are close to the maximum $\Delta d_{\text{isotherm}}$ regardless of the extension velocity.

A significant decision for the analysis of this paper, is the choice of the workflow to set up the steady-state models, which includes the choice of the parameter that represents the LAB. For better comparability of our results, we designed the steady-state models as similar to data-integrative modeling approaches as possible (Tesauro et al., 2012; Gac et al., 2016; Maystrenko et al., 2018). We have used snapshots of the deep structural configuration of the transient models as the counterpart to the LAB depth that is derived from temperature conversions of seismic tomography studies and used as lower boundary conditions of data-integrative thermal models. Alternatively to those models presented in Figures 2.4–2.6 that are based on the extracted material contour at the bottom of the lithosphere, a calculation of the steady-state models can also be based on the 1300°C isotherm as extracted from the transient model. Taking the transient 1300°C isotherm as the new thermal LAB for the steady-state models may seem to be the more direct approach, but it has the disadvantage that its geometrical evolution is significantly affected by the predefined initial vertical model size through thermal boundary conditions. On the other hand, our approach of converting a material discontinuity into an isotherm could also be questioned, but as its evolution is independent of the model size, we regard it as the more appropriate lower boundary condition for later snapshots. We tested the impact of both possibilities and despite the fundamental differences in the nature of the two approaches, we find that both lead to qualitatively similar results, proving our findings regarding the influence of the initial crustal thickness and extension velocity on the steady-stateness of transient systems (compare Fig. 2.4–2.6 to Fig. A.S1–

A.S3). The choice of 1300°C as the absolute model temperature at the LAB lies within the range of other lithospheric-scale models (Afonso et al. (2016): 1250°C, Balling et al. (2013): 1300°C, Carballo et al. (2015): 1330°C, Sippel et al. (2017): 1350°C). In Supplementary Figure A.S6 we show that the overall pattern of $\Delta d_{\text{isotherm}}$ remains comparable when using 1250°C as the temperature at the LAB.

An important finding of this study is that the discussed steady-state isotherms of 100°C and 400°C are almost everywhere deeper than the corresponding transient isotherms, independently of the representation of the LAB. This is due to the upward advection of hot material in a rift setting. Both sets of steady-state models are consistent in this point, regardless of whether a material LAB contour or an associated isotherm is extracted from the transient model (compare Figures A.S1–A.S3 in the supplement to Figures 2.4–2.6). However, when the 1300°C isotherm is extracted from a transient model, the values for $\Delta d_{\text{isotherm}}$ are larger, influence a wider rift domain and affect more rift-distant locations than for the case of a material discontinuity. This is because the 1300°C isotherm of a transient model is generally not as elevated as the lower boundary of the modeled compositional unit of the lithospheric mantle. Associated crustal steady-state isotherms hence remain deeper within the subsurface, which contrasts the corresponding transient isotherms that are further moved to shallow depths by advective material transport. Accordingly, the values for $\Delta d_{\text{isotherm}}$ increase. The difference of the two sets of models is especially important for slower rifts, as for faster rifts the 1300°C isotherm coincides better with the material discontinuity at the base of the lithosphere.

For both definitions of the LAB, the values for $\Delta d_{\text{isotherm}}$ increase with increasing extension velocity. The results hence show the expected positive relationship between $\Delta d_{\text{isotherm}}$ and the extension velocity. This is readily explained by faster advection of hot material for higher extension velocities, a process that dominates over the counteracting heat conduction that would re-equilibrate temperatures. This effect can also be seen in the Péclet numbers associated with the extension velocities. With the extension velocities of 0.5–10 mm/a, our models span the entire transition between predominantly conductive heat transport ($Pe < 1$) and predominantly advective heat transport ($Pe > 10$) (Sandiford, 2002), see Figure 2.6. This change in heat transport mechanism is reflected in the values for $\Delta d_{\text{isotherm}}$ that increase the more important heat advection becomes. However, our results show that Péclet numbers alone are too general to decide about the validity of the steady-state assumption as this also depends to a large degree on the structure of the rift, i.e. whether it classifies as narrow or wide rift type.

We translate the importance of heat advection into a threshold-based approach to represent thermal steady-stateness. Hence a temperature field from a dynamic model can be considered in steady-state when $\Delta d_{\text{isotherm}}$ is smaller than a given similarity threshold ϵ. An alternative approach would be to assess the change of a certain parameter of the evolution models over time such as the temperature at depth. However, this would still require the introduction of a threshold, e.g. the temperature change through time as a percentage of actual temperatures as in Peacock (1996) for subduction settings. By comparing transient models to steady-state models with the same material configuration, we stay closer to the setup of published lithospheric-scale thermal models and provide a reference basis for the development of this kind of models in the future.

2.5 Conclusion

Using numerical modeling, we investigate the validity of the thermal steady-state assumption in extensional continental settings. We show that neglecting tectonic transient thermal effects yields a systematic error in terms of the depth of crustal isotherms. Since these isotherms are advected upwards during rifting, they are always shallower than predicted by the steady-state assumption. For higher extension velocities, this process becomes more important and affects larger depths.

We find that wide rifts reside close to thermal steady-state even for relatively high extension velocities. For narrow rifts, however, we find a speed limit of roughly 0.5–2 mm/a for the applicability of the steady-state assumption. Thus, not only relatively fast rifts like the Main Ethiopian Rift, the Afar rift segments, the Red Sea, and the Gulf of Corinth, but even slow rifts like the Kenya Rift, the Rhine Graben, and Rio Grande Rift must be expected to feature a pronounced transient component in the temperature field and to therefore violate the thermal steady-state assumption for deeper crustal isotherms.

We furthermore illustrate that the speed limit depends on the exact depth and location studied. This is due to the fact that isotherms in steady-state models strongly follow the surface topography and

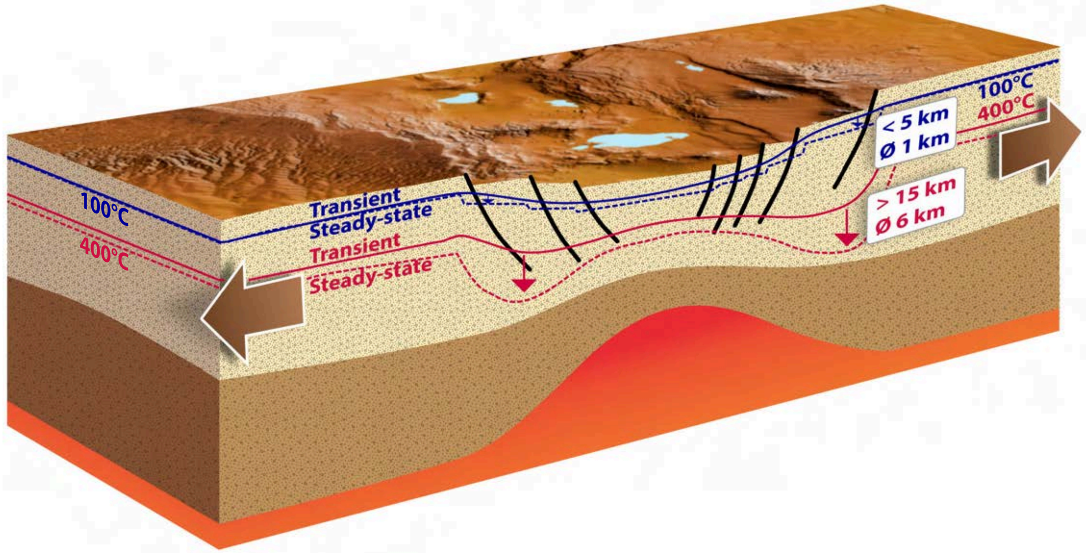

Figure 2.7: A cartoon of a continental narrow rift with sketches of faults in black (not to scale). The blue and red lines show the generalized main trends and features of the 100°C and 400°C isotherms of the narrow rift transient models (solid lines) and the corresponding steady-state models (dashed lines). The results suggest that isotherms from steady-state models are deeper than those from the corresponding transient models. The maximum difference for the 100°C isotherm is less than 5 km, but more than 10–15 km for the 400°C isotherm for rifts faster than 1 mm/a. Mean values for the thermal model difference are 1–1.5 km and 6 km, respectively.

the depth of the lithosphere-asthenosphere boundary, which results in a maximum difference between transient and steady-state models adjacent to the high topography of the rift shoulders. The influence of the thermal boundary conditions varies with depth and we therefore find that the steady-stateness of a model depends on the considered isotherm (Figure 2.7). Where shallow isotherms are investigated (e.g. the 100°C isotherm), the transient imprint of rifting appears to be negligible. Contrarily, steady-state assessments of intermediate isotherms (e.g. the 400°C isotherm) systematically lead to underestimations of crustal temperatures especially for narrow rift settings.

In light of these findings, our work does not only put a speed limit on the thermal steady-state assumption, but also provides a way to include the tectonothermal signal as an uncertainty range. This is especially useful for settings where there is no alternative to a steady-state modeling approach.

Acknowledgments

We are grateful for the detailed and constructive comments of J. C. Afonso and an unknown reviewer that substantially helped to improve the manuscript. This study was conducted within the Helmholtz Young Investigators Group CRYSTALS (VH-NG-1132). We thank the Computational Infrastructure for Geodynamics (`geodynamics.org`) which is funded by the National Science Foundation under award EAR-0949446 and EAR-1550901 for supporting the development of ASPECT. Computa-tions were performed on GFZ clusters and on Konrad, an HLRN cluster facility. Figures in this paper were made with ParaView, InkScape and Adobe Illustrator.

Data Availability Statement

The specific version of the geodynamic modeling software ASPECT that was used in this paper [Advanced Solver for Problems in Earth's ConvecTion, version 2.0.0-pre with deal.II version 8.5.1] is available from the Zenodo repository with the DOI `10.5281/zenodo.3778176`.

References

Afonso, Juan Carlos, Max Moorkamp, and Javier Fullea (2016). “Imaging the Lithosphere and Upper Mantle”. In: *Integrated Imaging of the Earth*. American Geophysical Union (AGU), pp. 191–218.

Afonso, Juan Carlos and Giorgio Ranalli (2004). “Crustal and mantle strengths in continental lithosphere: is the jelly sandwich model obsolete?” en. In: *Tectonophysics* 394.3, pp. 221–232.

Agemar, Thorsten, Jessica-Aileen Alten, Britta Ganz, Joerg Kuder, Klaus Kuehne, Sandra Schumacher, and Ruediger Schulz (2014). “The Geothermal Information System for Germany - GeotIS”. English. In: *Zeitschrift Der Deutschen Gesellschaft Fur Geowissenschaften* 165.2, pp. 129–144.

Armitage, John J., Kenni D. Petersen, and Marta Pérez-Gussinyé (2018). “The Role of Crustal Strength in Controlling Magmatism and Melt Chemistry During Rifting and Breakup”. In: *Geochemistry, Geophysics, Geosystems* 19.2, pp. 534–550.

Arndt, Daniel, Wolfgang Bangerth, Denis Davydov, Timo Heister, Luca Heltai, Martin Kronbichler, Matthias Maier, Jean-Paul Pelteret, Bruno Turcksin, and David Wells (2017). “The deal.II library, version 8.5”. In: *Journal of Numerical Mathematics* 25.3, pp. 137–145.

ArRajehi, Abdullah, Simon McClusky, Robert Reilinger, Mohamed Daoud, Abdulmutaleb Alchalbi, Semih Ergintav, Francisco Gomez, Jamal Sholan, Firyal Bou-Rabee, Ghebrebrhan Ogubazghi, Biniam Haileab, Shimelles Fisseha, Laike Asfaw, Salah Mahmoud, Ali Rayan, Rebecca Bendik, and Lewis Kogan (2010). “Geodetic constraints on present-day motion of the Arabian Plate: Implications for Red Sea and Gulf of Aden rifting”. en. In: *Tectonics* 29.3.

Artemieva, Irina M. (2006). “Global 1°x1° thermal model TC1 for the continental lithosphere: Implications for lithosphere secular evolution”. In: *Tectonophysics*. The Heterogeneous Mantle 416.1, pp. 245–277.

— (2009). “The continental lithosphere: Reconciling thermal, seismic, and petrologic data”. In: *Lithos* 109.1, pp. 23–46.

Balling, Philipp, Yuriy Maystrenko, and Magdalena Scheck-Wenderoth (2013). “The deep thermal field of the Glueckstadt Graben”. In: *Environmental Earth Sciences* 70.8, pp. 3505–3522.

Bangerth, Wolfgang, Juliane Dannberg, Rene Gassmoeller, Timo Heister, et al. (2018). *ASPECT v2.0.0 [software]*. Davis, CA: Computational Infrastructure for Geodynamics.

Bayer, U., M. Scheck, and M. Koehler (1997). “Modeling of the 3D thermal field in the northeast German basin”. In: *Geologische Rundschau* 86.2, pp. 241–251.

Bendick, R., S. McClusky, R. Bilham, L. Asfaw, and S. Klemperer (2006). “Distributed Nubia—Somalia relative motion and dike intrusion in the Main Ethiopian Rift”. In: *Geophysical Journal International* 165.1, pp. 303–310.

Bennett, R. A., B. P. Wernicke, and J. L. Davis (1998). “Continuous GPS measurements of contemporary deformation across the Northern Basin and Range Province”. In: *Geophysical Research Letters* 25.4, pp. 563–566.

Berglund, Henry T., Anne F. Sheehan, Mark H. Murray, Mousumi Roy, Anthony R. Lowry, R. Steven Nerem, and Frederick Blume (2012). “Distributed deformation across the Rio Grande Rift, Great Plains, and Colorado Plateau”. In: *Geology* 40.1, pp. 23–26.

Bousquet, Romain, Bruno Goffé, Xavier Le Pichon, Christian de Capitani, Christian Chopin, and Pierre Henry (2005). “Comment on “Subduction factory: 1. Theoretical mineralogy, densities, seismic wave speeds, and H $_2$ O contents” by Bradley R. Hacker, Geoffrey A. Abers, and Simon M. Peacock: commentary”. en. In: *Journal of Geophysical Research: Solid Earth* 110.B2.

Braun, Jean and Christopher Beaumont (1989). “A physical explanation of the relation between flank uplifts and the breakup unconformity at rifted continental margins”. In: *Geology* 17.8, pp. 760–764.

Braun, Jean, Peter van der Beek, and Geoffrey Batt (2006). *Quantitative Thermochronology: Numerical Methods for the Interpretation of Thermochronological Data*. Cambridge University Press.

Brun, J. P., M. -A. Gutscher, and dekorp-ecors teams (1992). “Deep crustal structure of the Rhine Graben from dekorp-ecors seismic reflection data: A summary”. en. In: *Tectonophysics*. Geodynamics of rifting, volume 1 Case history studies on rifts: Europe and Asia 208.1, pp. 139–147.

Brun, Jean-Pierre and Dimitrios Sokoutis (2018). “Core Complex Segmentation in North Aegean, A Dynamic View”. en. In: *Tectonics* 37.6, pp. 1797–1830.

Brune, S., C. Heine, M. Pérez-Gussinyé, and S. V. Sobolev (2014). “Rift migration explains continental margin asymmetry and crustal hyper-extension”. en. In: *Nature Communications* 5.1, pp. 1–9.

Brune, Sascha (2014). “Evolution of stress and fault patterns in oblique rift systems: 3-D numerical lithospheric-scale experiments from rift to breakup”. In: *Geochemistry, Geophysics, Geosystems* 15.8, pp. 3392–3415.

Brune, Sascha, Christian Heine, Peter D. Clift, and Marta Pérez-Gussinyé (2017). “Rifted margin architecture and crustal rheology: Reviewing Iberia-Newfound-land, Central South Atlantic, and South China Sea”. In: *Marine and Petroleum Geology* 79, pp. 257–281.

Buck, W. Roger (1991). “Modes of continental lithospheric extension”. In: *Journal of Geophysical Research: Solid Earth* 96.B12, pp. 20161–20178.

Burov, Evgene B. (2011). “Rheology and strength of the lithosphere”. In: *Marine and Petroleum Geology* 28.8, pp. 1402–1443.

Calais, Eric, Olivia Lesne, Jacques Déverchère, Vladimir San’kov, Andrei Lukhnev, Andrei Miroshnitchenko, Vladimir Buddo, Kirill Levi, Vjacheslav Zalutzky, and Yuri Bashkuev (1998). “Crustal deformation in the Baikal Rift from GPS measurements”. In: *Geophysical Research Letters* 25.21, pp. 4003–4006.

Carballo, A., M. Fernandez, I. Jiménez-Munt, M. Torne, J. Vergés, M. Melchiorre, D. Pedreira, J. C. Afonso, D. Garcia-Castellanos, J. Díaz, A. Villaseñor, J. A. Pulgar, and L. Quintana (2015). “From the North-Iberian Margin to the Alboran Basin: A lithosphere geo-transect across the Iberian Plate”. In: *Tectonophysics*. Special issue on Iberia geodynamics: An integrative approach from the Topo-Iberia framework 663, pp. 399–418.

Chapman, D. S. (1986). “Thermal gradients in the continental crust”. In: *Geological Society, London, Special Publications* 24.1, pp. 63–70.

Chenin, Pauline, Stefan M. Schmalholz, Gianreto Manatschal, and Thibault Duretz (2020). “Impact of crust–mantle mechanical coupling on the topographic and thermal evolutions during the necking phase of ‘magma-poor’ and ‘sediment-starved’ rift systems: A numerical modeling study”. en. In: *Tectonophysics* 786, p. 228472.

Chenin, Pauline, Stefan M. Schmalholz, Gianreto Manatschal, and Garry D. Karner (2018). “Necking of the Lithosphere: A Reappraisal of Basic Concepts With Thermo-Mechanical Numerical Modeling”. In: *Journal of Geophysical Research: Solid Earth* 123.6, pp. 5279–5299.

Corti, Giacomo, Paola Molin, Andrea Sembroni, Ian D. Bastow, and Derek Keir (2018). “Control of Pre-rift Lithospheric Structure on the Architecture and Evolution of Continental Rifts: Insights From the Main Ethiopian Rift, East Africa”. In: *Tectonics* 37.2, pp. 477–496.

Davies, D. R., G. Le Voci, S. Goes, S. C. Kramer, and C. R. Wilson (2016). “The mantle wedge’s transient 3-D flow regime and thermal structure”. In: *Geochemistry, Geophysics, Geosystems* 17.1, pp. 78–100.

Duclaux, Guillaume, Ritske S. Huismans, and Dave May (2018). “Rotation, narrowing and preferential reactivation of brittle structures during oblique rifting”. In: *EGU General Assembly Conference Abstracts*, p. 7247.

Duretz, T., B. Petri, G. Mohn, S. M. Schmalholz, F. L. Schenker, and O. Müntener (2016). “The importance of structural softening for the evolution and architecture of passive margins”. en. In: *Scientific Reports* 6.1, pp. 1–7.

Eaton, David W., Fiona Darbyshire, Rob L. Evans, Herman Grütter, Alan G. Jones, and Xiaohui Yuan (2009). “The elusive lithosphere–asthenosphere boundary (LAB) beneath cratons”. In: *Lithos*. Continental Lithospheric Mantle: The Petro-Geophysical Approach 109.1, pp. 1–22.

Ebinger, Cynthia and Christopher A. Scholz (2012). “Continental Rift Basins: The East African Perspective”. In: *Tectonics of Sedimentary Basins*. John Wiley & Sons, Ltd, pp. 183–208.

Ehlers, Todd A. and Kenneth A. Farley (2003). “Apatite (U–Th)/He thermochronometry: methods and applications to problems in tectonic and surface processes”. In: *Earth and Planetary Science Letters* 206.1, pp. 1–14.

Fischer, Karen M., Heather A. Ford, David L. Abt, and Catherine A. Rychert (2010). “The Lithosphere-Asthenosphere Boundary”. In: *Annual Review of Earth and Planetary Sciences* 38.1, pp. 551–575.

Freymark, Jessica, Judith Sippel, Magdalena Scheck-Wenderoth, Kristian Bär, Manfred Stiller, Johann-Gerhard Fritsche, and Matthias Kracht (2017). “The deep thermal field of the Upper Rhine Graben”. In: *Tectonophysics* 694, pp. 114–129.

Fullea, J., J. C. Afonso, J. a. D. Connolly, M. Fernàndez, D. García-Castellanos, and H. Zeyen (2009). “LitMod3D: An interactive 3-D software to model the thermal, compositional, density, seismological, and rheological structure of the lithosphere and sublithospheric upper mantle”. In: *Geochemistry, Geophysics, Geosystems* 10.8.

Fullea, J., S. Lebedev, M. R. Agius, A. G. Jones, and J. C. Afonso (2012). “Lithospheric structure in the Baikal–central Mongolia region from integrated geophysical-petrological inversion of surface-wave data and topographic elevation”. In: *Geochemistry, Geophysics, Geosystems* 13.8.

Gac, Sébastien, Peter Klitzke, Alexander Minakov, Jan Inge Faleide, and Magdalena Scheck-Wenderoth (2016). “Lithospheric strength and elastic thickness of the Barents Sea and Kara Sea region”. en. In: *Tectonophysics*. SI:Circum-Arctic Evolution 691, pp. 120–132.

Gawthorpe, Robert L., Mike R. Leeder, Haralambos Kranis, Emmanuel Skourtsos, Julian E. Andrews, Gijs A. Henstra, Greg H. Mack, Martin Muravchik, Jenni A. Turner, and Michael Stamatakis (2018). “Tectono-sedimentary evolution of the Plio-Pleistocene Corinth rift, Greece”. In: *Basin Research* 30.3, pp. 448–479.

Glerum, Anne, Cedric Thieulot, Menno Fraters, Constantijn Blom, and Wim Spakman (2018). “Nonlinear viscoplasticity in ASPECT: benchmarking and applications to subduction”. English. In: *Solid Earth* 9.2, pp. 267–294.

Golombek, Matthew P., George E. McGill, and Laurie Brown (1983). “Tectonic and geologic evolution of the Espanola Basin, Rio Grande Rift: Structure, rate of extension, and relation to the state of stress in the western United States”. In: *Tectonophysics*. Processes of Continental Rifting 94.1, pp. 483–507.

Gudmundsson, Jón-Steinar (1988). “The elements of direct uses”. en. In: *Geothermics* 17.1, pp. 119–136.

Guillou-Frottier, Laurent, James Buttles, and Peter Olson (1995). “Laboratory experiments on the structure of subducted lithosphere”. In: *Earth and Planetary Science Letters* 133.1, pp. 19–34.

Hacker, Bradley R., Geoffrey A. Abers, and Simon M. Peacock (2003). “Subduction factory 1. Theoretical mineralogy, densities, seismic wave speeds, and H2O contents”. en. In: *Journal of Geophysical Research: Solid Earth* 108.B1.

Hamilton, W. (1987). “Crustal extension in the Basin and Range Province, southwestern United States”. en. In: *Geological Society, London, Special Publications* 28.1, pp. 155–176.

Hammond, William C. and Wayne Thatcher (2004). “Contemporary tectonic deformation of the Basin and Range province, western United States: 10 years of observation with the Global Positioning System”. In: *Journal of Geophysical Research: Solid Earth* 109 (B8).

Hart, Nicole R., Daniel F. Stockli, Luc L. Lavier, and Nicholas W. Hayman (2017). “Thermal evolution of a hyperextended rift basin, Mauléon Basin, western Pyrenees”. en. In: *Tectonics* 36.6, pp. 1103–1128.

Heckenbach, E. L., B. Norden, and S. Fuchs (2019). “Evaluation of the glacial impact on the shallow heat-flow density in the North German Basin”. eng. In.

Heister, Timo, Juliane Dannberg, Rene Gassmöller, and Wolfgang Bangerth (2017). “High Accuracy Mantle Convection Simulation through Modern Numerical Methods. II: Realistic Models and Problems”. In: *Geophysical Journal International* 210.2, pp. 833–851.

Hirth, Greg and David Kohlstedt (2004). “Rheology of the Upper Mantle and the Mantle Wedge: A View from the Experimentalists”. In: *Inside the Subduction Factory*. American Geophysical Union (AGU), pp. 83–105.

Huismans, Ritske S. and Christopher Beaumont (2003). “Symmetric and asymmetric lithospheric extension: Relative effects of frictional-plastic and viscous strain softening”. In: *Journal of Geophysi-cal Research: Solid Earth* 108.B10.

Huismans, Ritske S., Susanne J. H. Buiter, and Christopher Beaumont (2005). “Effect of plastic-viscous layering and strain softening on mode selection during lithospheric extension”. In: *Journal of Geophysical Research: Solid Earth* 110 (B2).

Jammes, Suzon and Luc L. Lavier (2016). “The effect of bimineralic composition on extensional processes at lithospheric scale”. In: *Geochemistry, Geophysics, Geosystems* 17.8, pp. 3375–3392.

Jiménez-Munt, I., M. Torne, M. Fernàndez, J. Vergés, A. Kumar, A. Carballo, and D. García-Castellanos (2019). “Deep Seated Density Anomalies Across the Iberia-Africa Plate Boundary and Its Topographic Response”. In: *Journal of Geophysical Research: Solid Earth* n/a (n/a).

Kendall, J.-Michael and Carolina Lithgow-Bertelloni (2016). “Why is Africa rifting?” en. In: *Geological Society, London, Special Publications* 420.1, pp. 11–30.

Kogan, L., S. Fisseha, R. Bendick, R. Reilinger, S. McClusky, R. King, and T. Solomon (2012). “Lithospheric strength and strain localization in continental extension from observations of the East African Rift”. In: *Journal of Geophysical Research: Solid Earth* 117 (B3).

Koptev, Alexander, Evgueni Burov, Taras Gerya, Laetitia Le Pourhiet, Sylvie Leroy, Eric Calais, and Laurent Jolivet (2018). “Plume-induced continental rifting and break-up in ultra-slow extension context: Insights from 3D numerical modeling”. In: *Tectonophysics*. Understanding geological processes through modelling - A Memorial Volume honouring Evgenii Burov 746, pp. 121–137.

Kreemer, Corné, Geoffrey Blewitt, and William C. Hammond (2010). “Evidence for an active shear zone in southern Nevada linking the Wasatch fault to the Eastern California shear zone”. In: *Geology* 38.5, pp. 475–478.

Kronbichler, M., T. Heister, and W. Bangerth (2012). “High Accuracy Mantle Convection Simulation through Modern Numerical Methods”. In: *Geophysical Journal International* 191, pp. 12–29.

Lane, Alfred Church (1923). “Geotherms of Lake Superior copper country”. In: *Geological Society of America Bulletin* 34, pp. 703–720.

Lavier, Luc L. and Gianreto Manatschal (2006). “A mechanism to thin the continental lithosphere at magma-poor margins”. In: *Nature* 440.7082, pp. 324–328.

Maystrenko, Yuriy Petrovich and Laurent Gernigon (2018). “3-D temperature distribution beneath the Mid-Norwegian continental margin (the Vøring and Møre basins)”. en. In: *Geophysical Journal International* 212.1, pp. 694–724.

McClusky, Simon, Robert Reilinger, Ghebrebrhan Ogubazghi, Aman Amleson, Biniam Healeb, Philippe Vernant, Jamal Sholan, Shimelles Fisseha, Laike Asfaw, Rebecca Bendick, and Lewis Kogan (2010). “Kinematics of the southern Red Sea–Afar Triple Junction and implications for plate dynamics”. In: *Geophysical Research Letters* 37.5.

McQuarrie, Nadine and Brian P. Wernicke (2005). “An animated tectonic reconstruction of southwestern North America since 36 Ma”. In: *Geosphere* 1.3, pp. 147–172.

Meeßen, Christian (2019). “The thermal and rheological state of the Northern Argentinian foreland basins”. In.

Naliboff, John B., Susanne J. H. Buiter, Gwenn Péron-Pinvidic, Per Terje Osmundsen, and Joya Tetreault (2017). “Complex fault interaction controls continental rifting”. In: *Nature Communications* 8.1, pp. 1–9.

Oliva, S. J., C. J. Ebinger, C. Wauthier, J. D. Muirhead, S. W. Roecker, E. Rivalta, and S. Heimann (2019). “Insights Into Fault-Magma Interactions in an Early-Stage Continental Rift From Source Mechanisms and Correlated Volcano-Tectonic Earthquakes”. In: *Geophysical Research Letters* 46.4, pp. 2065–2074.

Oskin, Michael, Joann Stock, and Arturo Martín-Barajas (2001). “Rapid localization of Pacific–North America plate motion in the Gulf of California”. In: *Geology* 29.5, pp. 459–462.

Peacock, Simon M. (1996). “Thermal and Petrologic Structure of Subduction Zones”. In: *Subduction*. American Geophysical Union (AGU), pp. 119–133.

Pourhiet, Laetitia Le, Evgenii Burov, and Isabelle Moretti (2004). “Rifting through a stack of inhomogeneous thrusts (the dipping pie concept)”. en. In: *Tectonics* 23.4.

Reilinger, Robert, Simon McClusky, Demitris Paradissis, Semih Ergintav, and Philippe Vernant (2010). “Geodetic constraints on the tectonic evolution of the Aegean region and strain accumulation along the Hellenic subduction zone”. In: *Tectonophysics*. Extensional Tectonics in the Basin and Range, the Aegean, and Western Anatolia 488.1, pp. 22–30.

Rey, P. F., C. Teyssier, and D. L. Whitney (2009). “Extension rates, crustal melting, and core complex dynamics”. en. In: *Geology* 37.5, pp. 391–394.

Rose, I., B. A. Buffett, and T. Heister (2017a). “Stability and accuracy of free surface time integration in viscous flows”. In: *Physics of the Earth and Planetary Interiors* 262, pp. 90–100.

Rose, Ian, Bruce Buffett, and Timo Heister (2017b). “Stability and accuracy of free surface time integration in viscous flows”. In: *Physics of the Earth and Planetary Interiors* 262, pp. 90–100.

Rutter, E. H. and K. H. Brodie (2004). “Experimental grain size-sensitive flow of hot-pressed Brazilian quartz aggregates”. In: *Journal of Structural Geology* 26.11, pp. 2011–2023.

Rybacki, E., M. Gottschalk, R. Wirth, and G. Dresen (2006). “Influence of water fugacity and activation volume on the flow properties of fine-grained anorthite aggregates”. In: *Journal of Geophysical Research: Solid Earth* 111 (B3).

Sandiford, Mike (2002). “Low thermal Peclet number intraplate orogeny in central Australia”. In: *Earth and Planetary Science Letters* 201.2, pp. 309–320.

Saria, E., E. Calais, D. S. Stamps, D. Delvaux, and C. J. H. Hartnady (2014). “Present-day kinematics of the East African Rift”. In: *Journal of Geophysical Research: Solid Earth* 119.4, pp. 3584–3600.

Scheck-Wenderoth, Magdalena, Mauro Cacace, Yuriy Petrovich Maystrenko, Yvonne Cherubini, Vera Noack, Bjoern Onno Kaiser, Judith Sippel, and Lewerenz Bjoern (2014). “Models of heat transport in the Central European Basin System: Effective mechanisms at different scales”. English. In: *Marine and Petroleum Geology* 55, pp. 315–331.

Scheck-Wenderoth, Magdalena and Yuriy Petrovich Maystrenko (2013). “Deep Control on Shallow Heat in Sedimentary Basins”. In: *Energy Procedia*. European Geosciences Union General Assembly 2013, EGUDivision Energy, Resources & the Environment, ERE 40, pp. 266–275.

Sdrolias, Maria and R. Dietmar Müller (2006). “Controls on back-arc basin formation”. en. In: *Geochemistry, Geophysics, Geosystems* 7.4.

Sippel, Judith, Christian Meeßen, Mauro Cacace, James Mechie, Stewart Fishwick, Christian Heine, Magdalena Scheck-Wenderoth, and Manfred R. Strecker (2017). “The Kenya rift revisited: insights into lithospheric strength through data-driven 3-D gravity and thermal modelling”. In: *Solid Earth* 8.1, pp. 45–81.

Smye, Andrew J., Luc L. Lavier, Thomas Zack, and Daniel F. Stockli (2019). "Episodic heating of continental lower crust during extension: A thermal modeling investigation of the Ivrea-Verbano Zone". en. In: *Earth and Planetary Science Letters* 521, pp. 158–168.

Stamps, D. S., L. M. Flesch, and E. Calais (2010). "Lithospheric buoyancy forces in Africa from a thin sheet approach". en. In: *International Journal of Earth Sciences* 99.7, pp. 1525–1533.

Tesauro, Magdala, Christine Hollenstein, Ramon Egli, Alain Geiger, and Hans-Gert Kahle (2005). "Continuous GPS and broad-scale deformation across the Rhine Graben and the Alps". In: *International Journal of Earth Sciences* 94.4, pp. 525–537.

Tesauro, Magdala, Mikhail K. Kaban, and Sierd A. P. L. Cloetingh (2009). "A new thermal and rheological model of the European lithosphere". In: *Tectonophysics* 476.3, pp. 478–495.

— (June 2012). "Global strength and elastic thickness of the lithosphere". In: *Global and Planetary Change*. Coupled deep Earth and surface processes in System Earth: monitoring, reconstruction and process modeling 90-91, pp. 51–57.

Tetreault, J. L. and S. J. H. Buiter (2018). "The influence of extension rate and crustal rheology on the evolution of passive margins from rifting to break-up". In: *Tectonophysics*. Understanding geological processes through modelling - A Memorial Volume honouring Evgenii Burov 746, pp. 155–172.

Tissot, B. P., R. Pelet, and Ph Ungerer (1987). "Thermal History of Sedimentary Basins, Maturation Indices, and Kinetics of Oil and Gas Generation". en. In: *AAPG Bulletin* 71.12, pp. 1445–1466.

Tregoning, Paul, Kurt Lambeck, Art Stolz, Peter Morgan, Simon C. McClusky, Peter van der Beek, Herbert McQueen, Russell J. Jackson, Rodney P. Little, Alex Laing, and Brian Murphy (1998). "Estimation of current plate motions in Papua New Guinea from Global Positioning System observations". In: *Journal of Geophysical Research: Solid Earth* 103 (B6), pp. 12181–12203.

Turcotte, Donald and Gerald Schubert (2014). *Geodynamics*. Cambridge University Press. 639 pp.

Ulvrova, Martina M., Sascha Brune, and Simon Williams (2019). "Breakup Without Borders: How Continents Speed Up and Slow Down During Rifting". en. In: *Geophysical Research Letters* 46.3, pp. 1338–1347.

Vigny, Christophe, Philippe Huchon, Jean-Claude Ruegg, Khaled Khanbari, and Laike M. Asfaw (2006). "Confirmation of Arabia plate slow motion by new GPS data in Yemen". In: *Journal of Geophysical Research: Solid Earth* 111 (B2).

Zhang, Yue Qiao, Jacques Louis Mercier, and Pierre Vergély (1998). "Extension in the graben systems around the Ordos (China), and its contribution to the extrusion tectonics of south China with respect to Gobi-Mongolia". In: *Tectonophysics* 285.1, pp. 41–75.

3 Kinematics of Fault-Propagation Folding: Analysis of Velocity Fields in Numerical Modeling Simulations

This study was published in:
Berenice Plotek[1], Esther L. Heckenbach[2,3], Sascha Brune[2,3], Ernesto Cristallini[1], Jeremías Likerman[1] (2022): Kinematics of fault-propagation folding: Analysis of velocity fields in numerical modeling simulations. *Journal of Structural Geology*, 162, 104703.
https://doi.org/10.1016/j.jsg.2022.104703

[1] Laboratorio de Modelado Geológico (LaMoGe), Instituto de Estudios Andinos "Don Pablo Groeber" (IDEAN), Universidad de Buenos Aires-CONICET.
[2] GFZ German Research Centre for Geosciences, Potsdam, Germany.
[3] Institute of Geosciences, University of Potsdam, Potsdam, Germany

Abstract

Fault-propagation folding occurs when a shallow fold is created by an underlying propagating thrust fault. These structures are common features of fold and thrust belts and hold key economic relevance as groundwater or hydrocarbon reservoirs. Reconstructing a fault-propagation fold is commonly done by means of the trishear model of the forelimb, a theoretical approach that assumes simplistic rheological rock properties. Here we present a series of numerical models that elucidate the kinematics of fault-propagation folding within an anisotropic sedimentary cover using complex visco-elasto-plastic rheologies. We explore the influence of different parameters like cohesion, angle of internal friction, and viscosity during folding and compare the velocity field with results from the purely kinematic trishear model. In the trishear paradigm, fault-propagation folding features a triangular shear zone ahead of the fault tip whose width is defined by the apical angle that in practice serves as a freely tunable fitting parameter. In agreement with this framework, a triangular zone of concentrated strain forms in all numerical models. We use our models to relate the apical angle to the rheological properties of the modeled sedimentary layers. In purely visco-plastic models, the geometry of the forelimb obtained can be approximated using a trishear kinematic model with high apical angles ranging between 60° and 70°. However, additionally accounting for elastic deformation produces a significant change in the geometry of the beds that require lower apical angles (25°) for trishear kinematics. We conclude that all analyzed numerical models can be represented by applying the theoretical trishear model, whereby folds involving salt layers require high apical angle values while more competent sedimentary rocks need lower values.

Keywords:

- Fault-propagation folds
- Trishear kinematics
- Numerical modeling
- Velocity fields
- Fault-related folding

3.1 Introduction

Some thrust faults propagate gradually to the surface and, as slip accumulates, these faults develop a fault-propagation fold above their tip (Figure 3.1). This type of structure forms as a consequence of

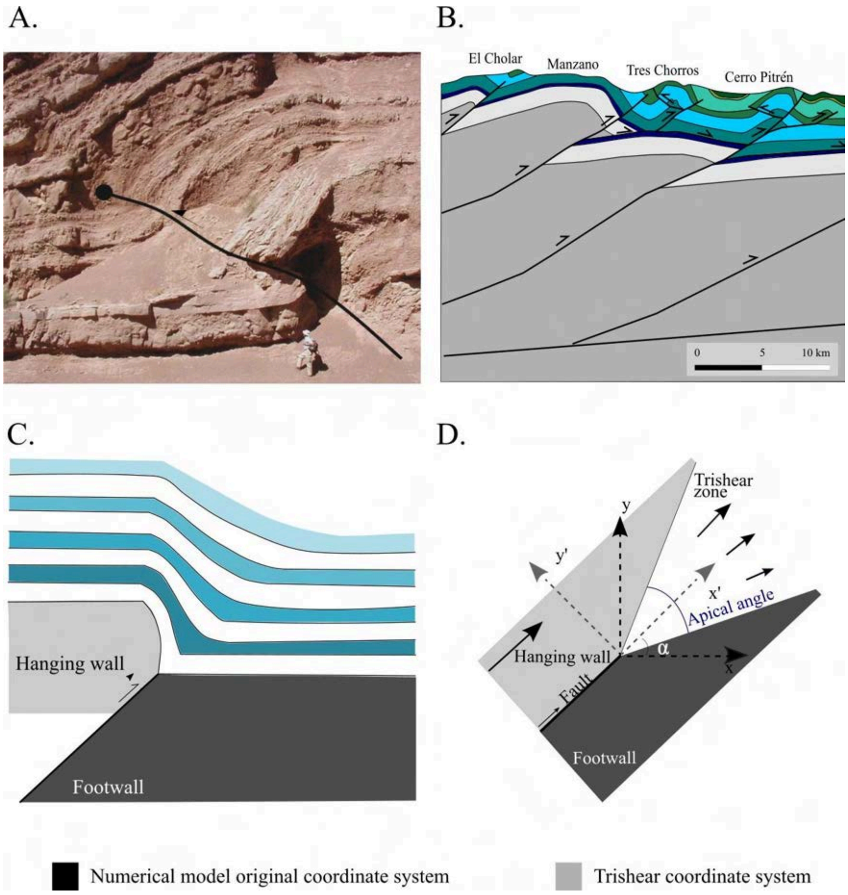

Figure 3.1: A. Fault-propagation fold located in Sierra de Las Peñas-Las Higueras (Mendoza Province, Argentina). Note the variations in slip along the fault and how the folding is attenuated in the upper layers (Ahumada et al., 2006). B. Cross-section of the northern Agrio fold and thrust belt, located in the Southern Central Andes of Argentina indicating major fault-related folds (Lebinson et al., 2020). C. Fault-propagation model by homogeneous, footwall-fixed trishear. The thickness of the beds is not preserved (modified from Erslev, 1991). D. General trishear geometry. The first analysis considered the footwall completely fixed (modified from Allmendinger, 1998). The figure illustrates the conversion from the original coordinate system of the numerical model (X and Y, in black) to the trishear coordinate system (X' and Y', in grey) with $V_x' = cos(\alpha)V_x - sin(\alpha)V_y$ and $V_y' = sin(\alpha)V_x + cos(\alpha)V_y$. Since α designates the fault dip, V_x' is parallel to the main fault while V_y' is perpendicular to it. The origin of the trishear coordinate system is located at the tip point of the main fault.

variations in the slip along the fault where a decrease in slip is compensated by folding of material above the fault (Suppe et al., 1990; Brandes et al., 2014). First kinematic models to address the evolution of fault-propagation folds (Chester et al., 1990; Mitra, 1990; Suppe et al., 1990) were based on the parallel kink-fold mechanism and allowed examination of the trajectory of the materials during folding (Dewey, 1965; Maillot et al., 2006). However, fault-propagation folds observed in nature (Figure 3.1A) usually display variations in stratigraphic thickness, footwall synclines, and changes in the forelimb inclinations that are inconsistent with simple parallel kink-fold kinematics (Figure 3.1) (Suppe et al., 1990; Allmendinger, 1998). Trishear, an alternative kinematic model, can explain these observations (Erslev, 1991; Allmendinger, 1998; Coleman et al., 2019) that cannot be explained by kink-fold kinematics. This theoretical model is characterized by a distribution of the deformation within a triangular zone located immediately above the tip-line of the fault (Hardy et al., 1997; Cristallini et al., 2001; Jabbour et al., 2012). Note that the trishear model is based on the assumption that deformation occurs only in the triangular shear zone, while in the hanging wall the particles experience rigid translation.

Fault-propagation folds have been studied with numerical modeling using finite-element methods (Braun et al., 1994; Khalifeh-Soltani et al., 2021), discrete-element techniques (Finch et al., 2002; Finch et al., 2004; Hughes et al., 2015) and boundary element modeling (Johnson, 2018). These mechanically-based models require an initial geometry in 2D or 3D of stratigraphic units and/or faults (Guiofski et al., 2009; Granado et al., 2019) as input, as well as rheological information about the materials involved

(Ruh, 2020; Huang et al., 2020; Granado et al., 2021). Cardozo et al., 2003 showed that if incompressible materials are used, the resulting fold geometries, velocity fields, and finite strain are very similar to those produced by the trishear kinematic model. Previous studies have shown that fault-propagation into the cover is strongly favored by homogeneous cover sequences (Hardy et al., 2007) and that the strength of bedding contacts, the thickness and stiffness of layering as well as the fault geometry, all contribute significantly to the resulting shape of the fold (Johnson, 2018).

Numerical models can help deciphering the kinematics involved in fold formation and migration, providing a dynamic understanding of these structures. Here, we aim to understand fault-propagation folds by means of finite-element modeling. This numerical approach is available in a variety of current research software packages and has been widely applied to model complex crustal deformation, both in compression (e.g. Ruh et al., 2012; Erdos et al., 2019; Ballato et al., 2019) and extension (e.g. Van Wijk et al., 2002; Jourdon et al., 2021; Richter et al., 2021). In particular, mechanical-based numerical modeling is a very powerful tool for investigating processes associated with the formation and evolution of geological features on small and large scales (Sanz et al., 2007; Albertz et al., 2012; Brune et al., 2013; Gray et al., 2014; Brune et al., 2016).

In this study we analyze numerical examples of simple fault-propagation folds, where folding affects three different lithologies. We show that the general configuration of the resulting folding can be approximated by the trishear kinematic method, even when plasticity parameters and viscosity of the beds vary significantly. We analyze the evolution of the kinematic field and strain rate during the process of folding and faulting and compare a series of modeled kinematic fields and their geometries to theoretical trishear shape and velocity fields obtained from the Andino 3D software (Cristallini et al., 2021; Plotek et al., 2021). We find that setups where weak, salt-like layers are included, and realistic dislocation creep parameters are used develop more heterogeneous velocity distributions. In the following section, we will first review the trishear kinematic model. Next, we will present the numerical models performed, and finally, we discuss our results and their implications.

3.2 The trishear kinematic model

The first kinematic models to balance fault-propagation folds were based on geometrical relationships (Suppe et al., 1990; Saffar, 1993). They imply ideal geometries where the main fault has a planar surface, and a kink band migration occurs during fold evolution (Woodward, 1997; Jabbour et al., 2012). The trishear kinematic model was first proposed by Erslev, 1991. In this theoretical model, fault-propagation folds have a triangular zone of heterogeneous deformation, surrounding the fault tip that can be modeled by non-parallel shear (Figures 3.1C & 3.1D). Originally, the only distortion and rotation in the system takes place in a triangular zone ahead of the fault tip. Brandenburg, 2013 presented a modification of the trishear model where faults are treated as continuously curved.

The trishear process can generate several characteristics of fault-propagation folds, such as the curved shapes of folds and the presence of footwall synclines, as well as variations in the thickness and progressive rotation of the forelimb (Allmendinger, 1998; Hardy et al., 1997; Cardozo et al., 2009; Hardy et al., 2011; Brandes et al., 2014). The trishear method can also approximate the complex strain patterns observed in natural examples (Allmendinger et al., 2005; Liu et al., 2012; Grothe et al., 2014), where strain is highly heterogeneous since it is dependent on the mechanical stratigraphy and the geometry of the main fault (Cristallini et al., 2001; Allmendinger et al., 2005; Cardozo, 2008).

The main variables of the trishear model are (1) the displacement of the hanging block, (2) the propagation/slip ratio, (P/S, being P the propagation of the fault and S the slip on the fault plane) and (3) the apical angle of the trishear zone (Figure 3.1D, Allmendinger, 1998). Trishear fold shape can vary considerably by changing any of these variables, being particularly sensitive to changes in the P/S ratio.

A general method for the derivation of velocity fields consistent with the basic kinematics of the trishear model of fault-propagation folding was presented by Zehnder et al., 2000. Velocity fields can be written as functions of the position within the deformation zone (Hardy et al., 1997; Zehnder et al., 2000). In the original model, the hanging wall moves at a velocity equal to the incremental slip while the footwall is fixed. Inside the triangular zone, particles move according to a velocity field that ensures preservation of area during deformation (Zehnder et al., 2000; Cardozo et al., 2003). The velocity field was found assuming a gradient for the velocity component parallel to the fault (V_x in trishear coordinate system; Zehnder et al., 2000) and calculating a velocity component perpendicular to the fault (V_y in trishear coordinate system; Zehnder et al., 2000), where it satisfies the zero-divergence criterion (area preservation condition) consistent with the velocity conditions at the limits of the triangular shear zone (Zehnder et al., 2000; Cardozo, 2008; Brandenburg, 2013). The equations introduced by Zehnder et al., 2000 enable the construction of velocity fields assuming incompressibility, continuity of the flow, and matching of the basic boundary conditions of the model. The deformation resulting from any of these fields can be obtained by numerical integration.

3.3 Numerical models

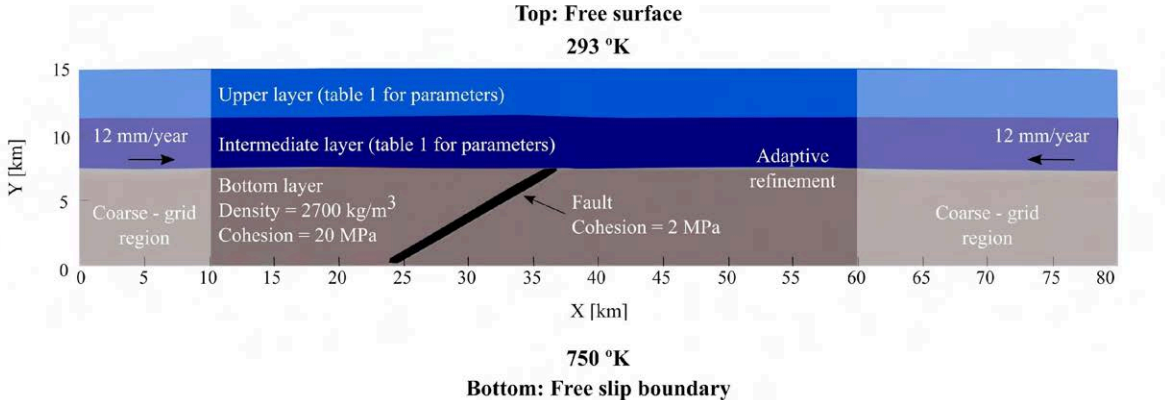

Figure 3.2: Numerical model setup. Parameters for upper and intermediate layers are summarized in Table 3.1. The highest mesh refinement corresponds to the location of the hanging wall of the fault and frontal limb of the folding, where the element size is 125 m (strong colors). The corners (light color areas) present an element size of 500 m. Compressional velocities are prescribed at the boundaries in the x-direction.

Numerical forward modeling has been used to simulate a wide range of processes from global mantle convection (Bello et al., 2014; Rubey et al., 2017; Colli et al., 2018) to fault-related processes (Nilfouroushan et al., 2012; Brune et al., 2013; Brune et al., 2014; Treffeisen et al., 2020; Luo et al., 2020; Sari, 2021). In this study, we apply the open-source code ASPECT (Advanced Solver for Problems in Earth's ConvecTion; Kronbichler et al., 2012; Heister et al., 2017; Rose et al., 2017; Glerum et al., 2018; Sandiford et al., 2021 that solves the conservation equations of momentum, mass and energy for an infinite Prandtl number (i.e., without inertia) using the Boussinesq approximation (i.e., incompressible flow). This finite element code has been originally designed for modeling mantle convection and plume dynamics (Dannberg et al., 2018; Zhang et al., 2018; Rajaonarison et al., 2020; Steinberger et al., 2019), but it has been significantly extended and was successfully applied to lithosphere deformation (Glerum et al., 2020; Heckenbach et al., 2021; Holt et al., 2021; Gouiza et al., 2021). The code is characterized by modern numerical methods, high-performance parallelism and extensibility (Glerum et al., 2018). We performed a series of finite element models simulating shortening in a multi-layer viscoplastic sequence to obtain the velocity field during the evolution of simple fault-propagation folds. We evaluate and compare the velocity field and the resulting geometries with those of the previously introduced kinematic trishear model.

The setup of our model is based on previously identified natural examples of fault-propagation folds at the Agrio fold and thrust belt, Andes of Neuquén, Argentina (Rojas Vera et al., 2015; Lebinson et al., 2018). The model domain has a width of 80 km and a height of 15 km (Figure 3.2). We include three material layers within a two-dimensional domain in the numerical model setup (Figure 3.2). All layers are initially horizontal. In all the simulations, the lowest layer is 7,5 km thick and has a density of 2700 kg/m3, an internal friction angle equal to 20°, and 20 MPa of cohesion (Table 3.1). To prescribe a master reverse fault, we incorporate a thin region of 1.5 km width and 50 km dipping by an angle of 30° in the bottom layer. Within this fault region, the internal angle of friction and the cohesion are reduced to 10° and 2 MPa, respectively. Two 3.75 km thick layers are defined, above the bottom layer (Figure 3.2). Plasticity parameters for these layers are varied for the different model runs (Table 3.1). Both beds represent a potentially weaker cover sequence for the fold. In this way, our simulations are comparable with the classical trishear example for fault-propagation folds proposed by (Erslev, 1991).

Introducing this configuration allows for testing how key material parameters (Table 3.1) affect the resulting kinematic field. The variations in the velocity and strain are studied in the context of a strongly mechanically differentiated sequence including a basement and a cover composed of two different layers.

We employ mesh refinement within predefined rectangular domains, such that the material located at the hanging wall of the fault and frontal limb of the structure is resolved with an element size of 125 m, while the corners are only represented by an element size corresponding to 500 m. Overall, our model contains 19,200 active cells, and 950,131 degrees of freedom. All models were run for 20 time-steps of 20,000 years each for a total of 400,000 years of deformation. This required a computation time of 10 hours on 10 cores.

For simplicity, the reference model M1 and most of our alternative models employ uniform viscosity deformation within the upper and intermediate layers, an approach used in many previous numerical models (Schuh-Senlis et al., 2020; Holt et al., 2021). The viscous flow law used in the bottom layer of our models is based on deformation experiments of wet anorthite (Rybacki et al., 2006). Model M2 assumes that the upper layer consists of evaporites and uses flow law parameters based on experimental salt deformation data (Bräuer et al., 2011; Baumann et al., 2018). We test for the impact of elastic deformation via Model M5, which additionally accounts for a modulus of rigidity of 10 MPa. Brittle deformation takes place where the viscous or visco-elastic stresses exceed the Drucker-Prager yield criterion, whereas the friction angle and cohesion of each model are listed in Table 3.1. We applied linear frictional weakening such that the plastic strain is used to weaken the plastic yield stress by up to 90% through cohesion and friction for strains larger than 1.5. Furthermore, viscous strain is used to weaken the pre-yield viscosity up to 90% when a strain magnitude of 1.5 is exceeded. Linear strain weakening is a simple, but very effective way to generate realistic fault networks in numerical forward models and has been successfully applied in various tectonics settings (Huismans et al., 2002; Selzer et al., 2007).

Contractional deformation is imposed through velocity boundary conditions, with the left and right sides of the model having a prescribed velocity of 12 mm/year resulting in a total convergence rate of 24 mm/year. Note that for better comparability to the trishear kinematic model, we present velocities in all figures in a reference frame where the right-hand model boundary is fixed. The model features a free surface at the top and free-slip boundary conditions at the base. The temperature is established following a linear gradient from 293 K at the surface to 750 K at the bottom of the model and the boundary temperatures are held constant throughout the model run. For simplicity, radiogenic heating within the layers is not considered.

We conduct a suite of 5 models including our reference Model M1 where both the intermediate and upper layers have uniform viscosity (Table 3.1) and the density equals 2700 kg/m3 for all layers. Alternative models M2 to M5 are designed to explore more complex setups by modifying particular aspects of the reference model. Model M2 is identical to M1, except that the upper layer represents an evaporite bed. This is realized by following the viscous flow originally proposed by Bräuer et al., 2011 and changing the plasticity parameters and density value as shown in Table 3.1. Evaporitic sequences are common in several fault propagation folds identified, such as Filo Morado in Neuquén Basin (Argentina), which was previously modeled as a trishear fold (Allmendinger et al., 2005). Like reference model M1, models M3 and M4 both include two layers with uniform viscosity. Here, the density for the intermediate and upper layers is equal to 2190 kg/m3. Besides the modification of this property, we also varied plasticity parameters to equal shale and salt rocks. In model M3, the angle of internal friction and cohesion of the upper and intermediate layers are comparable with values measured in shales (Heng et al., 2015) for comparison with the fault propagation folds identified in the Subandean thrust and fold belt of northwestern Argentina, where Silurian and Devonian shales are predominant (Echavarria et al., 2003). In model M4, the plasticity parameters are comparable with values obtained from salt rocks (Liang et al., 2006; Giambastiani, 2019). Finally, in simulation M5 elastic deformation is incorporated.

Model	M1		M2		M3		M4		M5		ALL MODELS	
Material	Up.*	Int.*	Up.	Int.*	Up.*	Int.*	Up.*	Int.*	Up.*	Int.*	Bot.	Fault
Density $[kg/m^3]$	2700		2190	2700	2190				2700		2700	
Cohesion [MPa]	20	25	10	25	30		10		20	25	20	2
Angle of internal friction [°]	20	20	30	20	10		30		20	20	20	10
Prefactor for dislocation creep $[Pa^{-n}s^{-1}]$	$0.5 \cdot 10^{-22}$	$0.5 \cdot 10^{-20}$	$5.21 \cdot 10^{-37}$	$0.5 \cdot 10^{-20}$	$0.5 \cdot 10^{-22}$	$0.5 \cdot 10^{-20}$	$0.5 \cdot 10^{-22}$	$0.5 \cdot 10^{-20}$	$0.5 \cdot 10^{-22}$	$0.5 \cdot 10^{-20}$	$7.13 \cdot 10^{-18}$	
Constant viscosity	X	X		X	X	X	X	X	X	X		
temperature-dependent viscosity			X								X	
Viscosity $[Pa\ s]$ in isoviscous layers	10^{22}	10^{20}	-	10^{20}	10^{22}	10^{20}	10^{22}	10^{20}	10^{22}	10^{20}	-	
Stress exponent for dislocation creep, n	1		5	1							3	
Activation energy for dislocation creep $[J/mol]$	0		$54 \cdot 10^3$	0							$345 \cdot 10^3$	
Activation volume for dislocation creep $[m^3/mol]$	0										$38 \cdot 10^{-6}$	
Modulus of rigidity $[MPa]$	-								10 (only in M5)			

Table 3.1: Rheological parameters for the intermediate and upper layers. In all models, the bottom layer and the prescribed fault feature a mafic flow law derived from deformation experiments of wet anorthite (Rybacki et al., 2006) while the fault is initialized through low brittle strength. M1 is the reference model. All models except model M2 involve uniform viscosity layers (marked with *). The upper layer in model M2 follows the viscous flow law obtained from experimental data for salt (Bräuer et al., 2011; Baumann et al., 2018). Model M5 includes elastic deformation accounting for a modulus of rigidity of 10 MPa. Up. - Upper layer, Int. - Intermediate layer, Bot. - Bottom layer

3.4 Results

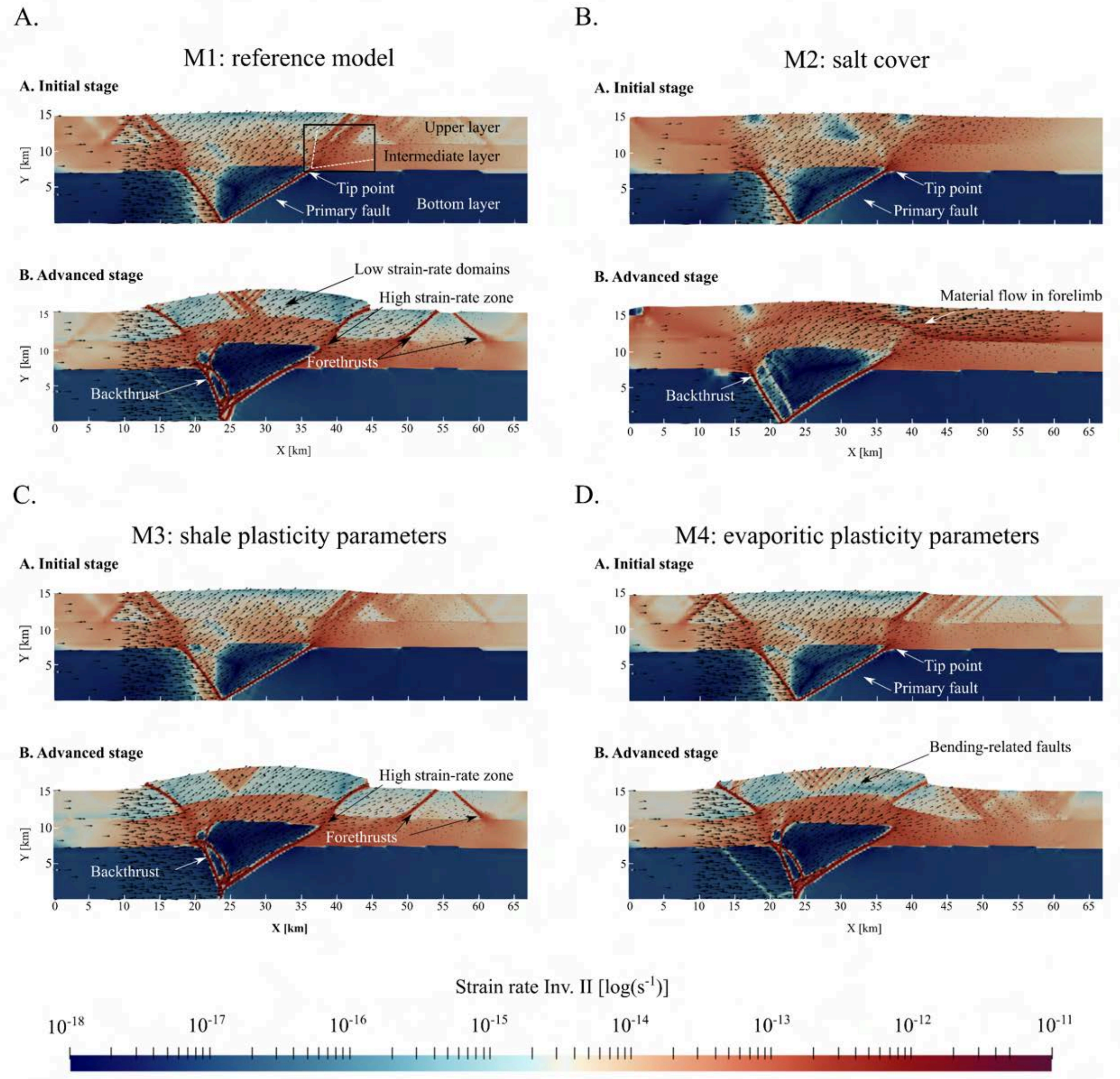

Figure 3.3: Evolution of the models M1, M2, M3, and M4 showing the second invariant of the strain rate in a color gradient scale and instantaneous velocity vectors relative to the footwall. Two time-steps are selected for each model: the initial stage (80,000 years) and the advanced stage (360,000 years). In close contact with the tip-line, in the middle layer, it is shown how vectors rotate from higher values to almost zero in the footwall. This area (black lines in the initial stage panel for model M1) is similar to the triangular zone defined by the trishear model, where internal deformation is concentrated.

We first analyze the development of fault propagation folding and further compare the velocity field and the resulting geometries of our simulations with the theoretical trishear kinematic model (Figure 3.3). Instantaneous deformation is depicted in terms of the second invariant of the strain rate tensor which is a common way to represent the strain rate magnitude as a scalar value. This value is also used to compute finite strain at each material point, by adding the product of strain rate and time step to the previously experienced finite strain. The strain rate is also used to generate the velocity output from Aspect which hence shows the instantaneous velocity field.

The reference model M1 simulates folding in a cover sequence over a lower layer of uniform strength, where the main reverse fault was established. Deformation localizes in the fault itself, the backthrust, and the limbs of the fold. The backthrust appears in the initial stages of convergence (Figure 3.3, model M1) and higher strain rate values are observed adjacently, affecting part of the backlimb. Higher

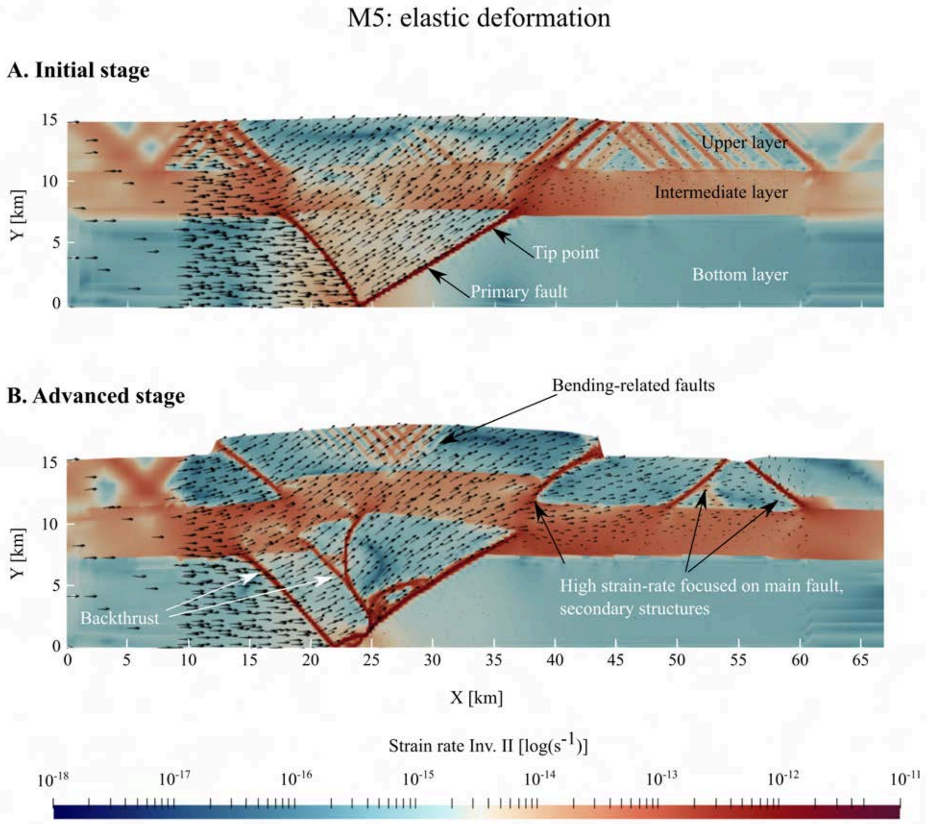

Figure 3.4: Evolution of model M5 where elastic deformation was incorporated. The figure shows the second invariant of the strain rate in a color gradient scale and instantaneous velocity vectors relative to the footwall. Two time-steps are selected for the model: the initial stage (80,000 years) and the advanced stage (360,000 years).

strain rate values of the frontal limb are focused especially in the area close to the tip point, where the displacement of the fault is accommodated by the folding. Concerning kinematics, the velocity vectors mainly consist of a horizontal component (V_x) close to the left corner (Figure 3.3). In the hanging wall there is a progressive rotation of the velocity field, where the vertical component (V_y) increases its value. However, as the simulation progresses, the overall velocity field of the hanging wall becomes parallel to the reverse fault. Inside the front limb, the velocity field exhibits another progressive rotation, where both components decrease until reaching minimum values in the footwall of the structure. This area can be considered equivalent to the triangular zone defined by the trishear model, where internal deformation is concentrated (Figure 3.3, model M1, initial panel). The resultant structure is asymmetric, characterized by the progressive tightening of the fold hinge and steepening of the frontal limb (Figure 3.3, model M1, advanced panel). In the advanced stages of the model (Figure 3.3, model M1, advanced panel), deformation is dominated by minor reverse faults similar to forethrusts, which break the upper layer.

Alternative models M2 to M5 exhibit an overall similar structural evolution albeit with several distinct differences (Figures 3.3 & 3.4). Model M2 investigates the effect of a weak, evaporitic cover layer situated on top of the sequence. Due to the relatively low strength of this layer, more diffuse deformation is observed where higher strain rate values are distributed laterally and are not limited to the main faults. This also leads to a much more symmetric distribution of deformation compared with the other examples (Figure 3.3, model M2). In further contrast with the previously described model M1, the progressive rotation in the front limb of M2 cannot be well identified. Besides, the velocity magnitude does not decrease in the upper layer, showing the predominance of the vertical component V_y even far from the frontal limb (Figure 3.3, model M2, advanced panel).

In models M3 and M4 (Figure 3.3), both the intermediate and upper layers have uniform viscosity, but plasticity parameters of model M3 imitate shale rocks (Wyllie et al., 1996; Heng et al., 2015) while in model M4 the parameters are equivalent to salt rocks (Gschwandtner et al., 2018; Giambastiani, 2019).

	Strain rate $[s^{-1}]$		Plastic strain	
Model	Maximum	Minimum	Maximum	Minimum
M1	$6.0{\cdot}10^{-12}$	$2.1{\cdot}10^{-19}$	2.33	-0.033
M2	$5.7{\cdot}10^{-12}$	$6.5{\cdot}10^{-19}$	2.29	-0.0096
M3	$6.1{\cdot}10^{-12}$	$1.6{\cdot}10^{-19}$	2.32	-0.0134
M4	$6.2{\cdot}10^{-12}$	$3.4{\cdot}10^{-19}$	2.28	-0.0129
M5	$5.4{\cdot}10^{-12}$	$3.7{\cdot}10^{-17}$	1.96	-0.0094

Table 3.2: Maximum and minimum values of strain rate $[s^{-1}]$ and plastic strain for all models, for the initial stage (80,000) inside the forelimb (Same area as in Figure 3.5).

Even with these differences, both resulting structures exhibit similar geometry, strain rate distribution, and kinematic velocity fields. The main differences can be found in the advanced stage where model M3 presents minor reverse faults similar to forethrusts, which affect the upper layer like in the reference model M1 (Figure 3.3). These features, however, do not appear in model M4.

In model M5 we include elastic deformation to evaluate how it affects the resulting fold (Figure 3.4). The overall deformation pattern does not change if compared to reference model M1. The main difference is that because of the incorporation of elastic deformation, previously rigid blocks are now able to accommodate elastic strain, which is seen by a relative increase in minimum strain rates (Figure 3.4). The resultant structure is asymmetric, with a higher prevalence of backthrusts. These backthrusts are branched and at advanced stages (Figure 3.4, advanced panel) all of them are merging at depth with the main fault. As in the case of the reference model M1 (Figure 3.3), this simulation also develops minor reverse faults similar to forethrusts, which break the upper layer (Figure 3.4). Velocity vectors show a similar pattern to the reference model M1. Vectors tend to become parallel to the main fault within the hanging wall. Then, the vector field exhibits a progressive rotation where both the horizontal and the vertical components decrease inside the front limb. This area is located in close contact with the tip point at the end of the fault. Generally, the distribution of the strain rate in model M5 is similar to reference model M1, with higher values concentrated in the faults and the intermediate layer.

3.4.1 Comparing fold shape & kinematic field with the trishear theoretical model

For the comparison of a simple propagation fold structure to the theoretical trishear kinematic model we selected the initial stage of the numerical models (Figures refp2-fig2:3 & 3.4, initial panels). In subsequent stages, the main fault increases displacement and is interacting with the front limb, altering the kinematic field inside the triangular zone. Due to this, the first stage is more appropriate to analyze trishear fitting (Figure 3.5).

First, we tested different trishear apical angles (Figure 3.5), using the development version of Andino 3D software (Cristallini et al., 2021). In all cases, we worked only with symmetric apical angles that were tested every 10–5 degrees. Then, we used the least squares method to verify the theoretical curves obtained in Andino 3D software, comparing them with the geometry of the beds in the numerical models. In this way, we can produce a better fitting of the layers using apical angle values between 60° and 70° for the forelimb (Figure 3.5). If we compare the resulting curves with the layers in the simulations, we can see that, in general, high apical angles approximate better the geometry of the forelimb. The only case in which the apical angle is lower is found in model M5, where it is equal to 25°. We then extracted the kinematic field from the numerical models and compared it with the theoretical trishear kinematic field (Figure 3.6) which was generated using the Andino 3D software with the best fitting apical angle as marked in Figure 3.5.

Figure 3.6 shows the comparison between the velocity fields of the numerical and the trishear model as arrows (using the theoretical model in Andino 3D, applying the best value for the apical angle obtained after the geometric adjustment) as well as the absolute difference of the velocity magnitudes as an underlain color scale. The angular misfit of the models therefore highlights those sectors that present the greatest differences. However, we want to stress that generally there is very good agreement between both kinematic fields for most model setups.

The greatest differences are concentrated in the backlimb sector, due to the presence of backthrusting.

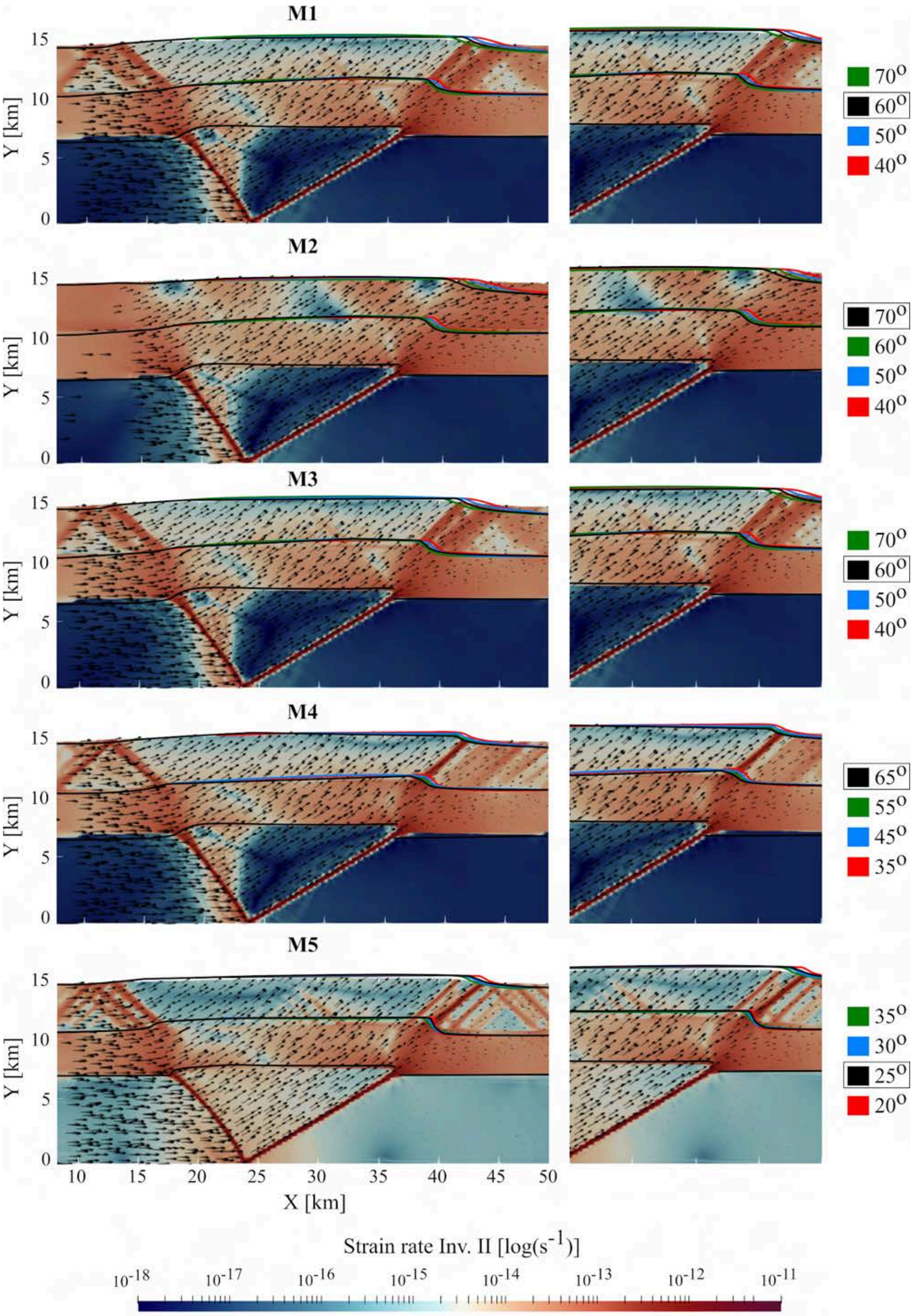

Figure 3.5: Comparison between initial stage numerical results (80,000 years) and trishear kinematic mode calculated with the Andino 3D software. For each model, results for selected apical angles are shown in the right column, where the black color indicates the value that approximates the shape of the layers best for each of the folds.

Contrary, in the zone corresponding to the hanging wall, no great differences are observed with both fields being parallel to the main fault. In the trishear zone, it can be seen that model M2 with a flow law corresponding to saline rocks is the one with the best fit, while the M5 model with incorporated elastic deformation has greater differences in this sector. The M4 model, with plasticity parameters corresponding to evaporite rocks, differs from the other models, and is presenting deviations from the trishear model as well. In this case, the forelimb also exhibits negative values corresponding to an anticlockwise rotation, but the difference is bigger compared to the reference model M1 and model M3.

The parameter P/S produces stronger changes than the apical angle in the geometry of the beds

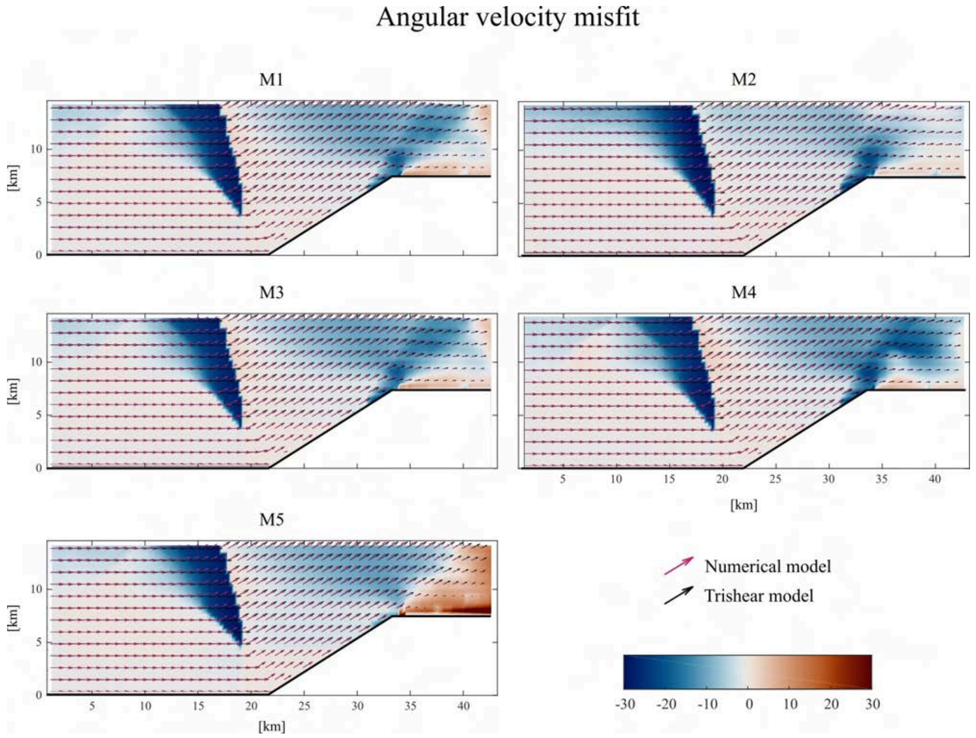

Figure 3.6: The panels depict the trishear model kinematic field results in black arrows and the numerical model velocity field in red. Same stage as in Figure 3.5. The dark grey line represents the main fault. The color gradient represents the resulting difference (in degrees) after subtracting the total component of the velocity vector of the numerical model from the theoretical trishear model. Negative values indicate anticlockwise rotation, while positive values indicate clockwise rotation. The models agree very well in the trishear zone, while greater differences are observed in the backlimb.

(Hardy et al., 2011; Allmendinger, 1998). The geometries of our five model setups are quite similar, suggesting in principle that the P/S ratio is the same for all of them. Due to this, this study focused on the apical angle value while P/S was always set equal to 2. However, we do not discard that non-constant P/S ratios or using asymmetric trishear apical angle values could be combined to give similar satisfactory results. To facilitate comparison between our model groups, we include Table 3.2 where the maximum and minimum values for the strain rate and the plastic strain for each model are shown (Table 3.2). We used the same stage as in Figures 3.5 & 3.6 (80,000 years), considering only the forelimb sector. Model M5 presents the highest differences but is still comparable to the other simulations.

3.4.2 Comparing velocity distribution inside the deformation zone

To conduct a detailed comparison to the kinematic model, we plot the velocity distributions of the different simulations within the trishear coordinate system (Figure 3.1D). The velocity values for the horizontal and vertical components of the vectors were transformed using the equations presented in Figure 3.1D. The area where both components are plotted is located from the fault tip up to the upper layer, similar to the zoom images in Figure 3.5. For models M1, M2, M4 and M5 we present two plots, one for V_x' (parallel to the main fault, in Figure 3.7) and V_y' (perpendicular to the main fault, in Figure 3.8). For each plot, we present 3 profiles that cross-cut the deformation zone illustrating the magnitude of V_x' or V_y', respectively. Model M3 was not included because the geometric comparison and the velocity fields are very similar to the reference model M1 (Figures 3.5 & 3.6).

The fault-parallel velocity component V_x' is comparable for all our simulations (Figure 3.7). In all of the models, this component gradually decreases in magnitude until reaching the footwall of the structure, where the velocity vanishes. Higher values are found closer to the tip of the fault in the hanging wall. The profiles closer to the tip of the fault (Figure 3.7, Profiles A) show an abrupt reduction of V_x' magnitude. As the high-strain zone grows, this reduction becomes more gradual (Figure 3.7, Profiles B & C). Model M4 presents a different pattern, where the high-strain zone is distorted.

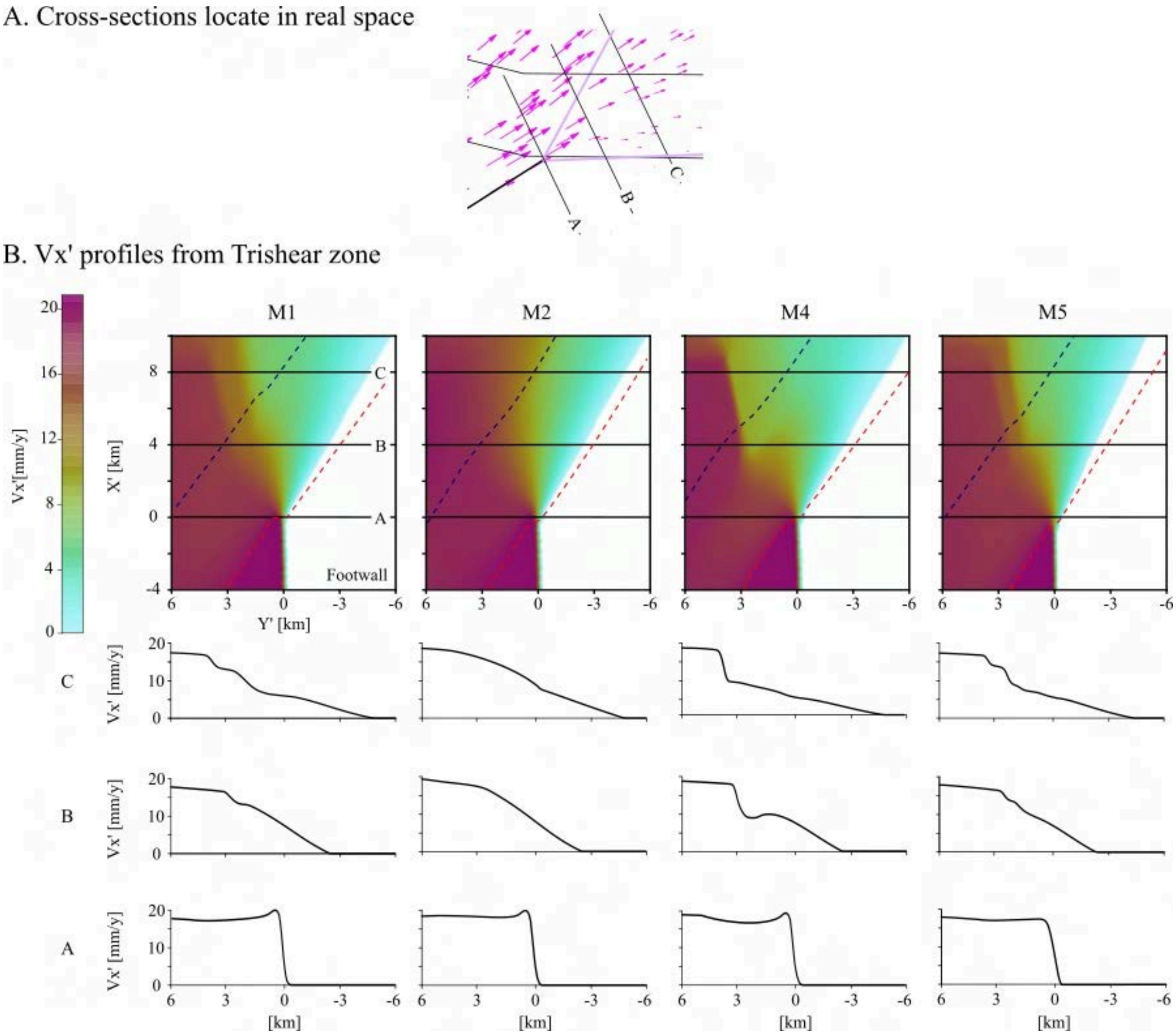

Figure 3.7: A. Scheme indicating the location of the cross-sections. The apical angle and main fault are included as a straight line. The location of the profiles is shown in black lines. The kinematic field corresponds to the numerical model M1. B. Numerical model results in trishear coordinate system showing V_x' (the component of the velocity vector parallel to the main fault). Same initial stage as in Figures 3.5 & 3.6. The trishear- like zone, from the tip line to the bottom of the upper layer was plotted after changing the coordinate system as explained in Figure 3.1D. Profiles from A to C show V_x' for each model in a direction perpendicular to the main fault. The profile locations are outlined with black lines in the plots of the top row. The boundaries between the bottom, intermediate and upper layers are shown in red and blue dashed lines, respectively.

The fault-perpendicular velocity component V_y' shows more variations than V_x' across models (Fig. 3.8). In the reference model M1, higher absolute velocity magnitudes are found inside the zone closer to the tip of the fault and in the hanging wall, located on the left side of the plot. Analyzing the profiles, we observed that the magnitude for V_y' in profile D is originally high and positive. When plotting the particles inside the trishear zone, the magnitude decreases until reaching negative values. By the middle of the profile, representing the center of the trishear-like area, a maximum absolute value is reached (Figure 3.8, model M1). In profiles E and F, V_y' values are negative from the beginning. The maximum absolute value is reached closer to the center. The distribution is not symmetric across the fault.

For model M2, the difference to the reference model is significant (Figure 3.8). The zone is more symmetric. In this model, V_y' is positive at the beginning of profiles E and F, contrary to the same profiles for reference model M1. Model M4 also shows a minor distortion in the plot (Figure 3.8, model M4), but the profiles have a similar shape as the ones for model M2 (Figure 3.8, model M2). The fault-perpendicular velocity component V_y' for model M5 follows the same spatial evolution as in model M1 but has overall lower V_y' magnitudes (Figure 3.8, model M5).

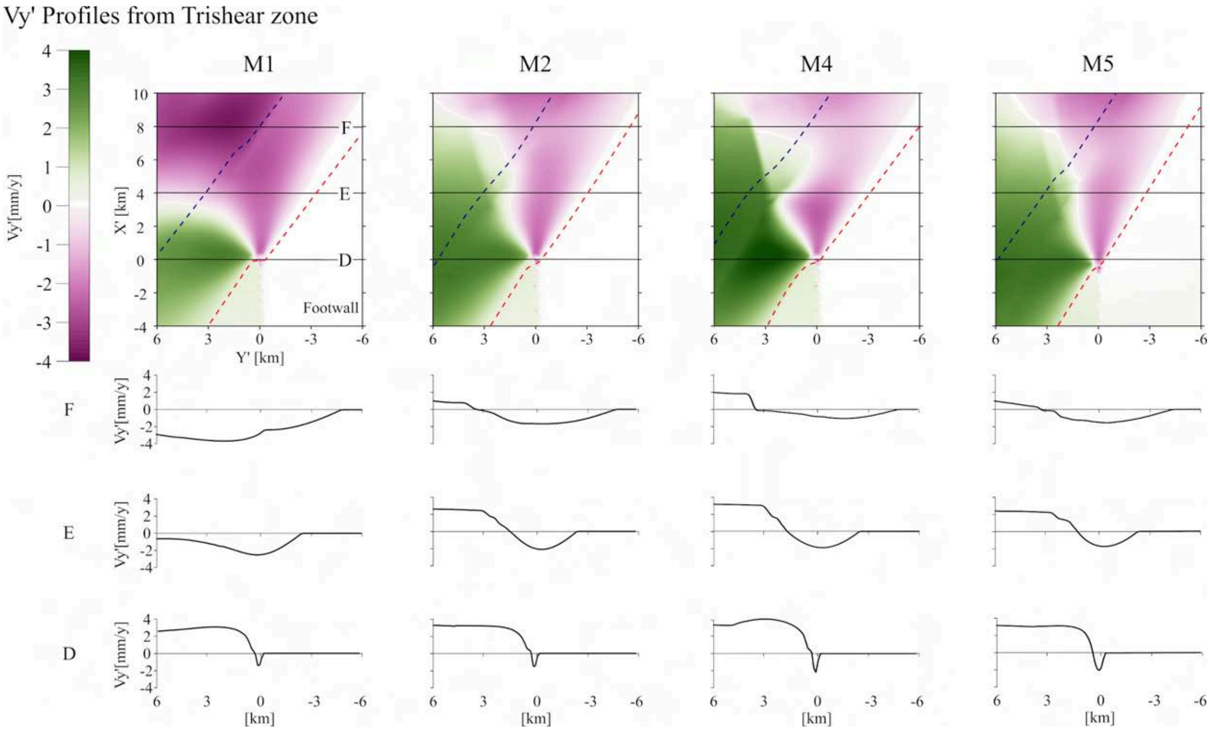

Figure 3.8: Numerical model results in trishear coordinate system depicting V'_y (the component of the velocity vector perpendicular to the main fault). Same initial stage as in Figures 3.5 & 3.6. Profiles from D to F show V'_y for each model in a direction perpendicular to the main fault. V'_y magnitude is considerably smaller than for V'_x. Inside the trishear zone, V'_y is always negative. The biggest distortion to the reference model M1 is found in M4. Boundaries between material layers are shown as dashed lines (see Figure 3.7).

3.5 Discussion

To compare with the trishear theoretical model we compare our numerical geodynamic models to the results of a fault-propagation fold calculated in Andino 3D software. For this, we applied the trishear model with an apical angle equal to 60° (Figure 3.9), which generated the best fit to approximate the beds in models M1 and M3. The rotation of the coordinate system is the same as in the case of the simulations (Figures 3.7 & 3.8). In Figure 3.9, we also plot both V'_x and V'_y using the trishear coordinate system as explained in Figure 3.1D. In general, we find that all simulations exhibit a kinematic field consistent with the trishear kinematic model (Figure 3.9). However, depending on the rheological parameters, the models show variations from the theoretical field. The triangular zone identified in the frontal limb for each of the folds develops shortly after the simulations began, suggesting that progressive rotation of the velocity vectors dominates the kinematic from the initial stages of the folding. The distribution of the strain is heterogeneous with the maximum values located in the central part of the triangular zone closer to the tip line. This is consistent with the description of trishear zones in previous studies, including experiments performed with analogue models (Mitra et al., 2013).

Model M1, used as the reference model, consists of two uniform viscosity layers acting like a sedimentary cover over a lower unit with higher strength representing basement rocks. This configuration produces an anticline similar to that proposed by Erslev, 1991 in his original trishear model. The distribution of the velocity magnitudes V'_x and V'_y (Figures 3.7 & 3.8, model M1), especially for V'_x, is equivalent to the theoretical distribution generated in the trishear method (Figure 3.9). The greatest difference is located in the left sector, where the distribution is affected by the main inverse fault (Figure 3.7, model M1). The variations introduced in the rest of the models allow discriminating the effect of each of the parameters involved.

Model M2 includes an upper layer with a variation in viscous dislocation creep parameters and plasticity parameters equivalent to evaporite rocks. This layer acts as a salt bed and even though a fault-propagation fold develops, the final shape of the fold is more symmetric (Figure 3.3). This unit flows from the hinge to the syncline in the frontlimb. Velocity vectors in the frontal limb should have

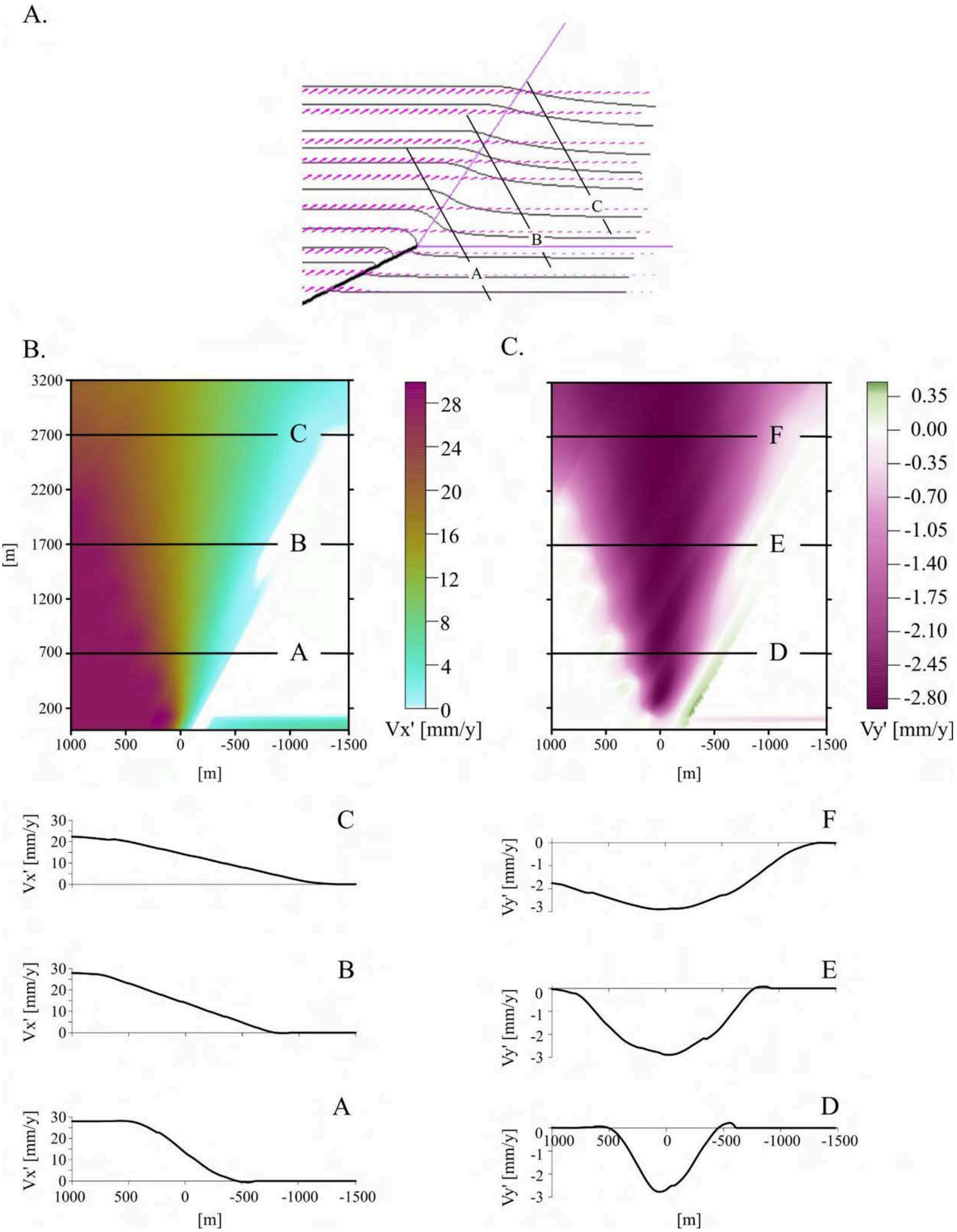

Figure 3.9: Analysis of a model performed using the Andino 3D software with an apical angle equal to 60°. A. Trishear velocity vector field. The apical angle and main fault are included as a straight line. The location of the profiles is shown in black lines. B. V_x' profiles from trishear zone showing the velocity magnitude in a color gradient scale. Profiles from A to C show V_x' and the tendency is considered similar to the one presented in the plots for the numerical simulations, especially for model M2. C. V_y' profiles from the trishear zone showing the velocity magnitude in a color gradient scale. V_y' is the component of the velocity vector perpendicular to the main fault.

a lower magnitude and be rather parallel to the main fault, as in the rest of the models (Figure 3.3). However, the kinematic field (Figure 3.3, model M2) shows an increase in the magnitude of the velocity vectors at the frontlimb, because of the flow of the particles previously described. Besides, the vectors are not parallel to the fault. Both of these observations could explain why in the trishear plot, the perpendicular component to the fault, V_y', is asymmetric and higher absolute magnitudes are located in the upper sector at the hanging wall. The flow described above produces the distortion and explains the pattern observed. Also, the observations presented above explain the difference observed in Figure 3.6 when subtracting both kinematic fields (theoretical Andino 3D trishear model and numerical model M2, Figure 3.6). Moreover, as the nature of the material is more prone to viscous flow rather than to brittle failure, the fault is not propagating through it. Because of this, the thrust is not generating the distortion seen in the other V_x' plots. In contrast to all other numerical models, the resulting figure for this model M2 is the only one that is truly symmetric (Figure 3.7, model M2). This model could also be explained by a low P/S ratio, close to 0. This could explain why the vectors located in the footwall exhibit higher magnitudes than the rest of the models. In models M1, M3 and M4 the P/S is greater, closer to 2 since the fault propagates more than twice its slip.

Model M3 has two uniform viscosity layers like reference model M1, the only difference between them being the plasticity parameters that are equivalent to shale rocks. The shape of the folding of both layers can be modeled by applying the same apical angle (60°). Plasticity parameters variations for this case did not produce a significant modification in the geometry of the folding, or of the kinematic field (Figures 3.5 & 3.6). Model M4, is also equivalent to model M3 except for the plasticity parameters that belong to salt rock. The folding could be approximated by applying a similar apical angle (65°). However, in this case, we identified differences with the reference model when plotting the perpendicular and parallel components for the velocity vector (V_y' & V_x' respectively). In both components the distortion observed is bigger, related to the interaction of the frontal thrust, which propagates more rapidly affecting the kinematic field in the frontal zone, even at early stages because of the nature of the material. The same distortion can be observed when subtracting the velocity vector in the numerical model velocity to the velocity vector for the theoretical trishear -applying the apical angle that produced the best geometrical fit (65°)- (Figure 3.6). Considering the observed deviation from the theoretical field, the trishear method could be applied with greater success for the reconstruction of structures in the early stages of deformation because the propagation of the main fault and the growth of the secondary structures modify the kinematic field, generating deviations with the proposed theoretical model. This leads us to the conclusion that the plasticity parameters of the rocks involved in the folding must be considered for a better understanding. These parameters influence the way the thrusts develop. In rocks where the mechanical behavior favors the rapid propagation of the main fault, the reconstruction of the structure and its kinematic field could differ from the trishear method.

Model M5 is the same as the reference model but with elastic deformation included. Even though brittle deformation mechanisms are dominant at low pressures and temperatures, and plastic deformation is usually assumed for models of fault-propagation folds (Jacquey et al., 2020), we included elastic deformation in model M5. The inclusion of elastic deformation modifies the shape of the folding compared to the other models: A low value for the apical angle in the trishear model is needed to approximate the shape of the fold in the visco-elastic-plastic model, while the angle needs to be high for the visco-plastic models. The subtraction of the numerical model kinematic field to the theoretical trishear kinematic field results in stronger differences in the frontal zone (Figure 3.6, model M5). Other main differences are the higher strain rate values in the bottom layer and more backthrusts.

For simplicity, we employed a constant P/S ratio of 2 for the entire model evolution which resulted in a best fit for all models. However, non-constant P/S ratios could be tested to produce similar results. Regarding this, it must be taken into consideration that P/S is a very sensitive parameter in the geometry of the beds, compared to the apical angle (Allmendinger, 1998). Therefore, we focused on the apical angle because the geometry of our models is quite similar. After performing the analysis of the apical angle values, the variations were small: most models exhibit values from 60° to 70°. Hence, we suggest that P/S does not vary significantly between most of our simulations. In model M5, the fault produces a more marked step in the upper layer, suggesting P/S may not have been constant during the development of the folding. The incorporation of elastic deformation to the model furthermore produced a significant change in the geometry of the beds. Previous studies have shown that the apical angle in triangular zones of deformation decreases with increasing heterogeneity of the cover (Hardy et al., 2007). The relation between cover heterogeneity and the elastic response incorporated into the simulation needs to be demonstrated. Further examples are required to determine how P/S influences the geometry of the structure, as we only performed a limited number of models with different rigidity modulus and in all cases, the geometry of the beds could be approximated by applying low apical angle values.

Preceding models have demonstrated that distortional strain is focused along the fault and backlimb axial surface and distributed throughout a triangular zone ahead of the fault in the structural forelimb (Hughes et al., 2015). Our results are similar to those obtained by previous authors: Johnson, 2018 pointed out that fault propagation is likely to have an important influence on resultant buckle fold geometry. In the study performed with boundary element modeling (Johnson, 2018), the models showed how folds widen as the fault propagates. The same evolution pattern can be observed in our finite element simulations. Regarding the strain distribution, our simulations in general present a pattern very similar to that obtained in the discrete models of mechanically homogeneous sequences (Hughes et al., 2015). This general distribution of internal deformation is maintained in all our models, even when the units differ in their mechanical behavior.

3.6 Conclusions

We constructed finite elements models of fault-propagation folding consisting of 3 layers and a prescribed reverse fault. We conducted several numerical simulations to examine the influence of various factors on the kinematic field and geometry of the fold. The obtained kinematic fields were compared with the trishear theoretical model.

All models, even with significantly different rheology parameters, exhibited similar velocity distributions that can be approximated using trishear. Each model developed a triangular zone where deformation was concentrated and the velocity vectors showed a progressive rotation. However, when plotting the velocity components according to the trishear coordinate system, some models exhibited distortions in the velocity field, which can be attributed to rheological changes such as the incorporation of a saline layer at the top of the sequence that flows in the zone of the forelimb (model M2); the use of plasticity parameters associated with evaporite rocks (model M4) and the generation of secondary structures when taking into account elastic deformation (model M5).

We propose that the greatest variations in the kinematic field with respect to the theoretical model can be found in structures with layers that present parameters equivalent to mechanically weak evaporite rocks. These variations can be identified in the kinematic field and the geometry of the folding and its evolution. In most of our simulations, deformation was dominated by minor reverse faults similar to forethrusts in the advanced stages, breaking the upper layer. However, models M2 and M4 where layers resembling evaporites were included do not develop this type of pattern. All geometries of the layers were approximated by applying the trishear model with high apical angle values of 60°–70°. The incorporation of elastic deformation in the numerical models produced a significant change in the geometry of the beds, where the layers were approximated by applying an apical angle value of 25°. Overall, this result demonstrates a strong effect of the elastic response in the geometry of the folding. This observation is consistent with studies showing that when the heterogeneity of the sedimentary cover increases, the reconstruction of the structure requires applying lower apical angle values (Hardy et al., 2007).

Our simulations contribute to modeling fault propagation folds where inverse modeling of the structure cannot be performed due to the difficulty of delineating deformed layers. The numerical models carried out in this work allow obtaining more information on longer-term deformation patterns with complex rheologies. By means of the numerical models it is possible to visualize the different stages of development of the fold. In this way, the presence of minor forethrusts and the geometry of the backthrusts can be inferred, contributing to the most accurate reconstruction of fold and thrust belts.

Author statement

Plotek: Methodology, Software, Validation, Formal analysis, Inves tigation, Data curation, Writing - original draft, Writing - review & editing.

Heckenbach: Methodology, Software, Validation, Formal analysis, Investigation, Data curation, Writing - original draft, Writing - review & editing.

Brune: Conceptualization, Methodology, Software, Validation, Formal analysis, Investigation, Data curation, Supervision, Project administration, Funding acquisition, Writing - original draft, Writing - review & editing.

Cristallini: Conceptualization, Methodology, Software, Validation, Formal analysis, Investigation, Data curation, Supervision, Project administration, Writing - original draft, Writing - review & editing.

Likerman: Formal analysis, Writing - review & editing.

Declaration of competing interest

The authors declare that they have no known competing financial interests or personal relationships that could have appeared to influence the work reported in this paper.

Acknowledgements

Work carried out with the support of a grant from the Agencia Nacional de Promoción Científica y Tecnológica (ANPCyT) BID PICT project 2019-3834. We thank LA. TE. Andes for the academic license of Andino 3D. IDEAN (Instituto de Estudios Andinos Don Pablo Groeber), Consejo Nacional de Investigaciones Científicas y Técnicas (CONICET), and University of Buenos Aires (UBA) are also recognized for their support during this research. The work was supported by the North-German Supercomputing Alliance (HLRN).

We thank the Computational Infrastructure for Geodynamics (`geodynamics.org`) which is funded by the National Science Foundation under award EAR-0949446 and EAR-1550901 for supporting the development of ASPECT and Anne Glerum for advice during model setup. The earlier version of this manuscript was greatly improved after constructive comments by two anonymous reviewers. The fruitful comments of the editor are also appreciated.

References

Ahumada, E.A., C.H. Costa, C.E. Gardini, and H. Diederix (2006). “La estructura del extremo sur de la Sierra de Las Peñas-Las Higueras, Precordillera de Mendoza”. In: *Assoc. Geol. Arg.* 6, pp. 11–17.

Albertz, M. and S. Lingrey (2012). “Critical state finite element models of contractional fault-related folding: Part 1. Structural analysis”. In: *Tectonophysics* 576-577, pp. 133–149.

Allmendinger, R.W. (1998). “Inverse and forward numerical modeling of trishear faultpropagation folds”. In: *Tectonics* 17.4, pp. 640–656.

Allmendinger, R.W., T. Zapata, R. Manceda, and F. Dzelalija (2005). “Trishear kinematic modeling of structures, with examples from the Neuquén Basin, Argentina”. In: *AAPG Memoir* 82, pp. 356–371.

Ballato, P., S. Brune, and M.R. Strecker (2019). “Sedimentary loading–unloading cycles and faulting in intermontane basins: Insights from numerical modeling and field observations in the NW Argentine Andes”. In: *Earth and Planetary Science Letters* 506, pp. 388–396.

Baumann, T.S., B.J. Kaus, and A.A. Popov (2018). “Deformation and stresses related to the Gorleben salt structure: Insights from 3D numerical model”. In: *Proc. Conf. Mech.Beh. Of Salt, Saltmech IX*, pp. 15–27.

Bello, L., N. Coltice, T. Rolf, and P.J. Tackley (2014). “On the predictability limit of convection models of the Earth’s mantle”. In: *Geochemistry, Geophysics, Geosystems* 15.6, pp. 2319–2328.

Brandenburg, J.P. (2013). “Trishear for curved faults”. In: *Journal of Structural Geology* 53, pp. 80–94.

Brandes, C. and D.C. Tanner (2014). “Fault-related folding: A review of kinematic models and their application”. In: *Earth-Science Reviews* 138, pp. 352–370.

Bräuer, V., R. Eickemeier, D. Eisenburger, C. Grissemann, J. Hesser, S. Heusermann, D. Kaiser, H.-K. Nipp, T. Nowak, I. Plischke, H. Schnier, O. Schulze, J. Sönnke, and J.R. Weber (2011). “Description of the Gorleben Site Part 4: Geotechnical Exploration of the Gorleben Salt Dome”. In: *Description of the Gorleben Site Part 4: Geotechnical Exploration of the Gorleben Salt Dome.*

Braun, J. and M. Sambridge (1994). “Dynamical Lagrangian Remeshing (DLR): A new algorithm for solving large strain deformation problems and its application to fault-propagation folding”. In: *Earth and Planetary Science Letters* 124.1-4, pp. 211–220.

Brune, S. and J. Autin (2013). “The rift to break-up evolution of the Gulf of Aden: Insights from 3D numerical lithospheric-scale modelling”. In: *Tectonophysics* 607, pp. 65–79.

Brune, S., C. Heine, M. Pérez-Gussinyé, and S.V. Sobolev (2014). “Rift migration explains continental margin asymmetry and crustal hyper-extension”. In: *Nature Communications* 5.

Brune, S., S.E. Williams, N.P. Butterworth, and R.D. Müller (2016). “Abrupt plate accelerations shape rifted continental margins”. In: *Nature* 536.7615, pp. 201–204.

Cardozo, N. (2008). “Trishear in 3D. Algorithms, implementation, and limitations”. In: *Journal of Structural Geology* 30.3, pp. 327–340.

Cardozo, N. and S. Aanonsen (2009). “Optimized trishear inverse modeling”. In: *Journal of Structural Geology* 31.6, pp. 546–560.

Cardozo, N., K. Bhalla, A.T. Zehnder, and R.W. Allmendinger (2003). “Mechanical models of fault propagation folds and comparison to the trishear kinematic model”. In: *Journal of Structural Geology* 25.1, pp. 1–18.

Chester, J.S. and F.M. Chester (1990). “Fault-propagation folds above thrusts with constant dip”. In: *Journal of Structural Geology* 12.7, pp. 903–910.

Coleman, A.J., O.B. Duffy, and C.A. Jackson (2019). “What is Trishear?” In.

Colli, L., S. Ghelichkhan, H.-P. Bunge, and J. Oeser (2018). “Retrodictions of Mid Paleogene mantle flow and dynamic topography in the Atlantic region from compressible high resolution adjoint mantle convection models: Sensitivity to deep mantle viscosity and tomographic input model”. In: *Gondwana Research* 53, pp. 252–272.

Cristallini, E., F. Sánchez, D. Balciunas, A. Mora, R. Ketcham, J. Nigro, J. Hernández, and R. Hernández (2021). “Seamless low-temperature thermochronological modeling in Andino 3D, towards integrated structural and thermal simulations”. In: *Journal of South American Earth Sciences* 105.

Cristallini, E.O. and R.W. Allmendinger (2001). “Pseudo 3-D modeling of trishear fault-propagation folding”. In: *Journal of Structural Geology* 23.12, pp. 1883–1899.

Dannberg, J. and R. Gassmöller (2018). “Chemical trends in ocean islands explained by plume–slab interaction”. In: *Proceedings of the National Academy of Sciences of the United States of America* 115.17, pp. 4351–4356.

Dewey, J.F. (1965). “Nature and origin of kink-bands”. In: *Tectonophysics* 1.6, pp. 459–494.

Echavarria, L., R. Hernández, R. Allmendinger, and J. Reynolds (2003). “Subandean thrust and fold belt of northwestern Argentina: Geometry and timing of the Andean evolution”. In: *American Association of Petroleum Geologists Bulletin* 87.6, pp. 965–985.

Erdos, Z., R.S. Huismans, and P. Van Der Beek (2019). “Control of increased sedimentation on orogenic fold-and-thrust belt structure-insights into the evolution of the Western Alps”. In: *Solid Earth* 10.2, pp. 391–404.

Erslev, E.A. (1991). “Trishear fault-propagation folding”. In: *Geology* 19.6, pp. 617–620.

Finch, E., S. Hardy, and R. Gawthorpe (2002). “Discrete element modelling of contractional fault-propagation folding above rigid basement fault blocks”. In: *Journal of Structural Geology* 25.4, pp. 515–528.

— (2004). “Discrete-element modelling of extensional fault-propagation folding above rigid basement fault blocks”. In: *Basin Research* 16.4, pp. 467–488.

Giambastiani, M. (2019). *Geomechanical Characterization of Evaporitic Rocks*, pp. 129–161.

Glerum, A., S. Brune, D.S. Stamps, and M.R. Strecker (2020). “Victoria continental microplate dynamics controlled by the lithospheric strength distribution of the East African Rift”. In: *Nature Communications* 11.1.

Glerum, A., C. Thieulot, M. Fraters, C. Blom, and W. Spakman (2018). “Nonlinear viscoplasticity in ASPECT: Benchmarking and applications to subduction”. In: *Solid Earth* 9.2, pp. 267–294.

Gouiza, M. and J. Naliboff (2021). “Rheological inheritance controls the formation of segmented rifted margins in cratonic lithosphere”. In: *Nature Communications* 12.1.

Granado, P. and J.B. Ruh (2019). “Numerical modelling of inversion tectonics in fold-and-thrust belts”. In: *Tectonophysics* 763, pp. 14–29.

Granado, P., J.B. Ruh, P. Santolaria, P. Strauss, and J.A. Muñoz (2021). “Stretching and Contraction of Extensional Basins With Pre-Rift Salt: A Numerical Modeling Approach”. In: *Frontiers in Earth Science* 9.

Gray, G.G., J.K. Morgan, and P.F. Sanz (2014). “Overview of continuum and particle dynamics methods for mechanical modeling of contractional geologic structures”. In: *Journal of Structural Geology* 59, pp. 19–36.

Grothe, P.R., N. Cardozo, K. Mueller, and T. Ishiyama (2014). “Propagation history of the Osaka-wan blind thrust, Japan, from trishear modeling”. In: *Journal of Structural Geology* 58, pp. 79–94.

Gschwandtner, G.G. and R. Galler (2018). “Long-term behaviour of complex underground structures in evaporitic rock mass – Experiences gained from calculations and geotechnical observations”. In: *Tunnelling and Underground Space Technology* 78, pp. 159–167.

Guiofski, C.A., J.P. Mueller, J.H. Shaw, P. Muron, D.A. Medwedeff, F. Bilotti, and C. Rivero (2009). “Insights into the mechanisms of fault-related folding provided by volumetric structural restorations using spatially varying mechanical constraints”. In: *AAPG Bulletin* 93.4, pp. 479–502.

Hardy, S. and R.W. Allmendinger (2011). “Trishear: A review of kinematics, mechanics,andapplications”. In: *AAPG Memoir* 94, pp. 95–119.

Hardy, S. and E. Finch (2007). “Mechanical stratigraphy and the transition from trishear to kink-band fault-propagation fold forms above blind basement thrust faults: A discrete-element study”. In: *Marine and Petroleum Geology* 24.2, pp. 75–90.

Hardy, S. and M. Ford (1997). “Numerical modeling of trishear fault propagation folding”. In: *Tectonics* 16.5, pp. 841–854.

Heckenbach, Esther L., Sascha Brune, Anne C. Glerum, and Judith Bott (2021). “Is There a Speed Limit for the Thermal Steady-State Assumption in Continental Rifts?” en. In: *Geochemistry, Geophysics, Geosystems* 22.3, e2020GC009577.

Heister, T., J. Dannberg, R. Gassmöller, and W. Bangerth (2017). “High accuracy mantle convection simulation through modern numerical methods - II: Realistic models and problems”. In: *Geophysical Journal International* 210.2, pp. 833–851.

Heng, S., Y. Guo, C. Yang, J.J.K. Daemen, and Z. Li (2015). “Experimental and theoretical study of the anisotropic properties of shale”. In: *International Journal of Rock Mechanics and Mining Sciences* 74, pp. 58–68.

Holt, A.F. and C.B. Condit (2021). “Slab Temperature Evolution Over the Lifetime of a Subduction Zone”. In: *Geochemistry, Geophysics, Geosystems* 22.6.

Huang, G., Z. Zhang, H. Zhang, P. Huangfu, and Z.-H. Li (2020). “Development of contrasting folding styles in the western Yangtze block, South China: Insights from numerical modeling”. In: *Tectonophysics* 792.

Hughes, A.N. and J.H. Shaw (2015). “Insights into the mechanics of fault-propagation folding styles”. In: *Bulletin of the Geological Society of America* 127.11-12, pp. 1752–1765.

Huismans, R.S. and C. Beaumont (2002). “Asymmetric lithospheric extension: the role of frictional plastic strain softening inferred from numerical experiments”. In: *Geology*, p. 2.

Jabbour, M., D. Dhont, Y. Hervouët, and J.-P. Deroin (2012). “Geometry and kinematics of fault-propagation folds with variable interlimb angle”. In: *Journal of Structural Geology* 42, pp. 212–226.

Jacquey, A.B. and M. Cacace (2020). “Multiphysics Modeling of a Brittle-Ductile Lithosphere: 1. Explicit Visco-Elasto-Plastic Formulation and Its Numerical Implementation”. In: *Journal of Geophysical Research: Solid Earth* 125.1.

Johnson, K.M. (2018). “Growth of Fault-Cored Anticlines by Flexural Slip Folding: Analysis by Boundary Element Modeling”. In: *Journal of Geophysical Research: Solid Earth* 123.3, pp. 2426–2447.

Jourdon, A., C. Kergaravat, G. Duclaux, and C. Huguen (2021). “Looking beyond kinematics: 3D thermo-mechanical modelling reveals the dynamics of transform margins”. In: *Solid Earth* 12.5, pp. 1211–1232.

Khalifeh-Soltani, A., S.A. Alavi, M.R. Ghassemi, and M. Ganjiani (2021). “Geomechanical modelling of fault-propagation folds: Estimating the influence of the internal friction angle and friction coefficient”. In: *Tectonophysics* 815.

Kronbichler, M., T. Heister, and W. Bangerth (2012). “High accuracy mantle convection simulation through modern numerical methods”. In: *Geophysical Journal International* 191.1, pp. 12–29.

Lebinson, F., M. Turienzo, N. Sánchez, V. Araujo, M.C. D’Annunzio, and L. Dimieri (2018). “The structure of the northern Agrio fold and thrust belt (37°30’ s), Neuquén Basin, Argentina [La estructura del sector norte de la faja plegada y corrida del Agrio (37°30’ s), Cuenca Neuquina, Argentina]”. In: *Andean Geology* 45.2, pp. 249–273.

Lebinson, F., M. Turienzo, N. Sánchez, E. Cristallini, V. Araujo, and L. Dimieri (2020). “Kinematics of a backthrust system in the Agrio fold and thrust belt, Argentina: Insights from structural analysis and analogue models”. In: *Journal of South American Earth Sciences* 100.

Liang, W.G., S.G. Xu, and Y.S. Zhao (2006). “Experimental study of temperature effects on physical and mechanical characteristics of salt rock”. In: *Rock Mechanics and Rock Engineering* 39.5, pp. 469–482.

Liu, C., H. Yin, and L. Zhu (2012). “TrishearCreator: A tool for the kinematic simulation and strain analysis of trishear fault-propagation folding with growth strata”. In: *Computers and Geosciences* 49, pp. 200–206.

Luo, B., B. Duan, and D. Liu (2020). “3d finite-element modeling of dynamic rupture and aseismic slip over earthquake cycles on geometrically complex faults”. In: *Bulletin of the Seismological Society of America* 110.6, pp. 2619–2637.

Maillot, B. and Y.M. Leroy (2006). “Kink-fold onset and development based on the maximum strength theorem”. In: *Journal of the Mechanics and Physics of Solids* 54.10, pp. 2030–2059.

Mitra, S. (1990). “Fault-propagation Folds: Geometry, Kinematic Evolution, and Hydrocarbon Traps”. In.

Mitra, S. and J.F. Miller (2013). “Strain variation with progressive deformation in basement-involved trishear structures”. In: *Journal of Structural Geology* 53, pp. 70–79.

Nilfouroushan, F., R. Pysklywec, and A. Cruden (2012). “Sensitivity analysis of numerical scaled models of fold-and-thrust belts to granular material cohesion variation and comparison with analog experiments”. In: *Tectonophysics* 526-529, pp. 196–206.

Plotek, B., C. Guzmán, E. Cristallini, and D. Yagupsky (2021). “Analysis of fault bend folding kinematic models and comparison with an analog experiment”. In: *Journal of Structural Geology* 146.

Rajaonarison, T.A., D.S. Stamps, S. Fishwick, S. Brune, A. Glerum, and J. Hu (2020). “Numerical Modeling of Mantle Flow Beneath Madagascar to Constrain Upper Mantle Rheology Beneath Continental Regions”. In: *Journal of Geophysical Research: Solid Earth* 125.2.

Richter, M.J.E.A., S. Brune, S. Riedl, A. Glerum, D. Neuharth, and M.R. Strecker (2021). “Controls on Asymmetric Rift Dynamics: Numerical Modeling of Strain Localization and Fault Evolution in the Kenya Rift”. In: *Tectonics* 40.5.

Rojas Vera, E.A., J. Mescua, A. Folguera, T.P. Becker, L. Sagripanti, L. Fennell, D. Orts, and V.A. Ramos (2015). “Evolution of the Chos Malal and Agrio fold and thrust belts, Andes of Neuquén: Insights from structural analysis and apatite fission track dating”. In: *Journal of South American Earth Sciences* 64, pp. 418–433.

Rose, I., B. Buffett, and T. Heister (2017). “Stability and accuracy of free surface time integration in viscous flows”. In: *Physics of the Earth and Planetary Interiors* 262, pp. 90–100.

Rubey, M., S. Brune, C. Heine, D. Rhodri Davies, S.E. Williams, and R. DIetmar Müller (2017). “Global patterns in Earth’s dynamic topography since the Jurassic: The role of subducted slabs”. In: *Solid Earth* 8.5, pp. 899–919.

Ruh, J.B. (2020). “Numerical modeling of tectonic underplating in accretionary wedge systems”. In: *Geosphere* 16.6, pp. 1385–1407.

Ruh, J.B., B.J.P. Kaus, and J.-P. Burg (2012). “Numerical investigation of deformation mechanics in fold-and-thrust belts: Influence of rheology of single and multiple décollements”. In: *Tectonics* 31.3.

Rybacki, E., M. Gottschalk, R. Wirth, and G. Dresen (2006). “Influence of water fugacity and activation volume on the flow properties of fine-grained anorthite aggregates”. In: *Journal of Geophysical Research: Solid Earth* 111.3.

Saffar, M.A. (1993). “Geometry of fault-propagation folds: method and application”. In: *Tectonophysics* 223.3-4, pp. 363–380.

Sandiford, D., S. Brune, A. Glerum, J. Naliboff, and J.M. Whittaker (2021). “Kinematics of Footwall Exhumation at Oceanic Detachment faults: Solid-Block Rotation and Apparent Unbending”. In: *Geochemistry, Geophysics, Geosystems* 22.4.

Sanz, P.F., R.I. Borja, and D.D. Pollard (2007). “Mechanical aspects of thrust faulting driven by far-field compression and their implications for fold geometry”. In: *Acta Geotechnica* 2.1, pp. 17–31.

Sari, M. (2021). “Secondary toppling failure analysis and optimal support design for ignimbrites in the Ihlara Valley (Cappadocia, Turkey) by finite element method (FEM)”. In: *Geotechnical and Geological Engineering* 39.7, pp. 5135–5160.

Schuh-Senlis, M., C. Thieulot, P. Cupillard, and G. Caumon (2020). “Towards the application of Stokes flow equations to structural restoration simulations”. In: *Solid Earth* 11.5, pp. 1909–1930.

Selzer, C., S.J.H. Buiter, and O.A. Pfiffner (2007). “Sensitivity of shear zones in orogenic wedges to surface processes and strain softening”. In: *Tectonophysics* 437.1-4, pp. 51–70.

Steinberger, B., E. Bredow, S. Lebedev, A. Schaeffer, and T.H. Torsvik (2019). “Widespread volcanism in the Greenland–North Atlantic region explained by the Iceland plume”. In: *Nature Geoscience* 12.1, pp. 61–68.

Suppe, J. and D.A. Medwedeff (1990). “Geometry and kinematics of fault-propagation folding”. In: *Eclogae Geol. Helv.* 83, pp. 409–454.

Treffeisen, T. and A. Henk (2020). “Representation of faults in reservoir-scale geomechanical finite element models – A comparison of different modelling approaches”. In: *J. Struct. Geol.* 131.

Van Wijk, J. W. and S. A. P. L. Cloetingh (2002). “Basin migration caused by slow lithospheric extension”. In: *Earth and Planetary Science Letters* 198(3–4), pp. 275–288.

Woodward, N. B. (1997). “Low-amplitude evolution of break-thrust folding”. In: *J. Struct. Geol.* 19, pp. 293–301.

Wyllie, D. and N. Norrish (1996). “Chapter 14: Rock Strength Properties and their measurement”. In: *Landslides: Investigation and Mitigation*, pp. 372–390.

Zehnder, A. and R. Allmendinger (2000). “Velocity field for the trishear model”. In: *J. Struct. Geol.* 22, pp. 1009–1014.

Zhang, N. and Z. X. Li (2018). “Formation of mantle “lone plumes” in the global downwelling zone — A multiscale modelling of subduction-controlled plume generation beneath the South China Sea”. In: *Tectonophysics* 723, pp. 1–13.

4 3D Interaction of Tectonics and Surface Processes explains Fault Network Evolution of the Dead Sea Fault

This study was submitted to *Tektonika* in December 2023 as:
Esther L. Heckenbach[1,2], Sascha Brune[1,2], Anne C. Glerum[1], Roi Granot[3], Yariv Hamiel[4], Stephan V. Sobolev[1,2], Derek Neuharth[1,5] (submitted): 3D Interaction of Tectonics and Surface Processes explains Fault Network Evolution of the Dead Sea Fault.

[1]GeoForschungsZentrum Potsdam, Potsdam, Germany
[2]Universität Potsdam,Potsdam, Germany
[3]Ben-Gurion University of the Negev, Beer-Sheva, Israel
[4]Geological Survey of Israel, Jerusalem, Israel
[5]ETH Zürich, Zürich, Switzerland

Additional material can be found at:
`https://zenodo.org/doi/10.5281/zenodo.10405076`

Abstract

Releasing and restraining bends are complementary features of continental strike-slip faults. The Dead Sea Basin of the strike-slip Dead Sea Fault is a classical example of a releasing bend with an asymmetric, deep basin structure. However, the intrinsic relationship to its northern counterpart, the restraining bend that created the Lebanese mountains, remains unclear. Here, we present 3D coupled geodynamic and landscape evolution models that include both the releasing and the restraining bend in a single framework. These simulations demonstrate that the structural basin asymmetry is a consequence of strain localization processes, while sediments control the basin depth. Local extension emerges due to strength heterogeneities and a misalignment of faults and the overall stress field in an area where regional tectonics are dominated by strike-slip motion. Furthermore, we reveal a crustal thinning and thickening pattern that intensifies with surface process efficiency. Along-strike deformation is linked through coupled crustal flow driven by gravitational potential energy which is opposed by deposition at the releasing bend and enhanced by erosion around the restraining bend. Due to the generic nature of our models, our results provide templates for the evolution of fault bends worldwide.

4.1 Introduction

Continental transform faults are highly localized strike-slip zones that accumulate tens to hundreds of kilometers of shear motion (Norris et al., 2014). They often form as a network of fault segments with clearly visible fault traces. Besides the Dead Sea Fault, other prominent continental transform faults are the San Andreas Fault of California, the North Anatolian Fault in Turkey, the Alpine Fault of New Zealand, and the Altyn Tagh Fault in Tibet (Duarte, 2019). While transform fault systems are primarily associated with strike-slip motion, stepovers and fault segmentation result in regional transpressional regimes at restraining bends and transtensional regimes at releasing bends (Crowell, 1974; Mann, 2007). Fault bends are responsible for distinct topographic features, including the formation of push-up mountains at restraining bends and deep pull-apart basins at releasing bends. The Dead Sea pull-apart basin has the world's lowest on-land elevation, namely 430 m below global sea level.

The Dead Sea Fault (DSF) system (Fig. 4.1a) formed less than 20 Ma during the fragmentation of the northeastern Nubian Plate into the Arabian and Sinai Plates (Garfunkel, 1981). It is embedded in a complex tectonic framework connecting the Red Sea rift in the south to the Bitlis-Zagros mountain range in the north (Quennell, 1959; DESERT Group et al., 2004). The southern part of the DSF accommodates several narrow pull-apart basins resulting from releasing bends with thick sedimentary infill (GARFUNKEL et al., 2001) contrasting the high elevations of the Lebanese mountains within the restraining bend in the north.

The DSF system has been intensively studied through various geophysical methods (Fig. 4.1). Major earthquakes are concentrated on the faults along the strike-slip and releasing bend sections, whereas the fault network is more complex and seismicity more wide-spread at the restraining bend (Elias et al., 2007; Smit et al., 2008; Wetzler et al., 2016). Gravity measurements show that the DSF is located where the 35 km thick continental crust of the Arabian Plate thins towards the Sinai Plate and the Mediterranean Sea (Götze et al., 2007) (Fig. 4.1d). Today, the Dead Sea Basin (DSB) is characterized by a prominent and well-defined gravitational low between these two plates (Fig. 4.1d) that exhibits intriguingly small heat flow, which can be as low as 27–40 mW/m^2 (Fig. 4.1b in white) (Ben-Avraham et al., 1978; Shalev et al., 2013; Schütz et al., 2014; Oryan et al., 2019). These values are, however, debated as they are in strong contrast to the heat flow values of 50–60 mW/m^2 seen farther from the basin (Förster et al., 2010; Shalev et al., 2013). Seismic data suggest that the sedimentary infill is 8–12 km thick, which makes the basin roughly as deep as it is wide (Ten Brink et al., 1993) (Fig. 4.1b). These data furthermore reveal that the sediments and basement topography feature a distinct asymmetry involving a steeply sloping eastern side and a gentler sloping western side. Together with this asymmetry, the steep basin-ward dipping strike-slip border faults led previous studies to suggest and explore an extensional component across the basin and the transform sections of the DSF (Quennell, 1959; Garfunkel, 1981; Ben-Avraham et al., 1992; DESERT Group et al., 2004; Sobolev et al., 2005; Petrunin et al., 2006; Smit et al., 2008; Smit et al., 2010; Petrunin et al., 2012). Far-field extension has been attributed to a shift in plate kinematics due to changes in the direction and velocity of the Red Sea opening around ∼10–5 Ma (e.g. Garfunkel, 1981; Joffe et al., 1987; Smit et al., 2010; Reilinger et al., 2011). However, inversions of regional GPS data do not disclose a present-day component of far-field extension (Le Beon et al., 2008; Hamiel et al., 2021). Instead, these demonstrated that local extension is confined to areas where faults deviate from the along-strike DSF direction within releasing bends. The origin of the low heat flow, the elongated basin geometry and whether temporal changes in plate kinematics shaped the observed asymmetry are among the major ongoing discussion points concerning the area.

In previous modeling studies, restraining and releasing bends such as found in the DSF system have primarily been investigated separately, and possible interactions during their evolution have been neglected. These studies underlined the crucial role of a thick ductile layer that decouples the brittle crust and upper mantle in the formation of narrow pull-apart basins (Petrunin et al., 2006; Smit et al., 2008). Additionally, they highlighted the significance of the development of an isolated crustal block for very thick sedimentary infill and low heat flow values (Ben-Avraham et al., 2006; Ben-Avraham et al., 2010). For restraining bends, previous studies have demonstrated that block rotation takes place prior to strain partitioning, as evidenced by paleomagnetic rotations, the present-day orientation of rivers and earthquake focal mechanisms (Gomez et al., 2007; Goren et al., 2015; Dembo et al., 2021).

In this study, we utilize geodynamic models to investigate the evolution of strike-slip faults that include both a releasing and a restraining bend. Our target region is the Dead Sea Fault, but due to the generic nature of our models, the results are transferable to other fault bends worldwide. First, we describe the mechanisms that control the evolution of the model pull-apart basin and compare it to observations from the DSB. We show that asymmetry and local extension along a modeled transform fault can result from strength heterogeneities without requiring far-field divergence. Additionally, we investigate how sediment deposition changes the longevity of the pull-apart basin. Finally, we present new insights into feedbacks between tectonics and surface processes and find that erosion and sedimentation can provide a far-field connection between a releasing and restraining bend at crustal scale.

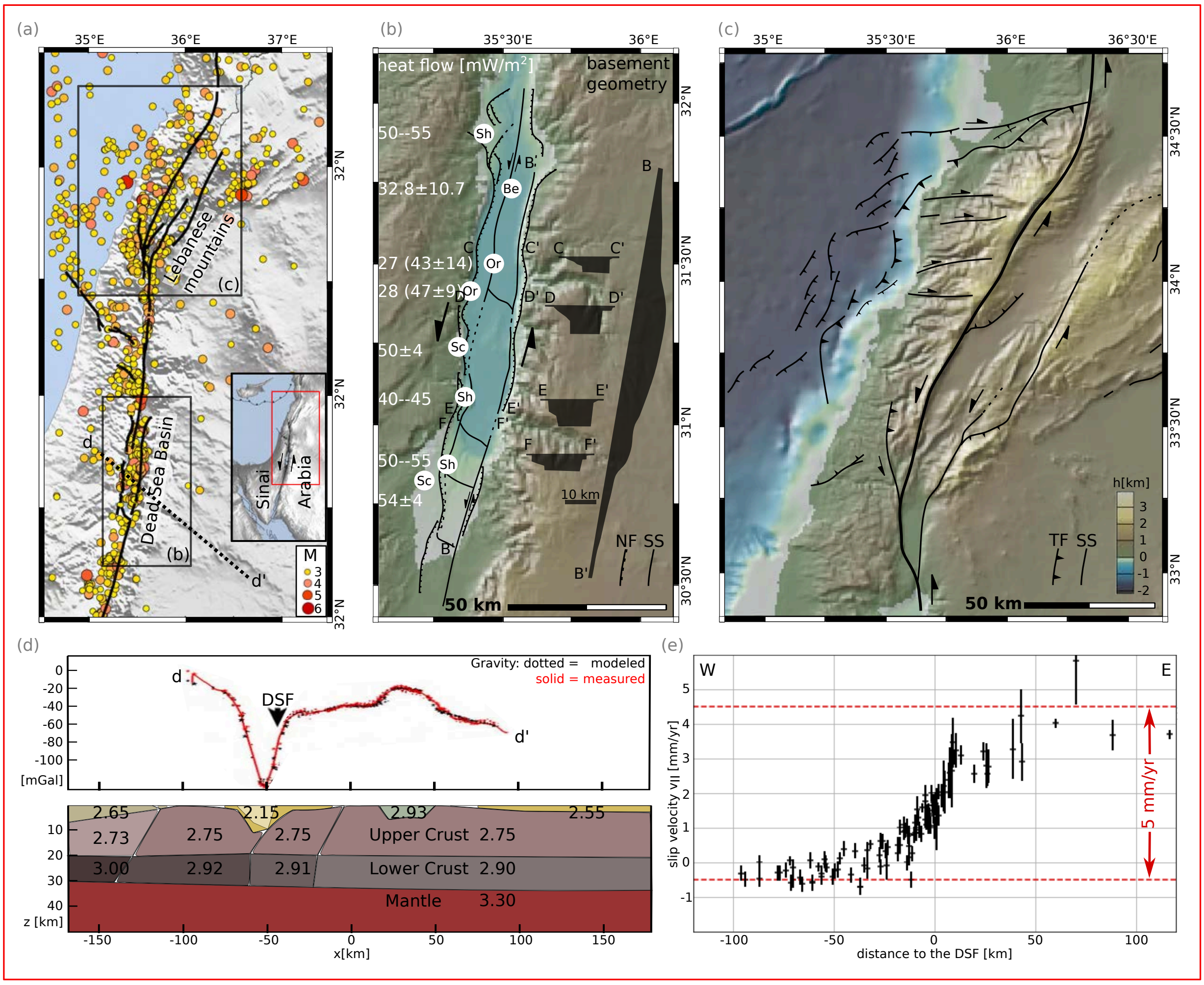

Figure 4.1: A summary of the available geophysical data along the Dead Sea Fault. (a) Topographical relief map (ETOPO 2022, `https://doi.org/10.25921/fd45-gt74`) with locations and magnitudes of recorded seismicity since 1985 according to the GSI seismic catalogue (`https://eq.gsi.gov.il/en/earthquake/searchEQS.php`) and main surface outlines of the DSF system (Hamiel et al., 2021). (b) Topographical map of the Dead Sea Basin with the fault network outlined after Fig. 1 in Smit et al., 2008 and the cross-sectional basement geometry after Fig. 7 in Ten Brink et al., 1993 in black. White locations and values show heat flow measurements obtained within the basin. Values belonging to locations marked as Sh (Shalev et al., 2013) indicate the range of their map. Be (Ben-Avraham et al., 1978) provide the mean of several measurement points, Or (Oryan et al., 2019) values show their measurement and the correction range in brackets while Sc (Schütz et al., 2014) provide an uncertainty range. (c) Topographical map of the Lebanese restraining bend with the fault network outlined after Fig. 1 in Elias et al., 2007. Topography of both (b) and (c) has been plotted using GeoMapApp with the same colour scale as shown in (c) (`www.geomapapp.org`, Ryan et al., 2009). See rectangles in (a) for locations of (b) and (c). (d) Gravity profile and crustal density [Mg/m^3] model modified from Fig. 5 in Götze et al., 2007. The location of profile d–d' is shown in (a). (e) Fault-parallel velocities as a function of distance from the fault obtained from GPS data of selected stations between 30°N and 32.3°N (Hamiel et al., 2021, Fig. 2, profiles B–E) representing strike-slip and transtensional deformation regimes in the area. Velocity is shown relative to the Sinai Plate (see (a)).

4.2 Methods

4.2.1 ASPECT and FastScape

Computations were performed with the geodynamic finite element software ASPECT (Advanced Solver for Planetary Evolution, Convection, and Tectonics, `https://aspect.geodynamics.org`, see Kronbichler et al., 2012; Heister et al., 2017; Gassmöller et al., 2018). We use ASPECT to solve for the conservation of mass, momentum, and energy under the extended Boussinesq approximation with an infinite Prandtl number (see Supplementary Material, eq. B.1–B.8). For each material (e.g., upper crust) and plastic strain, an additional advection equation is solved (continuous field method). Nonlinearities in the rheology (Glerum et al., 2018) are iterated out using a Newton solver scheme.

We employ the recently established two-way coupling between ASPECT and the surface-processes code FastScape (`https://fastscape.org`, Braun et al., 2013; Yuan et al., 2019). The coupling is illustrated in Fig. 4.2 and works as follows (Neuharth et al., 2021b; Neuharth et al., 2022): at the beginning of each geodynamic time step, ASPECT hands over the vertical and horizontal velocity at the surface to FastScape for use in uplift and horizontal advection, respectively. Then, equations describing river incision (extended stream power law), hillslope diffusion and marine sediment transport are solved. After a prescribed number of FastScape time steps, the updated surface topography is given back to ASPECT. The velocity of the mesh surface is then computed from the difference of the new surface with the stored mesh from before the call to FastScape divided by the ASPECT time step. The velocity of the mesh interior is obtained by solving a Laplace equation (see Rose et al., 2017). Subsequently, ASPECT solves the governing equations.

To account for the negative altitude of the Dead Sea water level, we need to discriminate between local and global sea level. We therefore introduce a new parameter, the regional erosional base level, in the ASPECT-FastScape coupling. The new parameter minimizes mass loss and assures that only a small lacustrine area at the releasing bend evolves, while the surroundings remain as a highland topography. Otherwise, sediment is moved out of the domain by FastScape when not enough marine area is present to accommodate the sediment held in rivers from the stream power law. The specific version of ASPECT and FastScape used in this paper can be found at `https://zenodo.org/doi/10.5281/zenodo.10405076`.

4.2.2 Model setup

We conducted a series of 3D box simulations to investigate the influence of boundary and initial conditions, as well as different surface process efficiencies, on the evolution of a generic strike-slip setup comprising two stepovers that evolve into a restraining and a releasing bend (Fig. 4.2). Model parameters are shown in the supplementary Tables B.S1 and B.S2. All ASPECT and FastScape parameter values can be found in the ASPECT input files provided at `https://zenodo.org/doi/10.5281/zenodo.10405076`.

Geometry and resolution. The geodynamic model domain is 600 km long (x-direction), 152 km wide (y-direction) and 100 km deep (z-direction). We use mesh refinement such that the uppermost 15 km and a box of 45 km depth and 36 km width along the fault have a resolution of 1 km, while resolution gradually decreases to 4 km at the bottom of the domain. The mesh of the FastScape 2D domain that spans the top surface of the 3D ASPECT model has a resolution of 500 m. For comparison with nature, model topography has been corrected by adding 1000 m of elevation everywhere during postprocessing such that the regional erosional base level fits the Mediterranean sea level. The local FastScape sea level that determines sediment accommodation space is set to be 500 m lower than the regional erosional base level as it represents the Dead Sea, while the latter represents global sea level.

Initial conditions. The initial model setup consists of five material layers: a sedimentary cover on top of a 20 km thick upper and a 13 km thick lower crust that are underlain by 67 km of lithospheric mantle and a very thin layer of asthenosphere (Fig. 4.2a). Unperturbed crustal layer thicknesses and all densities are chosen according to the eastern part of the gravity profile crossing the DSF (Götze et al., 2007) (see Supplementary Table B.S1for all material properties). It should be noted that these published densities are in-situ densities based on seismic velocities from the DESERT seismic line (DESERT Group et al., 2004), while the geodynamic models require reference densities as an input for the temperature-dependent density. In our models, the reference densities were chosen such that values at the center of each layer match the in-situ densities inferred from seismic experiments (see values in Fig. 4.2a). The

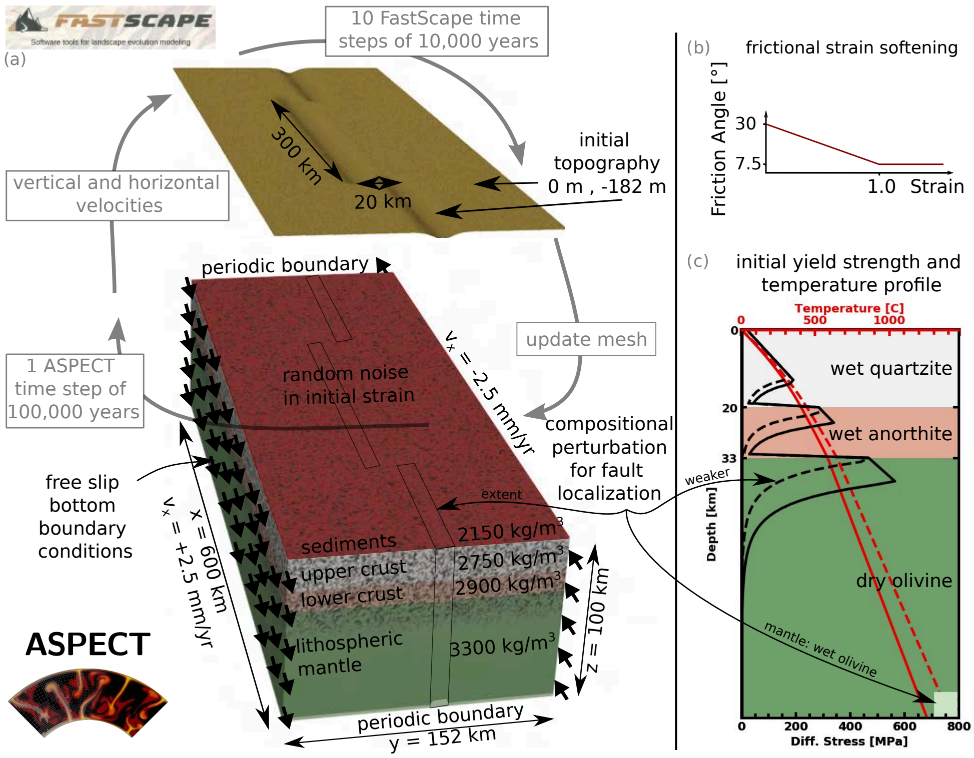

Figure 4.2: (a) The initial and boundary conditions of the reference model using the two-way coupled ASPECT-FastScape software. Rheological parameters showing (b) weakening of the internal angle of friction with accumulated plastic strain and (c) temperature and strength profiles for a representative strain rate of $1{\cdot}10^{-15}$ 1/s. Solid lines: unperturbed lithosphere. Dashed lines: weakened lithosphere. The spatial extent of the initial perturbation is shown in (a) by the three boxes in the ASPECT domain

chosen model lithosphere of 100 km is slightly thicker than the lithosphere along the DSF (Mohsen et al., 2011) to preserve the generic character of the models. The initial temperature distribution is based on a steady-state 1D conductive continental geotherm in the lithosphere and on an adiabat below the lithosphere (see Fig. 4.2c and Supplementary Table B.S1).

Boundary conditions. The ASPECT model setup is periodic along-strike to allow for self-consistent localisation of strike-slip faults without prescribing their width and fault-scale kinematics. Far-field deformation is driven through a prescribed tangential horizontal velocity on the lateral, strike-parallel model sides. The bottom side of the model is governed by free slip boundary conditions and the top is controlled through coupling with the FastScape code. The simulations are run for 20 Myr model time with geodynamic (ASPECT) computational time step sizes of 100,000 years. Each of these time steps includes 10 FastScape time steps of 10,000 years to account for the different time-scales of geodynamic and surface processes. Testing smaller time step sizes showed no impact on modeling results. We use a total strike-slip boundary velocity of 5 mm/yr, which is in the range of the proposed slip rates for the DSF in the Dead Sea area of 3.8–7 mm/yr (Le Beon et al., 2008; Hamiel et al., 2019; Hamiel et al., 2021). During 20 Myr, this results in a total displacement of 100 km in the models comparable to the accumulated displacement of 105–107 km at the DSF (Garfunkel, 1981; Joffe et al., 1987; Götze et al., 2007; Mohsen et al., 2011).

Rheology. Geodynamic deformation occurs through a viscoplastic rheology including pressure-, temperature- and strain rate-dependent flow laws for viscous diffusion and dislocation creep and Drucker-Prager plasticity for brittle faulting. The evolution of fault systems is furthermore influenced by frictional strain softening over the plastic strain interval of 0–1 (Fig. 4.2b), reducing the internal angle of friction from 30° to 7.5°. We introduced initial random noise in the plastic strain field to account for inherited heterogeneity within the geological units (Richter et al., 2021). By varying the seed value of this noise pattern, we can isolate the impact of early-stage fault localisation processes on overall model evolution. To better visualize deformation and fault offsets, we included a layer of 120,000 passive particles at an initial depth of 8–10 km as deformation markers.

Fault localization. Localisation of faults occurs in a self-consistent way. However, the location of major strike-slip faults is introduced by thinning the initial lithospheric mantle layer by 20% (Fig. 4.2c) along three linear segments parallel to the prescribed boundary velocity (Fig. 4.2a). Due to the periodicity of the model, the three segments effectively form two 300 km long fault segments of the evolving transform fault that link in a restraining bend at x = 150 km and a releasing bend at x = 450 km. The compositional perturbation of the lithospheric mantle has a Gaussian shape in the y-direction (east-west) with $\sigma = 5$ km. Thinning the lithosphere alters its internal density and strength distribution. Computing initial isostatic balance leads to initial topographical lows at the surface (Fig. 4.2a). At depth, higher temperatures form a weaker zone that facilitates fault localization. In this way, no initial fault geometries need to be prescribed but all faults form self-consistently according to the prevailing stress field. It should be noted that faults in our models do not occur as distinct planes but are represented by a concentration of high strain rates in planar areas with a thickness of a few cells.

The initial strike-perpendicular offset of the segments amounts to 20 km. During the model run, this leads to a border fault spacing of approximately 10 km at the releasing bend, which corresponds well with observations made at the DSB. Note that increasing or decreasing the offset too much prevents the generation of pull-apart basins. In the fault-parallel direction there is no underlap nor overlap in the prescribed perturbations to maintain the generic character of the models. For transform linkage in extensional settings, previous work (Neuharth et al., 2021a) showed no influence of this parameter on the primary model results, given that fault tips consistently propagate in the direction of strike.

Parameter testing. In this work, we present 11 models. Besides the reference model, we assess the impact of different seeds of the plastic strain initial random noise (1, 3, 5) and different prescribed total strike-slip boundary velocities (2.5 mm/yr, 4.5 mm/yr, 5 mm/yr, 5.5 mm/yr, 10 mm/yr) to investigate the importance of the localization phase (Supplementary Material, Fig. B.S1 and B.S2). In terms of surface processes, we present results for four different values of the river incision rate K_f ($1 \cdot 10^{-5}$, $0.5 \cdot 10^{-5}$, $0.25 \cdot 10^{-5}$, $1 \cdot 10^{-40}$ $\mathrm{m}^{0.2}$/yr). The first three values represent high, medium, and low surface process efficiency (Wolf et al., 2021) and are within the range of K_f values computed for rivers with varying lithology and climate (Stock et al., 1999). The hillslope diffusion coefficient is kept constant at a value of $1 \cdot 10^{-2}$ $\mathrm{m}^{0.2}$/yr, except for the fourth model, where, together with K_f, it was set to a very small value ($1 \cdot 10^{-40}$ $\mathrm{m}^{0.2}$/yr). These low values make surface processes very inefficient such that the resulting model evolves according to geodynamic processes only. Our reference model uses a river incision rate K_f of $0.5 \cdot 10^{-5}$ $\mathrm{m}^{0.2}$/yr. When assuming drainage areas of 1 to 15 km^2, this value of K_f is equivalent to the erodibility that has been used for simulating erosion in the Lebanese mountains in previous work (Goren et al., 2015).

Limitations. To derive results that are generally applicable to the dynamics of restraining and releasing bends, we deliberately decided to employ generic models. We therefore did not include the variations in crustal and lithosphere thicknesses observed in our focus area (Götze et al., 2007; Mohsen et al., 2011; Smit et al., 2008) nor melting, magmatism and potential changes in velocity and thermal boundary conditions (Garfunkel, 1981; Joffe et al., 1987; Sobolev et al., 2005; Smit et al., 2010; Reilinger et al., 2011; Petrunin et al., 2012; Reznik et al., 2021). At the along-strike model sides, we use periodic boundary conditions which allow for self-consistent strain localization close to the initial crustal perturbation instead of prescribing fault geometries. However, this results in a border fault spacing at the restraining bend that is smaller than the current Lebanese mountains (Gomez et al., 2007; Nemer et al., 2020; Dembo et al., 2021) as the perturbations' placing is configured to mimic the size of the Dead Sea. Nevertheless, our simulations capture the first-order structure of the focus region. More importantly, the simplified models allow us to derive robust conclusions concerning the key differences between the evolution of restraining and releasing bends, the interaction between surface processes and tectonics, and the emergence of strain partitioning and local extension in an area where regional tectonics are dominated by strike-slip motion.

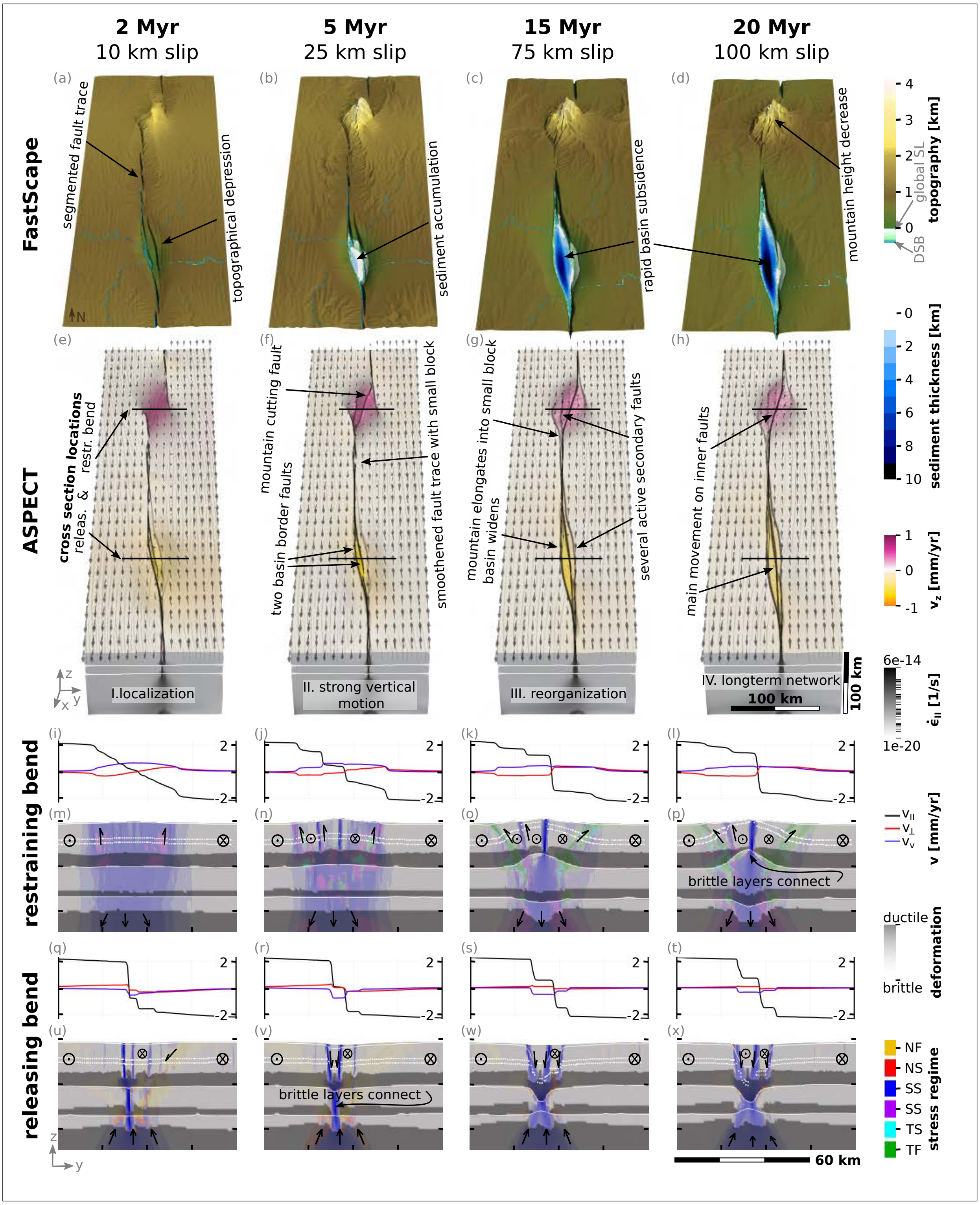
2 Myr
10 km slip
5 Myr
25 km slip
15 Myr
75 km slip
20 Myr
100 km slip
FastScape
(a)
segmented fault trace
topographical depression
N
(b)
sediment accumulation
(c)
rapid basin subsidence
(d)
mountain height decrease
topography [km]
4
3
2
1
0
global SL
DSB
ASPECT
(e)
cross section locations
releas. & restr. bend
I.localization
(f)
mountain cutting fault
two basin border faults
smoothened fault trace with small block
II. strong vertical motion
(g)
mountain elongates into small block
basin widens
several active secondary faults
III. reorganization
(h)
main movement on inner faults
IV. longterm network
100 km
100 km
z
y
x
sediment thickness [km]
0
2
4
6
8
10
v_z [mm/yr]
1
0
-1
6e-14
ε̇_II [1/s]
1e-20
restraining bend
(i)
(j)
(k)
(l)
2
-2
(m)
(n)
(o)
(p)
brittle layers connect
v [mm/yr]
v_∥
v_⊥
v_v
ductile
brittle
deformation
releasing bend
(q)
(r)
(s)
(t)
(u)
(v)
brittle layers connect
(w)
(x)
60 km
z
y
NF
NS
SS
SS
TS
TF
stress regime

Figure 4.3: The four evolutionary phases in the reference model. (a–d) Topography and sediment thickness in marine areas and rivers. Note the difference between the global sea level (global SL) and the local Dead Sea reference lake level (DSB) as indicated in the legend. Model topography is shown relative to global sea level. (e–h) 3D view of the geodynamic model shows uplift in pink and subsidence as yellow overlain by strain rate in black. Arrows represent the magnitude and direction of surface velocities. The outlines of the crustal layers are shown in white. (m–p) and (u–x) show cross sections at the initial stepovers which are marked in black in the geodynamic boxes in the upper part of the figure. The stress regime categories are based on the World Stress Map project following Zoback, 1992: NF normal faulting regime, NS transtensional, blue SS strike-slip with less oblique strain axes and therefore unambiguous orientation of the maximum horizontal stress, purple SS strike-slip with more oblique strain axes, TS transpressional, TF thrust faulting. Strong intensities of the stress regime colours coincide with regions of high strain rate. Light areas behave in a brittle manner, while ductile deformation prevails in darker areas. Arrows depict the direction of relative motion of the different blocks, analogous to geological cross sections. The white dotted lines show the current location of the initially horizontal layer of particles at 8–10 km depth. (i–l) and (q–t) depict the surface velocity components at the cross sections with black being fault-parallel motion v_{II}, red fault-perpendicular motion $v_{\perp}$, and blue the vertical motion v_v. See Supplementary Material for a full animation of the reference model.

4.3 Results

4.3.1 Model evolution

In this section, we describe the evolution of our reference model (Fig. 4.3, also see animation at `https://zenodo.org/doi/10.5281/zenodo.10405076` with explanations in the Supplementary Material). We find that the fault network evolution can be divided into four phases:

Phase I - Localization determines deformation geometry. Deformation in the model is distributed until the main faults localize at ∼2 Myr model time (Fig. 4.3e). Already at this early stage a significant difference exists between the ratios and dimensions of the geological structures at the two main stepovers. These differences develop even though the initial weakening, length, and spacing, of the fault at the left- and right-lateral stepovers are identical. At the releasing bend, the two transform segments connect through a straight and narrow deformation zone (Fig. 4.3e,q,u). Contrary, the fault tips at the restraining bend maintain an east-west distance of ∼25 km and accommodate diffuse deformation (Fig. 4.3e,i,m).

Phase II - Strong vertical motion. In the basin area, phase II starts at ∼5 Myr through the formation of an isolated crustal block that exhibits rapid subsidence (Fig. 4.3f,r). This process coincides with the strain rate induced connection of the brittle parts of the lower crust and lithospheric mantle (Fig. 4.3v). Basin floor subsidence continues until the end of the simulation with a rate of ∼0.6 mm/yr and creates accommodation space for ∼10 km of sediments. At the surface, a morphology similar to an asymmetric rift appears, where geological units are horizontal alongside the steep and highly active western fault. Simultaneously, the surface along the eastern fault is bent towards the topographical depression (Fig. 4.3a–b,u–v). The two faults bounding the mountainous area at the restraining bend develop horse-tail splays that then connect through a strike-slip fault, crosscutting the high elevations. This fault competes with the border faults and gradually takes up more strike-slip deformation, while the earlier faults begin to show reverse faulting components (Fig. 4.3j–l,n–p). The resulting strain partitioning remains until the end of the simulation. Time-wise, the formation of the new central fault is closely followed by the reaching of the absolute maximum mountain height. Afterwards, elevations decrease since the fault trace becomes less edgy, which reduces compressive stresses and crustal shortening. Note however, that there is vertical movement at the restraining bend at all times (Fig. 4.3j–l, v_v), but after phase II uplift is exceeded by erosion.

Phase III - Fault system reorganization. The third phase constitutes a gradual transition from phase II to phase IV and is exemplary shown at 15 Myr in Fig. 4.3. While in phase II, strike-slip displacement at the restraining bend is distributed over several faults (Fig. 4.3j), it becomes increasingly concentrated on the central fault later on (Fig. 4.3k–l,n–p), intensifying strain partitioning as the outer faults increasingly deform in a reverse faulting regime. Simultaneously, the viscous domain between the brittle parts of the upper and lower crust gradually vanishes. Eventually, a downward propagation of the central fault connects the brittle crustal layers through an interplay of lower crustal advection and strain rate driven changes in upper crustal rheological behaviour (Fig. 4.3o–p). In the mean time, at the releasing bend, several secondary faults form at the southern and northern ends of the basin. The strike-slip motion is partitioned between those faults, although the main displacement remains focused along the central fault (Fig. 4.3s, v_{II}). The basin floor subsequently splits into several blocks that form terraced basin sidewalls and subbasins with differential sediment accumulation.

Phase IV - Central faults dominate the long-term fault network. By the end of the model run at 20 Myr, the main strike-slip displacement is concentrated on the central faults for both stepovers. In the mountains, the outer faults mainly act in a reverse faulting regime (Fig. 4.3l,p (TF regime)) and the fault system undergoes simplification compared to pahse II (Fig. 4.3f,n vs. h,p). Contrarily, in the basin the fault network becomes more complex over model evolution (Fig. 4.3f,v vs. h,x). The outer faults show elements of normal and strike-slip faulting but accommodate minor displacement compared to the central fault (Fig. 4.3t,x). To examine the fault network's long-term stability, the simulation was prolonged till 40 Myr. The results indicate that the network established during phase IV at 20 Myr remains stable.

4.3.2 Comparison to the Dead Sea area

The model reproduces first-order evolution of the Dead Sea Fault and Basin. The DSF is thought to have formed over 3–4 Myr, likely between 18–14 Ma (Marco, 2007; Oren et al., 2020). Similarly, fault localization in the model postdates the onset of strike-slip movement by ∼2 Myr (phase I in Fig. 4.3). As in the model, the topographic depression presumably formed prior to the pull-apart basin and is wider than the spacing of the main border faults (Garfunkel et al., 1996), which surround the thickest part of the sedimentary succession (Brink et al., 1989; Garfunkel et al., 1996; Ben-Avraham et al., 2008). Basin subsidence is reported to have started at ∼16–15 Ma (Garfunkel et al., 1996; Calvo et al., 2001) (seen at 5 Myr model time, phase II in Fig. 4.3) and was enabled by the formation of an isolated crustal block (Ben-Avraham et al., 2006). The sedimentary record shows that the oldest sediments in the DSB came from the E–SE (Jordan/Saudi-Arabia), indicating that the elevated shoulders of the present-day DSB morphology formed later, presumably around 6–5 Ma when basin subsidence accelerated as well (Garfunkel, 1981; Calvo et al., 2001; Zilberman et al., 2013). Today's sediment flux into the DSB derives from various sources. Sediments are transported along-strike by the rivers of the Jordan and Arava valleys, but the main part comes with rivers and creeks from the Jordanian and Judea shoulders of the DSB (Steinitz et al., 1992). Similarly, our model shows several sediment sources with material from along-strike directions constituting only ∼30% of the sediment input.

The model captures first-order present-day structure and kinematics of the Dead Sea Fault system. Strike-slip motion at the Lebanese restraining bend is concentrated on the central Yammouneh and adjacent faults, while reverse faulting is reported for faults outlining the mountain area (e.g. Gomez et al., 2007; Elias et al., 2007; Nemer et al., 2020). This results in the same regional strain partitioning between strike-slip and reverse faults that we see in our model results (Fig. 4.3l,p), and that was also observed at other restraining bends (e.g. Jamaica; Wiggins-Grandison et al., 2005; Mann et al., 2007). The main fault pattern along the Dead Sea consists of two subparallel strike-slip to transtensional border faults along an elongated central block (e.g. Gomez et al., 2007; Elias et al., 2007; Smit et al., 2008; Nemer et al., 2020) (Fig. 4.4a). In the model results, broad-scale normal faulting is only observed in evolutionary phases I and II (Fig. 4.3e–f) before the second basin bordering fault has localized and strike-slip motion prevails. This two-stage evolution is similar to what has been proposed for the releasing stepover at Lake Kinneret (Gasperini et al., 2020) (Fig. 4.4a). The observed predominantly strike-slip motion along today's DSB (Hamiel et al., 2019) is hence predicted by our models for its present-day evolutionary state. GPS measurements from the Dead Sea area also show local fault-perpendicular motion on the order of 10% of the full strike-slip velocity in the vicinity of the border faults (Le Beon et al., 2008; Hamiel et al., 2009). Similarly, in our models, the fault-perpendicular velocity $v_\perp$ component in Fig. 4.3t amounts to ∼5% and the vertical velocity v_v to ∼15% of the prescribed fault-parallel velocity v_{II} of 5 mm/yr. These local displacements cause basin floor subsidence and result from the misalignment of the NNW-SSE-trending main fault trace with the N-S-trending far-field stresses.

Observed seismicity reaches 30 km depth with a maximum at 20–22 km beneath most of the DSB (Aldersons et al., 2003). In our simulations, this depth corresponds to a peak in the energy dissipation rate that occurs within the connected brittle parts of the lower crust and lithospheric mantle (Supplementary Material Fig. B.S4). The energy dissipation rate in model areas with brittle deformation can be used as the equivalent for seismic energy release, and therefore provide information on earthquakes over long time spans in geodynamic models (Petrunin et al., 2012).

Topography and structure of the DSB. Prominent topographical features of the DSB are the asymmetric slopes and the rift-like morphology (Quennell, 1959; Garfunkel, 1981; Ben-Avraham et al., 1992; DESERT Group et al., 2004). Observed topography and model topography generally agree well (Fig. 4.4a–b,d), especially around the releasing bend (blue lines in Fig. 4.4d). Our reference model does not only closely fit the width, height, and slopes of the basin bounding topography, but also matches the observed maximum sediment thickness of 8–12 km (Ten Brink et al., 1993; Garfunkel et al., 1996; Götze et al., 2007; Mohsen et al., 2011). Comparable to the actual DSB (Garfunkel et al., 1996; Ben-Avraham et al., 2006), the modeled pull-apart basin is divided into several subbasins. Additionally, our model results show asymmetry in the basin's basement topography (Fig. 4.4d) that is similar to the rift-like morphology of the DSB (Wdowinski et al., 1996; Lubberts et al., 2002) (Fig. 4.1b).

Present-day surface heat flow. Heat flow values of 27–40 mW/m^2 have been reported for the DSB (Ben-Avraham et al., 1978; Shalev et al., 2013; Schütz et al., 2014; Oryan et al., 2019; Oryan et al., 2021), which is unusually low for an active plate boundary. The low heat flow is corroborated by deep seismicity hinting at a brittle and comparably cold lower crust (Aldersons et al., 2003). However, taking accurate measurements of surface heat flow in the DSB environment is challenging (Oryan et al., 2019) and observational uncertainties range between ±2.5 and 14 mW/m^2, or possibly even more (Schütz et al., 2014; Oryan et al., 2019; Oryan et al., 2021).

In agreement with observations (Shalev et al., 2013), heat flow in the modeled pull-apart basin (Fig. 4.4c) is considerably lower than the ~60 mW/m^2 seen in the surrounding, undeformed, areas. This low heat flow area is closely confined by the basin bordering faults and thereby constrained to areas with a thick sediment cover. This distribution illustrates the major impact of fast sedimentation rates (e.g Wijk et al., 2019), which outpace conductive equilibration of basin temperatures and radioactive heat production. While the absolute values of the modeled heat flow are always higher than the observation-based curve, their spatial variations along the center of the pull-apart basin (Fig. 4.4e) show many similarities, e.g. in how they follow the subbasin-structure in both cases (Shalev et al., 2013). The fit of absolute values increases when considering the uncertainty range of available data points (shown in red in Fig. 4.4e), and the remaining differences may be attributed to the generic character of our models.

South of 33°N, observations suggest a distinct peak in heat flow at Lake Kinneret (Fig. 4.4e) that is similarly seen in our model results. In both observations and predictions, this heat flow signal is tightly bounded by faults. However, while the signal at Lake Kinneret is underlain by a small stepover, within our simulations the high heat flow occurs at a transform fault segment. Previous studies have proposed that this heat flow is related to a crustal heat source from a paleo-thermal event at 5.3–3.5 Ma (Heimann et al., 1996; Reznik et al., 2021). Our models, however, can alternatively explain this feature via a dominant role of shear heating through strike-slip tectonics.

According to our simulations, heat flow at the restraining bend is expected to be locally variable, with values in the valleys reaching up to 120 mW/m^2 and lower values of 60–70 mW/m^2 on the ridges. When considering the entire mountain range, the average heat flow is 80–90 mW/m^2. The high heat flow variability can be explained by the above-average erosion rate in the valleys leading to rock exhumation from greater depths. In the absence of heat flow measurements at the Lebanon mountains, our reference model provides a first-order approximation of the heat flow and its pattern in that region.

4.3.3 Interaction between surface processes and tectonics

We isolate the influence of surface processes by varying the efficiency of the stream power law (Supplementary Material, eq. B.9) through the river incision rate, K_f, while all other parameters of the reference model remain unchanged (Fig. 4.5). For increased erosional efficiency (increased K_f), mountain heights decrease and the volume of the sediment infill within the pull-apart basin increases. This supports previous work on sediment infill of basins without drainage (Berry et al., 2019). At the restraining bend, topography and strain partitioning patterns show gradual changes connected to the value of K_f. At the releasing bend, however, we find a stark contrast between models without surface processes and those with erosional efficiency. This contrast is expressed in first-order changes to the basin shape and topography (Fig. 4.5q vs. r–t). The availability of sediments triggers a threshold behaviour for pull-apart basin evolution that we describe in the following paragraph.

Sediments control longevity of pull-apart basin. In the simulation without surface processes, the maximum basement depth never exceeds 4 km below sea level. In the presence of sediments, this value increases to ∼10 km (Fig. 4.5r,s,t), clearly showing how sediments create their own accommodation space (e.g. Bond et al., 1988) in this spatially restricted continental setting. By filling the basin, the sediments load the hanging walls of steeply dipping strike-slip faults and thereby induce a flexural fault rotation towards shallower dip angles (Fig. 4.5q–t). This process enhances the misalignment of the NNW-SSE-trending Dead Sea Fault with the N-S-trending far-field stresses, which leads to more pronounced local extension (Sec. 4.3.2) that is not related to far-field divergence. The pull-apart basins of the models including sedimentation do not stop evolving but new main faults continuously form towards the center. In the model without sedimentation (Fig. 4.5q), on the contrary, basin evolution stops around 15 Myr and strike-slip faults do not renew nor change geometry. At the surface they are in close vicinity and tend to dip away from the basin.

Erosion increases strain partitioning. At the restraining bend, mountain heights vary between 2 km for high surface process efficiency (K_f=$1 \cdot 10^{-5}$ $\mathrm{m}^{0.2}$/yr) and $>$ 6 km without surface processes (K_f=$1 \cdot 10^{-40}$ $\mathrm{m}^{0.2}$/yr) (Fig. 4.5a–d). Elevations hence vary substantially with K_f, while spatial variations and changes in the surface outline of the fault network are minor. However, the along-strike surface velocity reveals that the number of strike-slip faults decreases with increasing K_f (see the steps in the black lines of Fig. 4.5e–h). This is in agreement with previous studies that found decreasing fault network complexity but increasing fault longevity caused by surface processes (Olive et al., 2014; Neuharth et al., 2022).

The unloading of the hanging wall at strike-slip faults with a thrust component leads to faster exhumation (Willett, 1999). The tectonic stress regime in Fig. 4.5e–l therefore shows a positive correlation between K_f and the amount of reverse faulting and associated uplift below the mountains (see $v_\perp$ and v_v). Such a connection has been hypothesized for the uplift at the Jamaican restraining bend (Cochran et al., 2017) and for the amount of topographical elevation of restraining bends in general (Cowgill et al., 2004) and is corroborated by our models.

Crustal deformation pattern. Crustal deformation patterns depend on the stepover orientation, with crustal thinning occurring around the releasing bend and thickening around the restraining bend. Both processes are enhanced by increased efficiency of surface processes (Fig. 4.6 and Supplementary Table B.S3). In the following, we quantify their impact by comparing the reference model to the model without surface processes. At the restraining bend, 39% of thickening occurs due to tectonic processes, while erosion balances this value with ∼15% of thinning to a total crustal thickening of ∼24%. The basement beneath the pull-apart basin experiences 23% of thinning in the simulation without surface processes, with an additional ∼18% of thinning related to sedimentation. The crust in the reference model's releasing bend therefore experiences a total thinning of 41%. However, due to diffuse off-fault deformation (Herbert et al., 2014), crustal deformation is not confined to the pull-apart and mountain area, both in nature and models. We observe a crustal deformation pattern that resembles coupled non-channelized crustal flow (Royden, 1996) with horizontal velocities continuously increasing towards the surface for the entire lithosphere. Crustal flow described for many orogens is driven by gravitational potential energy and moves crustal material away from thickened crust and high elevations (e.g. Royden et al., 1997). A similar flow is thickening the crust adjacent to the restraining bend in our models (Fig. 4.6). Notably, we isolate a second direction of material flow which is seemingly opposed to gravitational potential energy. This flow component is generated by the sediment infill of the pull-apart basin which generates crustal motions that are directed away from the basin.This type of sedimentation-driven return flow has been previously described in highly sedimented rifted margins surrounding South-East Asian orogens (Morley et al., 2006; Clift, 2015). The speed of return flow was shown to anti-correlate with crustal viscosity (Clift et al., 2015). Due to the relatively high strength of our model crust, this velocity component has only a maximum speed of 0.02 mm/yr. Nevertheless, we find that it enhances vertical movement at the restraining bend.

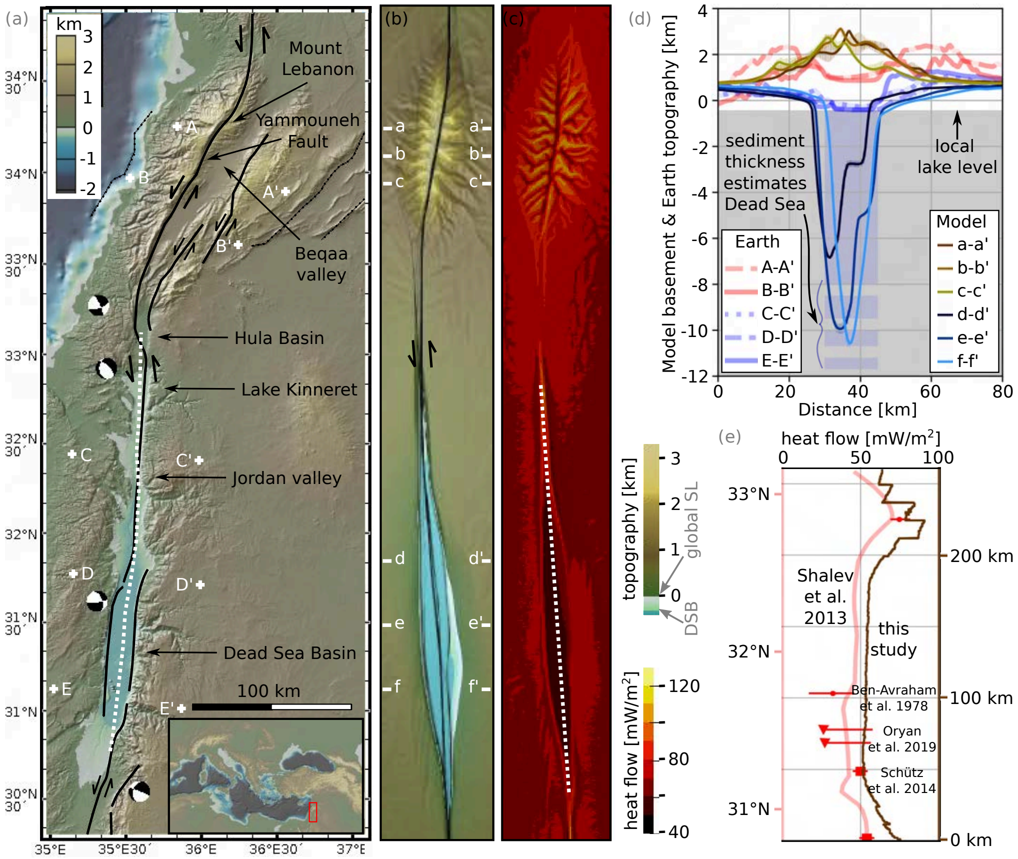

Figure 4.4: Comparison of the reference model results to observations from the Dead Sea Fault. (a) shows present day topography for the DSF area (`www.geomapapp.org`, Ryan et al., 2009). Fault traces (Styron, 2019) with an indication of the direction of motion are shown in black. Dotted black lines mark secondary faults (Elias et al., 2007). Earthquake focal mechanisms are taken from GeoMapApp (Ekström et al., 2012). (b) shows the topography of the reference model at the same scale and the same colour coding as a). Logarithmic strain rate is overlain in black and arrows depict the direction of fault motion. (c) shows the modelled surface heat flow. (d) shows profiles of model topography (lower-case letters and stronger colours) in direct comparison to topography profiles of the Dead Sea area (upper-case letters and transparent lines). The exact locations are shown in white in (a) and (b). The grey background marks the elevation of the local lake level and therewith gives an estimate of model sediment thickness. The transparent blue rectangle shows the range of published sediment thicknesses for the Dead Sea (8–12 km) (Götze et al., 2007; Mohsen et al., 2011) for comparison. (e) compares the model surface heat flow with a published heat flow profile for the DSB (Shalev et al., 2013). The locations of the profiles are shown as white dotted lines in (a) and (c). Values in red are heat flow measurements with uncertainty and correction ranges taken within the DSB: points (Ben-Avraham et al., 1978), triangles (Oryan et al., 2019), squares (Schütz et al., 2014). Their exact locations are shown in Fig. 4.1b.

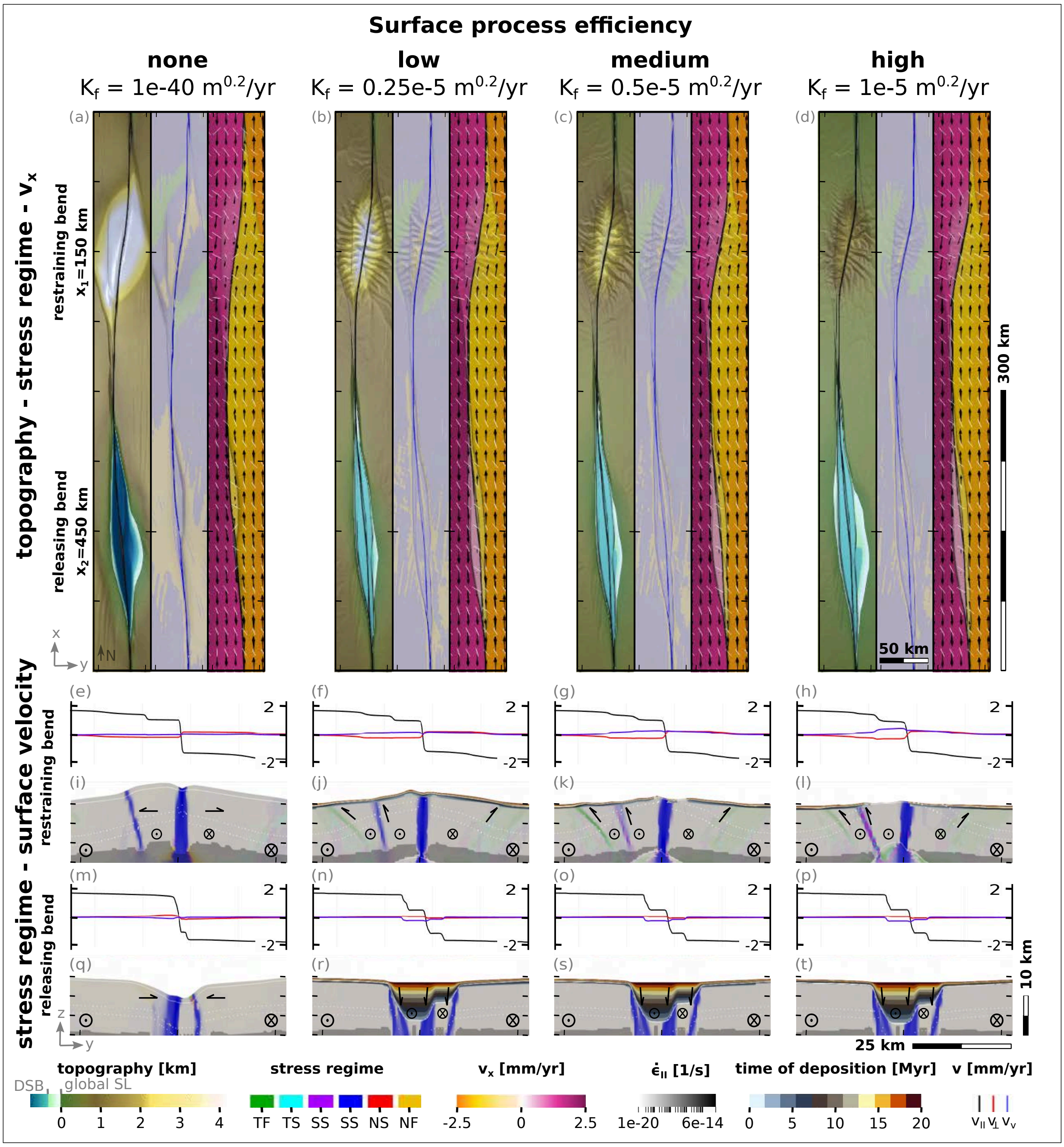

Figure 4.5: (a–d) show surface topography, stress regime and surface velocities (left to right) for the four different surface process efficiencies tested at 20 Myr model time. Note the two water tables with the global sea level and the local Dead Sea reference lake level as indicated in the legend. Topography and velocity are overlain by shaded logarithmic strain rate in black. The stress regime categories are based on the World Stress Map project following Zoback, 1992: NF normal faulting regime, NS transtensional, blue SS strike-slip with less oblique strain axes and therefore unambiguous orientation of the maximum horizontal stress, purple SS strike-slip with more oblique strain axes, TS transpressional, TF thrust faulting. Black arrows in the velocity plots show magnitude and direction of the full velocity while the x-component of velocity is also colour coded. (i–l) and (q-t) show cross sections of the stress regime at the locations of the initial stepovers with the restraining bend at $x_1 = 150$ km and the releasing bend at $x_2 = 450$ km. Strong intensities of the stress regime colours coincide with regions of high strain rate. Light areas behave in a brittle manner, while ductile deformation prevails in darker areas. Arrows depict relative motions of the different blocks analog to geological cross sections. The white dotted lines show the current location of the initially horizontal layer of particles as deformation markers. (e-h) and (m-p) depict the surface velocity components at the cross sections with black being fault-parallel motion v_{II}, red fault-perpendicular motion $v_\perp$, and blue the vertical motion v_v.

4.4 Discussion

A key controversy surrounding the DSB is whether or not far-field extension played a role in its creation. On one hand, plate kinematic studies inferred a change in Sinai's Euler pole ∼5 Ma (Garfunkel, 1981; Joffe et al., 1987; Reilinger et al., 2011), which added a small component of transverse extension at the southern sector of the DSF and a component of transverse contraction at the northern, Lebanese sector of the DSF. The timing corresponds to uplifting of the shoulders of the DSB (Chaldekas et al., 2021) and has also been used to explain the rift-like morphology of the basin (Quennell, 1959; Garfunkel, 1981; Ben-Avraham et al., 1992). On the other hand, regional GPS observations do not support a present-day component of far-field divergence across the fault (Le Beon et al., 2008; Hamiel et al., 2021). Our model shows that the velocity field near the releasing bend rotates, which creates a local component of east-west extension that varies between 5 and 10% of the relative plate motion (Fig. 4.3q-t) during the 20 Myr of model evolution. This effect is further enhanced by sedimentation (Sec. 4.3.3). To explicitly investigate the effect of far-field extension, we added 0.5 mm/yr of east-west divergence to our boundary conditions (i.e., 10% of the relative plate motion) during the last 5 Myr of the simulation. This results in a total extension of 2.5 km, a value used in previous studies of the DSF (Sobolev et al., 2005, and references therein). These boundary conditions result in a basin that is wider and longer than in the reference model (Supplementary Fig. B.S3). In addition, the restraining bend shows no reverse faulting and far too little elevation (<1 km). Because these model characteristics do not fit observations of the DSB, while the reference model without an extensional component does, we conclude that the asymmetric rift morphology of the DSB can form under pure strike-slip conditions. This finding is in agreement with previous 3D geodynamic models of the DSB (Petrunin et al., 2012) as well as with analog models of generic releasing bends (Smit et al., 2008) and the paired bend of the Marmara Sea and Ganos mountains (Bulkan et al., 2020). Our model basins, however, lacks uplifted shoulders (blue lines in Fig. 4.4d) that have been linked to compression near the fault tips (Wijk et al., 2017), a process that is yet also present in our models. We attribute this discrepancy either to elastic processes that are known to alter topography (Olive et al., 2016) or to events in the thermal evolution (Petrunin et al., 2012), both of which we do not include.

We further find that sedimentation prolongs tectonic activity of the pull-apart basin. Sediment loading creates a pressure that drives isostatic subsidence and balances horizontal gravitational potential energy gradients. This leads to both bordering faults remaining active (Zwaan et al., 2018) and facilitates local extension (Neuharth et al., 2021b). This finding changes the view on the longevity of pull-apart basins. While some studies suggested that the lifetime and growth of both narrow and wider pull-apart basins are limited by the development of a basin crossing fault (Wu et al., 2009; Sugan, 2014; Wijk et al., 2017), we see no sign of ceasing growth when running our setup to 40 Myr. Instead, continued sedimentation enables the basin to grow in length and depth while active faults are continuously being replaced by pairs of younger, more central faults. This leads to the formation of elongated terraces (e.g. Dooley et al., 1997; Wu et al., 2009) and a subbasin structure. Continuous fault replacement had been hypothesised by previous studies using prescribed faults (Wijk et al., 2017) and can now be confirmed by our models due to their ability to spontaneously form faults during the model evolution. Conversely, the evolution of the pull-apart basin in our model without surface processes stagnates at ∼15 Myr. We therefore conclude that the increasing sediment load plays a major role for the longevity of pull-apart basins, which has previously mainly been linked to the basin geometry (Wijk et al., 2017). Notably, only 30% of the model sediment infill arrives along-strike from the restraining bend, while the remaining 70% are derived from the areas bordering the basin. This makes our results also applicable to pull-apart basins without a restraining bend nearby.

Considering that the geometry of the crustal perturbations inducing the restraining and releasing bend is the same, we find a striking difference between the shapes of the pull-apart basin and the push-up mountain. The mountain fault system outline is ellipsoidal with a length-to-width ratio of ∼2, while this ratio for the basin border faults is ∼8 (Fig. 4.3h). The shape results from the favorable orientation of the local stress field. The NNW-SSE oriented strike-slip faults that accommodate the left-lateral stepover at the releasing bend coincide with the overall NNW-SSE directed maximum horizontal stress (Fig. 4.5), and therefore localize during the first phase of model evolution. The SSW-NNE directed faults of the restraining bend are, however, less favorably oriented so that it takes more time for a segment-connecting fault to develop. Examples for these characteristic shapes can be found in natural paired bends like the DSF system (Smit et al., 2008; Nemer et al., 2020), but also at the Hendrix pull-apart basin with the Jamaican restraining bend (Mann et al., 2007).

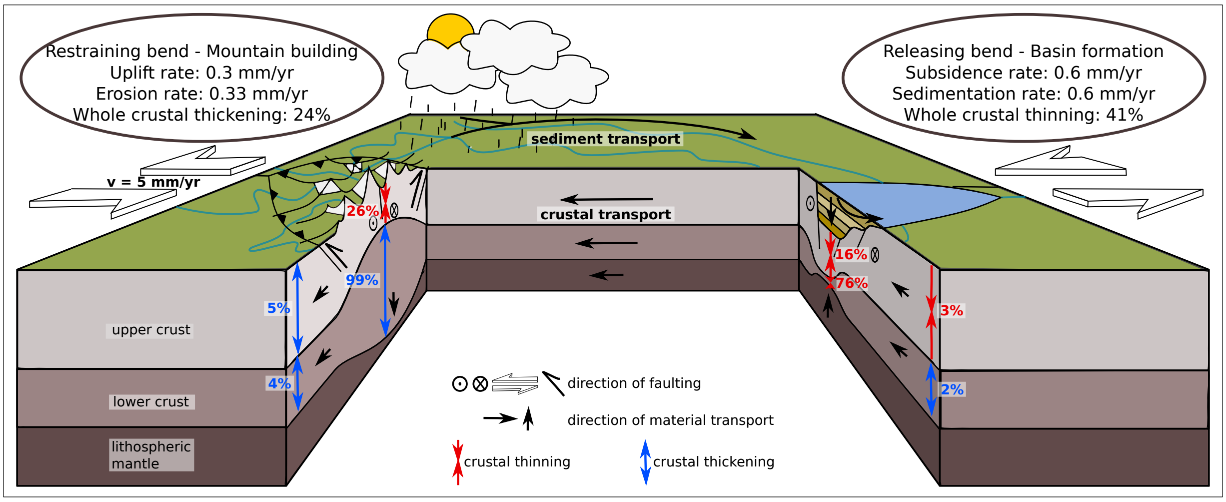

Figure 4.6: A summary sketch of the model results depicting the material transport between the releasing and restraining stepover with black arrows and the pattern of crustal thinning and thickening with red and blue arrows, respectively. The length of the arrows is not to scale. The values for velocities and changes in crustal thickness are computed from the reference model at 20 Myr. At the releasing bend on the right, higher surface process efficiency increases the basin growth and crustal thinning. At the restraining bend, crustal thickening is counteracted by erosion, which thins the upper crust. Most of the crustal thinning and thickening effects increase with increasing surface process efficiency, except for whole crustal thickening at the restraining bend and upper crustal thickening in the surrounding of the restraining bend due to enhanced erosion. Model sediments are transported from the higher elevations at and around the restraining bend towards the releasing bend where they are responsible for continued basin growth and subsidence. Basin growth fuels crustal transport in the direction of the restraining bend, which enhances uplift rates and strain partitioning. The changes in crustal thickness over 20 Myr are summarized in the Supplementary Material in Table B.S3 for models with different surface process efficiencies.

4.5 Conclusions

Despite their generic nature, our 3D models of a restraining and a releasing bend match a multitude of observables from the Dead Sea Fault System. The asymmetric basement and the unusually thick sediment infill of the DSB have been linked to a variety of processes. We show that both features can emerge under purely strike-slip boundary conditions and are a direct consequence of the localization processes. We further find that the very deep and narrow basin is a result of sediment loading within the basin. Observed surface heat flow values for the DSB area are ~50 mW/m^2 and show a particular pattern along the fault that is reproduced by our simulations. In the Lebanon Mountains, where observational heat flow data is sparse, the models predict higher heat flows.

In a more general way, our models demonstrate how erosion and sedimentation are key factors for the longevity and size of pull-apart basins in an active tectonic environment. Furthermore, we quantify the impact of surface processes on the crustal thinning and thickening pattern seen at the releasing and the restraining bend, respectively (Fig. 4.6). The model results reveal that the two fault bends are linked by along-strike material transport at a crustal level, which intensifies with surface process efficiency. This transport is driven by gravitational potential energy in conjunction with sediment deposition. At the restraining bend, this manifests as enhanced strain partitioning because of continued and accelerated vertical movement.

Acknowledgments

The work was supported by the North-German Supercomputing Alliance (HLRN). We thank the Computational Infrastructure for Geodynamics (geodynamics.org) which is funded by the National Science Foundation under award EAR-0949446 and EAR-1550901 for supporting the development of ASPECT. ELH is grateful for financial support from the Geo.X Young Academy. SVS was supported by the grant from the European Research Council (ERC) (Synergy Grant MEET, grant agreement no.856555).

Author contributions

Modeling, writing and visualization was mainly conducted by ELH in close cooperation with SB and ACG and guidance by SVS. Software development and model setup has been performed by ELH and DN. Regional geology of the DSF was contributed by RG and YH.

Data availability

Software and input files: `https://zenodo.org/doi/10.5281/zenodo.10405076`

References

Aldersons, F., Z. Ben-Avraham, A. Hofstetter, E. Kissling, and T. Al-Yazjeen (2003). “Lower-crustal strength under the Dead Sea basin from local earthquake data and rheological modeling”. en. In: *Earth and Planetary Science Letters* 214.1, pp. 129–142.

Ben-Avraham, Zvi, Zvi Garfunkel, and Michael Lazar (2008). “Geology and Evolution of the Southern Dead Sea Fault with Emphasis on Subsurface Structure”. en. In: *Annual Review of Earth and Planetary Sciences* 36.1, pp. 357–387.

Ben-Avraham, Zvi, Ralph Hänel, and Heinrich Villinger (1978). “Heat flow through the Dead Sea rift”. en. In: *Marine Geology* 28.3, pp. 253–269.

Ben-Avraham, Zvi, Vladimir Lyakhovsky, and Gerald Schubert (2010). “Drop-down formation of deep basins along the Dead Sea and other strike-slip fault systems”. In: *Geophysical Journal International* 181.1, pp. 185–197.

Ben-Avraham, Zvi and Gerald Schubert (2006). “Deep “drop down” basin in the southern Dead Sea”. en. In: *Earth and Planetary Science Letters* 251.3, pp. 254–263.

Ben-Avraham, Zvi and Mark D. Zoback (1992). “Transform-normal extension and asymmetric basins: An alternative to pull-apart models”. In: *Geology* 20.5, pp. 423–426.

Berry, M., J. van Wijk, D. Cadol, E. Emry, and D. Garcia-Castellanos (2019). “Endorheic-Exorheic Transitions of the Rio Grande and East African Rifts”. In: *Geochemistry, Geophysics, Geosystems* 20.7, pp. 3705–3729.

Bond, Gerard C. and Michelle A. Kominz (Dec. 1, 1988). “Evolution of thought on passive continental margins from the origin of geosynclinal theory (≈1860) to the present”. In: *GSA Bulletin* 100.12, pp. 1909–1933.

Braun, Jean and Sean D. Willett (2013). “A very efficient O(n), implicit and parallel method to solve the stream power equation governing fluvial incision and landscape evolution”. en. In: *Geomorphology* 180-181, pp. 170–179.

Brink, Uri S. ten and Zvi Ben-Avraham (1989). “The anatomy of a pull-apart basin: Seismic reflection observations of the Dead Sea Basin”. en. In: *Tectonics* 8.2, pp. 333–350.

Bulkan, Sibel, Pierre Henry, Paola Vannucchi, Fabrizio Storti, Cristian Cavozzi, and Jason P Morgan (2020). *The evolution of restraining and releasing bend pairs: analogue modelling investigation and application to the Sea of Marmara*. en. preprint.

Calvo, Rani and Josef Bartov (2001). “Hazeva Group, southern Israel: New observations, and their implications for its stratigraphy, paleogeography, and tectono-sedimentary regime.” In: 50.2-4, pp. 71–99.

Chaldekas, O., A. Vaks, I. Haviv, A. Gerdes, and R. Albert (Oct. 4, 2021). “U-Pb speleothem geochronology reveals a major 6 Ma uplift phase along the western margin of Dead Sea Transform”. In: *GSA Bulletin* 134.5, pp. 1571–1584.

Clift, Peter D. (Nov. 14, 2015). “Coupled onshore erosion and offshore sediment loading as causes of lower crust flow on the margins of South China Sea”. In: *Geoscience Letters* 2.1, p. 13.

Clift, Peter D., Sascha Brune, and Javier Quinteros (June 15, 2015). “Climate changes control offshore crustal structure at South China Sea continental margin”. In: *Earth and Planetary Science Letters* 420, pp. 66–72.

Cochran, William J., James A. Spotila, Philip S. Prince, and Ryan J. McAleer (2017). “Rapid exhumation of Cretaceous arc-rocks along the Blue Mountains restraining bend of the Enriquillo-Plantain Garden fault, Jamaica, using thermochronometry from multiple closure systems”. en. In: *Tectonophysics* 721, pp. 292–309.

Cowgill, Eric, An Yin, J Ramón Arrowsmith, Wang Xiao Feng, and Zhang Shuanhong (2004). "The Akato Tagh bend along the Altyn Tagh fault, northwest Tibet 1: Smoothing by vertical-axis rotation and the effect of topographic stresses on bend-flanking faults". In: *GSA Bulletin* 116.11-12, pp. 1423–1442.

Crowell, John C. (1974). "Origin of Late Cenozoic Basins in Southern California (Abstract-AAPG Bulletin, 1973, p. 774; article-SEPM Special Publication No. 22, 194, p. 190-204)". en-US. In: pp. 190–204.

Dembo, Neta, Roi Granot, and Yariv Hamiel (2021). "Mechanical contrast and asymmetric distribution of crustal deformation across plate boundaries: Insights from the northern Dead Sea fault system". In: *Geology* 49.5, pp. 498–503.

DESERT Group, M. Weber, K. Abu-Ayyash, A. Abueladas, A. Agnon, H. Al-Amoush, A. Babeyko, Y. Bartov, M. Baumann, Z. Ben-Avraham, G. Bock, J. Bribach, R. El-Kelani, A. Förster, H.-J. Förster, U. Frieslander, Z. Garfunkel, S. Grunewald, H. J. Götze, V. Haak, Ch. Haberland, M. Hassouneh, S. Helwig, A. Hofstetter, K.-H. Jäckel, D. Kesten, R. Kind, N. Maercklin, J. Mechie, A. Mohsen, F. M. Neubauer, R. Oberhänsli, I. Qabbani, O. Ritter, G. Rümpker, M. Rybakov, T. Ryberg, F. Scherbaum, J. Schmidt, A. Schulze, S. Sobolev, M. Stiller, H. Thoss, U. Weckmann, and K. Wylegalla (2004). "The crustal structure of the Dead Sea Transform". In: *Geophysical Journal International* 156.3, pp. 655–681.

Dooley, Tim and Ken McClay (1997). "Analog Modeling of Pull-Apart Basins1". In: *AAPG Bulletin* 81.11, pp. 1804–1826.

Duarte, João C. (2019). "Preface". en. In: *Transform Plate Boundaries and Fracture Zones.* Ed. by João C. Duarte. Elsevier, pp. xi–xii.

Ekström, G., M. Nettles, and A. M. Dziewonski (2012). "The global CMT project 2004-2010: Centroid-moment tensors for 13,017 earthquakes". In: 200-201, pp. 1–9.

Elias, Ata, Paul Tapponnier, Satish C. Singh, Geoffrey C.P. King, Anne Briais, Mathieu Daëron, Helene Carton, Alexander Sursock, Eric Jacques, Rachid Jomaa, and Yann Klinger (2007). "Active thrusting offshore Mount Lebanon: Source of the tsunamigenic A.D. 551 Beirut-Tripoli earthquake". In: *Geology* 35.8, pp. 755–758.

Förster, H. -J., A. Förster, R. Oberhänsli, and D. Stromeyer (2010). "Lithospheric composition and thermal structure of the Arabian Shield in Jordan". en. In: *Tectonophysics.* Insights into the Earth's Deep Lithosphere 481.1, pp. 29–37.

Garfunkel, Zvi (1981). "Internal structure of the Dead Sea leaky transform (rift) in relation to plate kinematics". en. In: *Tectonophysics.* The Dead Sea Rift 80.1, pp. 81–108.

GARFUNKEL, Zvi and Zvi BEN-AVRAHAM (2001). "Basins along the Dead Sea Transform". In: *Basins along the Dead Sea Transform* 186, pp. 607–627.

Garfunkel, Zvi and Zvi Ben-Avraham (1996). "The structure of the Dead Sea basin". en. In: *Tectonophysics.* Dynamics of Extensional Basins and Inversion Tectonics 266.1, pp. 155–176.

Gasperini, Luca, Michael Lazar, Adriano Mazzini, Matteo Lupi, Antoine Haddad, Christian Hensen, Mark Schmidt, Antonio Caracausi, Marco Ligi, and Alina Polonia (2020). "Neotectonics of the Sea of Galilee (northeast Israel): implication for geodynamics and seismicity along the Dead Sea Fault system". en. In: *Scientific Reports* 10.1, p. 11932.

Gassmöller, Rene, Harsha Lokavarapu, Eric Heien, Elbridge Gerry Puckett, and Wolfgang Bangerth (2018). "Flexible and Scalable Particle-in-Cell Methods With Adaptive Mesh Refinement for Geodynamic Computations". en. In: *Geochemistry, Geophysics, Geosystems* 19.9, pp. 3596–3604.

Glerum, Anne, Cedric Thieulot, Menno Fraters, Constantijn Blom, and Wim Spakman (2018). "Nonlinear viscoplasticity in ASPECT: benchmarking and applications to subduction". English. In: *Solid Earth* 9.2, pp. 267–294.

Gomez, F., T. Nemer, C. Tabet, M. Khawlie, M. Meghraoui, and M. Barazangi (2007). "Strain partitioning of active transpression within the Lebanese restraining bend of the Dead Sea Fault (Lebanon and SW Syria)". en. In: *Geological Society, London, Special Publications* 290.1, pp. 285–303.

Goren, Liran, Sébastien Castelltort, and Yann Klinger (2015). "Modes and rates of horizontal deformation from rotated river basins: Application to the Dead Sea fault system in Lebanon". In: *Geology* 43.9, pp. 843–846.

Götze, H.-J., R. El-Kelani, S. Schmidt, M. Rybakov, M. Hassouneh, H.-J. Förster, and J. Ebbing (2007). "Integrated 3D density modelling and segmentation of the Dead Sea Transform". en. In: *International Journal of Earth Sciences* 96.2, pp. 289–302.

Hamiel, Y., R. Amit, Z. B. Begin, S. Marco, O. Katz, A. Salamon, E. Zilberman, and N. Porat (2009). “The Seismicity along the Dead Sea Fault during the Last 60,000 Years”. In: *Bulletin of the Seismological Society of America* 99.3, pp. 2020–2026.

Hamiel, Yariv and Oksana Piatibratova (2019). “Style and Distribution of Slip at the Margin of a Pull-Apart Structure: Geodetic Investigation of the Southern Dead Sea Basin”. en. In: *Journal of Geophysical Research: Solid Earth* 124.11, pp. 12023–12033.

— (2021). “Spatial Variations of Slip and Creep Rates Along the Southern and Central Dead Sea Fault and the Carmel–Gilboa Fault System”. en. In: *Journal of Geophysical Research: Solid Earth* 126.9, e2020JB021585.

Heimann, A, G Steinitz, D Mor, and G Shaliv (1996). “The Cover Basalt Formation, its age and its regional and tectonic setting: Implications from K-Ar and 40Ar/39Ar geochronology”. In: *Isr. J. Earth Sci* 45.5.

Heister, Timo, Juliane Dannberg, Rene Gassmöller, and Wolfgang Bangerth (2017). “High accuracy mantle convection simulation through modern numerical methods – II: realistic models and problems”. In: *Geophysical Journal International* 210.2, pp. 833–851.

Herbert, Justin W., Michele L. Cooke, Michael Oskin, and Ohilda Difo (2014). “How much can off-fault deformation contribute to the slip rate discrepancy within the eastern California shear zone?” In: *Geology* 42.1, pp. 71–75.

Joffe, Sam and Zvi Garfunkel (1987). “Plate kinematics of the circum Red Sea—a re-evaluation”. en. In: *Tectonophysics*. Sedimentary basins within the Dead Sea and other rift zones 141.1, pp. 5–22.

Kronbichler, M., T. Heister, and W. Bangerth (2012). “High Accuracy Mantle Convection Simulation through Modern Numerical Methods”. In: *Geophysical Journal International* 191, pp. 12–29.

Le Beon, Maryline, Yann Klinger, Abdel Qader Amrat, Amotz Agnon, Louis Dorbath, Gidon Baer, Jean-Claude Ruegg, Olivier Charade, and Omar Mayyas (2008). “Slip rate and locking depth from GPS profiles across the southern Dead Sea Transform”. en. In: *Journal of Geophysical Research: Solid Earth* 113.B11.

Lubberts, Ronald K and Zvi Ben-Avraham (2002). “Tectonic evolution of the Qumran Basin from high-resolution 3.5-kHz seismic profiles and its implication for the evolution of the northern Dead Sea Basin”. en. In: *Tectonophysics*. Tectonics of Sedimentary Basins: from Crustal Structure to Basin Fill 346.1, pp. 91–113.

Mann, P., C. Demets, and M. Wiggins-Grandison (2007). “Toward a better understanding of the Late Neogene strike-slip restraining bend in Jamaica: geodetic, geological, and seismic constraints”. In: *Geological Society, London, Special Publications* 290.1, pp. 239–253.

Mann, Paul (2007). “Global catalogue, classification and tectonic origins of restraining- and releasing bends on active and ancient strike-slip fault systems”. en. In: 290, pp. 13–142.

Marco, Shmuel (2007). “Temporal variation in the geometry of a strike–slip fault zone: Examples from the Dead Sea Transform”. In: *Tectonophysics* 445.3, pp. 186–199.

Mohsen, A., G. Asch, J. Mechie, R. Kind, R. Hofstetter, M. Weber, M. Stiller, and K. Abu-Ayyash (2011). “Crustal structure of the Dead Sea Basin (DSB) from a receiver function analysis”. In: *Geophysical Journal International* 184.1, pp. 463–476.

Morley, Christopher K. and Rob Westaway (2006). “Subsidence in the super-deep Pattani and Malay basins of Southeast Asia: a coupled model incorporating lower-crustal flow in response to post-rift sediment loading”. In: *Basin Research* 18.1, pp. 51–84.

Nemer, Tony S. and Mustapha Meghraoui (2020). “A non-active fault within an active restraining bend: The case of the Hasbaya fault, Lebanon”. en. In: *Journal of Structural Geology* 136, p. 104060.

Neuharth, Derek, Sascha Brune, Anne Glerum, Christian Heine, and J. Kim Welford (2021a). “Formation of Continental Microplates Through Rift Linkage: Numerical Modeling and Its Application to the Flemish Cap and Sao Paulo Plateau”. en. In: *Geochemistry, Geophysics, Geosystems* 22.4, e2020GC009615.

Neuharth, Derek, Sascha Brune, Anne Glerum, Chris K. Morley, Xiaoping Yuan, and Jean Braun (2021b). “Flexural strike-slip basins”. In: *Geology* 50.3, pp. 361–365.

Neuharth, Derek, Sascha Brune, Thilo Wrona, Anne Glerum, Jean Braun, and Xiaoping Yuan (2022). “Evolution of Rift Systems and Their Fault Networks in Response to Surface Processes”. en. In: *Tectonics* 41.3, e2021TC007166.

Norris, Richard J. and Virginia G. Toy (2014). “Continental transforms: A view from the Alpine Fault”. en. In: *Journal of Structural Geology*. Continental Transpressive Fault Zones 64, pp. 3–31.

Olive, Jean-Arthur, Mark D. Behn, and Luca C. Malatesta (2014). “Modes of extensional faulting controlled by surface processes”. en. In: *Geophysical Research Letters* 41.19, pp. 6725–6733.

Olive, Jean-Arthur, Mark D. Behn, Eric Mittelstaedt, Garrett Ito, and Benjamin Z. Klein (2016). “The role of elasticity in simulating long-term tectonic extension”. en. In: *Geophysical Journal International* 205.2, pp. 728–743.

Oren, Omer, Perach Nuriel, Andrew R. C. Kylander-Clark, and Itai Haviv (2020). “Evolution and Propagation of an Active Plate Boundary: U-Pb Ages of Fault-Related Calcite From the Dead Sea Transform”. en. In: *Tectonics* 39.8, e2019TC005888.

Oryan, B., H. Villinger, M. Lazar, M. J. Schwab, I. Neugebauer, and Z. Ben-Avraham (2019). “Heat flow in the Dead Sea from the ICDP boreholes and its implication for the structure of the basin”. en. In: *Quaternary Science Reviews* 210, pp. 103–112.

Oryan, Bar and Heather Savage (2021). “Regional Heat Flow Analysis Reveals Frictionally Weak Dead Sea Fault”. en. In: *Geochemistry, Geophysics, Geosystems* 22.12, e2021GC010115.

Petrunin, Alexey and Stephan V. Sobolev (2006). “What controls thickness of sediments and lithospheric deformation at a pull-apart basin?” en. In: *Geology* 34.5, p. 389.

Petrunin, Alexey G., Ernesto Meneses Rioseco, Stephan V. Sobolev, and Michael Weber (2012). “Thermomechanical model reconciles contradictory geophysical observations at the Dead Sea Basin”. en. In: *Geochemistry, Geophysics, Geosystems* 13.4.

Quennell, Albert Mathieson (1959). *Tectonics of the Dead Sea rift.* Vol. 385.

Reilinger, Robert and Simon McClusky (2011). “Nubia-Arabia-Eurasia plate motions and the dynamics of Mediterranean and Middle East tectonics: Mediterranean and Middle East geodynamics”. en. In: *Geophysical Journal International* 186.3, pp. 971–979.

Reznik, Itay J. and Yuval Bartov (2021). “Present Heat Flow and Paleo-Geothermal Anomalies in the Southern Golan Heights, Israel”. en. In: *Earth and Space Science* 8.3, e2020EA001299.

Richter, Maximilian J. E. A., Sascha Brune, Simon Riedl, Anne Glerum, Derek Neuharth, and Manfred R. Strecker (2021). “Controls on Asymmetric Rift Dynamics: Numerical Modeling of Strain Localization and Fault Evolution in the Kenya Rift”. en. In: *Tectonics* 40.5, e2020TC006553.

Rose, Ian, Bruce Buffett, and Timo Heister (2017). “Stability and accuracy of free surface time integration in viscous flows”. In: *Physics of the Earth and Planetary Interiors* 262, pp. 90–100.

Royden, Leigh (1996). “Coupling and decoupling of crust and mantle in convergent orogens: Implications for strain partitioning in the crust”. In: *Journal of Geophysical Research: Solid Earth* 101 (B8), pp. 17679–17705.

Royden, Leigh H., B. Clark Burchfiel, Robert W. King, Erchie Wang, Zhiliang Chen, Feng Shen, and Yuping Liu (May 2, 1997). “Surface Deformation and Lower Crustal Flow in Eastern Tibet”. In: *Science* 276.5313, pp. 788–790.

Ryan, William B. F., Suzanne M. Carbotte, Justin O. Coplan, Suzanne O’Hara, Andrew Melkonian, Robert Arko, Rose Anne Weissel, Vicki Ferrini, Andrew Goodwillie, Frank Nitsche, Juliet Bonczkowski, and Richard Zemsky (2009). “Global Multi-Resolution Topography synthesis”. en. In: *Geochemistry, Geophysics, Geosystems* 10.3.

Schütz, F., H. -J. Förster, and A. Förster (2014). “Thermal conditions of the central Sinai Microplate inferred from new surface heat-flow values and continuous borehole temperature logging in central and southern Israel”. en. In: *Journal of Geodynamics* 76, pp. 8–24.

Shalev, Eyal, Vladimir Lyakhovsky, Yishai Weinstein, and Zvi Ben-Avraham (2013). “The thermal structure of Israel and the Dead Sea Fault”. en. In: *Tectonophysics* 602, pp. 69–77.

Smit, J., J. -P. Brun, S. Cloetingh, and Z. Ben-Avraham (2010). “The rift-like structure and asymmetry of the Dead Sea Fault”. en. In: *Earth and Planetary Science Letters* 290.1, pp. 74–82.

— (2008). “Pull-apart basin formation and development in narrow transform zones with application to the Dead Sea Basin”. en. In: *Tectonics* 27.6.

Sobolev, S, A Petrunin, Z Garfunkel, and A Babeyko (2005). “Thermo-mechanical model of the Dead Sea Transform”. en. In: *Earth and Planetary Science Letters* 238.1-2, pp. 78–95.

Steinitz, Gideon and Bartov Yosef . (1992). “The Miocene-Pleistocene history of the Dead Sea segment of the Rift in light of K-Ar ages of basalts”. In: *Israel Journal of Earth-Sciences* 38.2-4, pp. 199–208.

Stock, Jonathan D. and David R. Montgomery (1999). “Geologic constraints on bedrock river incision using the stream power law”. en. In: *Journal of Geophysical Research: Solid Earth* 104.B3, pp. 4983–4993.

Styron, Richard (2019). *GEMScienceTools/gem-global-active-faults: First release of 2019.*

Sugan, Monica (2014). “3D Analogue Modelling of Transtensional Pull-apart Basins: comparison with the Cinarcik Basin, Sea of Marmara, Turkey”. en. In.

Ten Brink, U. S., Z. Ben-Avraham, R. E. Bell, M. Hassouneh, D. F. Coleman, G. Andreasen, G. Tibor, and B. Coakley (1993). "Structure of the Dead Sea pull-apart basin from gravity analyses". en. In: *Journal of Geophysical Research: Solid Earth* 98.B12, pp. 21877–21894.

Wdowinski, S. and Ezra Zilberman (1996). "Kinematic modelling of large-scale structural asymmetry across the Dead Sea Rift". en. In: *Tectonophysics*. Dynamics of Extensional Basins and Inversion Tectonics 266.1, pp. 187–201.

Wetzler, Nadav and Ittai Kurzon (2016). "The Earthquake Activity of Israel: Revisiting 30 Years of Local and Regional Seismic Records along the Dead Sea Transform". In: *Seismological Research Letters* 87.1, pp. 47–58.

Wiggins-Grandison, Margaret D. and Kuvvet Atakan (2005). "Seismotectonics of Jamaica". In: *Geophysical Journal International* 160.2, pp. 573–580.

Wijk, J. van, G. Axen, and R. Abera (2017). "Initiation, evolution and extinction of pull-apart basins: Implications for opening of the Gulf of California". en. In: *Tectonophysics*. From continental to oceanic rifting in the Gulf of California 719-720, pp. 37–50.

Wijk, Jolante W. van, Samuel P. Heyman, Gary J. Axen, and Patricia Persaud (Aug. 14, 2019). "Nature of the crust in the northern Gulf of California and Salton Trough". In: *Geosphere* 15.5, pp. 1598–1616.

Willett, Sean D. (1999). "Orogeny and orography: The effects of erosion on the structure of mountain belts". In: *Journal of Geophysical Research: Solid Earth* 104 (B12), pp. 28957–28981.

Wolf, Sebastian G., Ritske S. Huismans, Josep-Anton Muñoz, Magdalena Ellis Curry, and Peter van der Beek (2021). "Growth of Collisional Orogens From Small and Cold to Large and Hot—Inferences From Geodynamic Models". In: *Journal of Geophysical Research: Solid Earth* 126.2, e2020JB021168.

Wu, Jonathan E., Ken McClay, Paul Whitehouse, and Tim Dooley (2009). "4D analogue modelling of transtensional pull-apart basins". en. In: *Marine and Petroleum Geology* 26.8, pp. 1608–1623.

Yuan, X. P., J. Braun, L. Guerit, B. Simon, B. Bovy, D. Rouby, C. Robin, and R. Jiao (2019). "Linking continental erosion to marine sediment transport and deposition: A new implicit and O(N) method for inverse analysis". en. In: *Earth and Planetary Science Letters* 524, p. 115728.

Zilberman, Ezra and Ran Calvo (2013). "Remnants of Miocene fluvial sediments in the Negev Desert, Israel, and the Jordanian Plateau: Evidence for an extensive subsiding basin in the northwestern margins of the Arabian plate". en. In: *Journal of African Earth Sciences* 82, pp. 33–53.

Zoback, Mary Lou (1992). "First- and second-order patterns of stress in the lithosphere: The World Stress Map Project". en. In: *Journal of Geophysical Research: Solid Earth* 97.B8, pp. 11703–11728.

Zwaan, Frank, Guido Schreurs, and Jürgen Adam (2018). "Effects of sedimentation on rift segment evolution and rift interaction in orthogonal and oblique extensional settings: Insights from analogue models analysed with 4D X-ray computed tomography and digital volume correlation techniques". en. In: *Global and Planetary Change*. From the deep Earth to the surface 171, pp. 110–133.

5 Preparing ASPECT for the Modeling of the Seismic Cycle of Great Earthquakes Using Rate-and-State Friction

5.1 Introduction

Giant earthquakes of magnitude 8.5 are rare events but have an immense destructive potential. This is a threat for human lives and infrastructure. It is relatively well understood that these earthquakes take place along sections of subducting plate interfaces with specific properties including a shallow slope and a thick sediment filling in the trench (Muldashev et al., 2020) (Fig. 5.1). Additionally, statistical, historical, and paleo-seismological methods can help to determine the probability for an event to happen in a certain time frame (e.g. Ishibashi, 2004; Sykes et al., 2006; Kagan et al., 2010; Nováková, 2016; Villegas-Lanza et al., 2016; Scholz, 2019, and references therein). This knowledge helps to increase the resilience of a society, e.g. by building policies that improve shake resistance for buildings (e.g. Joyner et al., 2020). Furthermore, rapid alert systems via cellphones, television or loudspeaker have succesfully been installed in many places to allow people to reach a safe spot before the ground starts to shake (e.g. Wu et al., 2016; Rahman et al., 2016; Suárez et al., 2021). The exact temporal forecasting of an event remains, nonetheless, unpredictable to date. We are thus lacking the basis of an early warning system suitable for alerts days, months, or a couple of years before an earthquake which would, however, be highly valuable to societies around the globe.

One reason for this missing time scale in the warning system is a lack of detailed observational data of the preseismic period. Only very few giant earthquakes have been recorded with modern instruments, including the 2011 M9.0 Tohoku (Duputel et al., 2012), the 2010 M8.8 Maule (Duputel et al., 2012), the 2004 M9.2 Sumatra (Duputel et al., 2012), the 1964 M9.2 Great Alaska (Kanamori et al., 1975), and the 1960 M9.5 Valdivia earthquakes (Kanamori et al., 1975). This sample size is very small in several aspects. 1) The trustworthiness of statistical analysis increases with the sample size. 2) None of the observed events can be compared well against each other as the locations differ in all sorts of properties. 3) Many locations on Earth where giant earthquakes could potentially occur experience a complete lack of precise instrumental data so far (e.g. Muldashev et al., 2020). Clearly, a prerequisite for a meaningful attempt to understand the preseismic period would be the existence of precise observational data from many earthquakes that all occured along the same fault section. This means that we need observations covering a multitude of seismic cycles at each subduction zone that is prone to host giant earthquakes. As only one complete cycle has been observed so far (Parkfield, California - Murray et al. (2006)) it is clear that this kind of data does not exist such that other ways to understand the crucial preseismic phase need to be explored.

One option is the geodynamic modeling where arbitrarily many seismic cycles can be modeled for any single location to overcome this lack of data, however, in a simplified model setup. This allows the use of statistical tools for the processes accompanying giant earthquakes, as well as the understanding of the prerequisites for such an event to happen (Lapusta et al., 2000; Lapusta et al., 2009; Kaneko et al., 2011; Barbot et al., 2012; Dinther et al., 2014; Herrendörfer et al., 2015; Jiang et al., 2016; Lambert et al., 2016; Pipping et al., 2016; Sobolev et al., 2017; Erickson et al., 2017; Barbot, 2018; Tong et al., 2018; Herrendörfer et al., 2018; Duan et al., 2019; Barbot, 2019; Dinther et al., 2019; Preuss et al., 2019; Muldashev et al., 2020; Erickson et al., 2020; Zelst, 2020). As the modeling of seismic cycles is computationally costly and requires good temporal and spatial resolution over many orders of magnitudes there are only a few modeling softwares that can handle this kind of problem. The desired features for the perfectly suitable software would be adaptive mesh refinement, adaptive time stepping, 2D and 3D computations, rate-and-state friction (RSF), inertia or at least radiation damping, free choice of the number of materials with different properties, free choice of fault location or better inherently selflocalizing faults, off-fault deformation, visco-elastic-plastic deformation, parallel computation on high performance clusters (e.g. Barbot et al., 2010; Kaneko et al., 2011; Barbot et al., 2012; Dinther et al., 2014; Jiang et al., 2016; Lambert et al., 2016; Pipping et al., 2016; Sobolev et al., 2017; Erickson et al., 2017; Tong et al., 2018; Herrendörfer et al., 2018; Barbot, 2019; Preuss et al., 2019; Duan et al., 2019; Zelst, 2020; Erickson et al., 2020).

The geodynamic open-source software ASPECT, the Advanced Solver for Planetary Evolution, Convection, and Tectonics, already combined many of these prerequisites prior to this project

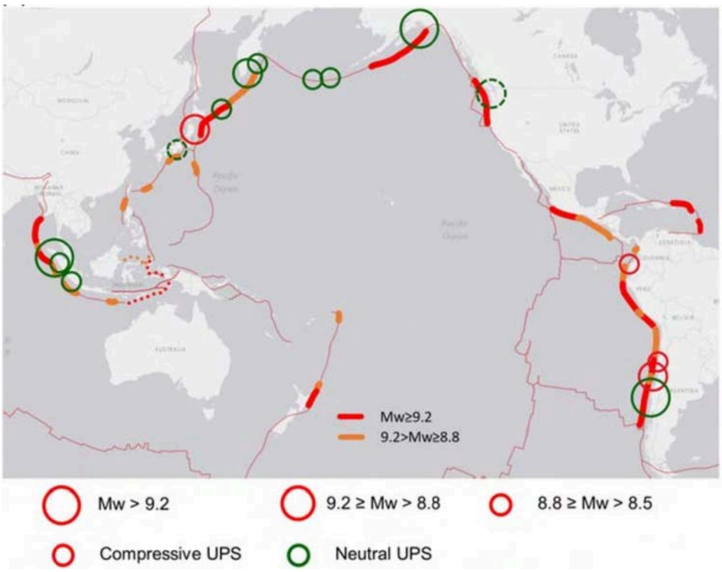

Figure 5.1: Locations of subduction zones and their predicted earthquake potential based on sea floor roughness and dipping angle as published in Muldashev et al. (2020), Fig. 8b. Thick orange lines mark zones where the predicted maximum events magnitudes (Mw) ranges between 8.8–9.2, while thick red lines predict Mw of more than 9.2. Dotted lines mark less reliable predictions because of a lack of data on seafloor roughness. Circles show the location of Mw ≥ 8.5 subduction interface earthquakes, where the size scales with magnitude and the color denotes upper plate strain regime (UPS)

(Kronbichler et al., 2012; Heister et al., 2017; Rose et al., 2017; Gassmöller et al., 2018; Fraters et al., 2019; Bangerth et al., 2021a; Bangerth et al., 2021b). For my thesis, I introduced rate-and-state friction into the visco-elastic-plastic material model along with many postprocessing options accompanied by further code improvement and testing outside of the friction rheology. However, as stated in the Introductory Explanations, a final testing of the rate-and-state friction rheology has not been performed yet.

In the following, I will briefly introduce the processes during one seismic cycle at a subduction zone, the principles of yield criteria and rate-and-state friction, the mineralogical basis for the parametrization of the seismogenic window, and the relevant ASPECT modules and their structure together with the additions associated with this work. Lastly, I will present an examplary input file for a simple RSF model in ASPECT and summarize the state of the implementation.

5.1.1 The seismic cycle in subduction zones

The term 'seismic cycle' or 'earthquake cycle' underlines the important observation that earthquakes are not singular geological events but merely represent one element in a sequence of reoccuring slip events on one fault segment (see a compilation in chapter 5 of Scholz, 2019, and the references therein). One cycle includes the timespan and the processes that happen between one earthquake and its successor. Though it has been found that seismic cycles for a specific earthquake site can have roughly similar recurrence times (e.g. see Figure 5.2), it should be noted that no perfect periodicity can be expected neither in length nor for the accompanying processes nor the size of the event. The study of the seismic cycle e.g. through paleoseismic methods may nonetheless reveal insights about future earthquakes.

The underlying concept of one cycle is the elastic strain energy accumulation, also called loading, over a longer timespan followed by a sudden release of stress during a slip event (e.g Govers et al., 2018). The accumulation of geodetic data from many sites revealed that one cycle can further be divided into four (or more) different phases (e.g Lyakhovsky et al., 2001; Wang et al., 2012; Govers et al., 2018; Scholz, 2019) due to characteristic surface motion patterns (see Figure 5.3): (1) the coseismic, (2) the postseismic, (3) the interseismic, and (4) the preseismic phase. In the following, I briefly want to introduce the processes that have been observed and associated to these phases for large subduction zone earthquakes worldwide.

(1) The very short coseismic phase is characterized by the slipping of the fault's seismogenic part when the accumulated elastic strain is released. The sudden motion leads to the appearance of seismic waves

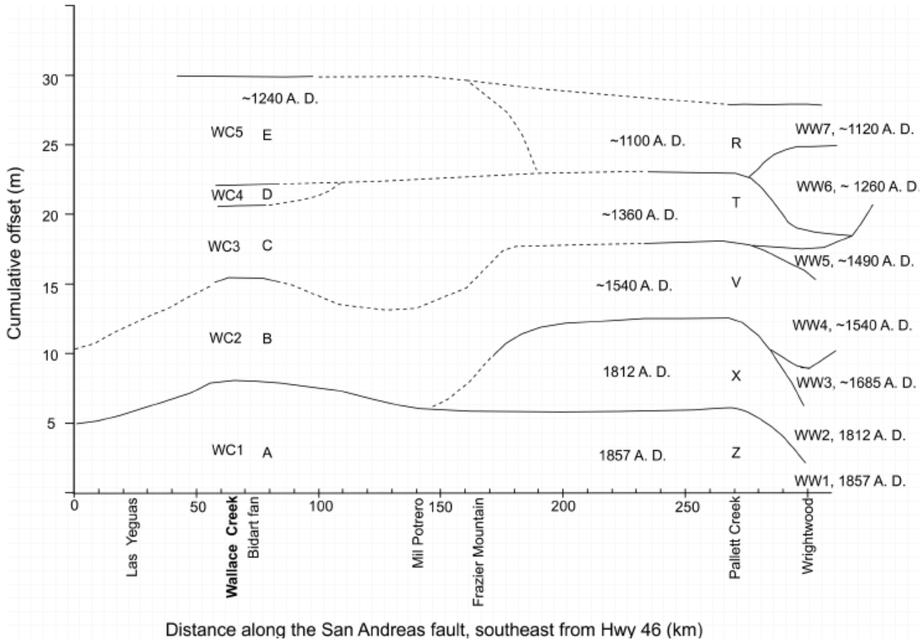

Figure 5.2: A compilation of the timing and slip of past earthquakes at Wallace Creek, Pallett Creek, and Wrightwood along the San Andreas Fault that reveal the cyclic nature of the events. Taken from (Liu-Zeng et al., 2006), Fig. 26.

which can be detected far from the hypocenter. In most cases slip happens on preexisting faults though the formation of new faults or prolongations of existing faults is possible (e.g. the review of Scholz, 1998). Coseismic displacement has been inferred at all depths from the surface down to depths below the brittle-ductile transition for especially large earthquakes(e.g. Jiang et al., 2016). For the 2011 M9.0 Tohoku-Oki earthquake, displacement reached as much as > 50 m (Simons et al., 2011). Slip may also be transferred from one segment to another or rupture multiple faults as observed for example during the complex 2016 M7.8 Kaikoura earthquake in New Zealand (Cesca et al., 2017). The heat generation during an earthquake may be extensive enough for frictional melt to be formed (e.g. Rice, 2006, and references therein). Its traces are visible in the form of pseudotachylytes that survive over geological time scales. The slip of the seismogenic part of the fault enables elastic rebound which is visible as horizontal and vertical surface motions (see Govers et al., 2018, and references therein). Recently it has been recognized that a secondary zone of uplift exists which is directly linked to the accelerated penetration of the subducting slab and can be observed a few hundred kilometers landward from the trench (Dinther et al., 2019).

(2) The postseismic phase starts directly after the rupture. The two transient deformation processes that operate during this time - afterslip and viscoelastic relaxation - can be resumed with the overlying term of postseismic relaxation (Govers et al., 2018). The initial postseismic phase is locally characterized by different sorts of afterslip which may last up to several years (Govers et al., 2018, and references therein). Afterslip can be seen as a mechanism to smooth out the contrasting states of stress of the ruptured area and its direct surroundings. This is based on the observation that afterslip dominantly appears on unruptured patches updip and downdip of the main event (Sobolev et al., 2017; Govers et al., 2018; Scholz, 2019, and references therein). Afterslip can occur both as seismic aftershocks and aseismic slip, with the latter containing most of the cummulative moment of the afterslip ($>90\%$) (Govers et al., 2018; Weiss et al., 2019). At the deeper part of the fault, afterslip may furthermore manifest as deep tremor (Scholz, 2019). While afterslip is a rather local phenomenon close to the fault, viscoelastic relaxation of the mantle wedge drives velocities of the overriding crust in a distance as far as several hundred kilometers landwards of the trench (Wang et al., 2012; Sun et al., 2015; Sobolev et al., 2017; Melnick et al., 2018). This process starts hours or days after the great earthquake as suggested by Sobolev et al. (2017) and may continue up to several decades for especially large slip events: Melnick et al. (2018) report about 45 years of relaxation for the 1960 M9.5 Chile earthquake. An important driving force seems to be the sudden drop in mantle wedge viscosity of a factor of up to 10–20 during an earthquake and the gradual increase following the event (Sobolev et al., 2017; Weiss et al., 2019, and references therein). The

surface displacement associated with viscoelastic relaxation is a trenchward motion. However, during the postseismic period this is gradually overprinted by a landward directed reevarsal of surface motions starting close to the trench due to the gradual relocking of the fault (Govers et al., 2018, and references therein).

(3) The total reversal of surface motions marks the onset of the interseismic phase (Wang et al., 2012; Govers et al., 2018; Scholz, 2019). This period is the longest in the seismic cycle. It is generally associated with elastic stress build-up in the shallow lithosphere driven by deep creep and the mechanical coupling of the plate boundary interfaces. While the deep creep may induce microseismicity, especially large earthquakes that penetrated below the brittle-ductile transition seem to be characterized by a seismically quiescent interseismic phase (Jiang et al., 2016).

(4) The transition from interseismic to preseismic phase is not well understood but is thought to correspond to a change of plate coupling and the onset of damage compared to a domination of healing during the interseismic period (e.g. Dieterich, 1978a; Lyakhovsky et al., 2001). Understanding and recognizing the processes of the preseismic phase probably is the most valuable and desired knowledge when it comes to earthquake forecasting. Unfortunately, a single typical precursor process has not been outfactored yet. Merely, a long list of possibilties has been found which is growing with each earthquake observed by instrumental data. However, foreshocks are among the most common observables and have been reported to occur years to months before the event (e.g. Tohoku-Oki and Iquique earthquakes Miyazaki et al., 2011; Ruiz et al., 2014). Often, it may, however, only be possible to qualify an earthquake as a foreshock once the main event has finally occured. Another characteristic of the preseismic phase of some earthquakes seems to be the occurrence of slow slip events (SSE) (e.g. Ruiz et al., 2014). These have been reported to be periodic (observed in the Japan megathrust Uchida et al., 2016), episodic (3 years before the Tohoku-Oki earthquake Ito et al., 2013) or propagating with < 10 km/day (44 min and 1 month before the Tohoku-Oki earthquake Kato et al., 2012). Furthermore, week-long seismic clusters about 9 months before the Iquique earthquake have been observed by Schurr et al. (2014), while seismic and aseismic slip downdip of the rupture area (Miyazaki et al., 2011) as well as gravity and mass changes (Panet et al., 2018) have been reported to have preceded the Tohoku-Oki earthquake. Other studies point out a reduction in v_p/v_s seismic velocities (Semenov, A.N., 1969), or changes in electrical resistivity or the magnetic field (review in Mogi, K., 1985), as well as changes in pressure, flow rate, color, taste, smell, and chemical composition of surface or subsurface water, oil, or gas (compiled in Scholz, 2019). With the nucleation of a new earthquake, the preseismic phase ends and the coseismic phase starts. These diverse processes, often based on observations of a single, event further underline the necessity for better understanding the crucial phase prior to giant earthquakes.

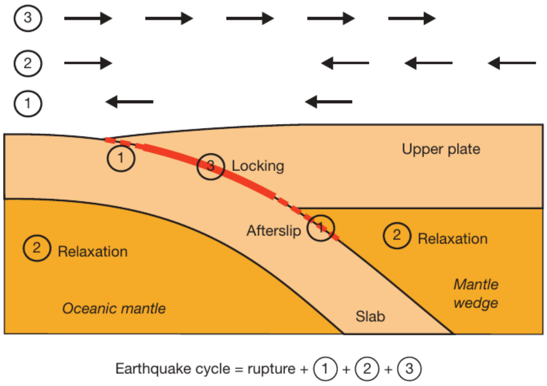

Figure 5.3: A summary of the principal processes during the postseismic and interseismic phase of an earthquake cycle in a subduction zone. The numbers in the plot mark where (1) aseismic afterslip occurs which is mostly around the rupture zone, (2) the coseismically stressed mantle that undergoes viscoelastic relaxation, and (3) the fault that is relocked. The arrows above show the associated directions of surface movements, relative to distant parts of the upper plate. Taken from (Wang et al., 2012), Fig. 2

5.1.2 Fractures, yielding, and friction

Plasticity in geodynamic models is based on the assumption that there is a material dependent yield stress which must be overcome by the current state of stress to allow for brittle failure to occur. The definition of this yield stress varies with the yield criterion and the formulation in use. In the following, I will give a brief overview over the history of yield criteria that evolved from the description of fractures to friction laws describing a wide range of slip behaviors.

The simplest criterion predicts failure based on a constant critical shear stress σ_{crit}. In Tresca (1864) this

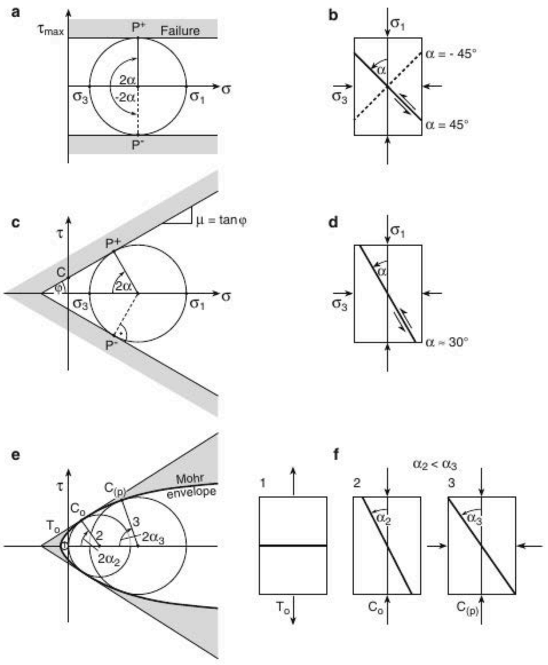

Figure 5.4: Left: Rock failure envelopes in Mohr diagrams plotted in the stress space. **Right:** orientation of rupture planes in laboratory fracture tests. (a, b) maximum shear stress criterion, (c, d) Coulomb fracture criterion, (e, f) generalized Mohr criterion. The shaded area shown is the failure regime of rock. ϕ is the internal angle of friction, μ the friction coefficent, α the fracture angle, $P^{\pm}$ represents the stress state on the plane of failure, τ is the shear stress, σ_1, σ_2, and σ_3 are the principal stress directions, T_0 is the uniaxial tensile strength, C_0 the uniaxial (unconfined) compressive strength, and $C_{(P)}$ the confined compressive strength of rock dependent on confining pressures. From Zang et al. (2009), Fig. 3.1.

is the case when $(\sigma_1 - \sigma_3)/2$ reaches σ_{crit}, while Mises (1913) uses the second invariant of the deviatoric stress tensor J_2 and thereby also includes the intermediate principal stress σ_2.

However, already in 1776 a linear dependence of yield stress and the state of stress has been proposed by Coulomb (Coulomb, 1776; Handin, 1969). He studied shear fractures in a prism of isotropic material under uniaxial compression and found the following relationship known as the Coulomb fracture criterion:

$$\begin{aligned} \tau &= c + \mu \cdot \sigma \\ &= c + tan(\phi) \cdot \sigma \end{aligned} \tag{5.12}$$

where τ is the shear stress, σ is the normal stress, c is cohesion, ϕ is the angle of internal friction, and μ is the friction coefficient. Coulomb therewith introduced the concept of internal friction which is a material property defining how easily a material fails. It can be represented as the angle between the σ-axis and the Coulomb yield stress in a plot of τ vs σ (Fig. 5.4).

Noticing that failure angles in nature decrease with increasing confining pressure, Mohr generalized Coulombs criterion by allowing for a variable coefficient of friction (Mohr, O., 1900; Zang et al., 2009). The resulting failure criterion is nonlinear, empirical, fits well experimental data and is widely used. However, similar to Tresca's yield criterion, it does not take into account the influence of the intermediate principal stress σ_2 which is however visible in triaxial testing (e.g. Wojciechowski, 2018).

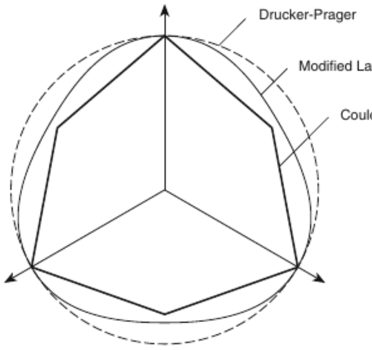

Figure 5.5: Visualization of different yield criteria as cross-sections in the plane normal to the (1, 1, 1) direction in the principal stress space for a friction angle of 22.5°. The arrows represent projections of the principal stress axes onto the plane. The criteria are scaled so that they have equal intercepts. From Zang et al. (2009), Fig. 3.3.

This shortcoming led to the introduction of the Drucker-Prager yield criterion in the 1950s (Drucker et al., 1952) by adding a term dependent on the mean normal stress I_1. In 2D the Drucker-Prager and the Mohr-Coulomb yield criteria are equivalent while they differ in 3D considerations. In the geodynamic modeling software ASPECT, the following formulations of the Drucker-Prager yield criterion is used (Bangerth et al., 2021b):

$$\sigma_{y:2D} = c \cdot cos(\phi) + I_1 \cdot sin(\phi) \tag{5.13}$$

$$\sigma_{y:3D} = \frac{6c \cdot cos(\phi)}{\sqrt{3}(3 + sin(\phi))} + \frac{6I_1 \cdot sin(\phi)}{\sqrt{3}(3 + sin(\phi))} \tag{5.14}$$

where $\sigma_{y:2D}$ and $\sigma_{y:3D}$ are the yield stresses in 2D and 3D, ϕ is the angle of internal friction and I_1 is the normal stress. For modelling purposes the Drucker-Prager yield criterion has the advantage of a smooth surface in principal stress state representation while the Mohr-Coulomb criterion has edges (Fig. 5.5) which is more difficult to implement (Zang et al., 2009).

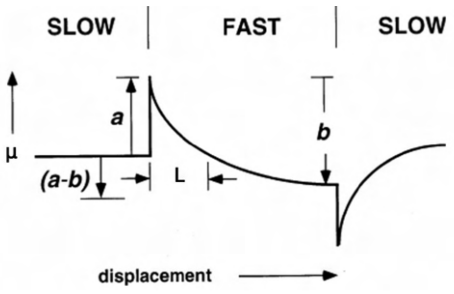

Figure 5.6: Visualization of the frictional response to changes in velocities based on RSF. Modified after Scholz (1998) and Scholz (2019).

Later, it was observed by conducting "slide-hold slide" and "velocity stepping" experiments that friction angles do not only depend on the confining pressure, but also on sliding velocity and the sliding history. This led to the development of rate-and-state friction (RSF) by Dieterich (1978b), Dieterich (1979), and Ruina (1983). This empirical equation can be used to simulate stick-slip behavior as it is witnessed in seismic cycles. The logarithmic formulation for a rate-and-state dependent friction coefficient (Ruina, 1983) consists of three terms:

$$\mu = \mu_0 + a \cdot ln\left(\frac{V}{V_0}\right) + b \cdot ln\left(\frac{\theta \cdot V_0}{L}\right) \tag{5.15}$$

μ_0 is the friction coefficient at reference velocity V_0. The second term is often referred to as the 'viscosity-like' direct effect (Rice et al., 1983), the magnitude of which is determined by the factor a. This term makes the friction coefficient increase when higher slip velocities V set in while it decreases when the slip velocities experience a sudden change towards lower values (Fig. 5.6). The third term is the 'evolution effect' which manifests after the direct effect. It determines how friction asymptotically approaches its steady-state value after the sudden change implied by the direct effect. The magnitude of this last term is prescribed by the factor b while the asymptotic evolution is governed by the state variable θ which itself evolves as a function of slip velocity. In this work, I use the aging law (also called Dietrich law or slowness law) for the evolution of θ through time:

$$\frac{\mathrm{d}\theta}{\mathrm{d}t} = 1 - \frac{\theta V}{L} \tag{5.16}$$

The sensitivity on velocity is determined by the critical slip distance L which is often interpreted as the sliding distance required to renew the contact population of the two sides of the fault surface (Scholz, 1998). Laboratory values of the critical slip distance are on the order of microns as it was shown to correlate with the roughness of the frictional surface and hence asperity size (e.g. Rabinowicz, 1958; Dieterich, 1978b; Scholz, 2019). For geodynamic modeling most publications, however, use a value in the order of centimeters (e.g. Kaneko et al., 2011; Sobolev et al., 2017; Barbot, 2018; Herrendörfer et al., 2018) which facilitates model convergence. The magnitudes of the competing direct and evolution effects either characterize a material as velocity weakening (VW) when $a - b < 0$ or as velocity strengthening (VS) when $a - b > 0$.

Because the classical RSF formulation is ill-posed for very small velocities, several strategies have been developed to overcome this deficiency: While geodynamic modeling software commonly uses a generalized, high-velocity approximation (e.g. Barbot et al., 2010; Herrendörfer et al., 2018; Erickson et al., 2020), a variational approach has been developed and implemented in Pipping et al. (2015). Generalized rate-and-state friction is also used in this work and is denoted as:

$$\mu = a \cdot sinh^{-1}\left[\frac{V}{2V_0} exp\left(\frac{\mu_0 + b \cdot ln(V_0\theta/L)}{a}\right)\right] \tag{5.17}$$

The term $sinh^{-1}$ prevents values of negative infinity at very small velocities.

As rate-and-state friction is an empirical set of equations that are derived from laboratory experiments, a major concern is that the laboratory scales may only loosely be scalable to the temporal and spatial scales found in nature (e.g. Scholz, 2019, chapter 2.5). Recently, much work has been done on the development of microphysical (Chen et al., 2016) and thermodynamic (Aharonov et al., 2018; Barbot, 2019) models to universally explain stick-slip behavior at all scales. Nonetheless, the classical RSF equations are still widely used, as these new models are complex and require parameters that are as yet only insufficiently characterized.

In the meantime, many additions to classical RSF have been proposed e.g. velocity dependence of more parameters than just the internal friction coefficient (Im et al., 2020) or a combination with linear slip weakening (Sobolev et al., 2017). Furthermore, there are several competing ways to compute the state variable θ, all of them describing a part of the observational data while lacking processes described by others (e.g Scholz, 2019). The aging law used in this work and many other geodynamic modeling studies (e.g. Kaneko et al., 2011; Barbot et al., 2012; Sobolev et al., 2017; Herrendörfer et al., 2018) is built on observations of healing at stationary contact over time, e.g. during the interseismic phase, meaning that state increases when $V = 0$ (Ruina, 1983). The slip law on the other hand properly describes the response to velocity jumps, e.g. during an earthquake, and requires $V > 0$ for θ to increase (Ruina, 1983; Dieterich, 1979). Amongst others, this led Nagata et al. (2012) to propose an evolution law where both processes are included, but the debate about the best model is ongoing (e.g. Scholz, 2019).

5.1.3 Mineralogical explanation of the seismogenic window

The parameterization of the theoretical and empirical concepts in Chapter 5.1.2 comes with many uncertainties. This is for example because of the upscaling issue from laboratory to geologic scales and the empirical nature of the parameters a and b. Frictional parameters of a plate boundary fault in geodynamic RSF models are usually chosen such that the uppermost sedimentary and lowermost viscous parts of the fault are velocity strengthening (VS) and characterized by stable sliding. Within the RSF framework, this is obtained when $(a - b) > 0$ regardless of the absolute values. The depth section in between is characterized by $(a - b) < 0$ and a velocity weakening (VW) behavior (e.g. Scholz et al., 1972; Lapusta et al., 2000). The VW zone corresponds to the 'seismogenic window' which is the term for the frictionally instable depth section of the fault surface where stick-slip behaviour prevails and earthquakes nucleate. This division into three depth sections is based on laboratory experiments of rock friction dependence on temperature. Frictional behavior is observed to transition from VS to VW around the isotherms of ≈150°C–≈350°C and from VW to VS around the isotherms of ≈300°C–≈500°C depending on the mineral composition of the rock (Chapter 2.3.4 in Scholz, 2019, and references therein). The first attempt of such a stability analysis was done for granite by Byerlee et al. (1968), Brace et al. (1970), and Stesky et al. (1974). For application to nature the isotherms are converted into depth according to the regional geothermal gradient. Explanations for these contrasting sliding behaviors is not straight-forward to obtain due to the impossibility of in situ observations and the many parameters involved.

One part of the explanation for the VS behavior in the topmost layer may lay in the abundance of clay minerals in this sediment-rich environment of the subduction trench. Clay minerals exhibit unusual frictional properties that violate Byerlee's law (Byerlee, 1968). They show VS behavior under all conditions that can be studied in a lboratory. Phyllosilicates have one perfect cleavage and absorb water between their atom-scale sheets which reduces friction. It is thus the alignment of the clay minerals due to the motion of the two tectonic plates that causes a change in frictional properties of the bulk material and gives them a dominant role despite their relatively small absolute amount. Clay minerals may furthermore coat clastic grains (Bos et al., 2000) which further increases the influence of their unusual frictional properties.

The temperature range where bulk rock behavior changes from VS to VW depends on the mineral content and seems to be controlled by mineral alterations due to temperature-induced onset of dehydration. One example is the transition of Montmorillonite from the Smectite group to Illite at ≈150°C (e.g. Morrow et al., 1992; Scholz, 2019, and references therein). While the clay minerals' mineralogical structure consists of tetrahedal sheets which mostly inhibit the healing of faults (Tesei et al., 2012), further increase in temperature ultimately enables quartz and other minerals to heal fractures by viscous creep which changes the frictional behavior from VW to VS. This temperature range is called the frictional plastic transition and is located at ≈300–400° and ≈15 km. The 'frictional plastic transition' is a term introduced by Scholz (e.g. see p. 93 in the textbook Scholz, 2019) to replace the term 'brittle ductile transition' used to describe a kink in the depth dependent yield strength envelope. This temperature range furthermore corresponds to the transition from Illite to Muscovite (e.g. Hartog et al., 2013; Scholz, 2019).

5.2 Rate-and-state friction in ASPECT

ASPECT has initially been designed to compute mantle flow dynamics. It has, however, successively been expanded to a wide range of processes including lithospheric problems with visco-elasto-plastic deformation. As further described in Chapter 1.4, ASPECT has a modular structure which results in a high flexibility when designing models but also when adding functionalities.

This Chapter focuses on the addition of a rate-and-state friction rheology into the visco-plastic rheology model, which is the base for the computation of visco-elastic-plastic (VEP) deformation. A new friction rheology model was implemented, enabling the user to choose between various frictional behaviors. In the following, I will first introduce the elements of the VEP rheology and the computational order of relevant parts of the code. Then, I will briefly summarize the functionalities that where added to ASPECT during the course of this work before describing the implementation of rate-and-state friction and a suitable time stepping model. Finally, I provide input files and further guidelines for a rate-and-state model setup for further use. Because final testing of RSF has not been finished yet, the code has not been merged into ASPECT's main line, but can be found at `https://github.com/EstherHeck/aspect/tree/cleanup-friction-branch`.

5.2.1 The visco-elastic-plastic rheology in ASPECT

The visco-elastic-plastic rheology in ASPECT provides the base for lithospheric deformation and thus rate-and-state friction models. Its implementation can be found at the following Pull Request (PR) #4370 and will be published by Glerum et al. (in prep.). Figure 5.7 visualizes the three rheological elements included in this complex rheology and how their particluar behavior sums up to a total stress and strain rate.

The function where changes in friction must be taken into account is called `calculate_isostrain_viscosities` and is located within the `visco_plastic` rheology of the `visco_plastic` material model. It is here that the friction module is called at several places. The following summarizes the structure of `calculate_isostrain_viscosities` by using the corresponding lines of the code. It also includes the places modified by rate-and-state friction which are mark as bold text.

- Initialize variables
- Loop over `volume_fractions` to calculate the effective viscosity for each compositional field

Step 1: Viscous behavior
  Step 1a: compute viscosity from diffusion creep law, at least if it is going to be used
  Step 1b: compute viscosity from dislocation creep law
  Step 1c: select what form of viscosity to use (diffusion, dislocation, fk, or composite)
  Step 1d: compute the viscosity from the Peierls creep law and harmonically average with current viscosities
  Step 1e: multiply the viscosity by a constant (default value is 1)
Step 2: calculate strain weakening factors for the cohesion, friction, and pre-yield viscosity
Step 3: calculate the viscous stress magnitude and strain rate. If requested compute visco-elastic contributions.
  Step 3a: calculate viscoelastic (effective) viscosity. Estimate the timestep size when in timestep 0. Scale the preyield viscoelastic viscosity with the timestep ratio.
  Step 3b: calculate non yielding (viscous or viscous + elastic) stress magnitude
Step 4: Friction and cohesion

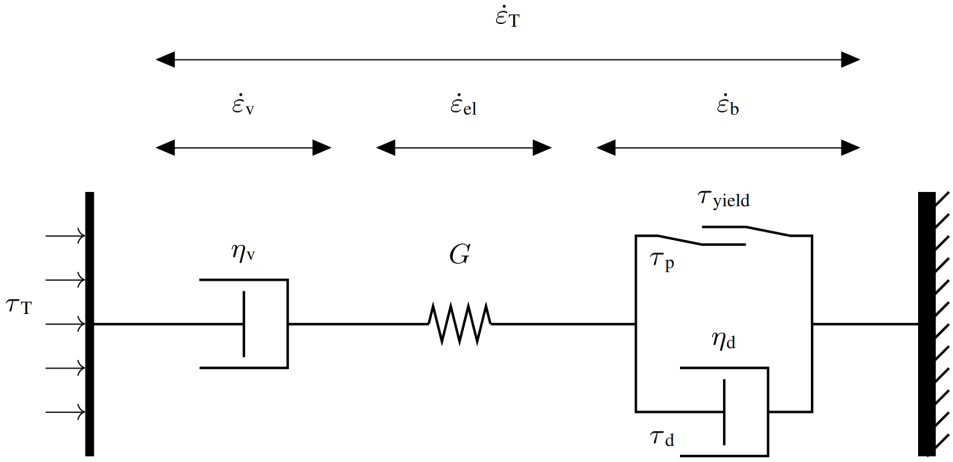

Figure 5.7: A sketch of the visco-elasto-viscoplastic rheology, including a plastic damper as implemented in PR #4370. The total strain rate $\dot{\varepsilon}_\text{T}$ is partitioned between three elements in series. τ_T is the applied total stress that is experienced by all elements. The element to the left represents viscous deformation by dislocation and diffusion creep with a viscosity of η_v and a viscous strain rate of $\dot{\varepsilon}_\text{v}$. The spring in the middle represents elastic deformation with a strain rate $\dot{\varepsilon}_\text{el}$ and an elastic shear modulus G. The element to the right represents Bingham viscoplasticity. It includes a plastic element based on τ_yield and a viscous damper with a viscosity of η_d. The plastic and viscous stresses $\tau_\mathbf{p}$ and $\tau_\mathbf{d}$ experienced by the parallel elements result in a strain rate of $\dot{\varepsilon}_\text{b}$ for the Bingham element. Taken from Glerum et al. (in prep.) thanks to Bob Myhill.

  Step 4a: calculate the strain-weakened friction and cohesion
  Step 4b: Step 4b: calculate friction angle **dependent on strain rate and/or state if specified and we are inside the fault or if dynamic friction is used**
Step 5: plastic yielding. **Modify `pressure_for_plasticity` with `effective_friction_factor` if requested**
  Step 5a: calculate the Drucker-Prager yield stress - **take radiation damping into account if requested**
  Step 5b: select if the yield viscosity is based on Drucker Prager or a stress limiter rheology
    Step 5b-1: `case stress_limiter`: always rescale the viscosity back to the yield surface
    Step 5b-2: `case drucker_prager`: if the non-yielding stress is greater than the yield stress, rescale the viscosity back to yield surface. **If this is the fault material and rate-and-state friction is used, assume that we are always yielding. Take radiation damping into account for computing the `effective_viscosity` if requested**
Step 6: limit the viscosity with specified minimum and maximum bounds

- return output paramters

5.2.2 New features in ASPECT that came along with rate-and-state friction

For the implementation of rate-and-state friction, the following features where added to the ASPECT code. Some have already been added to ASPECT main, while others exclusively exist in the RSF branch found here: `https://github.com/EstherHeck/aspect/tree/cleanup-friction-branch`. Merged changes in the list include the PR number in brackets.

The following is a list with bigger changes in the code due to the new **Rheology Model: `friction_models`** which is a structure to choose between the previous implementation of friction, defining friction as a function of space and time, dynamic friction, and different versions of rate-and-state friction (RSF) (parts of this is merged with my PRs #4357 and #4525).

- **Condition to use RSF:** if `use_theta()` returns true, RSF is used, this function is accessible through the `MaterialModel ViscoPlastic`

- **Particle Property**: `theta for RSF` which is the option to store and calculate the state variable θ on particles instead of fields.
- **Additional Output:** Have additional frictional output: `edot_ii`, a, b, L. Friction angles for output are now taken directly from the returned values of `calculate_isostrain_viscosities` instead of being computed based on input values and volume fractions of the different materials
- **Timestepping:** a Lapusta time step criterion and a RSF convection time step. The former is described in Chapter 5.2.4. The latter is based on a CFL criterion which varies according to maximum velocities in the model. It was useful during the work in progress, e.g. of the Lapusta time step, but may not be feasible for final RSF models.
- **Radiation Damping:** apply a radiation damping term to the `yield_stress` if specified by user
- **Yield condition:** change the `if` statement for the yield condition, as material is always assumed to be at yield within RSF framework
- **RSF material** input parameter to specify the name of the material(s) that shall deform according to rate-and-state friction
- **Structure:** make `calculate_isostrain_viscosities()` a structure that outputs: `composition_yielding`, `composition_viscosities`, `current_friction_angles`, `current_edot_ii`
- **Work in progress:** option to let aspect write the lengths of the different timestepping criteria into the statistics file.

Additionally to the list above, I have also implemented a couple of smaller changes. These rather rework existing functionalities instead of adding new ones.

- add function `get_time_stepping_model()` in `simulator_access`
- add many new references in manual.bib
- take elastic stresses into account in `stress` and `shear_stress` postprocessor (PR #4001)
- use particles, iterated advection, and elastic stress materials: initialize `reaction_terms` input with particle value, not with field value
- add an `effective friction factor` which is multiplied with pressure to take effects of pore fluids into account
- change the accuracy of the value for model time in output files like the log file to account for the different time scales used in RSF models. This prevents having several time steps that seemingly happen at exactly the same time
- work on the already existing dynamic friction model. Correctly convert the friction coefficient μ, and friction angles in RAD or degree. Add a `dynamic friction smoothness exponent` to prescribe the sensitivity of the frictional response to changes in velocity (PR #4357)
- rename compositional stress fields (PR #4002)

Furthermore, some features closely related to this project were implemented by other developers as stated behind the PR number. We were, however, in close contact and I took over the main testing of them.

- add elastic time scale factor (PR #3770 by Rene Gassmoeller)
- add yield stress and stress residual postprocessor (internal by Anne Glerum)
- have the option to repeat a time step (PR #3842 by Timo Heister)
- have the possibility to use a free surface with repeating timesteps (PR #3923 by Timo Heister and Anne Glerum)

- add minimum time step size parameter (PR #3860 Timo Heister)

Finally, there are a couple of changes in ASPECT that are crucial to this work but have lastly been implemented by other developers while I only initiated them. These changes have mainly already been merged into ASPECT main.

- fundamentally rework VEP material model (PR #4370 by Anne Glerum, Bob Myhill, John Naliboff, Rene Gassmoeller)
- have the possibility to use particles with mesh deformation (PR #3760 by Anne Glerum)
- have the possibility to use particles with repeating time steps (#3932 by Anne Glerum)
- change the use of the reference viscosity from fixed input parameter to time step dependent model outcome (PR #3681 by Rene Gassmoeller and follow-up PRs by Juliane Dannberg)

There are some minor issues left in the RSF rheology module and associated relevant parts of other modules. These are marked with the keyword `ToDo:` or `TODO:` at the relevant passages in the code.

5.2.3 Implementation of the friction rheology

I implemented rate-and-state friction in ASPECT as a rheology model called `friction_models`. This rheology model provides the functions to compute the evolution of the state variable θ and the dependence of the friction coefficient μ on strain rate and on θ. The user has the option to choose between several formulations of friction dependence including the logarithmic (Eq. 5.15) as well as the regularized (Eq. 5.17) version of the RSF equation, rate-dependence (Dinther et al., 2013), as well as slip rate dependence of the RSF parameters a and L (Im et al., 2020). To facilitate the transition from a long-term tectonic model into an RSF model that focuses on smaller time spans, I also added an option to use the steady-state friction equation from the RSF framework. Here, the friction coefficient is based on the distribution of the parameters a, b, and L but is not rate-dependent as it is assumed that the steady-state corresponding to a certain slip velocity is already achieved and the evolution according to this steady-state value is not resolved due to large time steps. In this case the friction coefficient is computed as follows (Ruina, 1983):

$$\mu = \mu_0 + (a - b) \cdot log\left(\frac{V_{stst}}{V_0}\right) \tag{5.18}$$

where V_{stst} is the user-defined input velocity at which a frictional steady-state is assumed. The implementation of further equations describing friction is facilitated by the structure provided.

The evolution of the state variable θ is currently only possible using the aging law (Eq. 5.16). With the assumption of constant velocities during any integration time step, Eq. 5.16 can be analytically integrated such that the state variable θ can be updated at the end of the time step through its value at the end of the previous time step using (Sobolev et al., 2017):

$$\theta_{n+1} = \frac{L}{V_{n+1}} + \left(\theta_n - \frac{L}{V_{n+1}}\right) \cdot exp\left(-\frac{V_{n+1}\Delta t}{L}\right) \tag{5.19}$$

To limit computation time, I limited the computation of both the updated value of θ as well as the dependent friction coefficient to those evaluation points where the sum of the volumes of all materials that the user defines to behave in a RSF manner exceeds 0.5. In the future, an input parameter for this value would be desirable.

Contrary to the original RSF theory, normal stress σ_n is replaced by mean pressure p and shear stress τ by the second invariant of the deviatoric stress tensor as in other continuum modeling approaches (e.g. Sobolev et al., 2017; Herrendörfer et al., 2018). Furthermore, the second invariant of the strain rate tensor $\dot{\varepsilon}_{ii}$ was used for the rate-dependence instead of slip velocity V. Ideally, one would only consider the plastic part of $\dot{\varepsilon}_{ii}$, but for high slip rates the plastic part is nearly equal to the full $\dot{\varepsilon}_{ii}$. Because ASPECT is lacking the inertial term in the momentum equation, I introduced a radiation damping term according to Rice (1993). This approximates the energy radiated as seismic waves with a flow of energy out of the model and ensures that slip velocities do not increase infinitely with decreasing time step sizes. The radiation damping term is currently added to the yield stress but lacks proper testing.

While classical Drucker-Prager implementations assume no slip when the yield stress is not overcome, the RSF theory is based on the assumption that there is always some slip occuring on a fault. In my implementation, this is realized through a change in the if-statement for the rescaling of viscosities due to plastic yielding. In the case of the use of RSF, plastical yielding and associated rescaling is always performed wherever the total volume of RSF materials exceeds 0.5 regardless of the magnitude of the current state of stress in relation to the yield stress.

In sum there are 4 places where the friction rheology changes the visco-elasto-plastic material behavior:

- `calculate_isostrain_viscosities`, step 4b, modify the friction angle according to strain rate
- `calculate_isostrain_viscosities`, step 5b, reduce yield stress according to radiation damping term
- `calculate_isostrain_viscosities`, step 5c-2, modified yielding condition
- `calculate_isostrain_viscosities`, step 5c-2, take radiation damping into account when computing the `effecitve_viscosity`

Because of its influence on velocities, RSF may strongly influence the size of time steps.

5.2.4 Implementation of new time stepping criteria

In order to capture all time scales relevant for earthquakes - from fractions of a second during a slip event to hundreds or thousands of years between two events - I use the methodology initially published by Lapusta et al. (2000) and further developed in Herrendörfer et al. (2018). Therein, the time step size necessary to resolve all processes is determined by taking the minimum of four different criteria: (1) the displacement time step (eq. 5.20), (2) the visco-elasto-plastic relaxation time step (eq. 5.21), (3) the state healing time step (eq. 5.22), and (4) the state weakening time step (eq. 5.23). These are the equations used in Herrendörfer et al. (2018):

$$\Delta t_d = \Delta d_{max} \cdot min\left[|\frac{\Delta x}{V_x}|, |\frac{\Delta x}{V_y}|\right] \tag{5.20}$$

$$\Delta t_{vep} = 0.2 \cdot \frac{\eta_{vep}}{G} \tag{5.21}$$

$$\Delta t_h = 0.2 \cdot \theta \tag{5.22}$$

$$\Delta t_w = \Delta\theta_{max} \cdot \frac{L}{V_p} \tag{5.23}$$

with

$$\xi = \frac{1}{4}\left[\frac{kL}{aP} - \frac{b-a}{a}\right]^2 - \frac{kL}{aP} \tag{5.24}$$

$$k = \frac{2G^*}{\pi\Delta x} \tag{5.25}$$

$$G^* = \frac{G}{1-\nu} \tag{5.26}$$

if $\xi > 0$:

$$\Delta\theta_{max} = min\left[\frac{aP}{kL-(b-a)P}, 0.2\right] \tag{5.27}$$

if $\xi < 0$:

$$\Delta\theta_{max} = min\left[1 - \frac{(b-a)P}{kL}, 0.2\right] \tag{5.28}$$

where a, b, L, and θ are rate-and-state friction parameters as described above in Chapter 5.1.2. V_p is the plastic or slip velocity which is approximated with $\dot{\varepsilon}_{ii} \cdot \Delta x$ in our implementation. P is the effective pressure which takes the effect of pore fluids into account. G is the elastic shear modulus and ν is the Poisson number. η_{vep} is the effective visco-elasto-plastic viscosity. Δx is the cellsize in x-direction, and V_x and V_y are the velocity components in x-direction and y-direction, respectively. In ASPECT I replaced Δ_x with the `minimum_vertex_distance` of the cell to account for the possibility of movement in all three spatial direction.

Equations 5.20–5.23 are evaluated at every quadrature point below the surface where the total of RSF materials exceeds a volume fraction of 0.5. The smallest resulting time step then prescribes the size for the next time step. Due to ASPECT's plugin structure it is easily possible to couple this time stepping scheme with other criteria, e.g. the possibility to repeat a time step with a smaller size if the two values are very different. This ensures that time step sizes don't become too large to resolve an earthquake.

5.2.5 Example input file

This is an example input file for a simple, 2D, periodic RSF model that can be run on one processor. It can be used as a starting point for testing and using RSF in ASPECT. It returns a long and thin model with the dimensions of 48x0.75 km or 128x2 cells. One of the short model sides is fixed, while the other side is moved with a constant velocity. The long model sides are periodic boundaries. The short side that is not moving has 4 cells of fault material which behaves according to RSF and is prestressed by initializing the shear stress `stress_xy` with 26e6. This allows the first earthquake to happen immediately without having to let the shear stress build up during model time. It is recommended to use particles instead of fields to prevent the diffusion of fault material. Key parameters for the testing of the RSF implementation are (1) the time stepping scheme and its sensibility to velocities, applicability to earthquake cycle modeling and feasibility in terms of computational resources, (2) the values and spatial distribution of RSF parameters a, b, L, (3) the radiation damping term.

Note: With discontinuous elements, which are needed for the VEP rheology, adaptive mesh refinement and periodic boundaries can not be used in a parallelized model to date. This input file should therefore be run on one processor only.

```
#### Periodic strike slip fault model
####  Global parameters
set Dimension                              = 2
set Start time                             = 0
set End time                               = 10e4
set Use years in output instead of seconds = true
set Nonlinear solver scheme                = iterated Advection and Stokes
set Nonlinear solver tolerance             = 1e-6
set Max nonlinear iterations               = 100
set Output directory                       = output
set Timing output frequency                = 1
set Maximum time step                      = 2

subsection Checkpointing
  set Steps between checkpoint             = 20
end
set Resume computation                     = auto

subsection Time stepping
  set List of model names                        = repeat on cutback, lapusta
     time step
  set Minimum time step size                     = 3.169e-10
  set Minimum time step size for first time step = true
  subsection Repeat on cutback
```

```
    set Relative repeat threshold                = 0.2
  end
end
set Maximum relative increase in time step       = 10

# Model geometry [m]
subsection Geometry model
  set Model name = box
  subsection Box
    set X repetitions = 2
    set Y repetitions = 128
    set X extent      = 750
    set Y extent      = 48e3
    set X periodic    = true
  end
end

subsection Mesh refinement
  set Initial global refinement          = 0
  set Initial adaptive refinement        = 0
  set Time steps between mesh refinement = 0
  set Strategy                           = minimum refinement function
  subsection Minimum refinement function
    set Coordinate system                = cartesian
    set Variable names                   = x,y,z
    set Function expression              = if(y<=1e3, 0, 0)
  end
end

# Velocity on boundaries characterized by functions
subsection Boundary velocity model
  set Prescribed velocity boundary indicators  = top:function, bottom:function
  subsection Function
    set Variable names                         = x,y
        # the BP1 of the SCEC-SEAS group requires a plate speed of 1e-9 m/s,
            which equals 31.5 mm/y.
        # Here I take half of it because I only model one side of the fault
    set Function constants                     = mm=0.001, year=1, outflow =
        15.75
        set Function expression                    = if(y<=0, 0, outflow*mm/
            year); 0
  end
end

# Number and names of compositional fields
# The four compositional fields represent the upper crust, lower crust, mantle
# and a vertical 'fault' with specific friction parameters.
subsection Compositional fields
  set Number of fields            = 8
  set Names of fields             = ve_stress_xx, ve_stress_yy, ve_stress_xy,
      ve_stress_xx_old, ve_stress_yy_old, ve_stress_xy_old, theta, fault
  set Compositional field methods = particles, particles, particles, particles,
       particles, particles, particles, particles
  set Mapped particle properties  = theta:theta, ve_stress_xx:ve_stress_xx,
      ve_stress_yy:ve_stress_yy, ve_stress_xy:ve_stress_xy, ve_stress_xx_old:
      ve_stress_xx_old, ve_stress_yy_old:ve_stress_yy_old, ve_stress_xy_old:
      ve_stress_xy_old, fault:initial fault
end

subsection Initial composition model
  set Model name                  = function
  subsection Function
    set Variable names            = x,y
```

```
        set Function expression       = 0;\
                                    0;\
                                    if(y>1.5e3,26e6,0);\
                                    0;\
                                    0;\
                                    0;\
                                    1.4e7;\
                                    if(y<=1.5e3,1,0);
  end
end

subsection Boundary composition model
  set List of model names                   = initial composition
end

# Temperature boundary conditions
subsection Boundary temperature model
  set Fixed temperature boundary indicators = bottom, top
  set List of model names                   = box
  subsection Box
    set Bottom temperature                  = 273
    set Top temperature                     =  273
  end
end

subsection Initial temperature model
  set Model name              = function
  subsection Function
    set Function expression = 273
  end
end

subsection Formulation
  # incompressible
  set Formulation             = Boussinesq approximation
  set Enable elasticity       = true
end

# Constant internal heat production values (W/m^3) for background material
# and compositional fields.
subsection Heating model
  set List of model names     = compositional heating
  subsection Compositional heating
    set Compositional heating values = 0.
  end
end

# Material model
subsection Material model
  set Model name                = visco plastic
  subsection Visco Plastic
    set Reference temperature = 293

    # The minimum strain-rate helps limit large viscosities values that arise
    # as the strain-rate approaches zero.
    # The reference strain-rate is used on the first non-linear iteration
    # of the first time step when the velocity has not been determined yet.
    set Minimum strain rate   = 1.e-50
    set Reference strain rate = 1.e-14

    # Limit the viscosity with minimum and maximum values
    set Minimum viscosity     = 1e6
    set Maximum viscosity     = 1.5e23
```

```
    # Thermal diffusivity is adjusted to match thermal conductivities
    # assumed in assigning the initial geotherm
    set Thermal diffusivities = 1.333333e-6
    set Heat capacities       = 750.
    set Densities             = 2670
    set Thermal expansivities = 2e-5
    set Elastic shear moduli  = 3.2e10

    # Viscosity
    set Viscosity averaging scheme = maximum composition
    set Viscous flow law = dislocation

    # Dislocation creep parameters for
    set Prefactors for dislocation creep          = 1e-23
    set Stress exponents for dislocation creep    = 1.0
    set Activation energies for dislocation creep = 0.0
    set Activation volumes for dislocation creep  = 0.0

    # Plasticity parameters
    set List of compositional field names to use rate and state friction =
       fault
    set Friction mechanism          = regularized rate and state dependent
       friction
        subsection Rate and state parameter a function
      set Variable names            = x,y
      set Function expression       = 0;0;0;0;0;0;0;0; 0.01
        end
        subsection Rate and state parameter b function
      set Variable names            = x,y
      set Function expression       = 0;0;0;0;0;0;0;0;0.015
    end
    set Angles of internal friction = 30
    set Cohesions                   = 20e6, 20e6,       20e6, 20e6,     20e6,
         20e6,   20e6,   20e6,   2e6
    subsection Critical slip distance function
      set Variable names            = x,y
      set Function expression       = 1;1;1;1;1;1;1;1;0.008
    end
    set Use fixed elastic time step = false
    set Fixed elastic time step     = 3.169e-10
    set Stabilization time scale factor = 1
    set Use radiation damping       = false
  end
end

# Gravity model
subsection Gravity model
  set Model name  = vertical
  subsection Vertical
    set Magnitude = 9.81
  end
end

# Post processing
subsection Postprocess
  set List of postprocessors             = velocity statistics, visualization,
     point values, particles, composition statistics, Stokes residual
  subsection Visualization
    set List of output variables         = viscosity, strain rate, error
       indicator, named additional outputs, stress
    set Output format                    = vtu
    set Time between graphical output    = 0
```

```
    set Interpolate output               = true
    set Write higher order output        = true
  end
  subsection Particles
    set Number of particles              = 0.25e6
    set Time between data output         = 0
    set Data output format               = gnuplot
    set List of particle properties      = velocity, theta for RSF, elastic
        stress, initial composition
    set Interpolation scheme             = quadratic least squares
    set Update ghost particles           = true
    set Particle generator name          = quadrature points
  end
  subsection Point values
    # A line of points to visualize slip with postprocessing scripts
    set Evaluation points                = 0.05,2000; 0.1,2000; 0.15,2000;
        0.2,2000; 0.25,2000; 0.3,2000; 0.35,2000; 0.375,2000; 0.4,2000;
        0.45,2000; 0.5,2000; 0.55,2000; 0.6,2000; 0.65,2000; 0.7,2000
        set Time between point values output = 0
  end
end

subsection Solver parameters
  subsection Stokes solver parameters
    set Number of cheap Stokes solver steps    = 400
    set Linear solver tolerance                = 1e-7
  end

  # Make sure to do only 1 splitting step
  subsection Operator splitting parameters
    set Reaction time step                     = 5000  # larger than maximum
        Stokes time step
    set Reaction time steps per advection step = 1
  end
end

subsection Discretization
  # DG for viscoelastic stresses
  set Use discontinuous composition discretization = true
end
```

5.3 Conclusion

Even though final testing of RSF in ASPECT has not been done yet because of a forced change in the subject of the thesis, the latest models using the input file of Chapter 5.2.5 look promising. The changes in the VEP rheology that I have been implementing within the last 2.5 years since the need for them was discovered during the work on this thesis, improve the RSF models substantially. Convergence is much better, such that a nonlinear tolerance of 1e-7 is now achieved within about 20 iterations during much of the model run. Time step sizes in a the range of milliseconds can be used such that a slip event spans more than one time step. Model velocities span many magnitudes without the model crashing, ranging from a root mean square velocity of 10^{10} m/year during an event to smaller than 10^{-2} only a few model seconds afterwards. These may not be realistic values yet but illustrate the capabilities of the software. Similarly, the values for the state variable θ as well as the shear stress in the fault instantly drop during an event as expected. However, the above model does not increase time step sizes after an event, such that no full cycle could be computed. Future work must overcome this deficiency. Furthermore, testing more values for the RSF parameters is needed such that ASPECT's RSF can be compared to other softwares, e.g. by using the benchmark problems from the SEAS-SCEC community (Luo et al., 2018; Erickson et al., 2020).

References

Aharonov, Einat and Christopher H. Scholz (2018). "A Physics-Based Rock Friction Constitutive Law: Steady State Friction". en. In: *Journal of Geophysical Research: Solid Earth* 123.2, pp. 1591–1614.

Bangerth, Wolfgang, Juliane Dannberg, Menno Fraters, Rene Gassmoeller, Anne Glerum, Timo Heister, and John Naliboff (2021a). *ASPECT v2.3.0.* Version v2.3.0.

— (2021b). ASPECT*: Advanced Solver for Problems in Earth's ConvecTion, User Manual.*

Barbot, Sylvain (2018). "Asthenosphere Flow Modulated by Megathrust Earthquake Cycles". en. In: *Geophysical Research Letters* 45.12, pp. 6018–6031.

— (2019). "Slow-slip, slow earthquakes, period-two cycles, full and partial ruptures, and deterministic chaos in a single asperity fault". en. In: *Tectonophysics* 768, p. 228171.

Barbot, Sylvain and Yuri Fialko (2010). "A unified continuum representation of post-seismic relaxation mechanisms: semi-analytic models of afterslip, poroelastic rebound and viscoelastic flow". en. In: *Geophysical Journal International* 182.3, pp. 1124–1140.

Barbot, Sylvain, Nadia Lapusta, and Jean-Philippe Avouac (2012). "Under the Hood of the Earthquake Machine: Toward Predictive Modeling of the Seismic Cycle". en. In: *Science* 336.6082, pp. 707–710.

Bos, B. and C. J. Spiers (Dec. 30, 2000). "Effect of phyllosilicates on fluid-assisted healing of gouge-bearing faults". In: *Earth and Planetary Science Letters* 184.1, pp. 199–210.

Brace, W. F. and J. D. Byerlee (June 26, 1970). "California Earthquakes: Why Only Shallow Focus?" In: *Science* 168.3939, pp. 1573–1575.

Byerlee, James D. (1968). "Brittle-ductile transition in rocks". In: *Journal of Geophysical Research (1896-1977)* 73.14, pp. 4741–4750.

Byerlee, James D. and W. F. Brace (1968). "Stick slip, stable sliding, and earthquakes—Effect of rock type, pressure, strain rate, and stiffness". In: *Journal of Geophysical Research (1896-1977)* 73.18, pp. 6031–6037.

Cesca, S., Y. Zhang, V. Mouslopoulou, R. Wang, J. Saul, M. Savage, S. Heimann, S. -K. Kufner, O. Oncken, and T. Dahm (2017). "Complex rupture process of the Mw 7.8, 2016, Kaikoura earthquake, New Zealand, and its aftershock sequence". In: *Earth and Planetary Science Letters* 478, pp. 110–120.

Chen, Jianye and Christopher J. Spiers (2016). "Rate and state frictional and healing behavior of carbonate fault gouge explained using microphysical model". en. In: *Journal of Geophysical Research: Solid Earth* 121.12, pp. 8642–8665.

Coulomb, C. A. (1776). "Sur une application des règles maximis et minimis à quelques problèmes de statique, relatif à l'architecture". In: 7, pp. 343–382.

Dieterich, J. H. (1978a). "Preseismic fault slip and earthquake prediction". In: *Journal of Geophysical Research: Solid Earth* 83 (B8), pp. 3940–3948.

Dieterich, James H. (1978b). "Time-Dependent Friction and the Mechanics of Stick-Slip". en. In: *Rock Friction and Earthquake Prediction.* Ed. by James D. Byerlee and Max Wyss. Contributions to Current Research in Geophysics (CCRG). Basel: Birkhäuser, pp. 790–806.

— (1979). "Modeling of rock friction: 1. Experimental results and constitutive equations". en. In: *Journal of Geophysical Research: Solid Earth* 84.B5, pp. 2161–2168.

Dinther, Y. van, T. V. Gerya, L. A. Dalguer, F. Corbi, F. Funiciello, and P. M. Mai (2013). "The seismic cycle at subduction thrusts: 2. Dynamic implications of geodynamic simulations validated with laboratory models". en. In: *Journal of Geophysical Research: Solid Earth* 118.4, pp. 1502–1525.

Dinther, Y. van, P. M. Mai, L. A. Dalguer, and T. V. Gerya (2014). "Modeling the seismic cycle in subduction zones: The role and spatiotemporal occurrence of off-megathrust earthquakes". en. In: *Geophysical Research Letters* 41.4, pp. 1194–1201.

Dinther, Ylona van, Lukas E. Preiswerk, and Taras V. Gerya (2019). "A Secondary Zone of Uplift Due to Megathrust Earthquakes". en. In: *Pure and Applied Geophysics* 176.9, pp. 4043–4068.

Drucker, D. C. and W. Prager (1952). "Soil mechanics and plastic analysis or limit design". en. In: *Quarterly of Applied Mathematics* 10.2, pp. 157–165.

Duan, Benchun, Zaifeng Liu, and Austin J. Elliott (2019). "Multicycle Dynamics of the Aksay Bend Along the Altyn Tagh Fault in Northwest China: 2. The Realistically Complex Fault Geometry". en. In: *Tectonics* 38.3, pp. 1120–1137.

Duputel, Zacharie, Luis Rivera, Hiroo Kanamori, and Gavin Hayes (2012). "W phase source inversion for moderate to large earthquakes (1990-2010)". en-GB. In: *Geophysical Journal International* 189.2, pp. 1125–1147.

Erickson, Brittany A., Eric M. Dunham, and Arash Khosravifar (2017). “A finite difference method for off-fault plasticity throughout the earthquake cycle”. en. In: *Journal of the Mechanics and Physics of Solids* 109, pp. 50–77.

Erickson, Brittany A., Junle Jiang, Michael Barall, Nadia Lapusta, Eric M. Dunham, Ruth Harris, Lauren S. Abrahams, Kali L. Allison, Jean-Paul Ampuero, Sylvain Barbot, Camilla Cattania, Ahmed Elbanna, Yuri Fialko, Benjamin Idini, Jeremy E. Kozdon, Valère Lambert, Yajing Liu, Yingdi Luo, Xiao Ma, Maricela Best McKay, Paul Segall, Pengcheng Shi, Martijn van den Ende, and Meng Wei (2020). “The Community Code Verification Exercise for Simulating Sequences of Earthquakes and Aseismic Slip (SEAS)”. en. In: *Seismological Research Letters* 91.2A, pp. 874–890.

Fraters, M. R. T., W. Bangerth, C. Thieulot, A. C. Glerum, and W. Spakman (2019). “Efficient and practical Newton solvers for nonlinear Stokes systems in geodynamics problems”. In: *Geophysics Journal International* 218.2, pp. 873–894.

Gassmöller, Rene, Harsha Lokavarapu, Eric Heien, Elbridge Gerry Puckett, and Wolfgang Bangerth (2018). “Flexible and Scalable Particle-in-Cell Methods With Adaptive Mesh Refinement for Geodynamic Computations”. In: *Geochemistry, Geophysics, Geosystems* 19.9, pp. 3596–3604.

Glerum, Anne, Robert Myhill, John Naliboff, Dan Sandiford, Rene Gassöller, Juliane Dannberg, Elbridge Gerry Puckett, Mack Gregory, Cedric Thieulot, Esther Heckenbach, Maaike Weerdesteijn, Dylan Vasey, David Quiroga, Daniel Douglas, Derek Neuharth, Sascha Brune, and Fiona Clerc (in prep.). “Particle-in-cell versus field methods in ASPECT”. In: *Preparation*.

Govers, R., K. P. Furlong, L. van de Wiel, M. W. Herman, and T. Broerse (2018). “The Geodetic Signature of the Earthquake Cycle at Subduction Zones: Model Constraints on the Deep Processes”. en. In: *Reviews of Geophysics* 56.1, pp. 6–49.

Handin, John (1969). “On the Coulomb-Mohr failure criterion”. en. In: *Journal of Geophysical Research (1896-1977)* 74.22, pp. 5343–5348.

Hartog, S. A. M. den, A. R. Niemeijer, and C. J. Spiers (July 1, 2013). “Friction on subduction megathrust faults: Beyond the illite–muscovite transition”. In: *Earth and Planetary Science Letters* 373, pp. 8–19.

Heister, Timo, Juliane Dannberg, Rene Gassmöller, and Wolfgang Bangerth (2017). “High Accuracy Mantle Convection Simulation through Modern Numerical Methods. II: Realistic Models and Problems”. In: *Geophysical Journal International* 210.2, pp. 833–851.

Herrendörfer, Robert, Ylona van Dinther, Taras Gerya, and Luis Angel Dalguer (2015). “Earthquake supercycle in subduction zones controlled by the width of the seismogenic zone”. en. In: *Nature Geoscience* 8.6, pp. 471–474.

Herrendörfer, Robert, Taras Gerya, and Ylona van Dinther (2018). “An Invariant Rate- and State-Dependent Friction Formulation for Viscoeastoplastic Earthquake Cycle Simulations”. en. In: *Journal of Geophysical Research: Solid Earth* 123.6, pp. 5018–5051.

Im, Kyungjae, Demian Saffer, Chris Marone, and Jean-Philippe Avouac (2020). “Slip-rate-dependent friction as a universal mechanism for slow slip events”. en. In: *Nature Geoscience* 13.10, pp. 705–710.

Ishibashi, K. (2004). “Status of historical seismology in Japan”. In: *Annals of Geophysics* 47.2-3.

Ito, Yoshihiro, Ryota Hino, Motoyuki Kido, Hiromi Fujimoto, Yukihito Osada, Daisuke Inazu, Yusaku Ohta, Takeshi Iinuma, Mako Ohzono, Satoshi Miura, Masaaki Mishina, Kensuke Suzuki, Takeshi Tsuji, and Juichiro Ashi (2013). “Episodic slow slip events in the Japan subduction zone before the 2011 Tohoku-Oki earthquake”. In: *Tectonophysics*. Great Earthquakes along Subduction Zones 600, pp. 14–26.

Jiang, Junle and Nadia Lapusta (2016). “Deeper penetration of large earthquakes on seismically quiescent faults”. en. In: *Science* 352.6291, pp. 1293–1297.

Joyner, Matthew D. and Mehrdad Sasani (2020). “Building performance for earthquake resilience”. en. In: *Engineering Structures* 210, p. 110371.

Kagan, Y. Y. and D. D. Jackson (2010). “Earthquake Forecasting in Diverse Tectonic Zones of the Globe”. en. In: *Pure and Applied Geophysics* 167.6, pp. 709–719.

Kanamori, Hiroo and Don L. Anderson (1975). “Theoretical basis of some empirical relations in seismology”. In: *Bulletin of the Seismological Society of America* 65.5, pp. 1073–1095.

Kaneko, Y. and Y. Fialko (2011). “Shallow slip deficit due to large strike-slip earthquakes in dynamic rupture simulations with elasto-plastic off-fault response”. en. In: *Geophysical Journal International* 186.3, pp. 1389–1403.

Kato, Aitaro, Kazushige Obara, Toshihiro Igarashi, Hiroshi Tsuruoka, Shigeki Nakagawa, and Naoshi Hirata (2012). “Propagation of Slow Slip Leading Up to the 2011 Mw 9.0 Tohoku-Oki Earthquake”. In: *Science* 335.6069, pp. 705–708.

Kronbichler, M., T. Heister, and W. Bangerth (2012). “High Accuracy Mantle Convection Simulation through Modern Numerical Methods”. In: *Geophysical Journal International* 191, pp. 12–29.

Lambert, Valère and Sylvain Barbot (2016). “Contribution of viscoelastic flow in earthquake cycles within the lithosphere-asthenosphere system”. en. In: *Geophysical Research Letters* 43.19, pp. 10, 142–10, 154.

Lapusta, Nadia and Yi Liu (2009). “Three-dimensional boundary integral modeling of spontaneous earthquake sequences and aseismic slip”. en. In: *Journal of Geophysical Research: Solid Earth* 114.B9.

Lapusta, Nadia, James R. Rice, Yehuda Ben-Zion, and Gutuan Zheng (2000). “Elastodynamic analysis for slow tectonic loading with spontaneous rupture episodes on faults with rate- and state-dependent friction”. en. In: *Journal of Geophysical Research: Solid Earth* 105.B10, pp. 23765–23789.

Liu-Zeng, Jing, Yann Klinger, Kerry Sieh, Charles Rubin, and Gordon Seitz (2006). “Serial ruptures of the San Andreas fault, Carrizo Plain, California, revealed by three-dimensional excavations”. In: *Journal of Geophysical Research: Solid Earth* 111 (B2).

Luo, Y., B. A. Erickson, J. Jiang, M. Barall, N. Lapusta, E. M. Dunham, R. Harris, L. Abrahams, K. L. Allison, J. P. Ampuero, S. Barbot, C. Cattania, A. E. Elbanna, Y. A. Fialko, B. Idini, J. E. Kozdon, V. Lambert, Y. Liu, X. Ma, P. Segall, P. Shi, and M. Wei (2018). “The Community Code Verification Exercise for Simulating Sequences of Earthquakes and Aseismic Slip (SEAS): Initial Benchmarks and Future Directions”. en. In: *AGU Fall Meeting Abstracts* 2018, T33F–0478.

Lyakhovsky, Vladimir, Yehuda Ben-Zion, and Amotz Agnon (2001). “Earthquake cycle, fault zones, and seismicity patterns in a rheologically layered lithosphere”. In: *Journal of Geophysical Research: Solid Earth* 106.B3, pp. 4103–4120.

Melnick, Daniel, Shaoyang Li, Marcos Moreno, Marco Cisternas, Julius Jara-Muñoz, Robert Wesson, Alan Nelson, Juan Carlos Báez, and Zhiguo Deng (2018). “Back to full interseismic plate locking decades after the giant 1960 Chile earthquake”. en. In: *Nature Communications* 9.1, pp. 1–10.

Mises, R. von (1913). “Mechanik der festen Korper in Plastisch deformablem Zustand [Mechanics of solid bodies undergoing plastic deformation]”. In: pp. 582–92.

Miyazaki, Shin’ichi, Jeffery J. McGuire, and Paul Segall (2011). “Seismic and aseismic fault slip before and during the 2011 off the Pacific coast of Tohoku Earthquake”. In: *Earth, Planets and Space* 63.7, p. 23.

Mogi, K. (1985). *Earthquake prediction*. Tokyo: Tokyo, Academic Press.

Mohr, O. (1900). “Welche Umstände bedingen die Elastizitätsgrenze und den Bruch eines Materiales?” In: 44, pp. 1524–1577.

Morrow, C., B. Radney, and J. Byerlee (Jan. 1, 1992). “Chapter 3 Frictional Strength and the Effective Pressure Law of Montmorillonite and lllite Clays”. In: *International Geophysics*. Ed. by Brian Evans and Teng-fong Wong. Vol. 51. Fault Mechanics and Transport Properties of Rocks. Academic Press, pp. 69–88.

Muldashev, Iskander A. and Stephan V. Sobolev (2020). “What Controls Maximum Magnitudes of Giant Subduction Earthquakes?” en. In: *Geochemistry, Geophysics, Geosystems* n/a.n/a, e2020GC009145.

Murray, Jessica R. and John O. Langbein (2006). “Slip on the San Andreas Fault at Parkfield, California, over Two Earthquake Cycles, and the Implications for Seismic Hazard”. In: *Bulletin of the Seismological Society of America* 96.

Nagata, K., M. Nakatani, and S. Yoshida (2012). “A revised rate- and state-dependent friction law obtained by constraining constitutive and evolution laws separately with laboratory data”. In: *Journal of Geophysical Research: Solid Earth* 117.B2.

Nováková, Lucie (2016). “Paleoseismology: evidence of earth activity”. en. In: *International Journal of Earth Sciences* 105.5, pp. 1467–1469.

Panet, Isabelle, Sylvain Bonvalot, Clément Narteau, Dominique Remy, and Jean-Michel Lemoine (2018). “Migrating pattern of deformation prior to the Tohoku-Oki earthquake revealed by GRACE data”. In: *Nature Geoscience* 11.5, pp. 367–373.

Pipping, Elias, Ralf Kornhuber, Matthias Rosenau, and Onno Oncken (2016). “On the efficient and reliable numerical solution of rate-and-state friction problems”. en. In: *Geophysical Journal International* 204.3, pp. 1858–1866.

Pipping, Elias, Oliver Sander, and Ralf Kornhuber (2015). “Variational formulation of rate- and state-dependent friction problems”. In: *ZAMM - Journal of Applied Mathematics and Mechanics / Zeitschrift für Angewandte Mathematik und Mechanik* 95.4, pp. 377–395.

Preuss, Simon, Robert Herrendörfer, Taras Gerya, Jean-Paul Ampuero, and Ylona van Dinther (2019). “Seismic and Aseismic Fault Growth Lead to Different Fault Orientations”. en. In: *Journal of Geophysical Research: Solid Earth* 124.8, pp. 8867–8889.

Rabinowicz, E (1958). “The Intrinsic Variables affecting the Stick-Slip Process”. In: *Proceedings of the Physical Society* 71.4, pp. 668–675.

Rahman, Munib ur, Soliha Rahman, Seema Mansoor, Vikas Deep, and M. Aashkaar (2016). “Implementation of ICT and Wireless Sensor Networks for Earthquake Alert and Disaster Management in Earthquake Prone Areas”. en. In: *Procedia Computer Science.* International Conference on Computational Modelling and Security (CMS 2016) 85, pp. 92–99.

Rice, J. R. and A. L. Ruina (June 1, 1983). “Stability of Steady Frictional Slipping”. In: *Journal of Applied Mechanics* 50.2, pp. 343–349.

Rice, James R. (1993). “Spatio-temporal complexity of slip on a fault”. en. In: *Journal of Geophysical Research: Solid Earth* 98.B6, pp. 9885–9907.

— (2006). “Heating and weakening of faults during earthquake slip”. en. In: *Journal of Geophysical Research: Solid Earth* 111.B5.

Rose, Ian, Bruce Buffett, and Timo Heister (2017). “Stability and accuracy of free surface time integration in viscous flows”. In: *Physics of the Earth and Planetary Interiors* 262, pp. 90–100.

Ruina, Andy (1983). “Slip instability and state variable friction laws”. en. In: *Journal of Geophysical Research: Solid Earth* 88.B12, pp. 10359–10370.

Ruiz, S., M. Metois, A. Fuenzalida, J. Ruiz, F. Leyton, R. Grandin, C. Vigny, R. Madariaga, and J. Campos (2014). “Intense foreshocks and a slow slip event preceded the 2014 Iquique Mw 8.1 earthquake”. In: *Science* 345.6201, pp. 1165–1169.

Scholz, Christopher, Peter Molnar, and Tracy Johnson (1972). “Detailed studies of frictional sliding of granite and implications for the earthquake mechanism”. In: *Journal of Geophysical Research (1896-1977)* 77.32, pp. 6392–6406.

Scholz, Christopher H. (1998). “Earthquakes and friction laws”. en. In: *Nature* 391.6662, pp. 37–42.

— (2019). *The Mechanics of Earthquakes and Faulting.* en. Cambridge University Press.

Schurr, Bernd, Günter Asch, Sebastian Hainzl, Jonathan Bedford, Andreas Hoechner, Mauro Palo, Rongjiang Wang, Marcos Moreno, Mitja Bartsch, Yong Zhang, Onno Oncken, Frederik Tilmann, Torsten Dahm, Pia Victor, Sergio Barrientos, and Jean-Pierre Vilotte (2014). “Gradual unlocking of plate boundary controlled initiation of the 2014 Iquique earthquake”. In: *Nature* 512.7514, pp. 299–302.

Semenov, A.N. (1969). “Variations of the travel time of transverse and longitudinal waves before violent earthquakes”. In: 3: 245–258.

Simons, Mark, Sarah E. Minson, Anthony Sladen, Francisco Ortega, Junle Jiang, Susan E. Owen, Lingsen Meng, Jean-Paul Ampuero, Shengji Wei, Risheng Chu, Donald V. Helmberger, Hiroo Kanamori, Eric Hetland, Angelyn W. Moore, and Frank H. Webb (2011). “The 2011 Magnitude 9.0 Tohoku-Oki Earthquake: Mosaicking the Megathrust from Seconds to Centuries”. In: *Science* 332.6036, pp. 1421–1425.

Sobolev, Stephan V. and Iskander A. Muldashev (2017). “Modeling Seismic Cycles of Great Megathrust Earthquakes Across the Scales With Focus at Postseismic Phase: SEISMIC CYCLE CROSS-SCALE MODEL”. en. In: *Geochemistry, Geophysics, Geosystems* 18.12, pp. 4387–4408.

Stesky, R. M., W. F. Brace, D. K. Riley, and P. -Y. F. Robin (July 1, 1974). “Friction in faulted rock at high temperature and pressure”. In: *Tectonophysics* 23.1, pp. 177–203.

Suárez, Gerardo, J. M. Espinosa-Aranda, Armando Cuéllar, Antonio Uribe, Gerardo Ibarrola, Armando García, Roberto Islas, and Lucio Camarillo (2021). “Evaluation of the Seismic Alert System of Mexico (SASMEX) during the June 23, 2020, Oaxaca Earthquake (Mw 7.4)”. en. In: *Natural Hazards* 108.3, pp. 3085–3098.

Sun, Tianhaozhe and Kelin Wang (2015). “Viscoelastic relaxation following subduction earthquakes and its effects on afterslip determination”. en. In: *Journal of Geophysical Research: Solid Earth* 120.2, pp. 1329–1344.

Sykes, L. R. and W. Menke (2006). “Repeat Times of Large Earthquakes: Implications for Earthquake Mechanics and Long-Term Prediction”. In: *Bulletin of the Seismological Society of America* 96.5, pp. 1569–1596.

Tesei, Telemaco, Cristiano Collettini, Brett M. Carpenter, Cecilia Viti, and Chris Marone (2012). “Frictional strength and healing behavior of phyllosilicate-rich faults”. In: *Journal of Geophysical Research: Solid Earth* 117 (B9).

Tong, Xinyue and Luc L. Lavier (2018). “Simulation of slip transients and earthquakes in finite thickness shear zones with a plastic formulation”. en. In: *Nature Communications* 9.1, pp. 1–8.

Tresca, H. (1864). “Sur l’écoulement des corps solides soumis à de fortes pressions [On the flow of solid bodies subjected to large pressures]”. In: 59, pp. 754–63.

Uchida, Naoki, Takeshi Iinuma, Robert M. Nadeau, Roland Bürgmann, and Ryota Hino (2016). "Periodic slow slip triggers megathrust zone earthquakes in northeastern Japan". In: *Science* 351.6272, pp. 488–492.

Villegas-Lanza, J.C., Mohamed Chlieh, Olivier Cavalié, H. Tavera, Patrice Baby, J. Chire-Chira, and J.-M Nocquet (2016). "Active tectonics of Peru: Heterogeneous interseismic coupling along the Nazca megathrust, rigid motion of the Peruvian Sliver, and Subandean shortening accommodation". In: *Journal of Geophysical Research: Solid Earth* 121.

Wang, Kelin, Yan Hu, and Jiangheng He (2012). "Deformation cycles of subduction earthquakes in a viscoelastic Earth". en. In: *Nature* 484.7394, pp. 327–332.

Weiss, Jonathan R., Qiang Qiu, Sylvain Barbot, Tim J. Wright, James H. Foster, Alexander Saunders, Benjamin A. Brooks, Michael Bevis, Eric Kendrick, Todd L. Ericksen, Jonathan Avery, Robert Smalley, Sergio R. Cimbaro, Luis E. Lenzano, Jorge Baron, Juan Carlos Baez, and Arturo Echalar (2019). "Illuminating subduction zone rheological properties in the wake of a giant earthquake". In: *Science Advances* 5.12, eaax6720.

Wojciechowski, Marek (2018). "A note on the differences between Drucker-Prager and Mohr-Coulomb shear strength criteria". In: *Studia Geotechnica et Mechanica* 40.

Wu, Yih-Min, Wen-Tzong Liang, Himanshu Mittal, Wei-An Chao, Cheng-Horng Lin, Bor-Shouh Huang, and Che-Min Lin (2016). "Performance of a Low-Cost Earthquake Early Warning System (P-Alert) during the 2016 ML 6.4 Meinong (Taiwan) Earthquake". In: *Seismological Research Letters* 87.5, pp. 1050–1059.

Zang, Arno and Ove Stephansson (2009). *Stress Field of the Earth's Crust*. en. Springer Science & Business Media.

Zelst, Iris van (2020). "Tsunamigenic earthquakes from tectonics to dynamic rupture". en. doctoral thesis. ETH Zurich.

6 General Discussion and Conclusion

This thesis explores the different scales and process interactions involved in the formation of continental plate boundaries by making use of state-of-the-art geodynamic modeling tools. I specifically studied the interaction (1) of a rifting crust with the heat flow field, (2) of rock softening with the kinematics of folding and faulting, (3) of neighboring restraining and releasing bends in a strike-slip model that includes geodynamic and surface processes. I furthermore prepared the ASPECT software for studying interactions related to earthquake-like behavior. Figure 6.1 summarizes the processes and interactions within and across Chapters, which I will discuss in the following in more detail.

6.1 Temperature Diffusion, Rifting and Faulting

The first interaction that I studied is the transient heat flow with the folding, faulting, and crustal thinning related to continental rifting. In Chapter 2, I investigate the strength and location of the transient temperature signal in relationship to a range of extension velocities varying between 0.5 and 10 mm/yr and crustal thicknesses between 20 and 50 km. I therewith include the conditions of most wide and narrow rifts worldwide. Since continental rifts are a major source for resources like hydrocarbons or geothermal heat(e.g. Brune et al., 2023, and references therein), the prediction of subsurface temperatures as correct as possible, is important. Changes of a few tenths of degrees Celsius may have a big impact, e.g. when determining the feasibility of a geothermal power plant (e.g. Bodvarsson, 1974; Nathenson, 1975).

Even though the heating effect of a thinning crust is well known, the transients of this heat flow component are mostly not taken into account when deducing present day heat flow fields. Instead, temperatures are mostly computed under the simplification of the 1D heat equation and the assumption of an immediately equilibrating temperature field (e.g. Scheck-Wenderoth et al., 2014; Freymark et al., 2017; Sippel et al., 2017). To take the long-term temporal component of diffusing temperatures in an ever-changing system into account, I set up a series of generic geodynamic simulations. This resulted in thresholds for the applicability of the steady-state assumption and guidelines for the uncertainty range in continental rifts. Both much depend on the exact location and the scale involved in the research question. The models show the largest deviation from the 1D temperature field for locations beneath the rift shoulders of narrow rifts. The mismatch becomes more important and concerns larger depths with increasing rifting velocities as isotherms are faster advected to the surface. We find that the 100°C isotherm is never shallower than 5 km compared to its steady-state counterpart with an average of about 1 km difference in depth. On a crustal scale this may seem small. However, when drilling, 1 km can make a difference of millions of Euros (e.g. Lukawski et al., 2014) which may change the feasibility of a planned project. When looking at deeper isotherms the transient rifting-related temperature signal becomes even larger. For the 400° isotherm, the tectonically-induced advection may be larger than 15 km at locations below the faults of the rift flanks.

This interaction of comparably slow temperature diffusion in crustal material with the much faster tectonic deformation may have implications on various other variables and processes. Amongst others, a rise in temperatures changes the stable phase of mineral assemblages (e.g. Matthes, 1990, and references therein), alters the solubility of minerals in a fluid and the saturation level of a fluid (e.g. Suleimenov et al., 1994), and may imply a transition from crystallized to molten rock in an extreme case. Higher temperatures furthermore change the frictional behavior of a fault (see Chapter 5.1.3 for details) which needs to be taken into account when analyzing the seismic hazard of a region. It is therefore important to incorporate this uncertainty of tectonic origin in the subsurface temperature modeling for many projects.

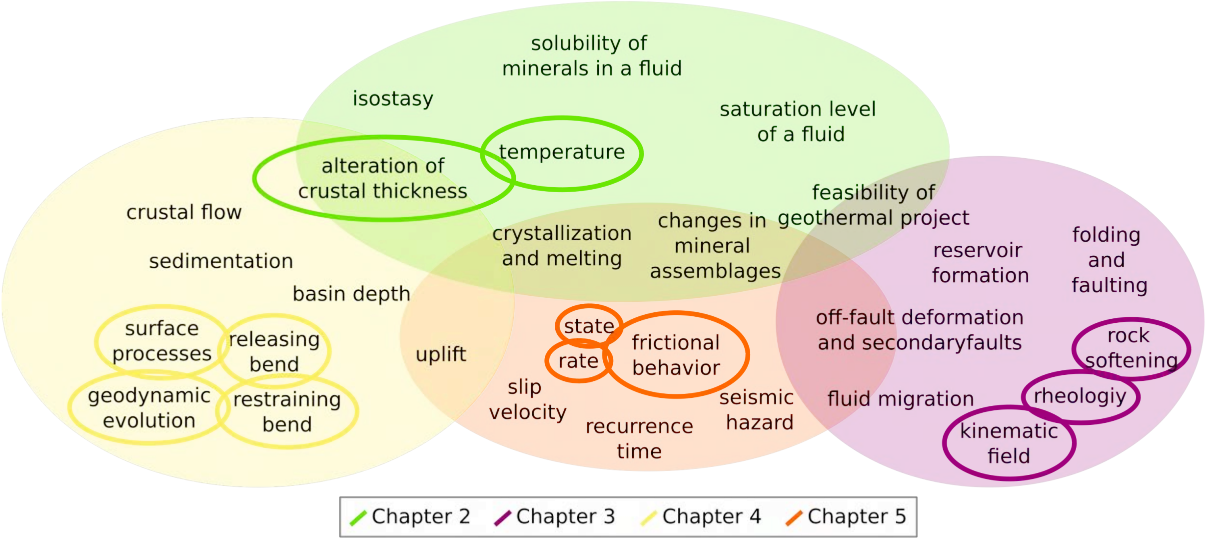

Figure 6.1: A graphical summary of examplary process interactions at plate boundaries discussed in this thesis. Colors indicate the Chapters where they are researched. Solid ellipses mark the processes studied while transparent areas enclose the resulting processes and interactions.

6.2 The Kinematics of Folding and Faulting, Rheological Contrasts, and Reservoirs

My second research question deals with the applicability of the theoretical and purely kinematic trishear model, which was first proposed by (Erslev, 1991), to more realistic setups of fault-propagation folds as described in Chapter 3. Therein I investigate the implications of different rheological parameters, such as changes in cohesion and the angle of friction and their impact on the velocity field and the style of folding and faulting. Large fault-propagation folds are typical structures of fold-and-thrust belts which are situated in the borders of a range of compressional plate boundaries such as the Himalayan-Pamir mountain belt, the Alps and the Andes (Fig. 1.2). However, fault-propagation folds can be found on a variety of scales ranging from millimeters to tens of kilometers (Fig. 3.1). In my models, I am simulating folding behind and above the tip of faults with a length of a few kilometers involving three rock layers with a total thickness of 15 km. Similar geological situations have been found to host fluid reservoirs of economic importance, which for example bear hydrocarbons such as oil and gas or water bodies (Cooper, 2007; Goffey et al., 2010; Hammerstein et al., 2020, and references therein). Identifying potential host structures and reconstructing their evolution is the first step to find and use these valuable resources.

The trishear model has succesfully been applied to the inverse reconstruction of fault-propagation folds (e.g. Hardy et al., 1997; Allmendinger et al., 2005; Grothe et al., 2014), even though it limits deformation to a triangular zone above the fault tip. Instead, our geodynamic forward models cover more complex setups with a variety of lithologies and rheological contrasts and deformation may occur everywhere. While the kinematic fields of both kind of models are comparable for structures of limited complexity as in the initial phases of folding and faulting, I show that later stage folding is not well represented by the purely kinematic model. This is due to the increased propagation of the main fault and the appearance of secondary structures and faults. I therewith contribute to the understanding of the rheological impact on the evolution of fault-propagation folds. The timing of folding in interaction with the presence of fluids may for instance determine if the forming anticline structure will act as a trap and form a reservoir or not (e.g. Roure et al., 2005). Furthermore its lifetime may be limited by the main fault breaking through the folded roof or by the appearance of secondary faults and cracks (Evans et al., 2012; Cosgrove, 2015, and references therein). In Chapter 3, I find for example that relatively weak cover layers, e.g. simluated by an evaporitic rheology, experience more diffuse deformation, which is the geodynamic modeling equivalence of small scale faulting. In reality, these faults might provide pathways for the migration of fluids. For the evalution of potential reservoir-bearing folds with complex folding and faulting histories, it is therefore important to take the rheological particularities and contrasts of all units involved into account.

The existence or non-existence of small-scale faulting in the upper layer may also make a difference in terms of landscape evolution. More fractured, weaker layers will facilitate erosion (e.g. Dühnforth et al., 2010), which in turn will change the principal stress directions and thus impact the kinematics of the underlying fault system (Fig. 1.1). Surface processes have been ignored in the model suite of Chapter 3 together with numerous other processes acting in the real-world. However, including more of them will again increase our understanding of the many interactions and feedbacks shaping small- and big-scale folding and faulting. With my models I made one further step out of the simplifying trishear model to more realistic rheologies.

6.3 Tectonics, Surface Processes, and Restraining and Releasing Bends

Chapter 4 deals with a variety of interactions. These include those between surface processes and tectonics through the coupling of ASPECT and FastScape as well as feedbacks between neighboring restraining and releasing bends of a major strike-slip fault. I included all of them in a single generic 3D model setup of a strike-slip fault with two stepovers. Its areal extent, boundary velocity and crustal thickness were roughly based on the Dead Sea Fault as an example region with adjacent pull-apart basin and push-up mountains, namely the Dead Sea Basin and the Lebanese mountains. I find that the efficiency of surface processes has no major impact on the general fault system outline but alters topograhical elevations and the stress regime. The basin's depth is controlled both by sediment deposition (e.g. Bond et al., 1988) and strike-slip velocity through the timing and complexity of the fault network evolution (see Chapter B.3 for details). This is in general accordance with previous studies (e.g. Berry et al., 2019) but had not been applied to bending strike-slip faults.

Furthermore, I find a crustal flow pattern that links the restraining and the releasing bend and intensifies with surface process efficiency. I see at least two components of the flow linking the bends. One is driven by gravitational potential energy and erosion of the restraining bend and moves crustal material from higher elevations and thicker crust to lower elevations and thinner crust, i.e. from the restraining to the releasing bend. The other component is smaller and is probably very obscured by the many other processes in observational data. However, with my novel models I am able to catch this second component of flow moving crustal material in the opposite direction, i.e. from the low elevations of the releasing bend to the high elevations and thicker crust of the restraining bend. It is driven by the deposition of sediments in the pull-apart basin. A similar return flow has been described earlier for continental margins that experience rapid sediment accumulation, e.g. those surrounding South-East Asian orogens (Morley et al., 2006; Clift, 2015). My work shows that also areas with sediment accumulation that is several magnitudes smaller experience this kind of flow. Accordingly, I find the flow to be several orders of magnitude slower. Nonetheless, uplift at the model restraining bend is detectably increased and prolonged.

These interactions between surface processes and tectonics at the two types of bends imply that restraining bends evolve differently depending on the existence and proximity of a releasing bend of the same fault and vice versa. Since there are very few studies that include both kinds of bends in a single framework (e.g. Bulkan et al., 2020), there might be many more interactions between the bends that are thus, to date, undescribed. Increased and prolonged uplift may for example alter the temperature distribution in the crust of the restraining bend (e.g. Čermák et al., 1996), which in turn influences the crustal rheology (e.g. Goetze et al., 1979; Beaumont et al., 2006) and the earthquake behavior of its fault system (Chapter 5.1.3).

6.4 Outlook

As described in Chapters 6.1 and 6.3, temperature variations may result from a variety of interactions. As known from various studies, temperature strongly influences rock properties including the transition from brittle to ductile rheology (e.g. Goetze et al., 1979; Beaumont et al., 2006) and the frictional strength of faults (Chapter 5.1.3).With the changes added to the ASPECT code as described in Chapter 5, it is possible to extend the work of Chapters 2–4 to study the impact of the tectonic history to various variables in the light of earthquake risk assessment. The additions from Chapter 5 yield the basis to restart any kind of crustal ASPECT model on smaller time-scales with earthquake-like behavior enabled. This may greatly increase our understanding of crustal interactions on shorter time-scales and has the potential of improving seismic hazard assessments of major faults worldwide. This would not only improve our general understanding but could also help to identify infrastructure at risk and modify it accordingly.

Improving geodynamic software to model even more realistic setups is an ongoing development in the field of geodynamic modeling and is accompanied and greatly supported by great advances in computational infrastructure. The possibility to use cross-scale code coupling and the development towards exa-scale computation does not only improve model resolution but also increases the options for more and more realistic interaction chains as an increasing number of processes can be included in the computation. Fast and recent progress is especially visible in the field of modeling the seismic cycle (e.g. Pipping et al., 2016; Erickson et al., 2017; Herrendörfer et al., 2018; Barbot, 2019; Zelst et al., 2019; Erickson et al., 2020). However, so far, merely software using the boundary integral equation method or boundary element method has proven sufficient for modeling recurrent earthquakes (e.g. Lapusta et al., 2009; Barbot, 2019). Conversely to software that uses the finite element method like ASPECT, this holds the disadvantage of a prescribed fault system. The rate-and-state implementation in ASPECT together with its improved visco-elasto-plastic rheology may overcome this obstacle with freely evolving fault systems. Additionally, this could open the possibility to shed light onto the many hidden and obscured interactions in the Earth's crust on a wide range of temporal and spatial scales in a single modeling framework.

6.5 General Conclusion

In this thesis I aim to qualify and quantify process interactions at continental plate boundaries. With my work, I cover a wide range of temporal and spatial scales, and include models of all three main plate boundary types. Since many processes are difficult to study with observational data, I use geodynamic modeling where I have full controll on the complexity and the efficiency of single processes and their interactions.

My main findings include

(1) a quantification of the transient tectonic thermal imprint on crustal temperatures in continental rifts in Chapter 2. I compare it to the 1D steady-state heat flow field often assumed for the modeling of crustal temperatures. This interaction between the comparably slow conduction of heat and the faster tectonic deformation of folding, faulting and creep has implication for all temperature-dependent processes. It may for example change conclusions on the feasibility of the exploitation of geothermal or hydrocarbon reservoirs, the prevailing mineral assemblage, the presence of melt, or the chemical composition of fluids.

(2) interactions between the kinematics of fault-propagation folding and the rheological properties of the rock units involved in Chapter 3. These structures are often modeled with the kinematic trishear model for which the results compare well to simple geologic settings in geodynamic models. However, geodynamic models can cover more complex and therewith realistic geologic settings which for example include off-fault deformation. Studying off-fault deformation and secondary faulting during the evolution of a fold structure may provide valuable insights on fluid migration, and reservoir formation.

(3) feedback mechanisms of geodynamic and surface processes which ultimately link neighboring releasing and restraining bends on a crustal level. In Chapter 4, I show that two opposing types of crustal flow exist. One is driven by gravitational potential energy and moves crustal material from the thickened crust of the restraining bend to the thinned crust of the releasing bend. This is influenced by surface processes through the thinning effect of erosion on the restraining bend crust. On the other hand, sediment deposition drives a small opposed component of crustal flow that moves material from the releasing to the restraining bend. This effect too is influenced by surface processes through its controll on sedimentation.

While these findings enhance our view on plate boundary processes and their interactions, it is yet only a small window into the big picture of process interactions at plate boundaries. Further improvement of geodynamic software will enable the study of more and more complex settings and reveal interactions on the many different spatial and temporal scales involved, e.g. by linking short-term tectonic events like earthquakes to processes that evolve more slowly as is the aim of Chapter 5. With the recent rapid increase in computational capabilities, we may soon find many more exciting interactions that shape the plate boundaries of the Earth.

References

Allmendinger, R.W., T. Zapata, R. Manceda, and F. Dzelalija (2005). “Trishear kinematic modeling of structures, with examples from the Neuquén Basin, Argentina”. In: *AAPG Memoir* 82, pp. 356–371.

Barbot, Sylvain (2019). “Slow-slip, slow earthquakes, period-two cycles, full and partial ruptures, and deterministic chaos in a single asperity fault”. en. In: *Tectonophysics* 768, p. 228171.

Beaumont, Christopher, M. H. Nguyen, R.A. Jamieson, and S. Ellis (2006). “Crustal flow modes in large hot orogens”. In: *Channel Flow, Ductile Extrusion and Exhumation in Continental Collision Zones*. Geological Society of London.

Berry, M., J. van Wijk, D. Cadol, E. Emry, and D. Garcia-Castellanos (2019). “Endorheic-Exorheic Transitions of the Rio Grande and East African Rifts”. In: *Geochemistry, Geophysics, Geosystems* 20.7, pp. 3705–3729.

Bodvarsson, G. (Sept. 1, 1974). “Geothermal resource energetics”. In: *Geothermics* 3.3, pp. 83–92.

Bond, Gerard C. and Michelle A. Kominz (Dec. 1, 1988). “Evolution of thought on passive continental margins from the origin of geosynclinal theory (≈1860) to the present”. In: *GSA Bulletin* 100.12, pp. 1909–1933.

Brune, Sascha, Folarin Kolawole, Jean-Arthur Olive, D. Sarah Stamps, W. Roger Buck, Susanne J. H. Buiter, Tanya Furman, and Donna J. Shillington (Apr. 2023). “Geodynamics of continental rift initiation and evolution”. In: *Nature Reviews Earth & Environment* 4.4, pp. 235–253.

Bulkan, Sibel, Pierre Henry, Paola Vannucchi, Fabrizio Storti, Cristian Cavozzi, and Jason P Morgan (2020). *The evolution of restraining and releasing bend pairs: analogue modelling investigation and application to the Sea of Marmara*. en. preprint.

Čermák, Vladimir and Louise Bodri (May 30, 1996). “Time-dependent crustal temperature modeling: Central Alps”. In: *Tectonophysics*. Geothermal aspects of lower crustal structure, heat flow and hydrothermal circulation 257.1, pp. 7–24.

Clift, Peter D. (Nov. 14, 2015). “Coupled onshore erosion and offshore sediment loading as causes of lower crust flow on the margins of South China Sea”. In: *Geoscience Letters* 2.1, p. 13.

Cooper, Mark (Jan. 1, 2007). “Structural style and hydrocarbon prospectivity in fold and thrust belts: a global review”. In: *Deformation of the Continental Crust: The Legacy of Mike Coward*. Ed. by A. C. Ries, R. W. H. Butler, and R. H. Graham. Vol. 272. Geological Society of London.

Cosgrove, J. W. (Jan. 2015). “The association of folds and fractures and the link between folding, fracturing and fluid flow during the evolution of a fold–thrust belt: a brief review”. In: *Geological Society, London, Special Publications* 421.1, pp. 41–68.

Dühnforth, Miriam, Robert S. Anderson, Dylan Ward, and Greg M. Stock (May 1, 2010). “Bedrock fracture control of glacial erosion processes and rates”. In: *Geology* 38.5, pp. 423–426.

Erickson, Brittany A., Eric M. Dunham, and Arash Khosravifar (2017). “A finite difference method for off-fault plasticity throughout the earthquake cycle”. en. In: *Journal of the Mechanics and Physics of Solids* 109, pp. 50–77.

Erickson, Brittany A., Junle Jiang, Michael Barall, Nadia Lapusta, Eric M. Dunham, Ruth Harris, Lauren S. Abrahams, Kali L. Allison, Jean-Paul Ampuero, Sylvain Barbot, Camilla Cattania, Ahmed Elbanna, Yuri Fialko, Benjamin Idini, Jeremy E. Kozdon, Valère Lambert, Yajing Liu, Yingdi Luo, Xiao Ma, Maricela Best McKay, Paul Segall, Pengcheng Shi, Martijn van den Ende, and Meng Wei (2020). “The Community Code Verification Exercise for Simulating Sequences of Earthquakes and Aseismic Slip (SEAS)”. en. In: *Seismological Research Letters* 91.2A, pp. 874–890.

Erslev, E.A. (1991). “Trishear fault-propagation folding”. In: *Geology* 19.6, pp. 617–620.

Evans, Mark A., Gray E. Bebout, and Carolyn H. Brown (Nov. 5, 2012). “Changing fluid conditions during folding: An example from the central Appalachians”. In: *Tectonophysics*. Into the Deformation History of Folded Rocks 576-577, pp. 99–115.

Freymark, Jessica, Judith Sippel, Magdalena Scheck-Wenderoth, Kristian Bär, Manfred Stiller, Johann-Gerhard Fritsche, and Matthias Kracht (2017). “The deep thermal field of the Upper Rhine Graben”. In: *Tectonophysics* 694, pp. 114–129.

Goetze, Christopher and Brian Evans (Dec. 1, 1979). “Stress and temperature in the bending lithosphere as constrained by experimental rock mechanics”. In: *Geophysical Journal International* 59.3, pp. 463–478.

Goffey, Graham P., Jonathan Craig, Tim Needham, and Robert Scott (Jan. 2010). “Fold–thrust belts: overlooked provinces or justifiably avoided?” In: *Geological Society, London, Special Publications* 348.1, pp. 1–6.

Grothe, P.R., N. Cardozo, K. Mueller, and T. Ishiyama (2014). “Propagation history of the Osaka-wan blind thrust, Japan, from trishear modeling”. In: *Journal of Structural Geology* 58, pp. 79–94.

Hammerstein, James A., Raffaele Di Cuia, Michael A. Cottam, Gonzalo Zamora, and Robert W. H. Butler (2020). “Fold and thrust belts: structural style, evolution and exploration – an introduction”. In: *Geological Society, London, Special Publications* 490.1, pp. 1–8.

Hardy, S. and M. Ford (1997). “Numerical modeling of trishear fault propagation folding”. In: *Tectonics* 16.5, pp. 841–854.

Herrendörfer, Robert, Taras Gerya, and Ylona van Dinther (2018). “An Invariant Rate- and State-Dependent Friction Formulation for Viscoeastoplastic Earthquake Cycle Simulations”. en. In: *Journal of Geophysical Research: Solid Earth* 123.6, pp. 5018–5051.

Lapusta, Nadia and Yi Liu (2009). “Three-dimensional boundary integral modeling of spontaneous earthquake sequences and aseismic slip”. en. In: *Journal of Geophysical Research: Solid Earth* 114.B9.

Lukawski, Maciej Z., Brian J. Anderson, Chad Augustine, Louis E. Capuano, Koenraad F. Beckers, Bill Livesay, and Jefferson W. Tester (June 1, 2014). “Cost analysis of oil, gas, and geothermal well drilling”. In: *Journal of Petroleum Science and Engineering* 118, pp. 1–14.

Matthes, Siegfried (1990). “Gleichgewichtsbeziehungen in metamorphen Gesteinen”. In: *Mineralogie: Eine Einführung in die spezielle Mineralogie, Petrologie und Lagerstättenkunde*. Ed. by Siegfried Matthes. Berlin, Heidelberg: Springer, pp. 334–337.

Morley, Christopher K. and Rob Westaway (2006). “Subsidence in the super-deep Pattani and Malay basins of Southeast Asia: a coupled model incorporating lower-crustal flow in response to post-rift sediment loading”. In: *Basin Research* 18.1, pp. 51–84.

Nathenson, M. (Oct. 1, 1975). *Physical factors determining the fraction of stored energy recoverable from hydrothermal convection systems and conduction-dominated areas*. USGS-OFR-75-525.

Pipping, Elias, Ralf Kornhuber, Matthias Rosenau, and Onno Oncken (2016). “On the efficient and reliable numerical solution of rate-and-state friction problems”. en. In: *Geophysical Journal International* 204.3, pp. 1858–1866.

Roure, F., R. Swennen, F. Schneider, J. L. Faure, H. Ferket, N. Guilhaumou, K. Osadetz, P. Robion, and V. Vandeginste (Jan. 1, 2005). “Incidence and Importance of Tectonics and Natural Fluid Migration on Reservoir Evolution in Foreland Fold-And-Thrust Belts”. In: *Oil & Gas Science and Technology* 60.1, pp. 67–106.

Scheck-Wenderoth, Magdalena, Mauro Cacace, Yuriy Petrovich Maystrenko, Yvonne Cherubini, Vera Noack, Bjoern Onno Kaiser, Judith Sippel, and Lewerenz Bjoern (2014). “Models of heat transport in the Central European Basin System: Effective mechanisms at different scales”. English. In: *Marine and Petroleum Geology* 55, pp. 315–331.

Sippel, Judith, Christian Meeßen, Mauro Cacace, James Mechie, Stewart Fishwick, Christian Heine, Magdalena Scheck-Wenderoth, and Manfred R. Strecker (2017). “The Kenya rift revisited: insights into lithospheric strength through data-driven 3-D gravity and thermal modelling”. In: *Solid Earth* 8.1, pp. 45–81.

Suleimenov, O. M. and R. E. Krupp (June 1, 1994). “Solubility of hydrogen sulfide in pure water and in NaCl solutions, from 20 to 320°C and at saturation pressures”. In: *Geochimica et Cosmochimica Acta* 58.11, pp. 2433–2444.

Zelst, I. van, S. Wollherr, A.-A. Gabriel, E. H. Madden, and Y. van Dinther (2019). “Modeling Megathrust Earthquakes Across Scales: One-way Coupling From Geodynamics and Seismic Cycles to Dynamic Rupture”. en. In: *Journal of Geophysical Research: Solid Earth* n/a.n/a.

7 Acknowledgements

For my PhD I have been financed by the Geo.X Young Academy as a fellow of the 2^{nd} cohort and my models have almost all been run using the clusters provided by the North-German Supercomputing Alliance. Furthermore, I was supported by the Computational Infrastructure for Geodynamics for my work on the development of ASPECT. I am very grateful for that!

I then want to thank Sascha and Anne for the great cooperation and supervision during my PhD, I always felt so well supported by you, even through all these homeoffice times during Covid restrictions. Thanks for always being there, following and supporting my work, thanks for all those weekly and long discussions, critical comments and kind words! It was an absolute pleasure to work with you!

Similarly, huge thanks to the rest of my lovely section 2.5, for the nice conversations at lunch and elsewhere, as well as the amazing and supportive athmosphere! I will so definitively miss you!

And then there are so many more people that accompanied me over the duration of this project that I want to thank. I especially want to mention my family, as well as Tim, Willi, Katja, Debby, and the GeoWunderWerkstatt :) But also all the rest of you amazing people around me that encouraged me, pushed me, helped me, and kindly distracted me when needed during these last four and half years. Thank you so much for having been there! I sincerely would not have made it without you!

A Supplementary Material Chapter 2: Is there a Speed Limit for the Thermal Steady-State Assumption in Continental Rifts?

Esther Heckenbach[1,2], Sascha Brune[1,2], Anne Glerum[1], Judith Bott [Sippel][1] (2021):
Is there a Speed Limit for the Thermal Steady-State Assumption in Continental
Rifts? *Geochemistry, Geophysics, Geosystems(G3)*, 22, 3, e2020GC009577.
https://doi.org/10.1029/2020GC009577

[1] GFZ German Research Centre for Geosciences, 14473 Potsdam, Germany
[2] Institute of Geosciences, University of Potsdam, 14476 Potsdam-Golm, Germany

Contents

1. Results for the alternative steady-state model series using the dynamic model 1300°C isotherm as steady-state thermal LAB, comparable to Figures 2.4–2.6 of the main text.
2. Figures of mean $\Delta d_{\text{isotherm}}$ for the evolution of four exemplary models.
3. Additional plots for isotherms between 100°C and 600°C.
4. Alternative setups of the steady-state models using a 1250°C boundary condition at the LAB or a 2D thermal steady-state equation.

A.1 Alternative definition of the LAB

Figures 2.4–2.6 of the main text, but for the alternative steady-state model series. Here, instead of the material contour at the bottom of the lithospheric mantle, the 1300°C isotherm is extracted from the dynamic model snapshot and used as the steady-state thermal LAB. Comparing Figures 2.4–2.6 of the main text to Figures A.S1–A.S3, it can be seen that the overall pattern of $\Delta d_{\text{isotherm}}$ is the same for both approaches. However, the values for $\Delta d_{\text{isotherm}}$ are smaller and have a more local effect when the material contour is chosen as the steady-state LAB, as is discussed in the main text.

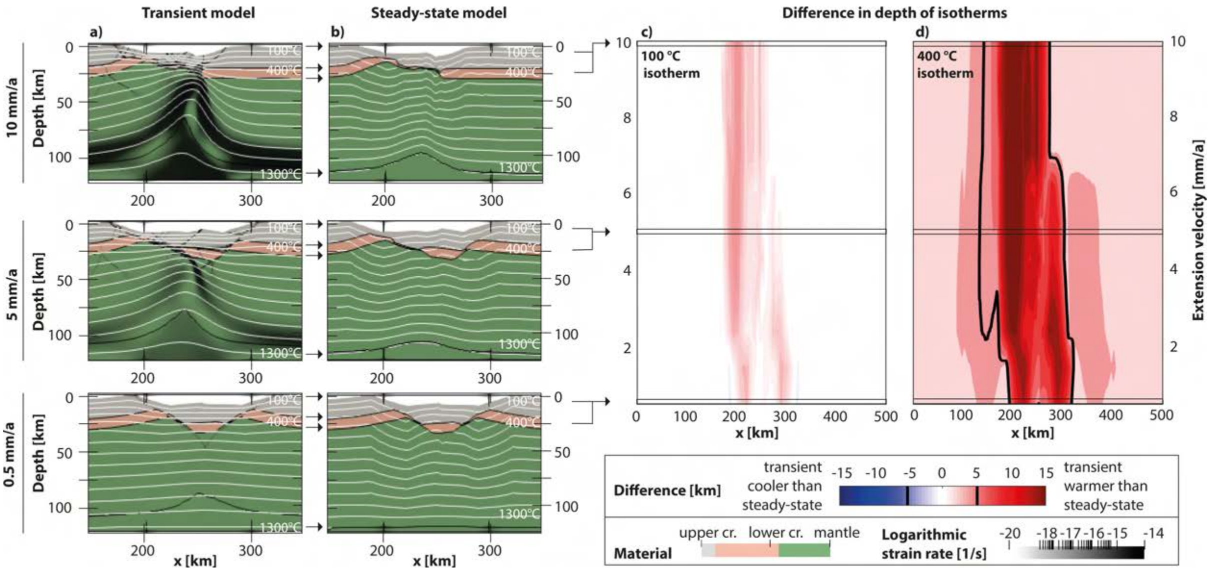

Figure A.S1: Impact of using the 1300°C isotherm to define the LAB of the steady-state models in narrow rift setups. The difference to the setup of Figure 2.4 in the main manuscript is best visible in (b), where the isotherms at the base of the model are more evenly distributed. However, shallower crustal isotherms are almost not affected, so that the differences in depth of isotherms (c,d) are very similar to those shown in Figure 2.4.

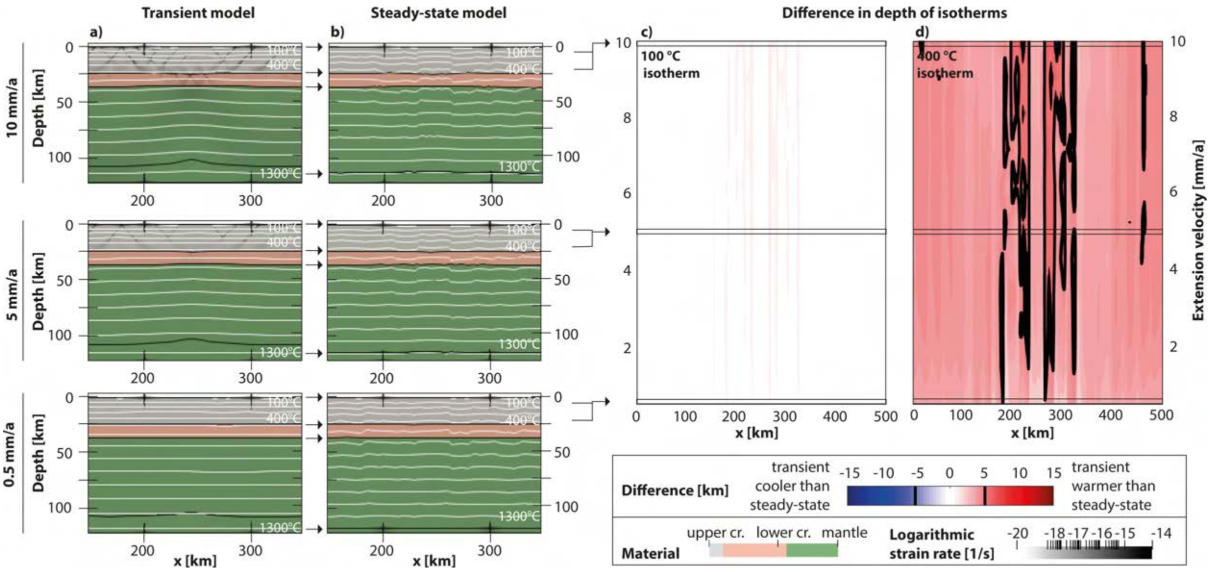

Figure A.S2: Impact of using the 1300°C isotherm to define the LAB of the steady-state models in wide rift setups. The difference to the setup of Figure 2.5 in the main manuscript is best visible in (b), where the isotherms at the base of the model are more distributed. However, shallower crustal isotherms are almost not affected, so that the differences in depth of isotherms (c,d) are very similar to those shown in Figure 2.5.

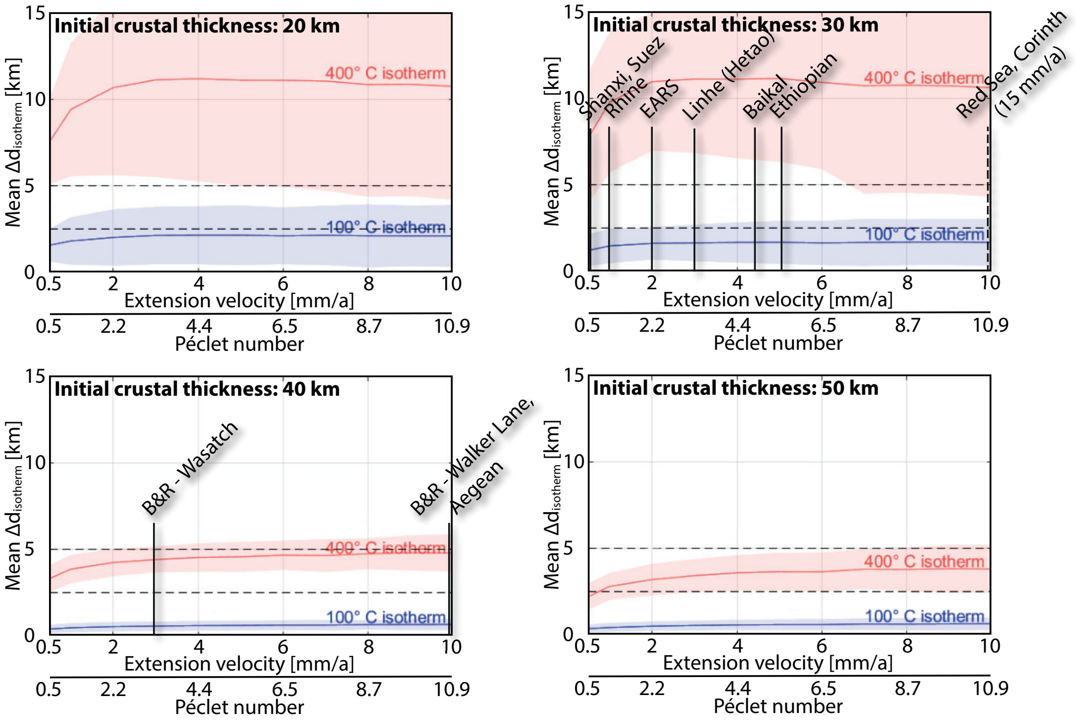

Figure A.S3: Impact of using the 1300°C isotherm to define the LAB of the steady-state models. The diagrams reveal a roughly 30% greater depth difference than for the reference LAB definition. For more figure details and abbreviations, see Figure 2.6 in the main manuscript.

A.2 Evolution of $\Delta d_{\mathrm{isotherm}}$ for four exemplary models

In the main text, we discuss $\Delta d_{\mathrm{isotherm}}$ after 50 km of extension only. Here, we show the entire evolution of the difference in isotherm depth for four exemplary models. It can be seen that the mean $\Delta d_{\mathrm{isotherm}}$ stays in the same range after a first build-up phase, making the analyses of the 50 km snapshots representative for almost the entire rift evolution.

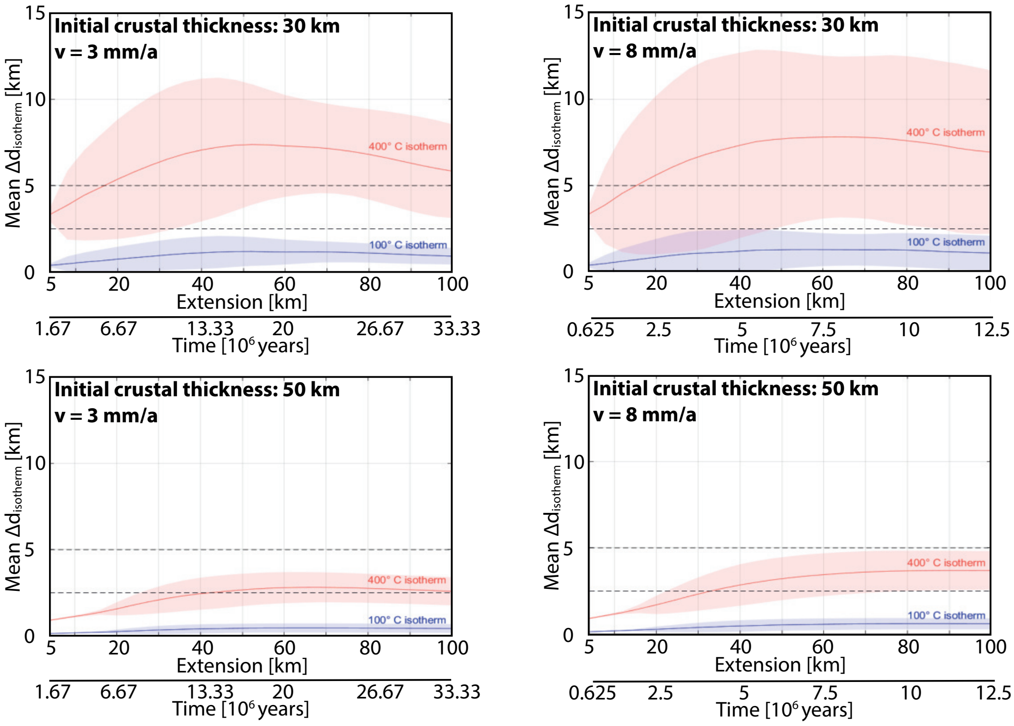

Figure A.S4: Differences of the isotherm depth for the evolution of four exemplary models with extension velocities of 3 and 8 mm/a and initial crustal thicknesses of 30 and 50 km. The x-axis indicates the amount of extension in km and the time after model start in million years. Solid lines give the arithmetic mean of $\Delta d_{\mathrm{isotherm}}$ in the central third of the model domain, which includes the entire rift region for all narrow rifts. The one standard deviation interval is shown as a colored envelop. The dashed lines represent the similarity thresholds $\epsilon = \pm 2.5$ and $\epsilon = \pm 5$ km.

A.3 Additional plots for isotherms between 100°C and 600°C

Here, we show the difference between transient and steady-state models in terms of $\Delta d_{\mathrm{isotherm}}$ for isotherms between 100°C and 600°C for all crustal thicknesses and extension velocities. These plots are analogous to the right-hand sides of Figures 2.5 and 2.6. Red colors indicate a warmer crust in the transient model with the isotherms being shallower compared to the steady-state model. The black contour marks a 5 km difference in depth.

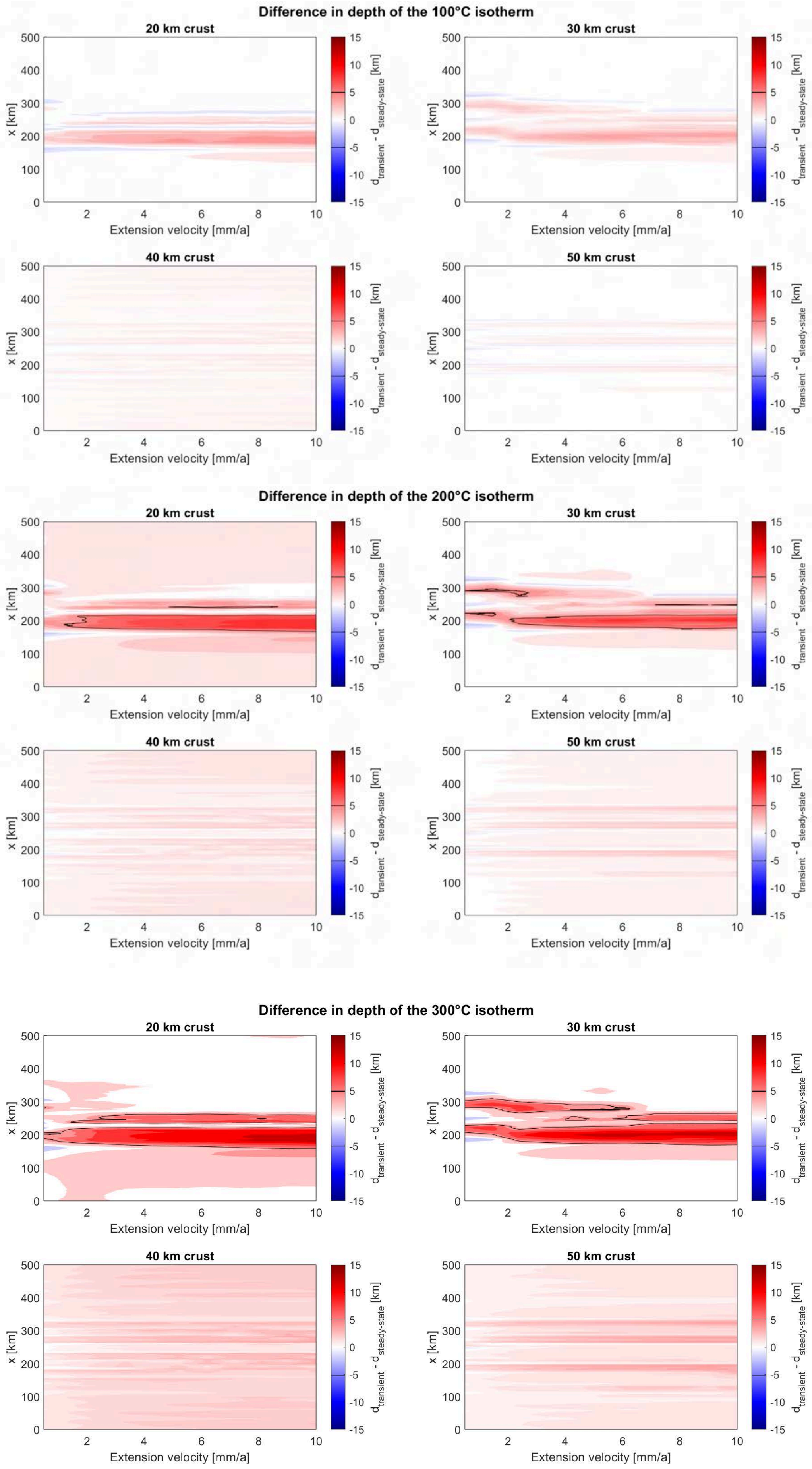

Figure A.S5: a) $\Delta d_{\mathrm{isotherm}}$ for the 100, 200, and 300°C isotherms for all crustal thicknesses and extension velocities.

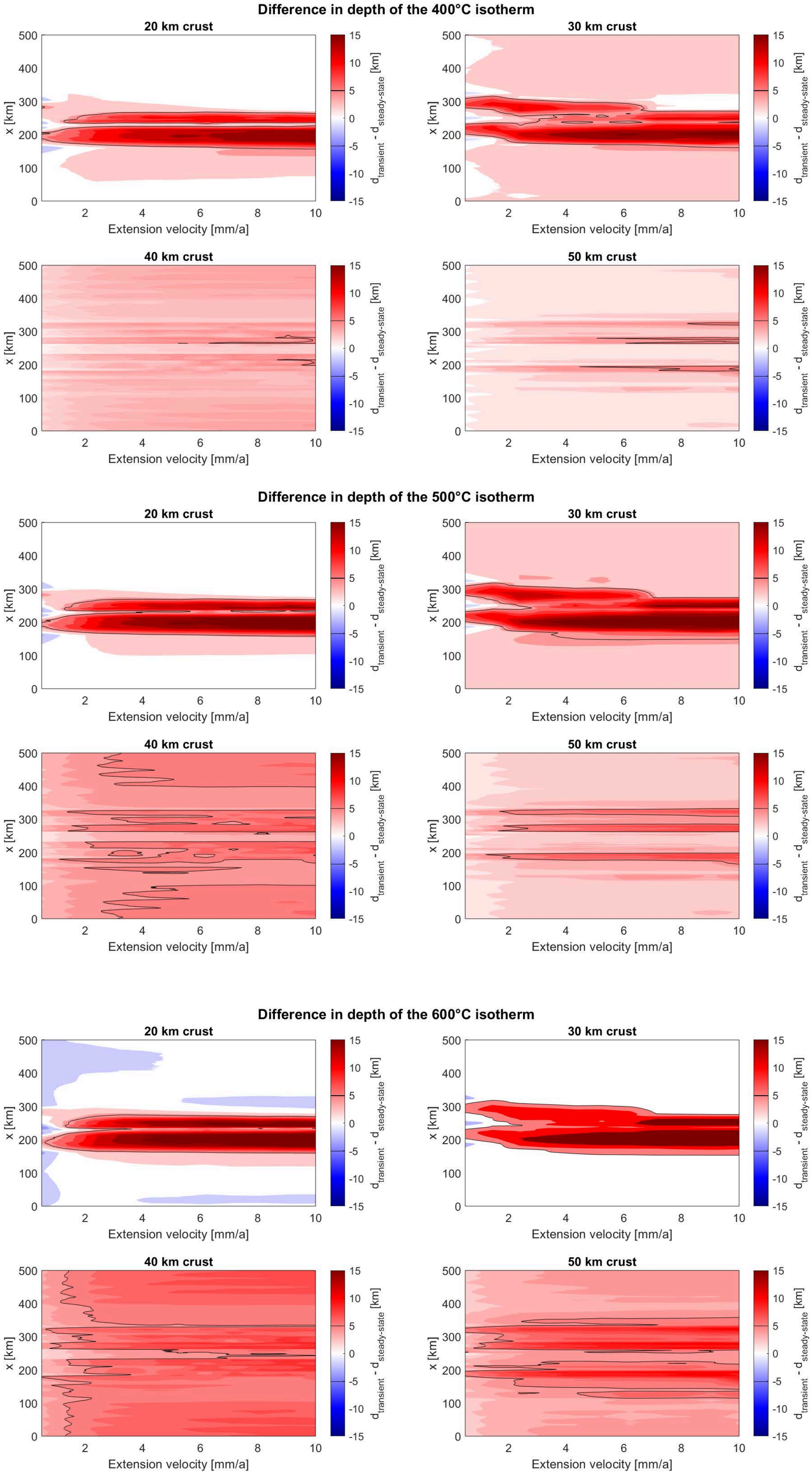

Figure A.S5: b) $\Delta d_{\text{isotherm}}$ for the 400, 500, and 600°C isotherms for all crustal thicknesses and extension velocities.

A.4 Alternative setups of the steady-state models

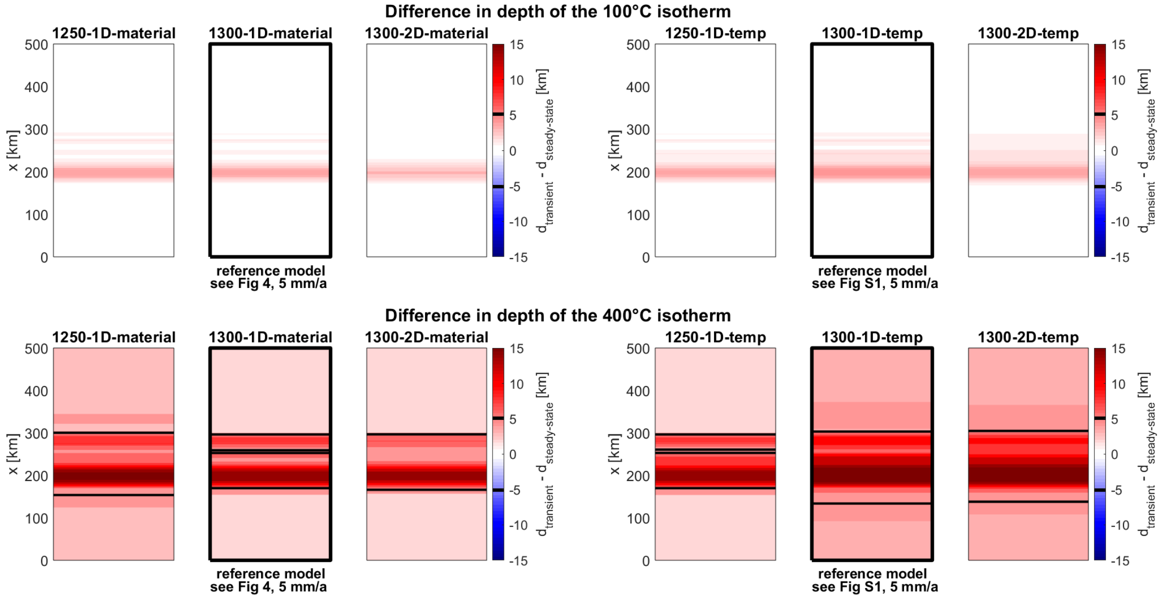

Figure A.S6: Comparison of the influence of alternative setups of the steady-state models.

In this section, we compare the models used in the analysis of the main text with alternative setups of the steady-state models. We use an exemplary model which has an initial crustal thickness of 30 km and an extension velocity of 5 mm/a to show the influence of different setups of the steady-state models. The steady-state models in the main text use the material contour extracted from the dynamic models as the new LAB which is associated with the 1300°C boundary condition (the plots with a thick black frame display the same model results as in Figure 2.5 in the main text). These models are shown on the left side of Figure A.S6. On the right of Figure A.S6, the same analysis is shown for steady-state models that use an isotherm from the dynamic model as the steady-state LAB (the plots with a thick black frame display the same model results as in Figure 2.2 in the supplement).

We compare these models to two other possibilities to set up the steady-state models: To the left of the plots for the reference models, we use 1250°C as the temperature of the LAB to account for the variation of LAB temperatures found in the literature. For these models we used the same dynamic models as in the main text, but associated the extracted material contour with a 1250°C boundary condition (left), or extracted the 1250°C isotherm from the dynamic model to use it as the steady-state LAB (right). To the right of the plots for the reference models, we use the same temperature for the LAB as in the main analysis (1300°C), but use a 2D thermal steady-state approach, while the models in the main analysis use a 1D steady-state approach.

While the 1D thermal steady-state was achieved by simply initializing a model without deformation (no time-stepping), the 2D thermal steady-state needed to employ a computationally more demanding method. We used the same structural snapshots of the dynamic model, but instead of only initializing a model, the 2D model was run for 1 Ma to allow the temperature field enough time to equilibrate through 2D thermal diffusion based on the given material properties. To ensure that only diffusional processes were active while the surface and the structural boundaries remained constant, zero velocity conditions were applied at the boundaries and only the temperature equation (Eq. 3) was solved. Furthermore, the thermal diffusivity of the asthenosphere was set to an unrealistically high value to prevent cooling at the LAB.

B Supplementary Material Chapter 4: 3D Interaction of Tectonics and Surface Processes explains Fault Network Evolution of the Dead Sea Fault

Esther L. Heckenbach[1,2], Sascha Brune[1,2], Anne C. Glerum[1], Roi Granot[3], Yariv Hamiel[4], Stephan V. Sobolev[1,2], Derek Neuharth[1,5] (submitted): 3D Interaction of Tectonics and Surface Processes explains Fault Network Evolution of the Dead Sea Fault.

[1]GeoForschungsZentrum Potsdam, Potsdam, Germany
[2]Universität Potsdam,Potsdam, Germany
[3]Ben-Gurion University of the Negev, Beer-Sheva, Israel
[4]Geological Survey of Israel, Jerusalem, Israel
[5]ETH Zürich, Zürich, Switzerland

B.1 Numerical model

The geodynamic modeling was carried out using the open-source code ASPECT (Kronbichler et al., 2012; Heister et al., 2017; Gassmöller et al., 2018). In this study, it solves the incompressible flow equations of momentum, mass and energy (assuming an infinite Prandtl number) for velocity $\mathbf{v}$, pressure P and temperature T, combined with advection equations for each Eulerian compositional field c_i:

$$-\nabla \cdot (2\eta\dot{\epsilon}) + \nabla P = \rho \mathbf{g} \tag{B.1}$$

$$\nabla \cdot \mathbf{v} = 0 \tag{B.2}$$

$$\begin{aligned} \bar{\rho} c_P \left(\frac{\partial T}{\partial t} + \mathbf{v} \cdot \nabla T \right) - \nabla \cdot k \nabla T = \bar{\rho} H & \qquad \text{radioactive heating} \\ + (2\eta\dot{\epsilon}) : \dot{\epsilon} & \qquad \text{shear heating} \\ + \alpha T (\mathbf{v} \cdot \nabla P) & \qquad \text{adiabatic heating} \end{aligned} \tag{B.3}$$

$$\frac{\partial c_i}{\partial t} + \mathbf{v} \cdot \nabla c_i = 0, \tag{B.4}$$

where η is the effective viscosity (see Eq. B.5-B.8), $\dot{\epsilon}$ is the deviator of the strain rate tensor $\frac{1}{2}(\nabla \mathbf{v} + (\nabla \mathbf{v})^T)$, density $\rho = \rho_0(1 - \alpha(T - T_0))$ with T_0 the reference temperature, and $\mathbf{g}$ gravity. $\bar{\rho}$ is the adiabatic reference density, c_P the specific isobaric heat capacity, k the thermal conductivity, and α the thermal expansivity, as given in Table B.S1.

We use a visco-plastic rheology (Glerum et al., 2018) with dislocation and diffusion creep rheologies as well as the Drucker-Prager yield criterion. In 2D, these are implemented within ASPECT through the following equations:

$$\eta_{eff}^{comp} = \left(\frac{1}{\eta^{df}} + \frac{1}{\eta^{ds}} \right)^{-1} \qquad \text{composite viscosity} \tag{B.5}$$

$$\text{with} \quad \eta_{ds|df} = \frac{1}{2} A^{-\frac{1}{n_{ds|df}}} d \frac{m_{ds|df}}{n_{ds|df}} \dot{\epsilon}_{ii} \frac{1 - n_{ds|df}}{n_{ds|df}} exp \left(\frac{E_{ds|df} + PV_{ds|df}}{n_{ds|df} RT} \right) \qquad \text{ds—df creep} \tag{B.6}$$

When $2\eta_{eff}^{comp}\dot{\epsilon} > \sigma_y$, the plastic effective viscosity (Eq. B.7) is used instead of the composite effective viscosity (Eq. B.5):

$$\eta_{eff}^{pl} = \frac{\sigma_y}{2\dot{\epsilon}_{ii}} \qquad \text{plastic effective viscosity} \tag{B.7}$$

$$\text{with} \quad \sigma_y = P \cdot sin(\phi) + C \cdot cos(\phi) \qquad \text{Drucker-Prager plasticity} \tag{B.8}$$

where η_{eff} is the effective viscosity, $ds|df$ corresponds to dislocation or diffusion creep, d is grain size, R is the gas constant, $A_{ds|df}$ are prefactors, $n_{ds|df}$ and $m_{ds|df}$ are stress and grain size exponents. For diffusion creep, $n_{df} = 1$, while for dislocation creep, $m_{ds} = 0$. $E_{ds|df}$ are the activation energies, $V_{ds|df}$ are the activation volumes, σ_y is the yield stress, ϕ is the internal angle of friction and C is cohesion. $\dot{\epsilon}_{ii}$ is defined as the square root of the second invariant of the deviatoric strain rate tensor. The final effective viscosity (Eq. B.5 or Eq. B.7) is capped by a user-defined minimum and maximum viscosity η_{min} and η_{max}. The parameters used are listed in Table B.S1.

	Sediments (wet quartzite)	Upper crust (wet quartzite)	Lower crust (wet anorthite)	Lithospheric mantle (dry olivine)	asthenosphere (wet olivine)	Unit
Thermal properties						
thermal diffusivity κ	0.728	0.926	0.585	0.838	0.833	mm^2 s^{-1}
heat capacitiy c_p		1200	1200	1200	1200	J kg^{-1} K^{-1}
density at surface conditions ρ	2118	2668	2835	3260	3300	kg m^{-3}
density at in-situ conditions ρ_0	2150	2750	2900	3300	3300	kg m^{-3}
thermal expansivity α	3.70	2.70	2.70	3.00	3.00	10^{-5} K^{-1}
radioactive heating H	1.2	1.5	0.2	0	0	μW m^{-3}
Dislocation creep	(a)	(a)	(b)	(c)	(c)	
prefactor A_{ds}	$8.57{\cdot}10^{-28}$	$8.57{\cdot}10^{-28}$	$7.13{\cdot}10^{-18}$	$6.54{\cdot}10^{-16}$	$2.12{\cdot}10^{-15}$	Pa^{-n} s^{-1}
stress exponent n_{ds}	4	4	3	3.5	3.5	-
activation energy E_{ds}	223	223	345	530	480	kJ mol^{-1}
activation volume V_{ds}	0	0	$3.80{\cdot}10^{-5}$	$1.80{\cdot}10^{-5}$	$1.10{\cdot}10^{-5}$	cm^3 mol^{-1}
Diffusion creep	(a)	(a)	(b)	(c)	(c)	
prefactor A_{df}	$5.97{\cdot}10^{-19}$	$5.97{\cdot}10^{-19}$	$2.99{\cdot}10^{-25}$	$2.25{\cdot}10^{-9}$	$1.5{\cdot}10^{-9}$	Pa^{-1} s^{-1}
grain size exponent m_{df}	2	2	3	0	0	-
activation energy E_{df}	223	223	159	375	335	kJ mol^{-1}
activation volume V_{df}	0	0	$3.80{\cdot}10^{-5}$	$6.00{\cdot}10^{-6}$	$4.00{\cdot}10^{-6}$	m^3 mol^{-1}
Drucker-Prager plasticity						
friction angle ϕ	30	30	30	30	30	°
cohesion C	20	20	20	20	20	MPa

Table B.S1: Material properties used in the geodynamic models. We assume a grain size of 1 mm that is included in the pre-exponential factors. These factors have further been converted from the experimental values to account for the usage of second invariants for strain rate and stress. The user-defined minimum and maximum viscosities are $\eta_{min} = 1 \cdot 10^{19}$ Pas and $\eta_{max} = 1 \cdot 10^{24}$ Pas. (a) Rutter et al., 2004, (b) Rybacki et al., 2006, (c) Hirth et al., 2004. Frictional strain softening is used, where the friction coefficient reduces linearly from 30° to 7.5° for brittle strain between 0 and 1. For strains larger than 1, it remains constant at 7.5°.

Surface processes are simulated using FastScape (Braun et al., 2013; Yuan et al., 2019), which solves the stream power law:

$$\frac{\partial h}{\partial t} = U - K_f A^m S^n + \frac{G}{A} \int_A \left(U - \frac{\partial h}{\partial t} \right) dA + K_d \nabla^2 h \tag{B.9}$$

where h is topographical height, U uplift, S slope, and A the drainage area. These parameters evolve with the model run and are taken from the surface mesh. Prescribed parameters are K_f - the bedrock river incision rate, m - the drainage area exponent, n - the slope exponent, G - the bedrock deposition coefficient and K_d - the bedrock diffusivity. All values used are listed in Table B.S2. For details about the coupling of ASPECT and FastScape, we refer the reader to Neuharth et al., 2021 and Neuharth et al., 2022.

	Value	Unit
Bedrock river incision rate K_f	$0.25{\cdot}10^{-5}$ / $0.5{\cdot}10^{-5}$ / $1{\cdot}10^{-5}$	$\mathrm{m}^{0.2}/\mathrm{yr}$
Bedrock diffusivity K_d	$1{\cdot}10^{-2}$	m^2/yr
Bedrock deposition coefficient G	1	-
Drainage area exponent m	0.4	-
Slope exponent n	1	-
Marine diffusivity	500	m^2/yr

Table B.S2: Prescribed FastScape parameters for simulations including surface processes

B.2 Influence of inheritance

We represent possible inherited heterogeneity (rock type, weaknesses) with initial non-zero plastic strain. The initial plastic strain magnitude is obtained by multiplying random numbers on the 0–1 interval with a Gaussian distribution of a user-set amplitude and standard deviation perpendicular to the initial fault seeds. The random numbers are controlled by the seed of the random number generator. Varying this seed allows us to generate different initial conditions while keeping all other parameters constant. This holds interesting ramifications because our models show that some aspects of the final basin geometry are controlled by the localization of the first faults around the releasing bend. These modulate the final basin width and the interbasinal structures, but they also affect the asymmetry of the basement surface observed at the Dead Sea, which has been subject to much discussion (Quennell, 1959; Garfunkel, 1981; Ben-Avraham et al., 1992; Wdowinski et al., 1996; Lubberts et al., 2002; DESERT Group et al., 2004). Figure B.S1 shows that minor variations in crustal heterogeneities can play a significant role in shaping the basin (compare Fig. B.S1a,c,e, with b,d,f). However, the asymmetric basement topography is a constant in all presented model results. We therefore suggest that the general asymmetry of the Dead Sea Basin is an inevitable consequence of this particular geological setting, while the details of its actual shape may be influenced by smaller-scale and less-predictable processes.

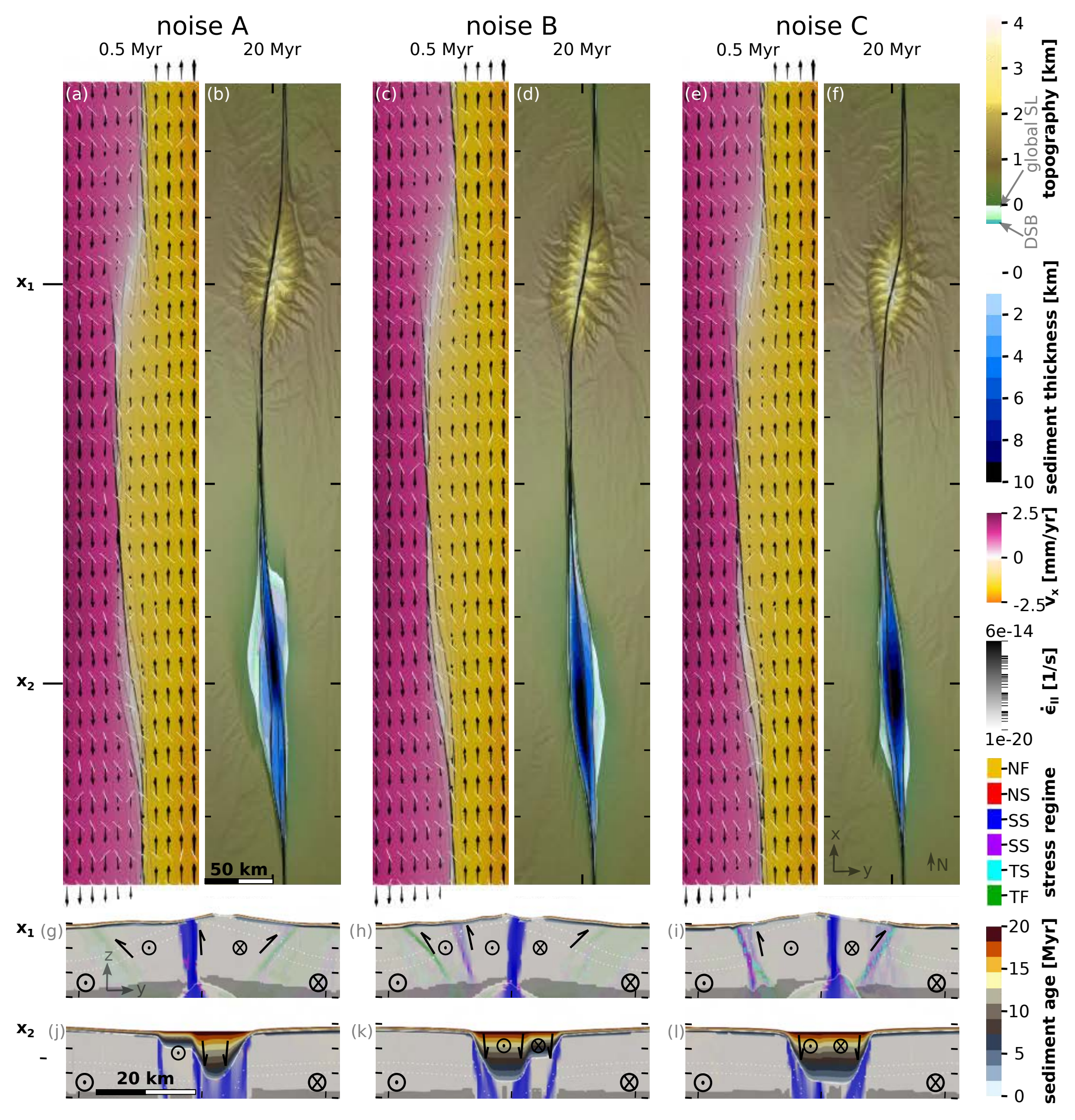

Figure B.S1: Models using different values for the seed of the random noise in initial strain, described with noise A,B,C. (a), (c), (e) Boundary parallel velocity v_x in colour overlain by strain rate in black during the localization phase at 0.5 Myr. The black arrows depict magnitude and direction of the surface velocity, while the white bars show the direction of maximum horizontal compressive stress. (b), (d), (f) Surface topography and sediment thickness overlain by strain rate in black at the end of the model runs at 20 Myr. (g–l) Upper crustal profiles of the stress regime at the locations of the initial stepovers at $x_1 = 150$ km and $x_2 = 450$ km at 20 Myr. Brighter colours correlate with higher strain rates. Lighter areas deform in a brittle, darker areas in a ductile manner. Sediment age is shown in a separate colour scale. Black arrows demonstrate relative motions of fault-separated blocks.

B.3 Influence of the boundary velocity

The reference model has a full strike-slip velocity of 5 mm/yr. We furthermore explored a variation of ± 10%, resulting in velocities of 4.5 and 5.5 mm/yr. These values are within the range of observed and assumed velocity variations for both present day and geological strike-slip motion of the Dead Sea area (Le Beon et al., 2008; Hamiel et al., 2019; Hamiel et al., 2021). For a more generic exploration of the influence of the boundary velocity, we also ran models with 2.5 mm/yr and 10 mm/yr, which is equivalent to half and double the reference velocity (Fig. B.S2). All models were run to the same amount of total displacement of 100 km.

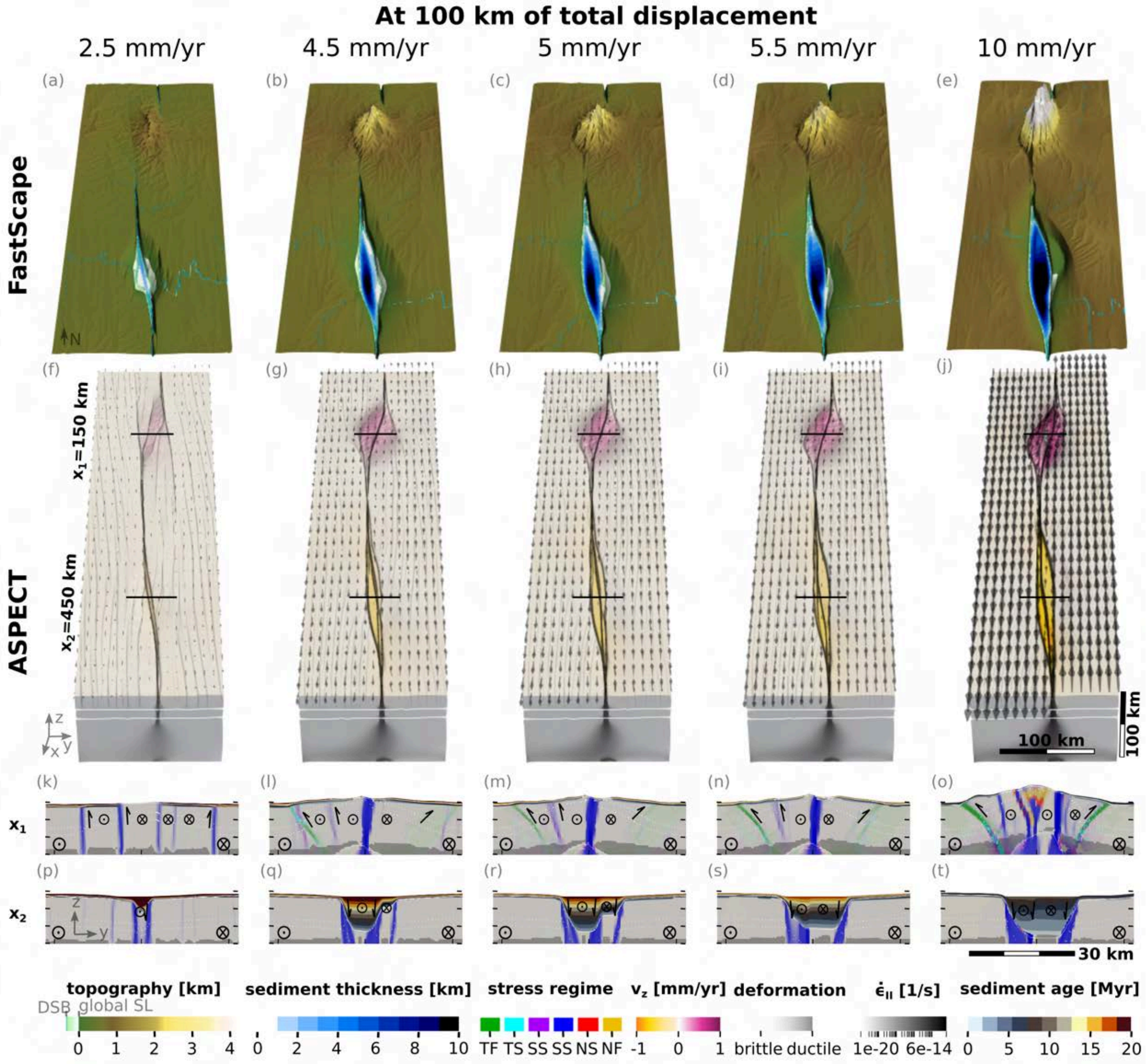

Figure B.S2: Final state of models that were run to a total displacement of 100 km using different boundary velocities (i.e., different velocities need a different amount of time to reach 100 km of displacement). Full strike-slip velocities and model times range from (a) 2.5 mm/yr over 40 Myr to (e) 10 mm/yr over 10 Myr. The reference model in this paper uses (c) 5 mm/yr over 20 Myr. (a–e) show topography, drainage network and sediment thickness. (f–j) vertical velocities shown in colour scale and overlain by strain rate in black and and arrows depicting the magnitude and direction of velocities in the x-y-plane. White lines show layer thicknesses. (k–o) profiles through the restraining bend and (p–t) profiles through the releasing bend. Their location is shown in (f–j). Stress regime is shown as a colour scale with brighter colours indicating higher strain rates. Light areas deform in a brittle and dark areas in a ductile manner. Arrows depict relative motion similar to geological cross sections. Sediment age is indicated in a separate colour scale within the basin. The white dotted lines show the current location of the initially horizontal layer of particles used as deformation markers.

Faster boundary velocities increase basin volume through timing of fault localization. Running the model with double or half the reference boundary velocity to the same amount of total displacement shows that velocity has a larger impact on the resulting basin than the coupling to surface processes. While varying the surface process efficiency mainly affects the topography of the surface and basement, the boundary velocity also has a major impact on the fault network that manifests during the localization phase. At the releasing bend of the slow model with a total strike-slipe velocity of 2.5 mm/yr, the fault localizes as a straight surface trace without many bends, no branching and no deep basin (Fig. B.S2a,f). Contrarily, in the fast model with 10 mm/yr (Fig. B.S2e,j), many faults quickly localize simultaneously and form a mosaic of blocks. The basin quickly elongates and deepens, forming a basin that is wider and deeper than the reference model basin (Fig. B.S2r vs. t). This relationship between opening velocity and sediment volume has also been described for other types of basins (Berry et al., 2019). For the more DSB-like variations of the boundary velocity of 5 mm/yr ± 10% (Fig. B.S2b,d), we see similar trends. Overall, the sediment thickness shows an almost linear relationship with the boundary velocity, where a variation of 0.5 mm/yr changes the sediment thickness by $\sim$1 km. This increase in sediment volume can likely be explained by the fast localization of several faults in the models with greater strike-slip motion. As described in Section 3.1 of the main manuscript, rapid subsidence and sediment accumulation only start with the formation of a second border fault around a distinct crustal block at the location of the future pull-apart basin. While many of these blocks exist early in the fastest model (by $\sim$4 km of strike-slip displacement), the one in the slowest model forms later ($\sim$10 km of strike-slip displacement), which limits sediment accumulation and subsidence.

Faster boundary velocities increase mountain heights and decrease off-fault deformation. At the fault network of the restraining bend, it is noticeable that lower boundary velocities result in longer bordering faults that take up more displacement. This goes hand in hand with the central connecting fault becoming decreasingly important with decreasing velocity. While this central fault is long-lived in most models, in the fastest model (10 mm/yr) several mountain cutting faults exist that are short-lived as the fault network evolves (Fig. B.S2j,o). Except for the fastest model, a decrease in the boundary velocity makes the fault-generated crustal block separation more diffuse and the fault trace more edgy (Fig. B.S2f–i,k–n). While a smoothening fault trace should reduce compressive stresses and therefore uplift, mountain heights in our models increase with increasing velocity. This trend can be explained by the balancing of tectonic and erosional forces and their temporal components (e.g. Willett, 1999). The faster the boundary velocity, the shorter the time for erosion to reduce elevations. For slower strike-slip velocities on the other hand there is more time for erosion to outbalance tectonic uplift. More erosion should hence provide a higher amount of sediments available to fill the pull-apart basin. However, this is not what we observe in our model series (Fig. B.S2p–t). Instead, the models show that sediment thickness is tightly bound to the timing of the formation of a fault-bounded basin floor, and therefore to the interaction of stress, strain and strain rate during the localization phase which limits the depositional space.

B.4 Influence of temporal changes in the boundary velocity

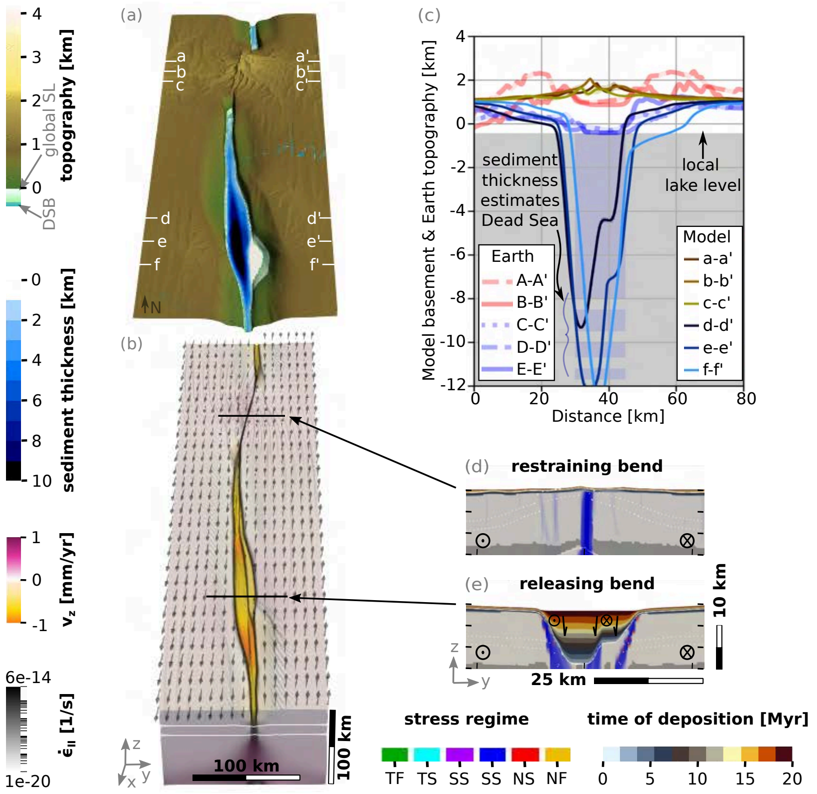

Figure B.S3: Plots of a model that equals the reference model until 15 Myr and has afterwards been restarted until 20 Myr with extension included in the boundary velocity. Extension equals 10% of the strike-slip velocity, so 0.5 mm/yr. (a) topography and sediment thickness. (b) vertical velocity and strain rate pattern. Almost no surface uplift occurs. (c) cross sections comparing model topography (locations shown in a) with the topography of the Dead Sea Basin locations shown in Fig. 4d of the main article) It can be seen that the model basin becomes wider and the mountains smaller than at the DSB. (d–e) cross sections at the restraining and the releasing bend showing the stress regime and the sediment age. The colors of the stress regime are more intense for areas with high strain rate.

B.5 Vertical axis rotations

Observed shortening at the Lebanese restraining bend amounts to only 5 km. This is relatively small, which is attributed to a 22–60° counterclockwise rotation of blocks around a vertical axis (Dembo et al., 2021a). The same applies to our model's restraining bend, showing only minor shortening in the fault-parallel direction but substantial rotation around the z-axis close to the faults. We attribute this rotation to the offset in initial weaknesses representing inherited structures (Glerum et al., 2020). As suggested for the Lebanese mountains (Gomez et al., 2007), the main part of our modeled rotation happens before the mountain-cutting fault forms, while strain partitioning emerges after this event. Model rotation of the block to the west of the central fault in the restraining bend amounts to 15–30°, while we see only 5–15° next to the basin border faults. With paleomagnetic data from the Hula and Kinneret releasing stepovers (see Fig. 4a in main article for location) indicating rotation magnitudes of 4–32° (Dembo et al., 2021b), the model block rotations are at the lower end of observations for both types of bends. Both predicted and observed rotation is clockwise in between the faults and anticlockwise otherwise.

B.6 Seismicity patterns

Concerning deep seismicity, our models show high strain-rate values along the basin bordering faults that induce local rheological changes towards a brittle regime at usually ductily behaving depths

(Supplementary Fig. B.S4). In our models, this analog to deep earthquakes exists in combination with relatively high surface heat flow values. Indeed, we find that ∼45% of the brittle energy dissipation rate resides in the layer below 20 km depth, which is consistent with 40% of observed micro-earthquakes nucleating below 20 km (Aldersons et al., 2003).

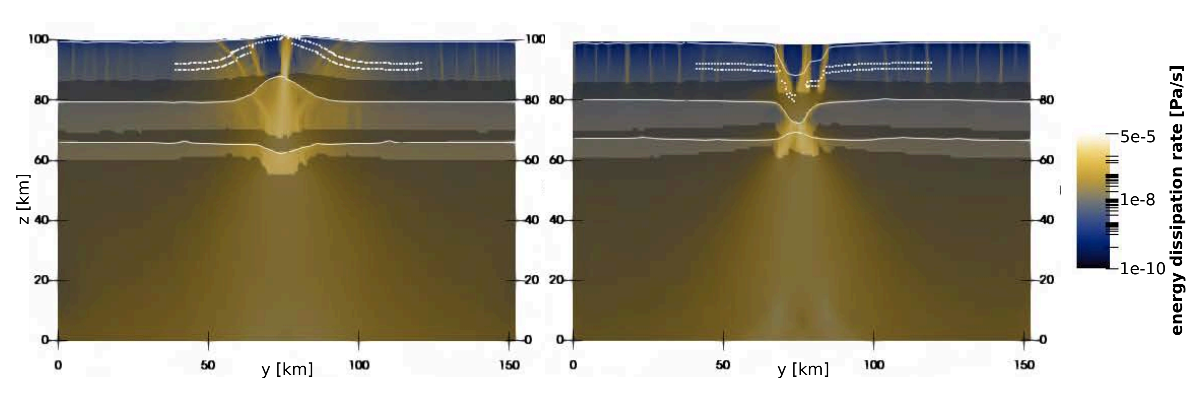

Figure B.S4: Cross sections at the restraining bend (x = 150 km) and the releasing bend (x = 450 km) showing the energy dissipation rate, which has been used as a model analog of the energy released by all earthquakes during the length of one time step (Petrunin et al., 2012). Layer outlines are shown as white lines and tracked particle locations as white dots to visualize deformation. Lighter areas behave in a brittle and darker areas behave in a ductile way.

B.7 Crustal deformation patterns

Crustal thinning and thickening occur near the releasing bend and restraining bend, respectively (Fig. 4.6 of the main manuscript). Thinning and thickening are correlated with the efficiency of surface processes. To assess its impact, we compared the three models using different surface process efficiencies and the model without any surface processes (Fig. 4.5 of the main text) as well as a model without erosion but with marine sedimentation regarding their crustal thickness changes over 20 Myr (Table B.S3). Below the pull-apart basin at the main fault, thinning in the model without surface processes amounts to 23%. However, when sedimentation is taken into account, the amount of crustal thinning increases to 38%. When erosion and sedimentation are included, thinning ranges between 40–41% for K_f between $0.25{\cdot}10^{-5}$ to $1{\cdot}10^{-5}$ $m^{0.2}$/yr. It should be noted that the lower crust experiences stronger thinning of ∼75%, while it is ∼15% for the upper crust. Below the highest elevations at the restraining bend, crustal thickening amounts to 39% for the purely geodynamic model, but is reduced to 24% for the reference model and to 16% for the model with high surface process efficiency. Crustal thickening at the restraining bend therefore shows a much stronger correlation with K_f than crustal thinning at the releasing bend. Moreover, while the lower crust is thickening more intensively for higher surface process efficiency with values between 85% and 106%, the upper crust experiences thinning for all models with erosion, and it only thickens when erosion is not accounted for. The thinning is more intensive for higher surface process efficiency (15% for K_f=0.25 $m^{0.2}$/yr, 45% for K_f=$1{\cdot}10^{-5}$ $m^{0.2}$/yr), which is a combined effect of erosion and increased uplift as described above. It is also the reason why at this place the amount of total crustal thickening decreases for higher surface process efficiencies. Additionally to these prominent changes directly at the restraining and the releasing bend, we also observe thinning and thickening of the crust away from the fault network. 25 km to the east of the pull-apart basin, crustal thinning increases with surface process efficiency just as below the basin, but it has values ranging between 6–16%. However, thinning of the upper crust amounts to >30% for all models including sedimentation. Contrarily, the lower crust experiences increasing thickening with increasing surface process efficiency ranging between 8–23%. Thickening of the lower crust surrounding the releasing bend is probably induced by the high amount of lower crustal thinning below the basin. 50 km to the east of the restraining bend, crustal thickening in both the lower and the upper crust amounts to ∼4% and slightly decreases with surface process efficiency. One exception from the low values is the upper crust of the purely geodynamic model without surface processes, which is thickened by 33%.

		Restraining bend		**Releasing bend**	
		x = 150 km		x = 450 km	
	surface process efficiency	**at the fault** y = 74 km	**surrounding** y = 125 km	**at the fault** y = 74 km	**surrounding** y = 100 km
upper crust	none	7	33	7	-2
	only sedimentation	6	5	-13	-3
	low	-14	4	-16	-3
	medium (ref model)	-26	5	-16	-3
	high	-45	2	-16	-4
lower crust	none	85	3	-68	1
	only sedimentation	85	3	-75	1
	low	105	5	-75	2
	medium (ref model)	98	4	-76	2
	high	106	4	-77	2
whole crust	none	39	4	-23	-1
	only sedimentation	38	4	-38	-2
	low	30	4	-40	-1
	medium (ref model)	24	4	-41	-1
	high	16	2	-41	-1

Table B.S3: Influence of the surface process efficiency on changes in crustal thickness for four locations. Values are given in percentage (%) of the initial layer thickness. Negative values indicate crustal thinning, positive values stand for crustal thickening. A value of 0 means no change in thickness, while -100% means complete thinning, while +100% means that the layer's thickness has doubled. The change in crustal thickness has been computed with $\Delta t = -(t_0 - t_{20})/t_0$, where t_0 is the initial thickness and t_{20} the thickness at 20 Myr. It can be seen that thinning and thickening mostly increases with increasing surface process efficiency. An opposite trend only exists at the restraining bend, for whole crustal thickness changes at y = 74 and 125 km and upper crustal changes at y = 125 km.

B.8 Animation

An animation of the reference model can be found at `https://zenodo.org/doi/10.5281/zenodo.10405076`. On the left side, the evolution of topography and sediment thickness are shown in two complementing color scales as a 3D surface. In the middle, cross sections of the stress regime at the two stepovers at $x_1 = 150$ km and $x_2 = 450$ km are shown. The white dotted lines show the initially horizontal layers of particles that are used as deformation markers. The line graphs on top show the x-, y- and z-components of the surface velocities of the two cross sections. On the right side, map views of topography, stress regime and boundary parallel velocity v_x are provided, from left to right, respectively. All three are overlain by strain rate. For more information on the parameters, see Fig. 4.5 of the main text.

References

Aldersons, F., Z. Ben-Avraham, A. Hofstetter, E. Kissling, and T. Al-Yazjeen (2003). “Lower-crustal strength under the Dead Sea basin from local earthquake data and rheological modeling”. en. In: *Earth and Planetary Science Letters* 214.1, pp. 129–142.

Ben-Avraham, Zvi and Mark D. Zoback (1992). “Transform-normal extension and asymmetric basins: An alternative to pull-apart models”. In: *Geology* 20.5, pp. 423–426.

Berry, M., J. van Wijk, D. Cadol, E. Emry, and D. Garcia-Castellanos (2019). “Endorheic-Exorheic Transitions of the Rio Grande and East African Rifts”. In: *Geochemistry, Geophysics, Geosystems* 20.7, pp. 3705–3729.

Braun, Jean and Sean D. Willett (2013). “A very efficient O(n), implicit and parallel method to solve the stream power equation governing fluvial incision and landscape evolution”. en. In: *Geomorphology* 180-181, pp. 170–179.

Dembo, Neta, Roi Granot, and Yariv Hamiel (2021a). “Mechanical contrast and asymmetric distribution of crustal deformation across plate boundaries: Insights from the northern Dead Sea fault system”. In: *Geology* 49.5, pp. 498–503.

Dembo, Neta, Yariv Hamiel, and Roi Granot (2021b). “The stepovers of the Central Dead Sea Fault: What can we learn from the confining vertical axis rotations?” en. In: *Tectonophysics* 816, p. 229036.

DESERT Group, M. Weber, K. Abu-Ayyash, A. Abueladas, A. Agnon, H. Al-Amoush, A. Babeyko, Y. Bartov, M. Baumann, Z. Ben-Avraham, G. Bock, J. Bribach, R. El-Kelani, A. Förster, H.-J. Förster, U. Frieslander, Z. Garfunkel, S. Grunewald, H. J. Götze, V. Haak, Ch. Haberland, M. Hassouneh, S. Helwig, A. Hofstetter, K.-H. Jäckel, D. Kesten, R. Kind, N. Maercklin, J. Mechie, A. Mohsen, F. M. Neubauer, R. Oberhänsli, I. Qabbani, O. Ritter, G. Rümpker, M. Rybakov, T. Ryberg, F. Scherbaum, J. Schmidt, A. Schulze, S. Sobolev, M. Stiller, H. Thoss, U. Weckmann, and K. Wylegalla (2004). “The crustal structure of the Dead Sea Transform”. In: *Geophysical Journal International* 156.3, pp. 655–681.

Garfunkel, Zvi (1981). “Internal structure of the Dead Sea leaky transform (rift) in relation to plate kinematics”. en. In: *Tectonophysics*. The Dead Sea Rift 80.1, pp. 81–108.

Gassmöller, Rene, Harsha Lokavarapu, Eric Heien, Elbridge Gerry Puckett, and Wolfgang Bangerth (2018). “Flexible and Scalable Particle-in-Cell Methods With Adaptive Mesh Refinement for Geodynamic Computations”. en. In: *Geochemistry, Geophysics, Geosystems* 19.9, pp. 3596–3604.

Glerum, Anne, Sascha Brune, D. Sarah Stamps, and Manfred R. Strecker (2020). “Victoria continental microplate dynamics controlled by the lithospheric strength distribution of the East African Rift”. en. In: *Nature Communications* 11.1, p. 2881.

Glerum, Anne, Cedric Thieulot, Menno Fraters, Constantijn Blom, and Wim Spakman (2018). “Nonlinear viscoplasticity in ASPECT: benchmarking and applications to subduction”. English. In: *Solid Earth* 9.2, pp. 267–294.

Gomez, F., T. Nemer, C. Tabet, M. Khawlie, M. Meghraoui, and M. Barazangi (2007). “Strain partitioning of active transpression within the Lebanese restraining bend of the Dead Sea Fault (Lebanon and SW Syria)”. en. In: *Geological Society, London, Special Publications* 290.1, pp. 285–303.

Hamiel, Yariv and Oksana Piatibratova (2019). “Style and Distribution of Slip at the Margin of a Pull-Apart Structure: Geodetic Investigation of the Southern Dead Sea Basin”. en. In: *Journal of Geophysical Research: Solid Earth* 124.11, pp. 12023–12033.

— (2021). “Spatial Variations of Slip and Creep Rates Along the Southern and Central Dead Sea Fault and the Carmel–Gilboa Fault System”. en. In: *Journal of Geophysical Research: Solid Earth* 126.9, e2020JB021585.

Heister, Timo, Juliane Dannberg, Rene Gassmöller, and Wolfgang Bangerth (2017). “High accuracy mantle convection simulation through modern numerical methods – II: realistic models and problems”. In: *Geophysical Journal International* 210.2, pp. 833–851.

Hirth, Greg and David Kohlstedt (2004). “Rheology of the Upper Mantle and the Mantle Wedge: A View from the Experimentalists”. In: *Inside the Subduction Factory*. American Geophysical Union (AGU), pp. 83–105.

Kronbichler, M., T. Heister, and W. Bangerth (2012). “High Accuracy Mantle Convection Simulation through Modern Numerical Methods”. In: *Geophysical Journal International* 191, pp. 12–29.

Le Beon, Maryline, Yann Klinger, Abdel Qader Amrat, Amotz Agnon, Louis Dorbath, Gidon Baer, Jean-Claude Ruegg, Olivier Charade, and Omar Mayyas (2008). “Slip rate and locking depth from GPS profiles across the southern Dead Sea Transform”. en. In: *Journal of Geophysical Research: Solid Earth* 113.B11.

Lubberts, Ronald K and Zvi Ben-Avraham (2002). “Tectonic evolution of the Qumran Basin from high-resolution 3.5-kHz seismic profiles and its implication for the evolution of the northern Dead Sea Basin”. en. In: *Tectonophysics*. Tectonics of Sedimentary Basins: from Crustal Structure to Basin Fill 346.1, pp. 91–113.

Neuharth, Derek, Sascha Brune, Anne Glerum, Chris K. Morley, Xiaoping Yuan, and Jean Braun (2021). “Flexural strike-slip basins”. In: *Geology* 50.3, pp. 361–365.

Neuharth, Derek, Sascha Brune, Thilo Wrona, Anne Glerum, Jean Braun, and Xiaoping Yuan (2022). “Evolution of Rift Systems and Their Fault Networks in Response to Surface Processes”. en. In: *Tectonics* 41.3, e2021TC007166.

Petrunin, Alexey G., Ernesto Meneses Rioseco, Stephan V. Sobolev, and Michael Weber (2012). “Thermomechanical model reconciles contradictory geophysical observations at the Dead Sea Basin”. en. In: *Geochemistry, Geophysics, Geosystems* 13.4.

Quennell, Albert Mathieson (1959). *Tectonics of the Dead Sea rift*. Vol. 385.

Rutter, E. H. and K. H. Brodie (2004). “Experimental grain size-sensitive flow of hot-pressed Brazilian quartz aggregates”. In: *Journal of Structural Geology* 26.11, pp. 2011–2023.

Rybacki, E., M. Gottschalk, R. Wirth, and G. Dresen (2006). “Influence of water fugacity and activation volume on the flow properties of fine-grained anorthite aggregates”. In: *Journal of Geophysical Research: Solid Earth* 111 (B3).

Wdowinski, S. and Ezra Zilberman (1996). “Kinematic modelling of large-scale structural asymmetry across the Dead Sea Rift”. en. In: *Tectonophysics.* Dynamics of Extensional Basins and Inversion Tectonics 266.1, pp. 187–201.

Willett, Sean D. (1999). “Orogeny and orography: The effects of erosion on the structure of mountain belts”. In: *Journal of Geophysical Research: Solid Earth* 104 (B12), pp. 28957–28981.

Yuan, X. P., J. Braun, L. Guerit, B. Simon, B. Bovy, D. Rouby, C. Robin, and R. Jiao (2019). “Linking continental erosion to marine sediment transport and deposition: A new implicit and O(N) method for inverse analysis”. en. In: *Earth and Planetary Science Letters* 524, p. 115728.